

**Many-body Effects in
Anisotropic Dielectric Colloids:
Polarization, Electrostatic Interactions,
and Van der Waals Forces**

Cover: A normal mode observed in a pair of 20×20 squares of Lorentz atoms. The arrows represent the amplitude of vibration of each atom's dipole moment. The front cover shows one square, while the back shows the other (both are not shown fully). The spine represents the gap between the squares, which is not to scale. As can be seen, this mode vibrates mostly near the gap, which means that it contributes to the squares' Van der Waals interaction.

PhD thesis, Utrecht University, the Netherlands, September 2013.

ISBN: 978-90-8891-686-1

A digital version of this thesis is available at <http://web.science.uu.nl/SCM/>

Printed by: Uitgeverij BOXPress, 's-Hertogenbosch

**Many-body Effects in Anisotropic Dielectric Colloids:
Polarization, Electrostatic Interactions,
and Van der Waals Forces**

Veeldeeltjeseffecten in Anisotrope Diëlektrische Colloïden:
Polarisatie, Elektrostatische Interacties,
en Vanderwaalskrachten

(met een samenvatting in het Nederlands)

Proefschrift

ter verkrijging van de graad van doctor aan de Universiteit Utrecht op gezag van de rector magnificus, prof. dr. G. J. van der Zwaan, ingevolge het besluit van het college voor promoties in het openbaar te verdedigen op maandag 9 september 2013 des ochtends te 10.30 uur

door

Bastiaan Willem Kwaadgras

geboren op 2 augustus 1985 te Dordrecht.

Promotoren: Prof. dr. ir. M. Dijkstra
Prof. dr. R. H. H. G. van Roij

Dit werk maakt deel uit van het onderzoeksprogramma van de Stichting voor Fundamenteel Onderzoek der Materie (FOM), die deel uitmaakt van de Nederlandse Organisatie voor Wetenschappelijk Onderzoek (NWO).

Contents

1	Introduction	1
1.1	Colloids and Nanoparticles	2
1.2	Polarization	3
1.3	Van der Waals Interactions	6
1.4	Coupled Dipole Method	7
1.5	Thesis Outline	8
2	Polarizability and Alignment of Dielectric Nanoparticles in an External Electric Field: Bowls, Dumbbells, and Cuboids	9
2.1	Introduction	10
2.2	Formalism of the CDM: Potential Energy, Polarizability, and Orientational Energy	10
2.2.1	Static Polarizability and Orientational Energy of Dipole Clusters in an External Electric Field	11
2.2.2	Rotationally Symmetric Clusters	14
2.2.3	Fourfold Rotationally Symmetric Clusters	15
2.2.4	Units of Distance	16
2.2.5	Comparison with Continuum Theory	16
2.3	Dielectric Rods and Platelets	17
2.4	Dielectric Bowls and Dumbbells	21
2.4.1	Bowls	22
2.4.2	Dumbbells	24
2.5	Conclusions and Outlook	26
3	Global and Local Enhancement Factor of Cubes and Spheres	27
3.1	Introduction	28
3.2	Theoretical Predictions	29
3.3	Numerical Methods	30
3.3.1	Exploiting Symmetry	30
3.3.2	The Gauss-Seidel Method	30
3.4	Numerical Results for Cubes	31
3.4.1	Global Enhancement Factor	31
3.4.2	Local Enhancement Factor	33
3.4.3	Polarization Charge	36
3.5	Numerical Results for Spheres	38
3.5.1	Global Enhancement Factor	38

3.5.2	Local Enhancement Factor	39
3.6	Conclusions and Outlook	41
4	The Optimal Shape for Alignment in an External Electric Field: Bowls, Dumbbells, and Cuboids	43
4.1	Introduction	44
4.2	Theory	44
4.3	Rods and Platelets	46
4.4	Bowls and Dumbbells	47
4.5	Conclusion	49
5	Can Nonadditive Dispersion Forces Explain Chain Formation of Nanoparticles?	51
5.1	Introduction	52
5.2	Methods	53
5.2.1	The Coupled Dipole Method	53
5.2.2	The Hamaker-de Boer Potential	55
5.2.3	The Axilrod-Teller Potential	56
5.2.4	A Note on Notation	57
5.3	Chains versus Compact Clusters	57
5.3.1	Atomic Chains and Clusters	57
5.3.2	Clusters and Chains of Spherical Nanoclusters	59
5.3.3	Clusters and Chains of Cubic Nanoclusters	62
5.4	Summary and Conclusion	63
6	The Self-Consistent Electric Field-Induced Dipole Interaction Energy of Particles in an External Electric Field: Spheres, Cubes, and Rods	67
6.1	Introduction	68
6.2	The CDM	69
6.3	Identical Inducible Dipoles with Isotropic Polarizability	73
6.3.1	Van der Waals Interaction	74
6.3.2	Induced-Dipole Interaction	75
6.4	Interaction between Cluster Pairs	78
6.4.1	Methods	78
6.4.2	Numerical Results for Spheres	81
6.4.3	Numerical Results for Cubes	85
6.4.4	Numerical Results for Rods	89
6.4.5	Numerical Results for Misaligned Particles	92
6.5	Conclusion	101
7	Miscellaneous	103
7.1	Introduction	104
7.2	Density of States of Dipole Polymers	104
7.2.1	Theoretical Calculation for an Infinite Polymer	107
7.2.2	Summary and Conclusion	111
7.3	Modes in Interacting Square Plates	111

7.3.1	Methods	112
7.3.2	Results	113
7.3.3	Summary and Conclusion	118
7.4	Coupled Dipoles near a Conducting Plate	120
7.4.1	Theory	120
7.4.2	Results and Discussion	121
7.4.3	Summary and Conclusion	125
A	Proof that the Cluster Polarizability is a Symmetric Matrix	127
A.1	Introduction	128
A.2	Proof of the Symmetry of the Polarizability Matrix	128
A.2.1	Proof of the Assertion $\mathbf{Y}_{ij} = \mathbf{Y}_{ji}^T$.	128
B	Exploiting Spatial Symmetries in Large Cubes and Spheres	135
C	Additional Mathematical and Numerical Comparisons	139
D	Additional Analytical Expressions for the Self-Consistent Electric Field-Induced Dipolar Interaction Energy	143
	References	147
	Summary	155
	Samenvatting	159
	Acknowledgments	163
	About the Author	165

Introduction

In this chapter we provide a brief introduction to the subject matter of this thesis. We introduce colloids and nanoparticles, discuss their relevance, and mention some recent developments in this research area. We then discuss the polarization of dielectrics, which is of primary importance to this thesis. We introduce the atomic polarizability and the Clausius-Mossotti relation. Subsequently, we give a brief introduction to Van der Waals forces and, more specifically, London dispersion forces, before going into specific methods for their calculation. Primarily, we focus on the Coupled Dipole Method, which is the method used throughout this thesis, for calculating not only London dispersion forces but also polarization and electrostatic interactions. We end with a brief outline of the remaining chapters.

1.1 Colloids and Nanoparticles

Colloids are particles with a size roughly between 1 nm and 1 μm , whose name is derived from the Greek word for glue, $\kappa\acute{o}\lambda\lambda\alpha$. Thomas Graham originally invented the term for substances that do not, or only very slowly, diffuse through parchment (e.g., glue and gelatin), unlike what he called crystalloids (such as salts, sugars, acids and bases), which diffuse quickly [1]. While this distinction turned out to be somewhat artificial, as under different circumstances Graham’s “colloids” may act as crystalloids or vice versa, the name stuck for substances that are suspensions of mesoscopic particles. We note that the term “colloid” seems to have originally been used to refer to a system of such mesoscopic particles [2], whereas it is now frequently used to refer to the particles themselves. In this thesis, we will always use the latter, newer definition, as given in the first sentence.

One of the defining characteristics of colloids is that they exhibit Brownian motion when suspended in a fluid. Named after botanist Robert Brown, who in 1827 described the phenomenon as observed in pollen grains suspended in water [3], Brownian motion refers to the erratic motion that colloidal particles display due to the constant bombardment by solvent atoms and/or molecules. Averaged over a long time, the number of collisions on each side of the particle will be roughly equal, but at shorter time scales the number of collisions per unit of time will fluctuate. As a result, the particle experiences “pushes” in random directions, causing its kinetic energy to undergo fluctuations of the order of the thermal energy $k_B T$, where k_B is Boltzmann’s constant and T is the temperature. For heavy objects, the thermal energy is too low for Brownian motion to have a noticeable effect on the object’s motion, while very small particles such as atoms and molecules are generally difficult to observe in real time and space. When it comes to size and mass, colloids are in the “sweet spot” in-between: still large enough to be reasonably easily observable using microscopes but light-weight enough to experience significant effects from Brownian motion. At the time of Brown’s publication, the atomic theory was still disputed and Brownian motion was a crucial factor in settling this dispute: Albert Einstein’s 1905 theoretical description [4] of Brownian motion in terms of atoms and molecules and Jean Perrin’s 1908 experimental verification [5] of this theory led to the final acceptance of the atomic theory Dalton had proposed more than a century earlier [6].

Colloids and nanoparticles are found in many everyday substances. Well-known examples include aerosols such as mist and smoke, emulsions such as milk, and sols such as blood. These examples occur naturally, but colloids have also appeared in man-made substances since prehistoric times, including in butter, cheese and, fittingly, some early glue types such as animal glue [7]. Of course, the fact that these substances contain colloids was not known until relatively recently, when the advent of the microscope made it possible to study samples at unprecedentedly small length scales. Today, control over the fabrication of colloids is extensive and, accordingly, their use has broadened spectacularly: for example, they are of medicinal use as drug deliverers or antibiotics, are used for catalytic purposes in the chemical industry, can be found in paints, are employed by the food industry to chemically stabilize as well as to control the various properties (e.g., texture) of foods, and are the crucial ingredient of LCD screens and electronic paper.

Not only has the variety of materials used for colloid fabrication increased, but the accessible size range has also widened and now comprises the nanoscale. Such nano-sized

colloids are called nanoparticles. Another, mostly recent, development is that the fabricated particles can be anisotropic. For example, by controlling the surface chemistry of the particles, for instance when synthesizing colloids with patches of different materials [8–10], or by using single-stranded DNA molecules as linkers [11, 12], interparticle interactions can be modified. However, the most obvious way of making particles anisotropic is by making them nonspherical. The collection of shapes that can be fabricated today is enormous [13], but in this thesis we will restrict ourselves to spheres, cubes [14], dumbbells [15–18], bowls [17, 19, 20], rods [21, 22] and platelets. The result of the anisotropy of the particles (and/or their interactions) is that they can, under certain conditions, spontaneously form interesting new ordered structures that one does not observe with isotropic particles [23–28]. The process by which ordered structures appear without external influence on the system is called self-assembly [29, 30]. We note that Brownian motion is essential for self-assembly because, without it, the system would not be able to effectively explore its phase space and find its optimal configuration. However, since the process of self-assembly is often difficult to achieve in practice and hampered by slow dynamics, several techniques can be employed to assist it [29, 31], such as introducing a substrate to the system [32, 33], employing fluid flows [34], or applying magnetic [35] or electric [36–39] fields. We note that, strictly speaking, this can no longer be called self-assembly because of the presence of an external influence; assembly that happens through thermodynamic processes but with certain pre-set external influences is often referred to as assisted self-assembly.

1.2 Polarization

The earliest account of experimentation involving electric charge and electric polarization is commonly attributed to Thales of Miletus (ca. 624 BC - ca. 547–546 BC), said to be the first Western philosopher [40, 41]. Although there are plenty of stories of how Thales rubbed amber (in Greek: ἤλεκτρον) with fur and noted that it subsequently attracted small objects, it is uncertain whether he in fact ever wrote down anything at all [42]. It seems that the only surviving antique reference to Thales’ amber experiment is by Diogenes Laërtius (3rd century AD) and it is rather minimalistic [43]: Laërtius only writes that Thales believed that inanimate objects had souls because of “Magnesian rock and amber”, citing Aristotle (384 BC - 322 BC) and Hippias (late 5th century BC), an Elean sophist contemporary to Socrates of whom no work survives. Aristotle indeed writes [44] that Thales’ belief that rock had a soul was based on the fact that rock could move iron, but he does not mention amber, likely making Hippias the first to have written about the amber experiment. In fact, Hippias might have also been Aristotle’s source for the reference to magnetism [42]. In any case, references to static electricity are widespread in the Mediterranean world from the time of Plato (427 BC - 347 BC), who himself hazarded a (rather vague) guess as to what might be the explanation for amber’s mysterious electrical properties.

It seems not unreasonable to assume that knowledge of the electrostatic phenomena associated with amber were in fact much older than Hippias or Thales. Since prehistory, amber had been used as jewelry and as material for buttons, and fur as clothing, making

the rubbing of amber and the resulting electrostatic effects phenomena likely to have been observed by humans. Thales may simply have used pre-existing knowledge to motivate his belief that all things had souls.

Electric polarization plays a role in Thales' experimentation because of the effect that the electrically charged amber had on other objects, such as hair, straw, feathers, or small pieces of papyrus [45]. The charge would induce a dipole moment in those objects, causing them to be attracted to the amber. This explanation was, of course, unknown to the ancients; it not only requires the concept of electric charge but also that of positive and negative charge and polarization, ideas which did not appear until the mid-18th century with the work of Benjamin Franklin. The idea of there being only one type of electricity but with opposite polarities was reinforced by Faraday's 1839 experiments [46].

Michael Faraday is also of interest to us because he was the first to conduct experiments showing that the capacitance of a capacitor increases when an insulator is placed between the capacitor plates, indicating that the insulator gains an induced polarization [47–50]. This behavior may at first seem counter-intuitive: if charges cannot move inside the insulator and the insulator is electrically neutral throughout, one may expect there to be no polarization at all and, thus, the capacitance to remain unaffected. If one places a conductor (instead of an insulator) between the plates, it can be easily shown [45] that the capacitance increases as the inverse of the fraction of space between the plates *not* occupied by the conductor. From this, Faraday and others reasoned that insulators in fact had small conducting regions inside them that would become polarized when the capacitor was charged. If one associates these regions with atoms, this explanation is not very far from the truth, although one significant problem is that the induced polarization is dependent on the volume that the atoms occupy.

Nowadays we know that atoms polarize depending not on the volume they occupy but on other atomic properties. A simple yet effective model for describing atomic polarization is the Lorentz model, which describes an atom as composed of a nucleus with charge e with a spherical electron cloud with total charge $-e$ around it. If the cloud is assumed to have a homogeneous negative charge density ρ , the equilibrium position for the nucleus is at the center of the cloud: a situation where the atom has no dipole moment. If the nucleus is displaced a distance d from the sphere center, the restoring force can be calculated by noting that the enclosed charge inside a spherical Gaussian surface of radius d is $Q = \frac{4}{3}\pi d^3 \rho$, so that the restoring force acting on the nucleus is $F = \frac{\frac{4}{3}\pi d^3 e \rho}{d^2} \propto d$, i.e., a harmonic force. Calling its characteristic frequency ω_0 , we can write the restoring force as $\mathbf{F} = -m_e \omega_0^2 \mathbf{d}$, where m_e is the mass of the electron. In effect, an atom described in this way is a harmonic oscillator with frequency ω_0 , sometimes called a Drude oscillator. If a static electric field \mathbf{E}_0 is applied, the charge is displaced until the restoring force is equal to the force resulting from the external electric field, so $m_e \omega_0^2 \mathbf{d} = e \mathbf{E}_0$ [51], such that the induced dipole moment $\mathbf{p} = e \mathbf{d}$ is

$$\begin{aligned} \mathbf{p} &= \frac{e^2}{m_e \omega_0^2} \mathbf{E}_0 \\ &\equiv \alpha_0 \mathbf{E}_0 \end{aligned}$$

where the proportionality factor

$$\alpha_0 = \frac{e^2}{m_e \omega_0^2} \quad (1.1)$$

is the atomic polarizability, which has units of volume (in CGS) and is typically of the order of cubic Ångströms. We note that the magnitude of \mathbf{d} is typically very small; e.g., for $\alpha_0 = 5 \text{ \AA}^3$ and a strong electric field of $E_0 = 100 \text{ statV cm}^{-1} = 3 \text{ V } \mu\text{m}^{-1}$, we find $d = \alpha_0 E_0 / e \approx 10^{-12} \text{ cm}$. For comparison, the Bohr radius is about three orders of magnitude larger. This suggests that even though the provided model of a homogeneous charge density may seem simplistic and we have ignored the complications of quantum mechanics, using a harmonic force seems sensible since, to first-order approximation, most spatially symmetric potential wells are harmonic wells.

Determining the exact numerical value to assign to α_0 is a highly nontrivial task. It is not reliable to simply insert a value for ω_0 into Eq. (1.1) since, due to the simplifications of the model, it is not clear what value to use. A more accurate method is to first determine the bulk (macroscopic) electrostatic properties of the material we wish to model and then, using the Clausius-Mossotti relation, work out the atomic polarizability. The Clausius-Mossotti relation, named after the physicists Ottaviano-Fabrizio Mossotti and Rudolf Clausius, gives an approximate relationship between a material's dielectric constant ϵ and its atomic polarizability α_0 . It supposes that when an electric field \mathbf{E}_0 is applied to a material, the atoms experience a total electric field equal to \mathbf{E}_0 plus a contribution due to the macroscopic polarization of the material, such that the average atomic dipole moment obeys [51]

$$\langle \mathbf{p}_0 \rangle = \alpha_0 \left(\mathbf{E}_0 + \frac{4\pi}{3} \mathbf{P} \right).$$

Using $\mathbf{P} = n \langle \mathbf{p}_0 \rangle$, where n is the atomic number density of the material, and substituting $\mathbf{P} = \frac{1}{4\pi} (\epsilon - 1) \mathbf{E}_0$ (in CGS), we have

$$\alpha_0 n = \frac{3}{4\pi} \left(\frac{\epsilon - 1}{\epsilon + 2} \right). \quad (1.2)$$

This equation is approximately accurate for a piece of material (particle) with dielectric constant ϵ in vacuum. If the particle is suspended in a medium with dielectric constant ϵ_m , we instead have an effective atomic polarizability given by

$$\alpha_0 n = \frac{3}{4\pi} \epsilon_m \left(\frac{\epsilon/\epsilon_m - 1}{\epsilon/\epsilon_m + 2} \right). \quad (1.3)$$

If indices of refraction are used instead of dielectric constants, the equation is usually referred to as the Lorenz-Lorentz equation [51]. We note that for 3-dimensional lattices, $n \propto a^{-3}$, where a is the lattice constant. Inserting this into Eq. (1.3), we see that the dimensionless lattice constant $a/\alpha_0^{1/3}$ could be used instead of ϵ/ϵ_m to characterize a material's electrostatic properties. This dimensionless lattice constant also appears naturally in the theoretical method that we will be using in this thesis (the Coupled Dipole Method, elaborated in Sec. 1.4), as a parameter controlling atom-atom coupling.

1.3 Van der Waals Interactions

Van der Waals interactions are named after Dutch physicist Johannes van der Waals, who in the 7th chapter of his PhD thesis derived an equation of state for a system of particles with short-range repulsion and long-range attraction, reasoning that the former could be modeled by reducing the volume available to the particles and the latter by a term proportional to the square of the particle density. Today, we denote by Van der Waals forces all the intermolecular forces that are not due to bond formation or to the electrostatic interaction of ions or ionic groups with one another or with neutral molecules [2]. These forces include interactions between permanent dipoles, between a permanent dipole and a dipole induced by that permanent dipole, and between two instantaneously induced dipoles (the London dispersion force, elaborated on below). Because we do not consider particles with permanent dipoles in this thesis, we will refer to this London dispersion force as “Van der Waals” force. Another force that we are interested in is the force between two induced dipoles under the influence of an electric field. We will refer to such forces as induced dipole interactions.

The London dispersion force is named after German physicist Fritz London, who, using quantum mechanical perturbation theory, first derived the interaction energy between a pair of noble gas atoms [52–54]. He found that this interaction energy was proportional to r^{-6} (hence the force is proportional to r^{-7}), where r is the distance between the atoms. It was found later that by modeling the atoms as dipoles with a Boltzmann-weighted random orientation distribution and calculating their average interaction energy, the same r -dependence could be recovered, which is why the force is often also referred to as the instantaneous induced dipole-induced dipole force. Of course, since colloids are made of atoms, the London dispersion force does not only occur between single atoms but also between colloidal particles in suspension. The force is, because of its strong decay as a function of r , mostly negligible over long distance, but can be extremely strong at short distances, causing particles to aggregate and form larger clumps of material. To prevent this aggregation, experimentalists often add steric molecules to the surface of the particles: the resulting steric interactions ensure that the particles do not get close enough to aggregate. Another way to keep the particles apart is to electrically charge them and tune the salt concentration of the medium appropriately: the resulting combination between a London dispersion attraction and a screened Coulomb repulsion is described by Derjaguin-Landau-Verwey-Overbeek (DLVO) theory [55, 56], which features a strong short-range attraction, a medium-range repulsion, and a long-range attraction, allowing for the possibility of “trapping” particles at a certain distance controllable by varying the salt concentration.

There are various methods of calculating the interaction between colloidal particles or other spatially extended bodies such as films. Arguably the simplest method is by summation of the London interaction between pairs of atoms, an approach known as the Hamaker-de Boer approach [57]. Another approach is to instead treat each particle as a continuum and integrate the pairwise interaction between volume elements, which is what Hamaker first did for pairs of spheres [58]. In his 1955 paper [59], Lifshitz also took a continuum approach but arrived at an interaction energy by introducing fluctuating terms to the Maxwell equations and assigning the energy of a harmonic oscillator to

each mode. The resulting calculations are rather involved but also general, being able to account for the effects of retardation and finite temperature. A significant problem, though, is that Lifshitz theory requires values for the dielectric function at imaginary frequencies. These can only be calculated via the Kramers-Kronig relation, but this relation requires knowledge of the dielectric function over a wide range of frequencies, of which the low frequencies are particularly problematic since no optical experimental data is available for low-enough frequencies. Recently, a solution was proposed that weighs the Kramers-Kronig integral such that the low frequencies do not contribute as much [60]. In this thesis we will not employ continuum theories but will instead describe particles as discrete “chunks” of matter.

1.4 Coupled Dipole Method

The Coupled Dipole Method (CDM) was introduced by Renne and Nijboer in the 1960s [61–63]. For this method, dielectric matter is supposed to be built up of discrete Lorentz atoms (i.e., inducible dipoles with no permanent dipole moment) located on certain fixed lattice sites. A cluster of these atoms then represents a particle. The atoms interact with each other: if one atom gains a polarization, it will produce an electric field which will induce a polarization in the other atoms. The harmonic modes of this system of N coupled dipoles can be calculated by diagonalizing a large $(3N \times 3N)$ matrix. As in Lifshitz’s method, each of these modes is assigned an energy equal to that of a harmonic oscillator with the same frequency, and the sum of all these harmonic oscillator energies then results in a potential energy. In other words, the system can be seen as a harmonic oscillator in $3N$ dimensions, with characteristic frequencies in each dimension given by a normal mode of the oscillator. The CDM, which can be shown to yield the Van der Waals interaction between two atoms [61, 64, 65], was originally intended to calculate the London dispersion forces between dielectric particles consisting of multiple atoms and has been applied as such relatively recently [64, 66–70]. Because it includes many-body effects, the CDM can be expected to give more accurate London dispersion forces than pairwise approaches such as the aforementioned Hamaker-de Boer theory. However, the CDM is not limited to calculating London dispersion forces: we will show in this thesis that its Hamiltonian can also be extended to include an external electric field, such that the polarizability and the induced dipolar interaction of particles of arbitrary shape can be calculated as well. An important limitation of the CDM is that, due to its reliance on the Lorentz model in which electrons are bound to their respective atoms, it can not be used to describe metals because those contain free (unbound) electrons.

The effect of an electric field on systems of coupled dipoles has been studied before in scattering calculations within the Discrete Dipole Approximation, which involves an incident oscillating electric field [71–74]. Forces on particles in optical traps have also been calculated using the CDM [75–80]. Moreover, polarizability has also been studied in recent years by replacing the oscillating external field with a permanent one [81]. In this thesis, we only consider homogeneous static electric fields and use a Hamiltonian approach, leading straightforwardly to orientational potential energies of particles subjected to such an electric field.

At the time that the CDM was conceived of, it was infeasible to computationally perform the large-scale matrix manipulations involved in the CDM, but everyday computers of today can easily handle atom numbers of the order of 10^4 . Still, this is lower than the number of atoms found in most colloidal particles. To remedy this limitation, we remember that not just atoms but any “chunk” of matter will, in first-order approximation, gain a polarization proportional to the applied electric field. Therefore, the Lorentz atoms employed by the CDM do not necessarily have to represent physical atoms but can instead be thought of as a discretization of matter necessary for employing a coupled dipole scheme. In the first three chapters (chapters 2, 3 and 4) we will still work with Lorentz atoms that have atomic proportions, while in chapter 5 we will present a slight generalization of the CDM which will enable us to also compute results if the dipoles represent larger chunks of matter.

1.5 Thesis Outline

In this thesis, we will employ the CDM to investigate various electrostatic properties of dielectric particles of various shapes. In Chapter 2, we calculate the polarizability tensor of cuboid-shaped (rods and platelets), bowl-shaped and dumbbell-shaped particles and use it to calculate the orientation-dependent energy of these particles in an external electric field. In Chapter 3, we take a close look at the local polarization inside a cubic and a spherical particle. In Chapter 4, we investigate the minimum size for which dielectric particles may be aligned by an external electric field and the dependence of this minimum size on the shape of the particle. In chapter 5, we calculate the London dispersion forces between single inducible dipoles, spheres and cubes and investigate whether these particles prefer to form linear or compact particle clusters. Moreover, we study in detail the accuracy of various other calculation techniques with respect to the CDM. In Chapter 6, we investigate the electric field-induced dipolar interactions between particles and again compare the accuracy of various calculation techniques to the CDM. Chapter 7 contains a number of incomplete studies, which may form an interesting basis for future research.

Polarizability and Alignment of Dielectric Nanoparticles in an External Electric Field: Bowls, Dumbbells, and Cuboids

We employ the Coupled Dipole Method (CDM) to calculate the polarizability tensor of various anisotropic dielectric clusters of polarizable atoms, such as cuboid-, bowl-, and dumbbell-shaped nanoparticles. Starting from a Hamiltonian of a many-atom system, we investigate how this tensor depends on the size and shape of the cluster. We use the polarizability tensor to calculate the energy difference associated with turning a nanocluster from its least to its most favorable orientation in a homogeneous static electric field and we investigate the dependence of this energy difference on the cluster size.

2.1 Introduction

Monodisperse (colloidal) particles with a wide variety of shapes can nowadays be synthesized in the nano- to micrometer size regime [13, 15]. These particles can serve as building blocks for new materials and devices with great technological potential. Self-assembly of the particles is an important process by which large-scale nano-structures can be formed. This self-assembly process can be spontaneous in the case of favorable thermodynamic conditions and suitable effective particle-particle interactions [23–27, 29–31], but can also be steered and further manipulated by external fields. Rodlike particles in a liquid dispersion, for instance, can spontaneously align at sufficiently high concentrations solely due to their excluded volume interactions [28], but their self-organization has also been driven by external magnetic or electric fields [33, 35–39], by substrates that preferentially orient the rods [32, 38], or by fluid flow [34]. More complicated shapes have also been synthesized and studied, for instance dumbbells [15–18], cubes [82], and bowls [17, 19, 20].

In this chapter we study the electric-field assisted alignment of anisotropic nanoparticles by calculating their polarizability tensor using the Coupled Dipole Method (CDM) [61, 64, 66–69, 83–85]. We first describe the formalism of the CDM, deriving, through a Hamiltonian approach, expressions for the polarizability tensor, potential energy and orientational electrostatic energy of non-spherical clusters of Lorentz atoms. We then proceed to numerically calculate these quantities for specific particle shapes. We focus here on cuboid-shaped (rods and platelets), bowl-shaped, and dumbbell-shaped particles, for which we consider various shape and size parameters. For alignment experiments, quantities such as the polarizability and the resulting orientational electrostatic energy are highly relevant because the value of the latter relative to the thermal energy determines the degree of orientational order that can be achieved in systems where interparticle interactions are negligible. We elaborate more on the relationship between the orientational energy and the nematic order parameter in Chapter 4. The polarizability of shapes similar to the ones considered here has in recent years been studied using continuum electrostatics [86–90] and, on several occasions, we briefly compare those results to ours.

2.2 Formalism of the CDM: Potential Energy, Polarizability, and Orientational Energy

As mentioned in Chapter 1, the CDM models matter as being built up out of Lorentz atoms. In this chapter, we assume each atom to be identical, such that each has the same atomic polarizability α_0 as given by Eq. (1.1) and, by extension, the same characteristic frequency ω_0 . If N of these atoms are brought together and allowed to interact, the dipole-dipole interactions will influence the electric properties of the cluster as a whole. In general, the total polarizability of the cluster cannot be expected to equal $N\alpha_0$, but will instead be modified because the atoms are subject to each other's induced electric field.

2.2.1 Static Polarizability and Orientational Energy of Dipole Clusters in an External Electric Field

The Hamiltonian of a set of N Lorentz atoms at fixed positions \mathbf{r}_i ($i = 1, \dots, N$) has been given and studied in Refs. [61, 64, 66–69]. In the present work, we use the same Hamiltonian but add an extra term to allow for an externally exerted, spatially homogeneous electric field \mathbf{E}_0 , such that the complete expression for the Hamiltonian is

$$H = \sum_{i=1}^N \frac{\mathbf{k}_i^2}{2m_e} + \sum_{i=1}^N \frac{m_e \omega_0^2 \mathbf{d}_i^2}{2} - \sum_{i,j=1}^N \frac{e^2 \mathbf{d}_i \cdot \mathbf{T}_{ij} \cdot \mathbf{d}_j}{2} - \sum_{i=1}^N e \mathbf{d}_i \cdot \mathbf{E}_0, \quad (2.1)$$

where we denote the momentum of the electron of atom i by \mathbf{k}_i , and its displacement from the atom nucleus by \mathbf{d}_i . The 3×3 matrix \mathbf{T}_{ij} is the dipolar tensor, given in terms of the separation vector $\mathbf{r}_{ij} = \mathbf{r}_i - \mathbf{r}_j$ of atoms i and j , by

$$\mathbf{T}_{ij} = \begin{cases} \frac{(3\mathbf{r}_{ij}\mathbf{r}_{ij}/|\mathbf{r}_{ij}|^2 - \mathbf{I})}{|\mathbf{r}_{ij}|^3} & \text{if } i \neq j, \\ \mathbf{0} & \text{if } i = j, \end{cases} \quad (2.2)$$

where \mathbf{I} denotes the 3×3 identity matrix and $\mathbf{0}$ denotes the 3×3 null matrix. Note that the dipolar tensor is not only symmetric in its indices, $\mathbf{T}_{ij} = \mathbf{T}_{ji}$, but also in its elements, $\mathbf{T}_{ij} = \mathbf{T}_{ij}^T$. As is clear from the Hamiltonian (2.1) and the form of \mathbf{T}_{ij} , this model describes interatomic interactions in an instantaneous, non-retarded way. Therefore, the validity of the theory for Van der Waals interactions is limited to model systems where the relevant length scales are small enough for the speed of light to be essentially infinite. This is because these interactions are due to dipolar fluctuations with time scales comparable to the time it takes for light to travel across the system size. However, quantities such as polarization and polarizability are static quantities and are expected to be accurate for any system size.

We now introduce $3N$ -dimensional vectors \mathcal{K} , \mathcal{D} and \mathcal{E}_0 , which are built up from the \mathbf{k}_i , \mathbf{d}_i and N copies of \mathbf{E}_0 , respectively. We also introduce a $3N \times 3N$ -dimensional matrix \mathcal{T} , built up from the \mathbf{T}_{ij} . In terms of these objects, the Hamiltonian (2.1) is given by

$$H = \frac{\mathcal{K}^2}{2m_e} + \frac{1}{2} m_e \omega_0^2 \mathcal{D} \cdot (\mathcal{I} - \alpha_0 \mathcal{T}) \cdot \mathcal{D} - e \mathcal{D} \cdot \mathcal{E}_0,$$

where α_0 is given in Eq. (1.1), and \mathcal{I} denotes the $3N \times 3N$ -dimensional identity matrix. Next, we introduce a $3N$ -dimensional vector \mathcal{D}_0 that satisfies

$$m_e \omega_0^2 (\mathcal{I} - \alpha_0 \mathcal{T}) \cdot \mathcal{D}_0 = e \mathcal{E}_0, \quad (2.3)$$

and use it to complete the square in the Hamiltonian, obtaining

$$H = H_0 + V_E, \quad (2.4)$$

with

$$H_0 = \frac{\mathcal{K}^2}{2m_e} + \frac{1}{2} m_e \omega_0^2 (\mathcal{D} - \mathcal{D}_0) \cdot (\mathcal{I} - \alpha_0 \mathcal{T}) \cdot (\mathcal{D} - \mathcal{D}_0) \quad (2.5)$$

$$V_E = -\frac{1}{2} \alpha_0 \mathcal{E}_0 \cdot (\mathcal{I} - \alpha_0 \mathcal{T})^{-1} \cdot \mathcal{E}_0. \quad (2.6)$$

Note that V_E is constant with respect to the generalized momenta and coordinates \mathcal{K} and $\mathcal{D} - \mathcal{D}_0$, respectively. The $3N$ oscillatory modes associated with the (harmonic) Hamiltonian H_0 are given by

$$\left(\mathcal{D}^{(k)} - \mathcal{D}_0\right)(t) = \left(\mathcal{D}^{(k)} - \mathcal{D}_0\right)(0) \exp(-i\omega_k t) \quad (k = 1, \dots, 3N), \quad (2.7)$$

where the amplitude vectors $\left(\mathcal{D}^{(k)} - \mathcal{D}_0\right)(0)$ and the frequencies ω_k are given by an eigenvalue equation for the matrix $(\mathcal{I} - \alpha_0 \mathcal{T})$:

$$\frac{\omega_k^2}{\omega_0^2} \left(\mathcal{D}^{(k)} - \mathcal{D}_0\right)(0) = (\mathcal{I} - \alpha_0 \mathcal{T}) \left(\mathcal{D}^{(k)} - \mathcal{D}_0\right)(0). \quad (2.8)$$

If we denote the eigenvalues of the matrix \mathcal{T} by λ_k , we see that the eigenvalues of $(\mathcal{I} - \alpha_0 \mathcal{T})$ are $(1 - \alpha_0 \lambda_k)$, and thus that the allowed frequencies are

$$\omega_k = \omega_0 \sqrt{1 - \alpha_0 \lambda_k}.$$

Assuming the system to be in the electronic ground state, we arrive at the total potential energy

$$V = V_0 + V_E, \quad (2.9)$$

where V_0 is the ground state energy of H_0 , given by the sum of mode frequencies,

$$V_0 = \frac{1}{2} \hbar \sum_{k=1}^{3N} \omega_k, \quad (2.10)$$

where \hbar is the reduced Planck constant.

We note that V_0 depends solely on the matrix $(\mathcal{I} - \alpha_0 \mathcal{T})$ and, thus, only on the relative coordinates \mathbf{r}_{ij} of the atoms with respect to each other. It follows that this term is completely independent of the orientation of the cluster with respect to the electric field. In the absence of other clusters, V_0 can therefore be interpreted as the self-energy of the cluster; in the presence of other clusters, the term also contains the interaction energy between the clusters [66]. For the analysis of the response of the clusters to an external electric field, however, we turn to the second term V_E of Eq. (2.9); this term, given in Eq. (2.6), contains all the orientational potential energy of the cluster in the external electric field.

Clearly, the Hamiltonian of Eq. (2.4) describes a set of harmonic oscillators with equilibrium positions given by \mathcal{D}_0 and a shifted ground state energy V . Using this interpretation of \mathcal{D}_0 , we show in the following that V_E is the energy of the total time-averaged dipole moment of the cluster in the external electric field. We first rewrite Eq. (2.3) in terms of the mean polarization vector $\mathcal{P} \equiv e\mathcal{D}_0$,

$$(\mathcal{I} - \alpha_0 \mathcal{T}) \cdot \mathcal{P} = \alpha_0 \mathcal{E}_0, \quad (2.11)$$

and use this equation in combination with the expression for V_E given in Eq. (2.6) to derive

$$V_E = -\frac{1}{2} \mathcal{E}_0 \cdot \mathcal{P} = -\frac{1}{2} \mathbf{E}_0 \cdot \mathbf{p}_c, \quad (2.12)$$

where

$$\mathbf{p}_c \equiv \sum_{i=1}^N \mathbf{p}_i \quad (2.13)$$

denotes the total polarization of the cluster and $\mathbf{p}_i \equiv e\mathbf{d}_{0,i}$ denotes the mean (time-averaged) polarization of atom i , as given by the elements of \mathcal{P} . From the form of Eq. (2.12), it is clear that V_E is the energy of an induced dipole \mathbf{p}_c in an electric field \mathbf{E}_0 [51]. If we divide the matrix $(\mathcal{I} - \alpha_0\mathcal{T})^{-1}$ into 3×3 subblocks \mathbf{Y}_{ij} , it can easily be seen from Eq. (2.11) that $\mathbf{p}_i = \sum_j \mathbf{Y}_{ij} \cdot \mathbf{E}_0$ and thus that

$$\mathbf{p}_c = \alpha_0 \sum_{i,j=1}^N \mathbf{Y}_{ij} \cdot \mathbf{E}_0 \equiv \boldsymbol{\alpha}_c \cdot \mathbf{E}_0, \quad (2.14)$$

where we define the 3×3 cluster polarizability matrix by

$$\boldsymbol{\alpha}_c \equiv \alpha_0 \sum_{i,j=1}^N \mathbf{Y}_{ij}. \quad (2.15)$$

An alternative derivation of Eqs. (2.11)-(2.14) is given in Ref. [81]. Note that $\boldsymbol{\alpha}_c$ depends solely on the spatial configurational properties of the cluster, not on the external electric field. Moreover, one can prove mathematically that $\boldsymbol{\alpha}_c$ is a symmetric matrix as long as each atom has an equal polarizability α_0 . This is done in Appendix A.^a This symmetry of $\boldsymbol{\alpha}_c$ implies that its eigenvectors are orthogonal, which in turn implies that it is always possible to transform the system to an orthogonal basis, formed by these eigenvectors, in which $\boldsymbol{\alpha}_c$ is diagonal.

Computationally, Eq. (2.15) is not a practical way of determining $\boldsymbol{\alpha}_c$, since it involves the very expensive operation of explicitly calculating the inverse of a large matrix. Numerically, the most favorable approach is to use Eq. (2.14): after choosing a suitable coordinate system, we apply an electric field in the x -direction and calculate the cluster polarization by solving Eq. (2.11). Efficient numerical algorithms for solving a set of linear equations are readily available, for example in the LAPACK package [91]. Having solved Eq. (2.11) for \mathcal{P} , we calculate the sum in Eq. (2.13), then divide the resulting vector by the electric field strength; the result is the first column of $\boldsymbol{\alpha}_c$. To gain the remaining two columns, this procedure is then repeated in the other two Cartesian directions.

If we were to neglect the dipolar interactions within the cluster, the cluster's polarization would be $N\alpha_0\mathbf{E}_0$, i.e., the cluster polarizability would simply be a scalar $N\alpha_0$. The ratio of the “actual” polarizability $\boldsymbol{\alpha}_c$ and this “naive” guess for the polarizability,

$$\mathbf{f} = \frac{\boldsymbol{\alpha}_c}{N\alpha_0}, \quad (2.16)$$

^aThe proof relies on the fact that $\mathbf{Y}_{ij} = \mathbf{Y}_{ij}^T$, which in turn can be proven by using induction in combination with the general expression for the inverse of a matrix built up of submatrices:

$$\begin{pmatrix} \mathbf{K} & \mathbf{L} \\ \mathbf{M} & \mathbf{N} \end{pmatrix}^{-1} = \begin{pmatrix} \mathbf{K}^{-1} + \mathbf{K}^{-1}\mathbf{L}\mathbf{S}^{-1}\mathbf{M}\mathbf{K}^{-1} & -\mathbf{K}^{-1}\mathbf{L}\mathbf{S}^{-1} \\ -\mathbf{S}^{-1}\mathbf{M}\mathbf{K}^{-1} & \mathbf{S}^{-1} \end{pmatrix},$$

where

$$\mathbf{S} = (\mathbf{N} - \mathbf{M}\mathbf{K}^{-1}\mathbf{L}).$$

is a measure of how much the polarizability is enhanced due to dipole-dipole interactions and may therefore be called the “enhancement factor” of the dipole cluster [81].

In terms of $\boldsymbol{\alpha}_c$, we can rewrite Eq. (2.12) compactly as

$$V_E = -\frac{1}{2} \mathbf{E}_0 \cdot \boldsymbol{\alpha}_c \cdot \mathbf{E}_0. \quad (2.17)$$

This expression can then be written in terms of the eigenvalues α_n and the corresponding normalized eigenvectors \mathbf{v}_n ($n = 1, 2, 3$) of $\boldsymbol{\alpha}_c$:

$$\begin{aligned} V_E &= -\frac{1}{2} \sum_{n,m=1}^3 (\mathbf{E}_0 \cdot \mathbf{v}_n) (\mathbf{v}_n \cdot \boldsymbol{\alpha}_c \cdot \mathbf{v}_m) (\mathbf{v}_m \cdot \mathbf{E}_0) \\ &= -\frac{1}{2} \sum_{n=1}^3 (\mathbf{E}_0 \cdot \mathbf{v}_n)^2 \alpha_n. \end{aligned} \quad (2.18)$$

In the first line, we twice inserted a complete orthonormal set of eigenvectors while, in the second line, we made use of the fact that $\boldsymbol{\alpha}_c \cdot \mathbf{v}_m = \alpha_m \mathbf{v}_m$ and $\mathbf{v}_n \cdot \mathbf{v}_m = \delta_{nm}$. The inner products obey the rule $\sum_n (\mathbf{E}_0 \cdot \mathbf{v}_n)^2 = E_0^2$, from which follows that $\sum_{n=1}^3 (\mathbf{E}_0 \cdot \mathbf{v}_n)^2 \alpha_n \leq \alpha_{max} E_0^2$, where $\alpha_{max} = \max(\{\alpha_n\})$ and the equality is achieved if and only if $\mathbf{E}_0 \parallel \mathbf{v}_{max}$, where \mathbf{v}_{max} is the eigenvector corresponding to α_{max} . It follows that V_E is minimized by an electric field in the direction of \mathbf{v}_{max} . A similar reasoning leads to the observation that V_E is maximized by an electric field in the direction of the eigenvector with the smallest eigenvalue, α_{min} . The difference $|\Delta|$ between maximum and minimum orientational energy V_E is thus given by

$$|\Delta| = \frac{1}{2} (\alpha_{max} - \alpha_{min}) E_0^2.$$

Here, for future purposes, we intentionally kept the freedom of choosing the sign of Δ .

2.2.2 Rotationally Symmetric Clusters

The bowl- and dumbbell-shaped nanoparticles considered in this chapter are clusters with an axis of rotational symmetry. The rotational invariance implies that the polarization that would be induced by an electric field in the direction of the symmetry axis must lie along this symmetry axis and, therefore, that this axis is an eigenvector of the cluster’s polarizability matrix $\boldsymbol{\alpha}_c$. Since it is known that $\boldsymbol{\alpha}_c$ must be a symmetric matrix, we know that its eigenvectors must be perpendicular to each other. This leads to the conclusion that the preferred direction of any rotationally symmetric cluster must lie either along the rotational symmetry axis or perpendicular to it. In this chapter, we always choose our coordinate system such that this rotational symmetry axis lies along the z -axis, and choose the x - and y -directions such that $\boldsymbol{\alpha}_c$ is diagonal (i.e., the Cartesian axes are the eigenvectors of $\boldsymbol{\alpha}_c$). Moreover, for rotationally symmetric clusters, $\alpha_{xx} = \alpha_{yy}$, and hence we are left with only two independent entries on the diagonal of $\boldsymbol{\alpha}_c$, one of which will be α_{max} and the other α_{min} . For the remainder of this chapter, we define the orientational

energy difference as^b

$$\Delta \equiv \frac{1}{2} (\alpha_{zz} - \alpha_{xx}) E_0^2, \quad (2.19)$$

where we choose the sign of Δ such that Δ is positive when the preferred direction of the cluster is along the rotational symmetry axis (which is equivalent to $\alpha_{zz} > \alpha_{xx}$).

Using Eq. (2.16), we can write Eq. (2.19) as

$$\Delta = \frac{1}{2} \Delta_f N \alpha_0 E_0^2, \quad (2.20)$$

where

$$\Delta_f = f_{zz} - f_{xx}.$$

As will be shown for all the cluster shapes in this chapter, the quantity Δ_f is largely independent of the cluster size, provided that the number of atoms is large enough. In this regime, Δ_f depends only on the shape of the cluster and on the dimensionless interatomic distance $a/\alpha_0^{1/3}$. This assertion does not state anything about the individual values of f_{zz} and f_{xx} as a function of cluster size. From the numerical data, it turns out (as we will see) that these quantities can still depend on cluster size, albeit usually only weakly. From Eq. (4.1), we note that because Δ_f is independent of N , Δ is linear in N and can thus be extrapolated to larger clusters than considered in this chapter. This possibility will be investigated in detail in Chapter 4.

2.2.3 Fourfold Rotationally Symmetric Clusters

One of the discussed cluster shapes in this chapter is a cluster with a cubic shape. If we choose the coordinate axes along the ribs of the cube, it can be easily seen from symmetry considerations that an electric field applied in the x -direction must induce a total cluster polarization $\mathbf{p}_c^{(\text{cube})}$ with a nonzero component only in the x -direction. Similarly, the polarizations resulting from electric fields in the y - and z -directions will also point along the y - and z -axes, respectively. Because these resulting polarizations are proportional to the columns of $\boldsymbol{\alpha}_c^{(\text{cube})}$, it follows that $\boldsymbol{\alpha}_c^{(\text{cube})}$ must be diagonal in this basis. Moreover, because the cube is invariant under 90° rotations, we do not expect the induced polarization of the cube to be dependent on whether the electric field is applied in the x -, y -, or z -direction and, therefore, the entries on the diagonal of $\boldsymbol{\alpha}_c^{(\text{cube})}$ must be equal. Hence,

$$\boldsymbol{\alpha}_c^{(\text{cube})} \propto \mathbf{I}. \quad (2.21)$$

^bFrom Eq. (2.18), we could also have derived an explicit expression for the orientational energy of the cluster shapes discussed in this chapter:

$$\begin{aligned} V_E &= -\frac{1}{2} \left[(\mathbf{E}_0 \cdot \hat{x})^2 + (\mathbf{E}_0 \cdot \hat{y})^2 \right] \alpha_{xx} - \frac{1}{2} (\mathbf{E}_0 \cdot \hat{z})^2 \alpha_{zz} \\ &= -\frac{1}{2} (\alpha_{xx} + (\alpha_{zz} - \alpha_{xx}) \cos^2 \theta) E_0^2, \end{aligned}$$

where in the first line we used $\alpha_{xx} = \alpha_{yy}$ and, in the second line, we introduced the angle θ between \mathbf{E}_0 and the z -axis. From the resulting expression, it is clear that the extrema of the orientational energy are located at $\theta = 0$ and $\theta = \pi/2$ and that the difference in orientational energy between the two extrema is indeed given by Eq. (2.19).

Substance	a (Å)	α_0 (Å ³)	\tilde{a}
Hexane	6.009	11.85	2.64
Silica	3.569	5.25	2.05
Sapphire	3.486	7.88	1.75

Table 2.1: Lattice spacings a , atomic polarizabilities α_0 , and dimensionless lattice spacings $\tilde{a} \equiv a/\alpha_0^{1/3}$ of some typical substances [81].

Note that, in this case, both the polarizability and the enhancement factor can be described by a scalar: the former by the proportionality factor between $\boldsymbol{\alpha}_c^{(\text{cube})}$ and \mathbf{I} , the latter by this “scalar polarizability” divided by $N\alpha_0$. Since, in this case, $\alpha_{xx} = \alpha_{yy} = \alpha_{zz}$, we find from Eq. (2.19) that $\Delta = 0$. This kind of cluster will therefore *not* have a preferred orientation within an external electric field. Physically, this is a surprising result since, *a priori*, one could expect an anisotropic cluster such as a cube to prefer to align one of its features (such as its ribs, faces, or vertices) along the electric field. However, simple symmetry arguments negate this expectation. For cuboid-shaped rods and platelets, on the other hand, as is the case for bowls and dumbbells, $\alpha_{xx} = \alpha_{yy} \neq \alpha_{zz}$ and hence $\Delta \neq 0$.

2.2.4 Units of Distance

Throughout the remainder of this chapter, we will usually measure distances, lattice spacings in particular, in units of $\alpha_0^{1/3}$. The reason is that, throughout the theory, the matrix \mathcal{T} is always multiplied by a factor α_0 . Upon applying this multiplication to the submatrices \mathbf{T}_{ij} , we get

$$\alpha_0 \mathbf{T}_{ij} = \frac{(3\mathbf{s}_{ij}\mathbf{s}_{ij}/|\mathbf{s}_{ij}|^2 - \mathbf{I})}{|\mathbf{s}_{ij}|^3} \quad (i \neq j),$$

where

$$\mathbf{s}_{ij} = \mathbf{r}_{ij}/\alpha_0^{1/3}.$$

Clearly, the relevant parameters are not the \mathbf{r}_{ij} themselves, but rather the dimensionless combinations $\mathbf{s}_{ij} = \mathbf{r}_{ij}/\alpha_0^{1/3}$. Using these dimensionless distances, we eliminate the atomic polarizability as an explicit input parameter. At the same time, the dimensionless combinations are $\mathcal{O}(1)$ in magnitude (for typical lattices and atomic polarizabilities), which is convenient for computational purposes. Some values of dimensionless lattice spacings

$$\tilde{a} \equiv a/\alpha_0^{1/3}$$

of a few substances are given in Table 2.1 [81]. For clarity, we note here that all other physical quantities remain unscaled in this chapter.

2.2.5 Comparison with Continuum Theory

At various instances in this chapter and Chapter 3, we are going to compare results derived using continuum theory [86–90] with our results. It might be of interest to mention how

we relate our enhancement factor to the dimensionless polarizability calculated in the mentioned references. Starting with a dimensionless lattice constant and assuming that the particles are inside a vacuum, we infer the relative permittivity ϵ using the Clausius-Mossotti relation in (CGS) [51],

$$\begin{aligned}\epsilon &= 1 + 4\pi\chi_e \\ &= 1 + \frac{4\pi n\alpha_0}{1 - \frac{1}{3}4\pi n\alpha_0} \\ &= 1 + \frac{4\pi}{\tilde{a}^3 - \frac{4}{3}\pi},\end{aligned}\tag{2.22}$$

where χ_e is the electric susceptibility and n is the number density of atoms, for a cubic lattice equal to $n = 1/a^3$. We then plug this ϵ into one of the formulas provided in Refs. [86–90] to gain a dimensionless polarizability α_n , which we convert to an enhancement factor by

$$f = \frac{\alpha_c}{\alpha_0 N} = \frac{\alpha_c \tilde{a}^3}{V} = \frac{\alpha_{SI} \tilde{a}^3}{4\pi\epsilon_0 V} = \frac{\alpha_n \tilde{a}^3}{4\pi},\tag{2.23}$$

where α_{SI} is the polarizability of the cluster in SI units (whereas we use CGS), ϵ_0 is the dielectric permittivity of vacuum, and we used the definition of dimensionless polarizability

$$\alpha_n = \frac{\alpha_{SI}}{\epsilon_0 V}$$

as given in Refs. [86–90].

2.3 Dielectric Rods and Platelets

A simple (but useful) example illustrating the introduced quantities are dielectric rods and platelets. We consider cuboid-shaped clusters, with the atoms on a simple cubic lattice with a dimensionless lattice constant $\tilde{a} = 2$. Let L be the number of atoms along the edge parallel to the axis of 90° rotational symmetry and l the number of atoms along the other two edges. Then the shape of the $l \times l \times L$ cuboid is defined by the ratio l/L . This cluster shape is rod-like for $l/L < 1$, cubic-shaped for $l/L = 1$, and platelet-shaped for $l/L > 1$.

The cuboid's edge of length L is the axis of fourfold rotational symmetry, and we choose the z -axis along this edge. In this coordinate system, the polarizability matrix is diagonal, with only two independent elements, $\alpha_{xx} = \alpha_{yy}$ and α_{zz} .

A well-known property of parallel dipoles is that it is energetically favorable for them to lie head-to-toe and unfavorable to lie side-by-side. Therefore, for $l/L < 1$ (rods), if we apply an electric field in the z -direction, thus inducing a polarization of the dipoles along the “head-to-toe direction,” we expect the dipole-dipole interactions between the atoms to enhance the induced polarization, because there are more dipoles lying head-to-toe than side-by-side. On the other hand, an electric field in the transverse direction (x - y plane) would induce more atomic polarizations lying side-by-side than head-to-toe and therefore, in this case, we expect the interactions to reduce the induced polarization. Also, we expect this effect to be stronger for smaller l/L ratios since, the smaller this ratio, the

more extreme the difference in the number of head-to-toe and side-by-side interactions will be. We expect the opposite to happen for $l/L > 1$ (platelets), for similar reasons.

In Fig. 2.1(a), we plot the elements of the enhancement factor $f_{xx} = \alpha_{xx}/N\alpha_0$ and $f_{zz} = \alpha_{zz}/N\alpha_0$, as a function of l/L , for $L = 10$. Our heuristic expectation that the enhancement in the z -direction is larger than that in the x -direction for $l/L < 1$ is confirmed by this plot. For small l/L , the interatomic interactions reduce the polarization when the electric field is applied in the x -direction, while they enhance it when the electric field is applied in the z -direction. However, f_{xx} becomes larger than unity for $l/L \gtrsim 0.73$, where atomic interactions enhance the polarization in both directions. We note that f_{xx} and f_{zz} cross over at $l/L = 1$, which is the special case of a dielectric cube-shaped particle. Here, the enhancements in both directions equal each other, as was predicted in Eq. (2.21). The value of the enhancements for $l/L = 1$ is $f_{xx} = f_{zz} \approx 1.05687$. The L -dependence of the enhancement factor of cubic clusters will be discussed in chapter 3. For $l/L > 1$ (platelets), the cuboid polarizability is more enhanced in the x -direction than in the z -direction, and f_{zz} becomes smaller than unity for $l/L \gtrsim 1.17$, which means that the interatomic interactions start reducing the z -polarizability for sufficiently flat platelets.

In Fig. 2.1(b) we plot the orientational energy difference Δ (as defined in Eq. (2.19)), for a typical electric field strength of $E_0 = 100 \text{ V mm}^{-1}$, an atomic polarizability $\alpha_0 = 5.25 \text{ \AA}^3$, at room temperature ($T = 293 \text{ K}$), as a function of the number of cluster atoms, for several values of $l/L < 1$ (rods). The lattice is simple cubic with lattice spacing $a = 2\alpha_0^{1/3} \approx 3.48 \text{ \AA}$.^c Clearly, Δ is linear in the number of particles. We fit the data to the functional form of Eq. (4.1), with Δ_f as fit parameter.

For sufficiently large N , we can confirm from Fig. 2.1(b) that Δ_f is constant with respect to the particle size, and that Δ_f hence depends only on the shape parameter l/L (save for the internal parameter \tilde{a}). As mentioned before, the individual values for f_{zz} and f_{xx} are allowed to vary with size, but the numerical data shows that they do so only slightly in the case of rods. This means we can extrapolate Δ to larger cluster sizes; this possibility will be explored in detail in Chapter 4.

In Fig. 2.1(c), we plot Δ_f as a function of l/L , for several values of L . Interestingly, these graphs overlap for sufficiently large N , again confirming the independence of Δ_f of L . It appears that, for cuboids, a ‘‘sufficiently large N ’’ is easily achieved: already for $l \times l \times 5$ cuboids there is almost perfect collapse of the data.

Dielectric Strings

A special case of a dielectric rod is a cluster consisting of L Lorentz atoms positioned on a straight line, separated by an interatomic distance a . This shape can be viewed as a $L \times 1 \times 1$ cuboid for which l/L becomes arbitrarily small as L increases. We will briefly discuss this cluster shape here, because it has been investigated previously [81].

For lattice spacing $\tilde{a} = 2$, the enhancement factor matrix elements f_{xx} and f_{zz} are plotted, as a function of L in Fig. 2.2(a). We note that this is not a new result, Kim *et al.* produced a similar plot in Ref. [81]. From $f_{zz} > f_{xx}$, it is clear that an electric

^cUsing Eq. (2.22), we can convert the value $\tilde{a} = 2$ into a permittivity: the result is $\epsilon \approx 4.3$.

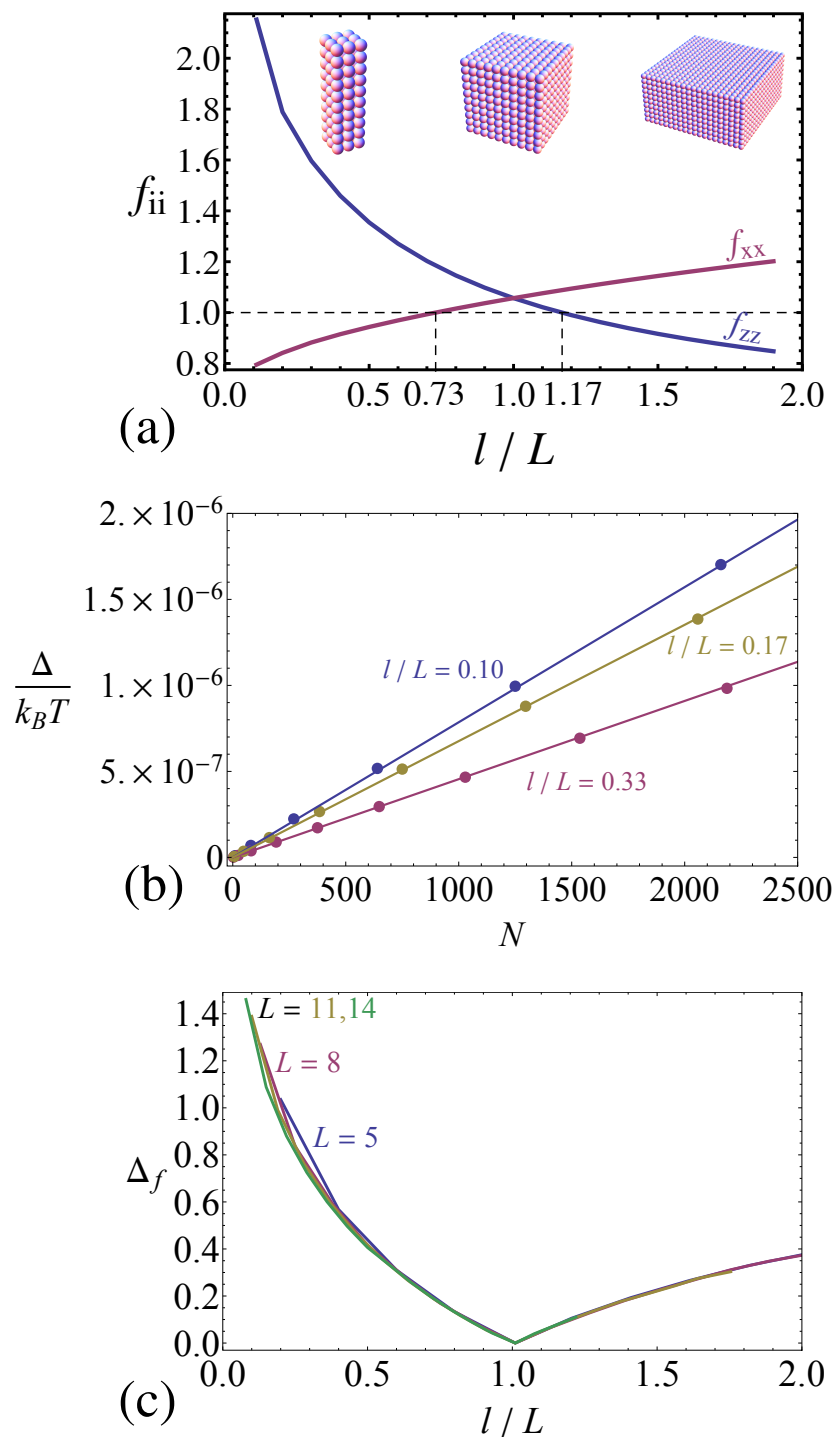


Figure 2.1: Properties of an $l \times l \times L$ cuboid-shaped cluster of atoms with atomic polarizability α_0 on a simple cubic lattice with spacing $\tilde{a} = 2$. (a): The elements f_{xx} (red) and f_{zz} (blue) of the enhancement factor matrix as a function of the shape parameter l/L , for $L = 10$. Note that $f_{xx} = 1$ at $l/L \approx 0.73$, that $f_{zz} = 1$ at $l/L \approx 1.17$, and that $f_{xx} = f_{zz} = 1.05687$ at $l/L = 1$. (b): The energy difference Δ (in units of $k_B T$) of turning the cuboidal rod from its least to its most favorable orientation in an external electric field, as a function of the number of atoms N in a rod, with shape parameters $l/L = 0.10$, $1/6 \approx 0.17$ and $1/3 \approx 0.33$. System parameters are given in the text, and the solid lines are linear fits to the data. (c): The difference $\Delta_f = f_{zz} - f_{xx}$ of the enhancement factor elements as a function of l/L , for several values of L .

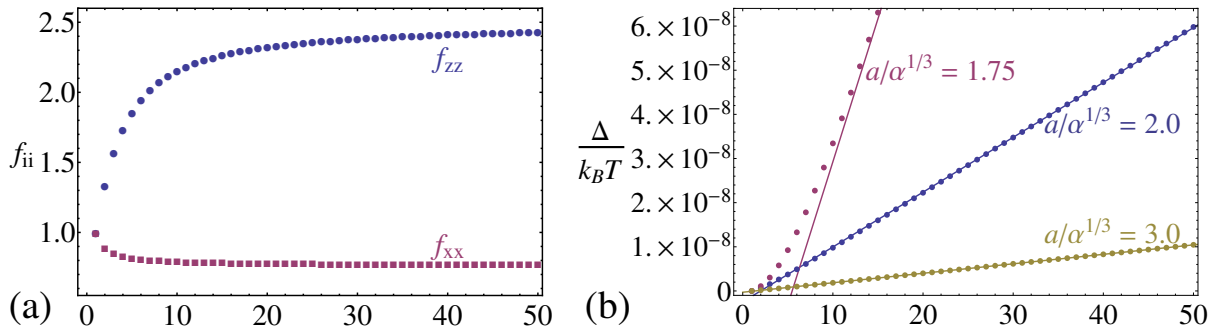


Figure 2.2: (a): The diagonal elements f_{xx} (red squares) and f_{zz} (blue circles) of the enhancement factor matrix of a straight line of L dipoles along the z -axis. The spacing between the atoms is $\tilde{a} = 2$. (Note that for f_{ii} , no other parameters are needed to define this system) (b): The energy difference Δ associated with turning this string from its least to its most favorable orientation in an external electric field $E_0 = 100 \text{ V mm}^{-1}$, for three different values of the dimensionless interatomic distance, $\tilde{a} = 1.75$ (red), $\tilde{a} = 2$ (blue) and $\tilde{a} = 3$ (yellow). Choosing atomic polarizability $\alpha_0^{1/3} = 5.25 \text{ \AA}^3$ (silica), these values correspond to spacings of, respectively, $a \approx 3.04 \text{ \AA}$, 3.48 \AA and 5.21 \AA . The temperature is $T = 293 \text{ K}$ (room temperature).

field applied in the z -direction will induce a higher polarization than one applied in the x -direction. The enhancement in the z -direction, f_{zz} , is greater than unity, meaning that the interactions enhance the induced polarization, as expected. On the other hand, f_{xx} is smaller than unity, meaning that the polarizability is reduced by the interactions. The limiting value of f_{zz} for $L \rightarrow \infty$ is $f_{zz}(L \rightarrow \infty) \approx 2.5064$ while, in the transverse direction, $f_{xx}(L \rightarrow \infty) \approx 0.7689$ [81].

In Fig. 2.2(b), we plot the orientational energy difference (2.19) for three values of the dimensionless interatomic distance \tilde{a} , for a typical electric field strength of $E_0 = 100 \text{ V mm}^{-1}$, an atomic polarizability of 5.25 \AA^3 , and at room temperature ($T = 293 \text{ K}$). To the numerical results, linear functions of the form

$$\Delta = \frac{1}{2} \Delta_f \alpha_0 E_0^2 (L - L_0) \quad (2.24)$$

have been fitted with Δ_f and L_0 as fit parameters. We note here that Eq. (2.24) is compatible with Eq. (2.20) when $L \gg L_0$. In this regime, atomic strings will have a negligible end effect. We usually find that $L_0 \lesssim \mathcal{O}(10)$ so, often, $L \gg L_0$. As an example, the fit parameters for $\tilde{a} = 2$ turn out to be

$$\Delta_f \approx 1.72, \quad L_0 \approx 1.98. \quad (2.25)$$

Because this cluster shape is not considered in Chapter 4, we include here a prediction of the length L^* of an atomic string for which the orientational energy difference becomes of the order of $k_B T$, which, as will be shown in Chapter 4, is the energy difference at which the electric field is first able to significantly orient a cluster. Using Eq. (2.24) and Eq. (2.25), and equating $\Delta = k_B T$, it is easily seen that

$$L^* = \frac{2k_B T}{\Delta_f \alpha_0 E_0^2} + L_0 \approx 8.1 \times 10^8.$$

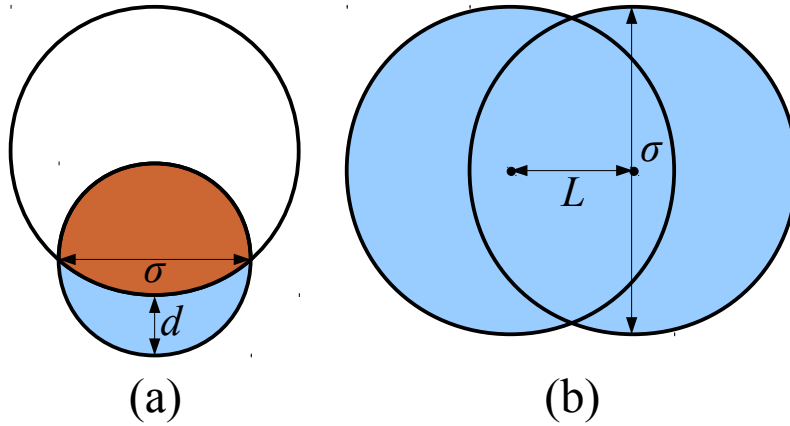


Figure 2.3: Construction and definition of parameters for (a) bowl and (b) dumbbell. (a): The bowl diameter σ and the bowl thickness d completely define the bowl’s shape, as follows. If $d < \sigma/2$, the shape of the bowl is defined by set-theoretic subtraction of one sphere from another (the blue area). [17] If $d > \sigma/2$, we let $d \rightarrow \sigma - d$ and use the same construction, but take the intersection of the spheres instead of the difference (the orange area). Note that in the latter case, the shape is no longer a “bowl” in the traditional sense of the word. (b): The shape of the dumbbell is constructed by set-theoretic addition of two (overlapping) spheres. The sphere diameter σ and the distance between the sphere centers L completely define the shape of the dumbbell. Note that if $L > \sigma$, the “dumbbell” in fact consists of two separate spheres.

Since in this case $a = 2\alpha_0^{1/3} \approx 3.5 \text{ \AA}$, we find a minimum string length of about a meter in order to experience any significant effect from the electric field. Atomic strings a meter in length are clearly unphysical; we will consider more realistic cluster shapes in Chapter 4.^d

2.4 Dielectric Bowls and Dumbbells

In this section we consider two other shapes of dipole clusters, namely bowl-shaped and dumbbell-shaped clusters. As mentioned in Chapter 1, these shapes have recently been synthesized [17, 19, 20] and show self-assembly behavior that can be influenced by an external electric field. It is of interest to investigate how the shape and size of such particles influence their interaction with the electric field.

The shape parameters of the bowl and dumbbell, d/σ (the ratio of the maximum thickness of the bowl and its diameter^e) and L/σ (the ratio of the center-to-center distance of the composing spheres and their diameter), respectively, as well as their theoretical construction, are given in Fig. 2.3. For the bowl, $d/\sigma = 0$ is the limit of an infinitesimally thin hemispherical shell, $d/\sigma = 1/2$ corresponds to a half sphere, and $d/\sigma = 1$ to a sphere. For the dumbbell, $L/\sigma = 0$ refers to a sphere, $L/\sigma = 1$ corresponds to two

^dAnother difference from the extrapolation done in Chapter 4 is that in the latter, the extrapolation is done for constant aspect ratio, while the aspect ratio of an atomic string changes if the number of atoms is increased.

^eThe bowl thickness d should not be confused with the Hamiltonian variable \mathbf{d}_i , which is never used as an explicit input parameter in any of the studied systems.

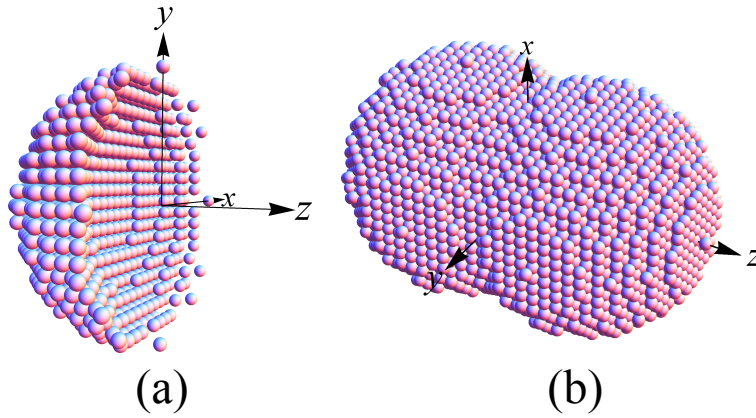


Figure 2.4: Examples of the dipole setup for (a) a bowl (shape parameter $d/\sigma = 0.275$) and (b) a dumbbell (shape parameter $L/\sigma = 0.55$), both intersected with a simple cubic lattice. Each sphere corresponds to an inducible dipole (Lorentz atom).

touching spheres, and for $L/\sigma > 1$, the spheres are actually separated by a gap. The locations of the atoms in the clusters can be inferred by intersecting the cluster shape with a lattice of our choice. In this chapter, we will focus on a simple cubic lattice.^f Examples of resulting clusters are depicted in Fig. 2.4, in which our choice of coordinate system is also defined, such that the cluster polarizabilities are diagonal with $\alpha_{xx} = \alpha_{yy}$.

2.4.1 Bowls

In Fig. 2.5(a), we plot α_{xx} and α_{zz} for a bowl-shaped particle, consisting of atoms on a simple cubic (sc) lattice with lattice spacing $\tilde{a} = 2$ and fixed bowl diameter $\sigma/a = 20$, as a function of the shape parameter d/σ , defined in Fig. 2.3. As expected, both α_{xx} and α_{zz} rise as d/σ increases from $d/\sigma = 0$ (a hemispherical shell) to $d/\sigma = 1$ (a sphere), because the number of atoms increases. Clearly, however, $\alpha_{xx} > \alpha_{zz}$ for all d/σ except $d/\sigma = 1$, meaning that the bowl is more polarizable in the x -direction and, hence, from Eq. (2.12), has a lower orientational energy when the field is along the x -direction.

Plotting the diagonal elements of the enhancement factor matrix in Fig. 2.5(b), we note that f_{xx} increases upon decreasing d , but that f_{zz} reaches a minimum at around $d/\sigma \approx 0.5$, where the interactions' diminishing effect on the polarizability in the z -direction is largest. In the same figure, we indicate the results for a hemisphere (corresponding to $d/\sigma = 0.5$), as presented in Ref. [88]. Considering that the theoretical approach presented in that work is completely different from ours, the agreement is excellent.

The orientational energy difference Δ for bowls composed of atoms on a sc lattice is plotted in Fig. 2.5(c) as a function of the number of atoms N for several values for d/σ , for an electric field strength $E_0 = 100 \text{ V mm}^{-1}$, an atomic polarizability $\alpha_0 = 5.25 \text{ \AA}^3$, and

^fFor bowls and dumbbells, calculations were also done using a face-centered cubic lattice. The results are qualitatively the same. Quantitatively, the enhancement factors tend to differ from unity more with an fcc lattice than with an sc lattice, which can be attributed to the higher density of atoms, resulting in stronger atom-atom interactions and hence stronger many-body effects.

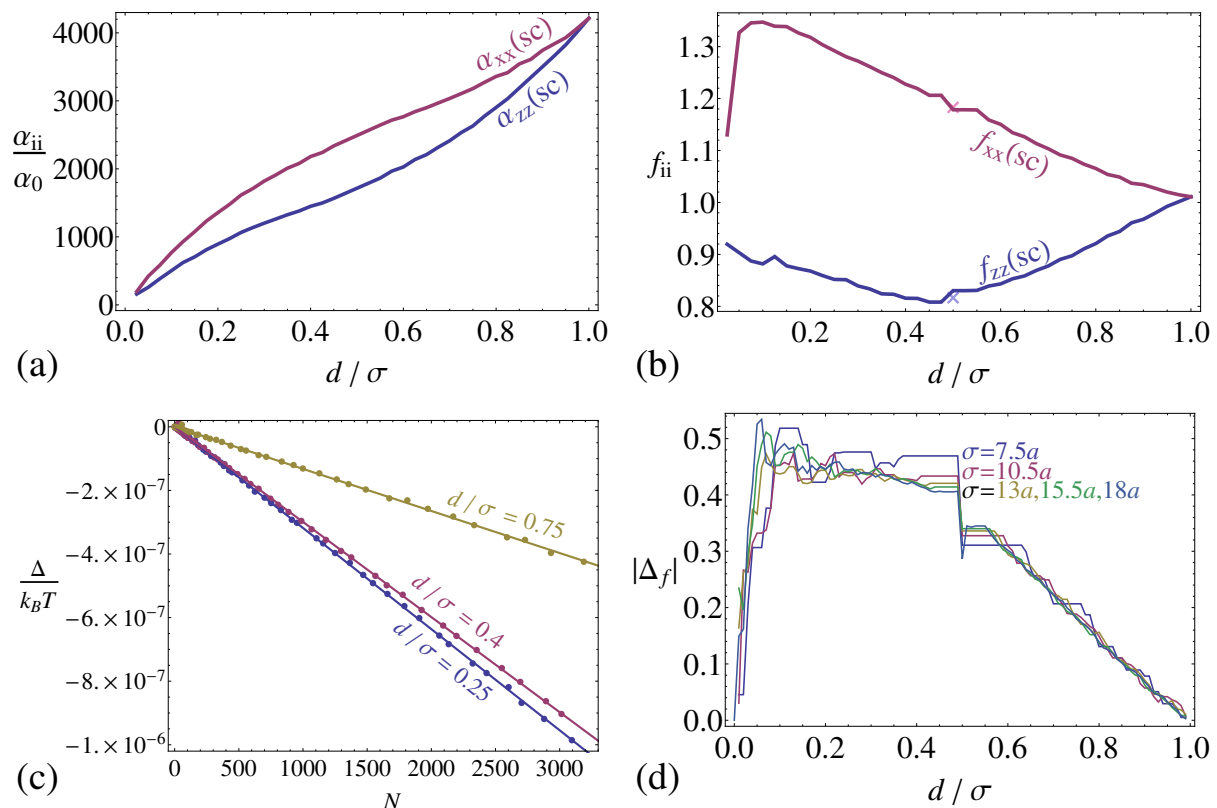


Figure 2.5: Quantities associated with a bowl-shaped cluster of atoms on a simple cubic (sc) lattice with dimensionless lattice constant $\tilde{a} = 2$, shape parameter d/σ , and diameter σ (illustrated in Fig. 2.3a). For $\sigma/a = 20$, panel (a) shows the elements α_{xx} (red) and α_{zz} (blue) of the polarizability tensor, and (b) the elements f_{xx} (red) and f_{zz} (blue) of the enhancement factor tensor, both as a function of d/σ . The light red and blue crosses in panel (b) indicate the enhancement factor elements of a hemisphere as calculated using continuum theory in Ref. [88]. Panel (c) shows the energy difference of turning a bowl from its least to its most favorable orientation in an external electric field $E_0 = 100 \text{ V mm}^{-1}$, as a function of the number of atoms in the bowl, for $d/\sigma = 0.25, 0.4$ and 0.75 . The atomic polarizability is 5.25 \AA^3 (yielding lattice constant $a \approx 3.48 \text{ \AA}$) and the temperature is $T = 293 \text{ K}$. Panel (d) shows the difference $|\Delta_f| = |f_{zz} - f_{xx}|$ of the enhancement factor elements in the z - and x -directions, as a function of d/σ , for $\sigma/a = 7.5, 10.5, 13, 15.5$ and 18 , showing a strong dependence on the shape parameter d/σ and a weak dependence on the size parameter σ/a .

at room temperature ($T = 293$ K). To the numerical results, linear functions of the form (4.1) have been fitted to determine Δ_f , which we now find to be negative. This implies that the axis of rotational symmetry is, for bowl-shaped particles, the least favorable direction for the external field. The numerical data show that the individual values of f_{xx} and f_{zz} vary (slightly) with cluster size but that the difference Δ_f is essentially constant. The latter is illustrated in Fig. 2.5(d) where we plot $|\Delta_f|$ as a function of the shape parameter d/σ , for several different bowl diameters σ . These graphs clearly overlap for higher values of σ or d/σ , which means that for those values, Δ_f is indeed independent of the particle size parameter σ . In Chapter 4, we investigate the implications of this independence for extrapolation to much larger bowls than considered here.

2.4.2 Dumbbells

In Fig. 2.6(a), we plot α_{xx} and α_{zz} for a dumbbell particle with fixed sphere diameter $\sigma/a = 20$, consisting of atoms on an sc lattice with spacing $\tilde{a} = 2$, as a function of the shape parameter L/σ , defined in Fig. 2.3. With increasing L/σ (and thus increasing L , since σ is fixed), the number of atoms increases, resulting in a rising trend of α_{ii} for $L/\sigma < 1$. For $L/\sigma > 1$ (two separate spheres), an increase in L no longer increases the number of particles and instead only increases the distance between particles in both spheres, reducing their interactions. The result is that α_{zz} decreases, while α_{xx} , which benefits from less interactions, keeps increasing. We note here that α_{zz} already starts decreasing *before* $L/\sigma = 1$, which can be explained by the fact that close to $L/\sigma = 1$, the number of particles does not increase enough with increasing L to make up for the larger distance between particles in different spheres.

We plot the enhancement factor elements f_{xx} and f_{zz} in Fig. 2.6(b). We notice here again that f_{zz} already “stalls” at $L/\sigma \approx 0.7$ and decreases before L/σ reaches unity, while f_{xx} displays the opposite behavior. Also note that, for $L > \sigma$, as the distance between the separate spheres increases, the enhancement factors decay to that of a single sphere. This was to be expected as the enhancement factor of two spheres at infinite separation is equal to that of a single sphere. Again, we indicate in the graph the results that are calculated in Ref. [89] using continuum theory for two touching spheres ($L/\sigma=1$) and note the excellent agreement with our work.

The energy difference between the most and least favorable orientations is given by Eq. (2.19) and is plotted in Fig. 2.6(c) as a function of N for three different values of L/σ , for $E_0 = 100$ V mm⁻¹, $\alpha_0 = 5.25$ Å³, $\tilde{a} = 2$, and room temperature $T = 293$ K. Each of the plotted energy differences appears linear with respect to the number of dipoles N .

In Fig. 2.6(d), we plot Δ_f as a function of the dumbbell shape parameter L/σ , for several size parameters σ . Clearly, since the graphs overlap, Δ_f for dumbbells is also largely independent of the overall size and depends only on the shape. As is the case for rods and bowls, we extrapolate the energy difference of dumbbells and estimate the dependence on L/σ of the minimum required size of the dumbbell for alignment in an electric field in Chapter 4.

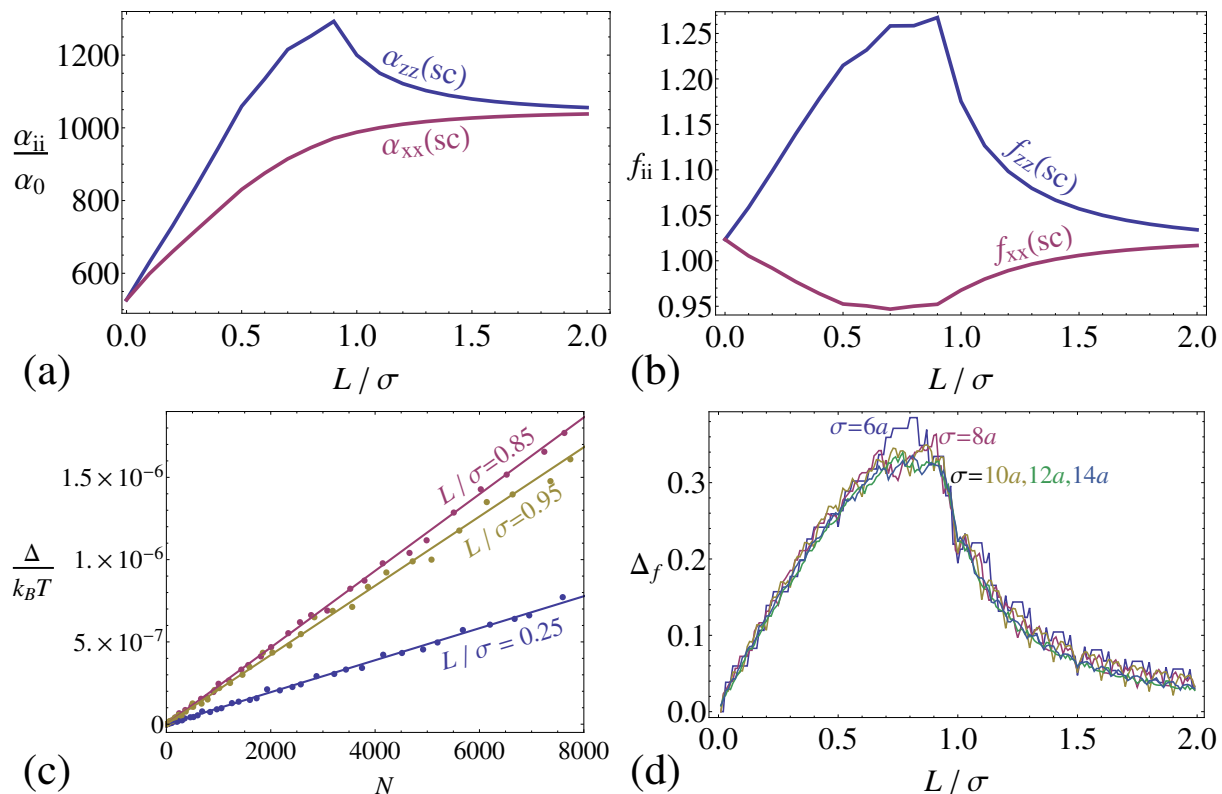


Figure 2.6: Quantities associated with a dumbbell-shaped cluster of atoms on an simple cubic (sc) lattice with dimensionless lattice constant $\tilde{a} = 2$, with shape parameter L/σ , and dumbbell sphere diameter σ (illustrated in Fig. 2.3(b)). For $\sigma/a = 20$, panel (a) shows the elements α_{xx} (red) and α_{zz} (blue) of the polarizability matrix and (b) the elements f_{xx} (red) and f_{zz} (blue) of the enhancement factor matrix as a function of L/σ . The light red and blue crosses in panel (b) indicate the enhancement factor elements of two touching spheres as calculated using continuum theory in Ref. [89]. Panel (c) shows the energy difference of turning the dumbbell from its least to its most favorable orientation in an external electric field $E_0 = 100 \text{ V mm}^{-1}$, as a function of the number of atoms in the dumbbell, for $L/\sigma = 0.25, 0.85$ and 0.95 . The atomic polarizability is 5.25 \AA^3 (yielding lattice constant $a \approx 3.48 \text{ \AA}$) and the temperature is $T = 293 \text{ K}$. Panel (d) shows the difference $\Delta_f = f_{zz} - f_{xx}$ of the enhancement factor elements in the z - and x -directions, as a function of L/σ , for $\sigma/a = 6, 8, 10, 12$, and 14 , again showing a strong shape- and a weak size-dependence.

2.5 Conclusions and Outlook

The CDM is a rigorous tool for including many-body interatomic interactions on the basis of a polarizable atom model not only in the potential energy but also in other quantities such as the polarizability of a cluster of atoms. The applicability of the method is limited by computing power and becomes unfeasible for atom numbers larger than $\mathcal{O}(10^4)$. This corresponds to very small nanoparticles, slightly below the experimentally realizable regime. However, as has been shown in this chapter, it is in most cases fairly straightforward to extrapolate some of the key properties to larger cluster sizes.

We have discussed the polarizability and orientational energy of cuboids, bowls, dumbbells, and cubes. In general, these clusters are all most polarizable in the direction of their largest dimension: for cuboids along their longest rib, for bowls in the directions perpendicular to their axis of rotational symmetry, and for dumbbells along their rotational symmetry axis. These directions are also the preferred orientations of the cluster in an external electric field. Cubes are equally polarizable in all directions and thus have no preferred orientation in an external electric field.

We then turned our attention to the magnitude of the energy difference Δ between the most- and least-favored orientations of each cluster shape. We found that, for typical experimental values for electric field strength, temperature and atomic polarizability, these energy differences are small compared to the thermal energy (for the atom numbers that are feasible with our computer resources). However, we also found an essentially linear dependence of Δ on the number of cluster atoms N , and related the slope of the graph to the difference Δ_f in enhancement factor diagonal elements, a quantity that turns out to be independent of the cluster size and that depends only on the cluster shape and lattice spacing. The dependence of Δ_f on the cluster shape was then investigated. This was done for several cluster sizes in order to prove the size-independence of Δ_f . Using the linear dependence of Δ on N , we will, in Chapter 4, estimate the minimum required size for alignment in an electric field as a function of the aspect ratio of the cluster, for rods, platelets, bowls, and dumbbells.

Global and Local Enhancement Factor of Cubes and Spheres

Using the Coupled Dipole Method (CDM), we study in detail the global and local polarizability of a cubic and a spherical cluster, and the dependence of these quantities on material properties and cluster size. We compare the results from the CDM with those obtained using continuum electrostatics and draw the conclusion that the CDM and continuum electrostatics are equivalent if the number of dipoles in the CDM is sufficiently large. Since the CDM is relatively simple to use, this indicates that it may be useful for solving complex electrostatic problems.

3.1 Introduction

In Chapter 2, we investigated the polarizability and enhancement factor of anisotropic particles. In this chapter we turn our attention to two particle shapes that exhibit an isotropic polarizability, namely cubes and spheres. For both of these shapes, we first investigate the enhancement factor as a function of the number of atoms and then take a look into the interior of the particles, plotting the local enhancement factor as a function of position. We also compare our results with those from continuum electrostatics of dielectric bodies. The polarizability of a sphere is a well-known problem in electrostatics and has a straightforward solution [51]. The cube is a more challenging problem, but its polarizability has also been numerically calculated using continuum theory [87]. Small cubes have been considered in the CDM before [81], and spheres have been compared to continuum theory in the context of scattering calculations [71, 72, 74], but here we consider electrostatic quantities of larger clusters. We find an apparent asymptotic agreement between the two theories, especially for cubes, and conclude that for large atom numbers the CDM is equivalent to continuum theory. Since the CDM is readily applicable to any geometrical setup (and can possibly even be applied to systems with nonuniform dielectric constant), this could make it possible to solve complicated electrostatic problems using the CDM. We note here that for the cube and sphere specifically, the CDM might not be the best choice for calculating the polarizability, since analytical expressions for both have been derived in the aforementioned references [51, 87], and since the sphere is especially hard to model using discrete dipoles.

The (global) enhancement factor has been defined in Chapter 2, but not the local enhancement factor. Choosing the z -direction to lie along the external electric field \mathbf{E}_0 (see Fig. 3.3(a)), we define the local enhancement factor f' as the z -component of the polarization of the local atom, divided by $\alpha_0 E_0$. Note that, using this definition, the analogy with the global enhancement factor \mathbf{f} is not complete, because even when the electric field is applied in the z -direction, the polarization of the individual atoms can have nonzero components in the x - and y -directions. Consequently, if we were to express the local polarization as

$$\mathbf{p} = \mathbf{f}' \cdot \alpha_0 \mathbf{E}_0,$$

where \mathbf{f}' would be a 3×3 matrix, \mathbf{f}' would not be diagonal.

In Ref. [81], the enhancement factor of 1-dimensional lines and 2-dimensional squares of atoms was determined and investigated in detail. For these low-dimensional systems, the r^{-3} dipole-dipole interaction is short-ranged, such that a more or less constant local enhancement factor is found in the "middle" of these clusters, independent of the boundary layers. In this chapter, we aim to perform a similar study for a cubic-shaped and a spherical particle with atoms on a cubic lattice. As we will show, we were not able to determine the limiting value of the global enhancement factor of a cube for the cube sizes studied (up to $120 \times 120 \times 120$), but we do observe that it comes very close to the electrostatic value. For spheres, we find similar results, although the numerical value of the global enhancement factor for the studied sphere sizes is somewhat further removed from the value predicted by continuum electrostatics (unity; see below) than was the case for cubes.

3.2 Theoretical Predictions

In Ref. [81], the (scalar) enhancement factor for a cubic $L \times L \times L$ cluster of atoms on a cubic lattice is plotted as a function of the cube length L . The enhancement factor is seen to increase with increasing cube size, seemingly approaching some limiting value greater than unity. In contrast, when it is assumed on the basis of translational invariance that all dipoles have the same polarization, it is possible to prove that [51, 81] $f(\infty \times \infty \times \infty) = 1$. However, by assuming the same polarization for all dipoles, we neglect the effect of the surfaces of the cube, making this a questionable assumption given the long range of the dipole-dipole potential ($\propto r^{-3}$).

In Ref. [81] the enhancement factor is plotted for cube sizes up to $10 \times 10 \times 10$. This is still far from the regime where the surface can be expected to be negligible; the ratio of dipoles at the surface is, for this cube size, still $(10^3 - 8^3)/10^3 \approx 0.49$. In the present work, we will therefore consider larger cubic clusters, of sizes up to $120 \times 120 \times 120$. For these clusters, the fraction of surface dipoles is approximately 0.05.

In Ref. [87], the normalized polarizability of a cubic particle of dielectric constant ϵ is calculated using continuum electrostatics. Moreover, the numerical results are then approximated using a Padé approximation, leading to the equation

$$\alpha_n \approx \alpha_n^{(\infty)} (\epsilon - 1) \frac{\epsilon^3 + 4.83981\epsilon^2 + 5.54742\epsilon - \alpha_n^{(0)}}{\epsilon^4 + 8.0341\epsilon^3 + 19.3534\epsilon^2 + 15.4349\epsilon + \alpha_n^{(\infty)}}, \quad (3.1)$$

where $\alpha_n^{(\infty)} = 3.6442$, $\alpha_n^{(0)} = -1.6383$. In this chapter, we determine ϵ by Eq. (2.22) and convert α_n to an enhancement factor using Eq. (2.23). It is reasonable to expect the CDM to agree with this continuum result in the limit where the number of coupled dipoles is large.

The polarization of a sphere in an electric field is a well-known problem in electrostatics. A sphere of radius R of a material with relative dielectric constant ϵ in vacuum in an electric field \mathbf{E}_0 has a polarization [51]

$$\mathbf{P}_{sphere} = \left(\frac{\epsilon - 1}{\epsilon + 2} \right) R^3 \mathbf{E}_0.$$

On the other hand, from the point of view of the CDM, the polarization is

$$\mathbf{P}_{sphere} = N\alpha_0 f_{sphere} \mathbf{E}_0,$$

where N is the number of Lorentz atoms and f_{sphere} is the sphere's enhancement factor, such that we have

$$N\alpha_0 f_{sphere} = \left(\frac{\epsilon - 1}{\epsilon + 2} \right) R^3.$$

Assuming that for large enough spheres α_0 follows the Clausius-Mossotti relation [Eq. (1.2)], we can express α_0 in terms of ϵ . After dividing out equal terms, this results in

$$f_{sphere} = \frac{4\pi R^3}{3N} n,$$

where n is the number density of atoms and is, in the limit of large spheres, equal to $N \left(\frac{4\pi}{3} R^3 \right)^{-1}$, such that, for large spheres, we can expect

$$f_{sphere} = 1.$$

Furthermore, since electrostatics predicts a uniform polarization inside the sphere, we expect the local enhancement factor f' to be homogeneous as well.

3.3 Numerical Methods

Special optimization techniques were used in the case of large dielectric cubes and spheres. Because the number of atoms in the cluster increases rapidly with the rib length of the cube or the diameter of the sphere, we encounter practical problems such as memory limitations. However, these problems can be alleviated using two techniques (and their combination), which we will now briefly discuss.

3.3.1 Exploiting Symmetry

In this technique, we use the symmetries of the cube and sphere to reduce the order of the linear equation to be solved. It is possible to express the polarizations of all the dipoles in terms of only those in one octant of the particle. If we insert these relations into the set of equations (2.11), we reduce the number of dipoles by a factor 8. Note that, in this way, we also increase the computational cost of calculating a matrix element by (roughly) a factor 8, but since the cost of solving a set of linear equations scales much faster than linearly (the exact scaling is dependent on the algorithm used), we significantly increase the computation speed. We elaborate on the exploitation of symmetries more explicitly in Appendix B.

3.3.2 The Gauss-Seidel Method

The second technique uses the Gauss-Seidel method [92] for solving a set of linear equations, trading computation speed for less memory use. The Gauss-Seidel method is an iterative method for solving \mathcal{P} from an equation of the form (2.11). The method starts with a guess (discussed below) for \mathcal{P} , which we shall call $\mathcal{P}^{(0)}$. The next approximation for \mathcal{P} , $\mathcal{P}^{(1)}$, is calculated using the following formula:

$$p_i^{(k+1)} = \frac{1}{z_{ii}} \left(e_i - \sum_{j>i} z_{ij} p_j^{(k)} - \sum_{i>j} z_{ij} p_j^{(k+1)} \right), \quad (3.2)$$

where the $p_i^{(k)}$ are the elements of $\mathcal{P}^{(k)}$, the e_i are the elements of \mathcal{E} , and the z_{ij} are the elements of the matrix $(\mathcal{I} - \alpha_0 \mathcal{T})$. Note that in our case $z_{ii} = 1$, and that we can write

Eq. (3.2) in terms of more familiar quantities,^a

$$\mathbf{p}_i^{(k+1)} = \mathbf{E}_0 - \sum_{j>i} \mathbf{Z}_{ij} \cdot \mathbf{p}_j^{(k)} - \sum_{i>j} \mathbf{Z}_{ij} \cdot \mathbf{p}_j^{(k+1)},$$

where the \mathbf{Z}_{ij} are 3×3 blocks in the matrix $(\mathcal{I} - \alpha_0 \mathcal{T})$. With this technique, it is not necessary to store a “new” and an “old” copy of \mathcal{P} , because only elements that have been calculated previously are needed; i.e., we can simply keep overwriting the elements of \mathcal{P} .

As an initial guess, we construct $\mathcal{P}^{(0)}$ as follows: we sum the \mathbf{Z}_{ij} horizontally and then solve the equation

$$\left(\sum_{j=1}^N \mathbf{Z}_{ij} \right) \cdot \mathbf{p}_i^{(0)} = \mathbf{E}_0$$

for each $\mathbf{p}_i^{(0)}$. Using this guess, the enhancement factor could be calculated to a precision of 10 digits within 20 iterations.

Since \mathbf{Z}_{ij} can be (re-)calculated on the fly as needed and the elements of \mathcal{E} can be inferred using only a 3-dimensional vector, we only need to store approximately $3N$ numbers, namely the elements of \mathcal{P} . This effectively eliminates the memory problem. However, as a consequence, the resulting calculation is much slower than the ones that use the efficient routines provided in the LAPACK library [91], which were used in Chapter 2.

By combining the two techniques (symmetry exploitation and the Gauss-Seidel method), we were able to calculate the enhancement factor for cubes as large as $120 \times 120 \times 120$ and spheres with up to 120 atoms along their diameter (making for a total of 881960 atoms). The data points for cubes, presented in Subsection 3.4, have been calculated using various methods corresponding to combinations of applying the two aforementioned techniques. In Table 3.1, we give an overview of these methods and define the acronyms that are used in the caption of Fig. 3.1. For spheres, we only used the SGS method, i.e., the Gauss-Seidel solution where symmetries were exploited.

The different methods have all been tested for consistency and the agreement between them is excellent. Computationally, the most practical techniques were the SDL-method for small cube rib lengths, because of its speed and simple implementation, and the SGS-method for large rib lengths, because of its negligible memory usage.

3.4 Numerical Results for Cubes

3.4.1 Global Enhancement Factor

In Fig. 3.1(a), the (scalar) enhancement factor f of $L \times L \times L$ cubes, as calculated numerically, is plotted as a function of L for several (dimensionless) lattice spacings \tilde{a} . For all of the lattice spacings, the qualitative behavior of the enhancement factor is the same: for low L , it increases rapidly as a function of L , but starts to level off at $L \approx 10$, seemingly reaching a limiting value $f(L) > 1$ around $L \approx 20$. This contradicts the

^aNote that, in this expression, i and j run from 1 to N whereas, in Eq. (3.2), they run from 1 to $3N$. Therefore, by using $j > i$ and $i > j$ as summation range, we exclude some of the elements of \mathcal{Z} that were present in Eq. (3.2). Fortunately, these elements are zero, because $\mathbf{Z}_{ii} = \mathbf{I}$.

Acronym	Method	Symmetries	Precision	L_{max}
NDL	LAPACK	No	Double	20
SDL	LAPACK	Yes	Double	40
SSL	LAPACK	Yes	Single	48
NGS	Gauss-Seidel	No	Double	60
SGS	Gauss-Seidel	Yes	Double	120

Table 3.1: An overview of techniques used for calculating the polarizability of a cubic cluster of atoms on a simple cubic lattice, and their associated acronyms, as used in the caption of Fig. 3.1. In the LAPACK Methods, we load the elements of the matrix in memory to the numerical precision specified in the “Precision” column and use the routines in the LAPACK package to solve the relevant set of linear equations. The Gauss-Seidel Methods involve (re-)calculating the elements of the matrix on the fly and, starting from an initial guess, using 20 iterations of the Gauss-Seidel method to solve the set of linear equations. The “Symmetries” column refers to whether or not the symmetries of the dielectric cube were exploited. The “ L_{max} ” column lists estimates for largest feasible rib lengths that each method can handle, given our available resources.

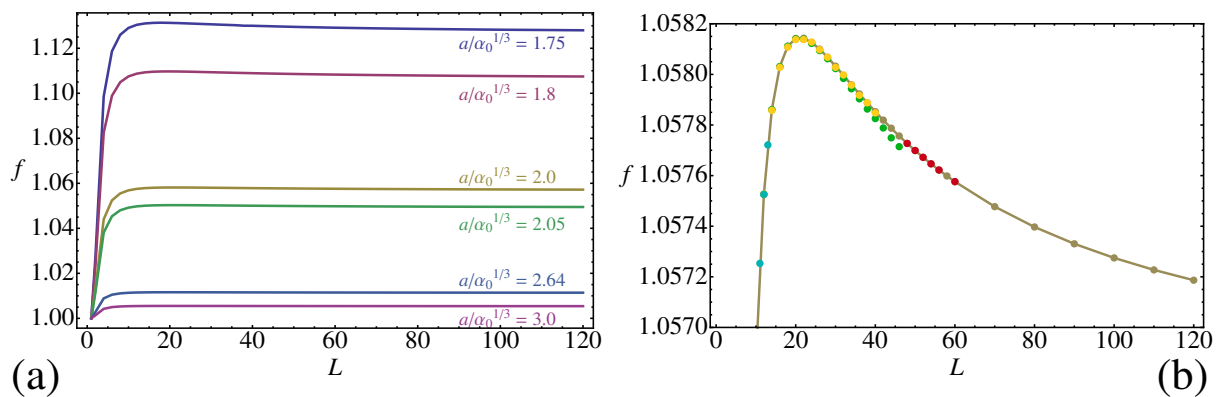


Figure 3.1: The enhancement factor f of a cubic $L \times L \times L$ cluster with atoms on a cubic lattice, as a function of the number of atoms along the rib L , in panel (a) for the dimensionless lattice spacings $\tilde{a} = 1.75$ (blue), $\tilde{a} = 1.8$ (red), $\tilde{a} = 2.0$ (yellow), $\tilde{a} = 2.05$ (green), $\tilde{a} = 2.64$ (light blue) and $\tilde{a} = 3.0$ (purple). Panel (b) displays a zoom-in (along the vertical axis) for $\tilde{a} = 2.0$ with the data points generated by different numerical methods (see text and Table 3.1): SGS (dark yellow points and curve), NGS (red points), SSL (green points), SDL (bright yellow points), and NDL (light blue points). Note that SSL slightly underestimates f for $L \approx 40$.

prediction $f(\infty) = 1$ made by ignoring the edges of the cube. We investigate the behavior with a particular lattice spacing, $\tilde{a} = 2$, in full detail. Fig. 3.1(b) shows a (vertical) zoom-in of Fig. 3.1(a), including data points as generated by various numerical methods. It can be seen from Fig. 3.1(b) that the enhancement factor (for $\tilde{a} = 2$) reaches a maximum value of $f \approx 1.05814$ at $L = 20$, after which it starts decreasing, where the rate of decrease reaches a maximum at $L = 34$. This behavior is the same for all other values of \tilde{a} , albeit with different values of f .

The decrease of f observed beyond $L = 34$ is so slow that it could, conceivably, be caused by systematic rounding errors in the calculation of the elements of the matrix. This is still an open question that may be approached in a number of different ways, for example by increasing the cube size and observing whether the enhancement factor keeps decreasing; another approach might be to increase the precision to which the elements of the matrix are calculated and observe whether this affects the value of the enhancement factor. A relevant observation here is that the single precision method SSL gives slightly lower results (for large L) than the double precision methods. However, the difference does not appear to be large enough to expect the decline to vanish for asymptotically large precisions.

Technically, we have not been able to determine a large- L limiting value for f . The decay observed beyond $L = 34$ slows down as L increases but a reliable extrapolation to asymptotically large cubes could not be determined. However, the residual decay for large L is slow and variation only occurs in the fifth decimal. We note, furthermore, that the continuum limit for $\tilde{a} = 2$ is $f \approx 1.0567$; a value that, judging from the plot, could very well be f 's asymptotic limit for large L . It therefore seems physically reasonable to expect the CDM to asymptotically reach the continuum limit for large L and to conclude that a $120 \times 120 \times 120$ cube, or even a $10 \times 10 \times 10$ one, is a good approximation for a cube composed of a continuous material.

The latter conclusion becomes even more obvious when, as done in Figure 3.2, we plot the enhancement factor of a $120 \times 120 \times 120$ and a $10 \times 10 \times 10$ cube as a function of the dimensionless lattice constant \tilde{a} , together with the results from continuum theory [87], which we quote in Eq. 3.1. From the figure, we note an excellent agreement between these three results, illustrating that f changes very little for $L > 10$, and that the CDM result for both small and large cubes agrees very well with the continuum result, despite the fact that the latter is calculated using a completely different method than the CDM.

3.4.2 Local Enhancement Factor

In Figs. 3.3(b) and 3.3(c), we plot the local enhancement factor f' along two planes cut through the middle of a $120 \times 120 \times 120$ cube, as illustrated in Fig. 3.3(a). From the shape of the graph we clearly see that f' is not a spatial constant and varies most pronouncedly on the faces and in the corners of the cube. In Fig. 3.3(b) we observe that the sides of the cube normal to the electric field ($z = \pm 60a$) experience a clear polarization reduction (i.e., $f' < 1$), reaching a local enhancement factor of $f' \approx 0.71335$ in the middle of the face (at $x = 0$, $y = 0$ and $z = \pm 60a$). The interior of the cube turns out to experience a slight enhancement of $f' \approx 1.04530$ in the center $x = y = z = 0$ (not visible from the graphs). A more dramatic enhancement is experienced by the faces of the cube that lie

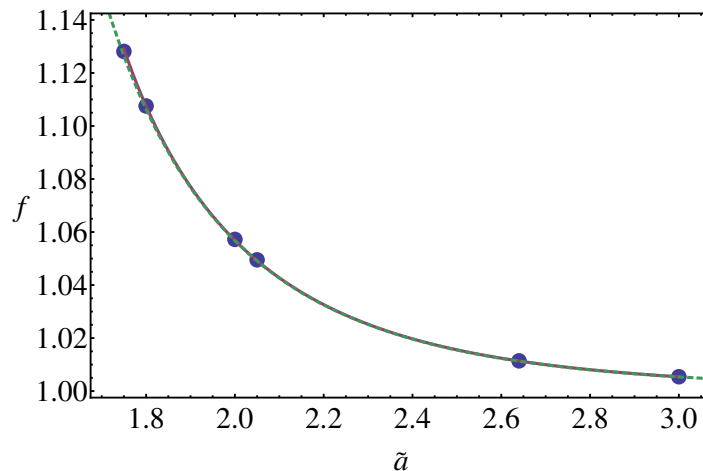


Figure 3.2: The enhancement factor f of a $120 \times 120 \times 120$ (blue dots) and a $10 \times 10 \times 10$ (solid red line) cube of atoms, as a function of the (dimensionless) lattice constant $\tilde{a} = a/\alpha_0^{1/3}$, plotted together with the result from Ref. [87] (green dashed line), where the enhancement factor is numerically calculated using continuum theory (See Eq. (3.1)). We note the excellent agreement between the latter and our results for both small and large cubes, despite the completely different approaches.

in-plane with the electric field (e.g., $x = \pm 60a$); for example at $z = 0$, the enhancement on the faces is $f' \approx 1.23876$, while in the corner ($z = \pm 60a$), $f' \approx 1.29005$, as mentioned earlier.

In Fig. 3.4, we plot the local enhancement factor along one line parallel and one perpendicular to the electric field, in both cases through the middle of the cube (these lines are also illustrated in Fig. 3.3), for several values of L , as a function of scaled coordinates. The behavior of the local enhancement factor, as seen in Figs. 3.3 and 3.4, shares many features also seen in the case of two-dimensional squares, as discussed in Ref. [81]: we observe high local enhancement on all edges of planes perpendicular to the electric field, high local enhancement on the edges parallel to the electric field of planes in-plane with the electric field, and low local enhancement on the edges perpendicular to the electric field of planes in-plane with the electric field. Furthermore, the local enhancement varies by far the most rapidly at locations close to the edge. Like in Ref. [81], for all values of L the outer layer of atoms in faces parallel to the electric field is especially polarized. This is illustrated in the inset of Fig. 3.4(a), but also visible in Fig. 3.3. In this layer of atoms, the local enhancement factor appears to depend more strongly on L and a limiting value for the on-edge local enhancement was not reached for the cube sizes considered in the present work (up to $L = 120$). Whether such a limiting value exists for the edge is therefore unclear at this point.

An important difference with two-dimensional squares is that the local enhancement factor in a cube varies significantly in the interior of the cube (albeit less than on the edge). Focusing now on Fig. 3.4, we observe that, upon varying L , the local enhancement factor in the interior of the cube, as a function of scaled coordinates, goes to a limiting behavior for large L . This means that the (absolute) “penetration depth” of the electric field into the cluster is *not* independent of the cluster size but is instead approximately

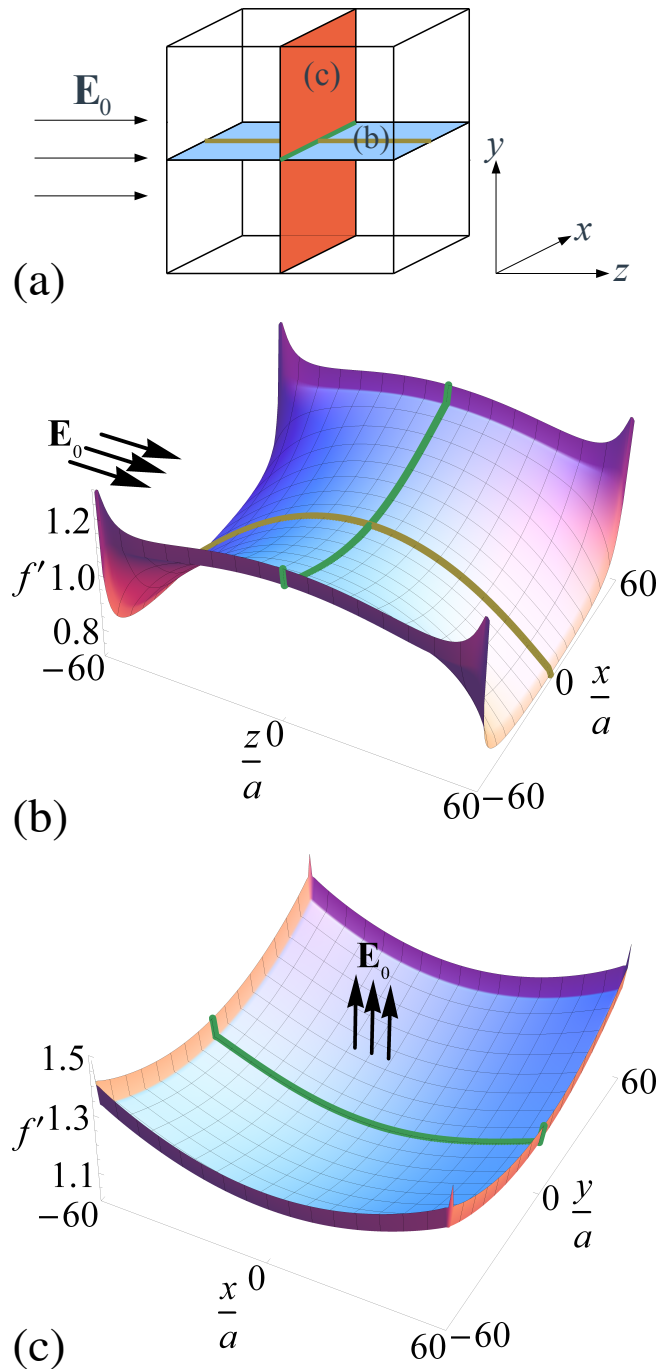


Figure 3.3: (a): The orientation of the planes, cube, electric field, and coordinate system with respect to each other: the planes are cut through the middle of the cube, in the x - z plane and the x - y plane, while the electric field is applied in the z -direction. The cube is oriented such that the ribs lie along the Cartesian directions. The (green) line along the x -axis denotes the intersection of the two planes and is also represented in panels (b) and (c). (b, c): The local enhancement factor f' (defined in the text) of two sheets of dipoles lying on perpendicular planes, cut through the middle of a $120 \times 120 \times 120$ cube of dipoles on a cubic lattice, with lattice constant $\tilde{a} = 2$. Panel (b) corresponds to the blue and panel (c) to the red plane as depicted in panel (a). The yellow and green lines appearing in this figure also correspond to the directions along which we plot the local enhancement factor in Fig. 3.4.

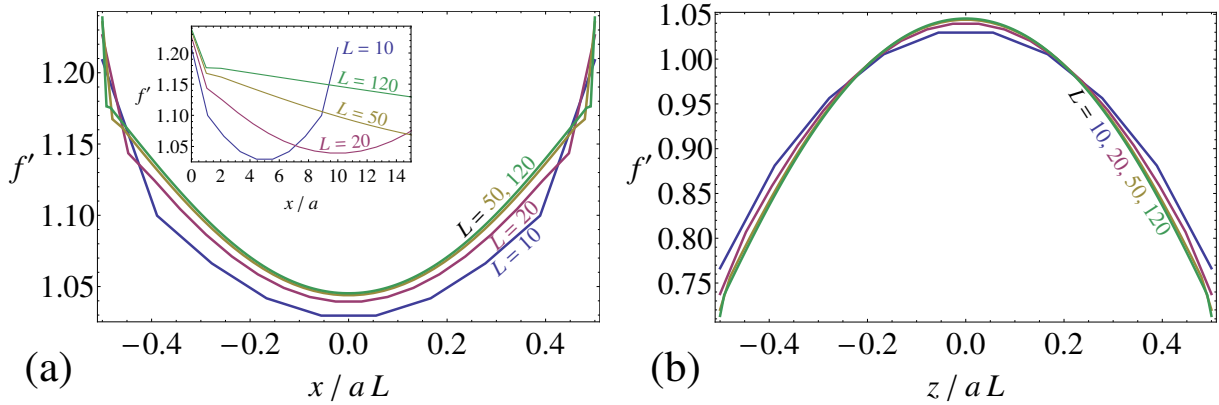


Figure 3.4: The local enhancement factor f' along a straight line in (a) the x -direction ($\perp \mathbf{E}_0$, illustrated in green in Fig. 3.3) and (b) the z -direction ($\parallel \mathbf{E}_0$, illustrated in yellow in Fig. 3.3), through the middle of a cubic cluster of atoms on a simple cubic lattice with lattice spacing $\tilde{a} = 2$, for cube rib lengths $L = 10, 20, 50$, and 120 . In both panels, the rib length was scaled out but, in the inset of panel (a), we also plot f' as a function of the absolute x -coordinate.

proportional to L , unlike the penetration depth of the lower-dimensional objects studied in Ref. [81].

3.4.3 Polarization Charge

Since our algorithm outputs the enhancement $\frac{\mathbf{P}_i}{\alpha_0 E_0}$ of all atoms, it is possible to calculate the dimensionless polarization charge $\tilde{\rho}_p = \frac{a \nabla \cdot \mathbf{P}_i}{\alpha_0 E_0}$ inside the dielectric cube. In continuum theory, the polarization charge in the interior is identically zero, because $\nabla \cdot \mathbf{D} = 0$ (the divergence of the displacement field \mathbf{D} is zero since there is no free charge), therefore $\nabla \cdot \mathbf{E} = 0$ (since the local electric field \mathbf{E} is given by $\mathbf{D} = \epsilon \mathbf{E}$, where we assume a homogeneous dielectric constant ϵ), hence $\rho_p \propto \nabla \cdot \mathbf{P} = 0$ (since the polarization density $\mathbf{P} = \chi_e \mathbf{E}$, where χ_e is the electric susceptibility). In contrast, such an inherent requirement is not present in the CDM and it is therefore interesting to investigate to what extent a polarization charge is present in our work.

In Fig. 3.5, $\tilde{\rho}_p$ is plotted, for a $120 \times 120 \times 120$ cube, along the plane denoted by (b) in Fig. 3.3. We see that $\tilde{\rho}_p$ is nonzero in most regions. However, it should be noted that the observed charge density is very small, judging from the fact that the typical magnitude of $\frac{\mathbf{P}_i}{\alpha_0 E_0}$ is of the order of 10^0 , while the divergence measured in units of lattice spacing is of the order of 10^{-2} .

It is interesting to investigate how the polarization charge varies with the cube rib length L . We therefore plot $\tilde{\rho}_p$ along the line $x = 0$, for several different values of L , as a function of normalized coordinates $2z/aL$, in Fig. 3.6(a). Clearly, the slopes of the graphs display a downward trend, indicative of a smaller polarization charge for larger L . In Fig. 3.6(b), the slope s of a linear fit^b to the graphs in Fig. 3.6(a) is plotted. It turns

^bTo be precise, for the fit, we do not take into account the two outermost points of the graph ($2z/L = \pm 1$).

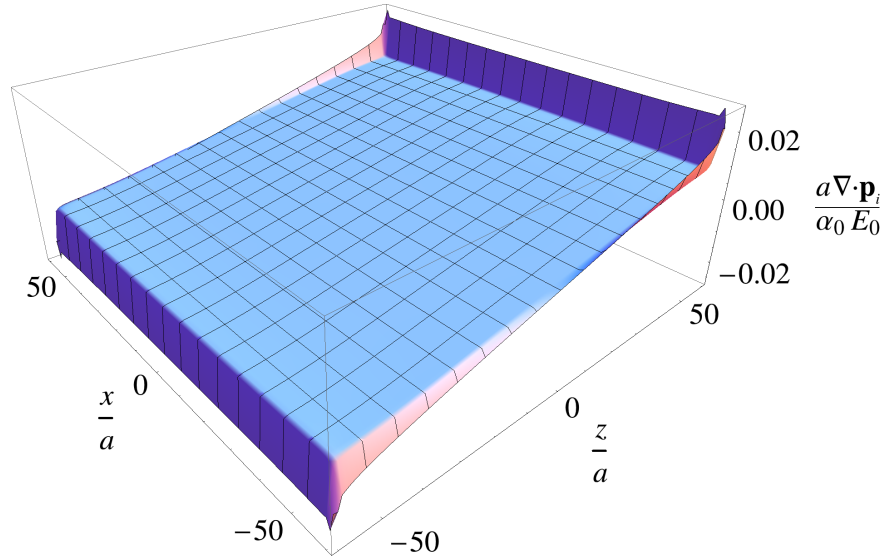


Figure 3.5: The polarization charge density $a \nabla \cdot \mathbf{p}_i / \alpha_0 E_0$ of a $120 \times 120 \times 120$ cube along the plane denoted by (b) in Fig. 3.3(a).

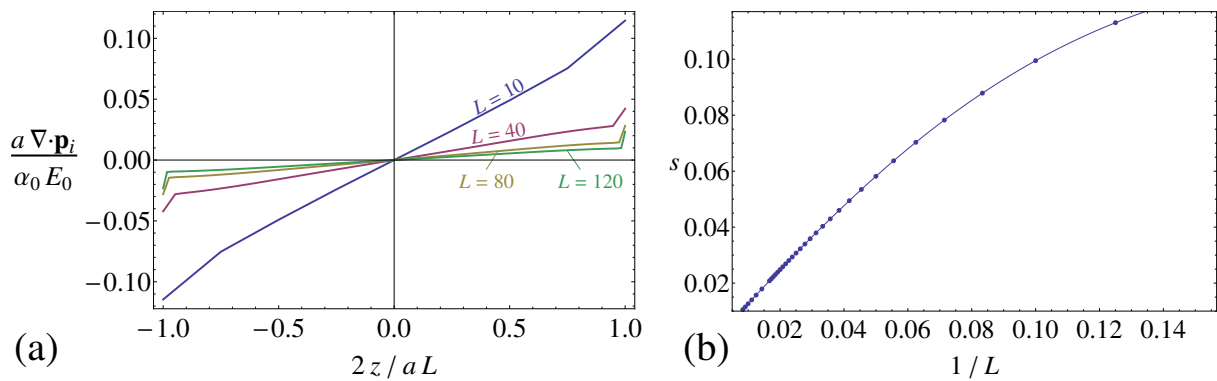


Figure 3.6: (a): The polarization charge density $a \nabla \cdot \mathbf{p}_i / \alpha_0 E_0$ along the line $x, y = 0$ of an $L \times L \times L$ cube, for $L = 10$ (blue), 40 (red), 80 (yellow), and 120 (green). (b): The slope s of linear fits $a \nabla \cdot \mathbf{p}_i / \alpha_0 E_0 = 2zs/aL$ to the functions in (a), as a function of $1/L$ (dots). The solid line is a fit to the data, $s(L) = \sum_{n>0} c_n L^{-n}$. Clearly, $s(L)$ goes as L^{-1} for large L (i.e., small $1/L$).

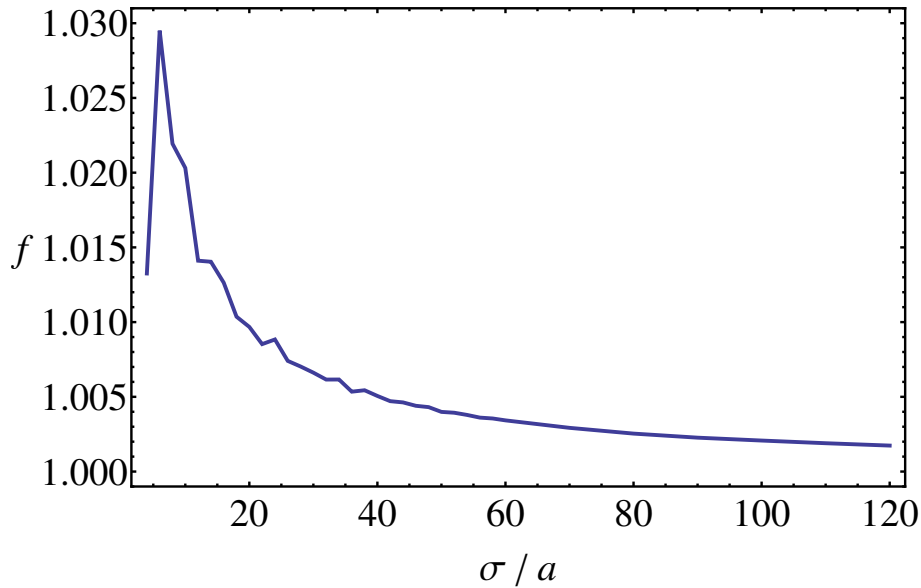


Figure 3.7: The enhancement factor f of a spherical cluster of atoms on a simple cubic lattice, as a function of the number of atoms along the diameter σ/a , for the dimensionless lattice spacing $\tilde{a} = 2$.

out that, to the data of s , a function of the form

$$s(L) = \sum_{n>0} c_n L^{-n}$$

can be fitted with great accuracy, which is also shown in Fig. 3.6(b). The coefficients c_n increase as n increases, but it turns out that the relative size of the terms at $L = 120$ becomes smaller for increasing n . Hence, for large L , we have $s(L) \propto L^{-1}$ and we can be fairly certain that $s(L \rightarrow \infty) = 0$. This is an indication that the polarization charge will vanish for large enough L and that, hence, the continuum limit can be reached asymptotically by increasing the cube size.

3.5 Numerical Results for Spheres

3.5.1 Global Enhancement Factor

In Fig. 3.7, we plot the enhancement factor of a sphere with dimensionless lattice spacing $\tilde{a} = 2$ as a function of its dimensionless diameter σ/a . We note, first of all, that the typical values achieved by the enhancement factor are lower than in the case of cubes. The maximum of the graph, at $\sigma/a = 6$, is $f \approx 1.030$, which is about half as much above unity as the maximum of the enhancement factor for a cube with the same lattice spacing. Moreover, while the enhancement factor for cubes stays at values only slightly below this maximum for large L , the enhancement factor of a sphere decays very quickly with increasing σ/a , such that at $\sigma/a = 120$, the enhancement factor is only $f \approx 1.0017$. We note that f continues to decline even at $\sigma/a = 120$ such that the limiting value was

not reached. Therefore, we cannot be entirely sure what this limiting value will be, but intuitively it does appear that f is headed asymptotically towards unity. We also note that the graph displays some bumps at low σ/a ; we ascribe this to the fact that we can not create an exactly spherical shape using a cubic lattice and, especially for low σ/a , the achieved shape can vary somewhat.

3.5.2 Local Enhancement Factor

In Figs. 3.8(b) and 3.8(c), we plot the local enhancement factor f' along two planes cut through the middle of a $\sigma/a = 120$ sphere, as illustrated in Fig. 3.8(a). We see that, contrary to the observation for cubes, the local enhancement factor is a constant throughout most of the sphere, only varying, rather erratically, near its edge. This constant value is, in the center of the sphere, $f' \approx 1.00336$ and, in most of the plotted region, only the last two digits of this number vary. Such a constant f' seems consistent with continuum theory, which predicts a uniform polarization throughout the interior of the sphere.

Of course, as with the cubes, we can also plot f' along a straight line through the middle of the sphere, done in Fig. 3.9 for two straight lines parallel with, and perpendicular to, the electric field (these lines are also illustrated in Fig. 3.8), for various sphere sizes, as a function of scaled coordinates. We note, as already seen in Fig. 3.8, that the local enhancement factor is much more constant throughout the sphere than it is throughout the cube, and that the flat region becomes wider for larger spheres. The graphs also seem to fall less onto a similar behavior than observed for the cube, and the jump of local enhancement near the edge is somewhat more extreme. As was the case for cubes, a certain “penetration depth” of the electric field is exhibited, which is still contracting (in relative coordinates) as a function of the sphere size when comparing the cases of $\sigma/a = 80$ and $\sigma/a = 120$, but not as fast as the sphere is expanding: from plots as a function of absolute position (not shown), we observe that the absolute penetration depth still becomes somewhat longer from $\sigma/a = 80$ to $\sigma/a = 120$. For the sphere sizes shown, we can therefore not reliably conclude whether this absolute penetration depth will become independent of the sphere size for large σ/a (such that it becomes negligible for large sphere sizes), or whether it will start scaling with the sphere size (such that the relative penetration depth will become constant).

A related complication is that there is a certain arbitrariness as to how the sphere is oriented in the electric field due to the underlying simple cubic lattice. In our case, we have made the choice to orient one lattice vector with the electric field and to plot the local enhancement along the lattice vectors, but we could have made other choices. In the chosen orientation, the sphere surface is very likely to gain flat facets perpendicular and in-plane with the electric field, which likely influences the local enhancement factor near the surface. From the erratic behavior of the local enhancement factor along the cube edge seen in Fig. 3.8, it is not difficult to imagine that plots along lines through the middle might look very different if the cubic lattice were oriented differently.

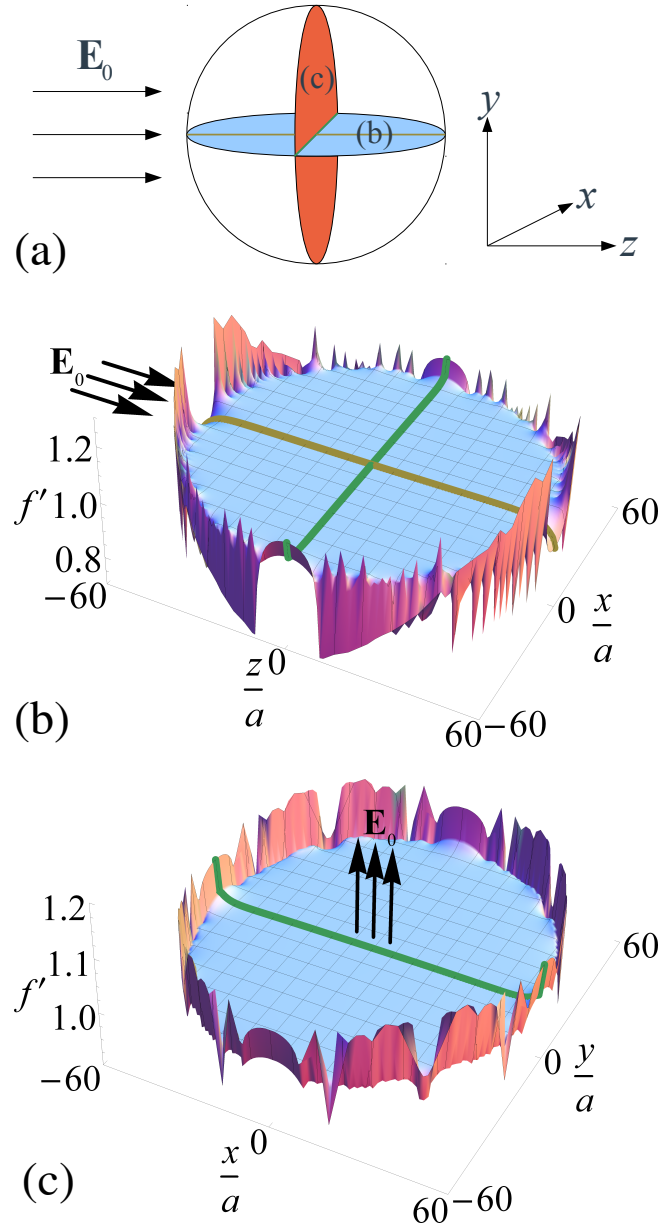


Figure 3.8: (a): The orientation of the planes, sphere, electric field, and coordinate system with respect to each other: the planes are cut through the middle of the sphere, in the x - z plane and the x - y plane, while the electric field is applied in the z -direction. The sphere is oriented such that the lattice vectors of its composing simple cubic lattice lie along the Cartesian directions. The (green) line along the x -axis denotes the intersection of the two planes and is also represented in panels (b) and (c). (b, c): The local enhancement factor f' (defined in the text) of two sheets of dipoles lying on perpendicular planes, cut through the middle of a $\sigma/a = 120$ sphere of dipoles on a cubic lattice, with lattice constant $\tilde{a} = 2$. Panel (b) corresponds to the blue and panel (c) to the red plane as depicted in panel (a). The yellow and green lines appearing in this figure also correspond to the directions along which we plot the local enhancement factor in Fig. 3.9.

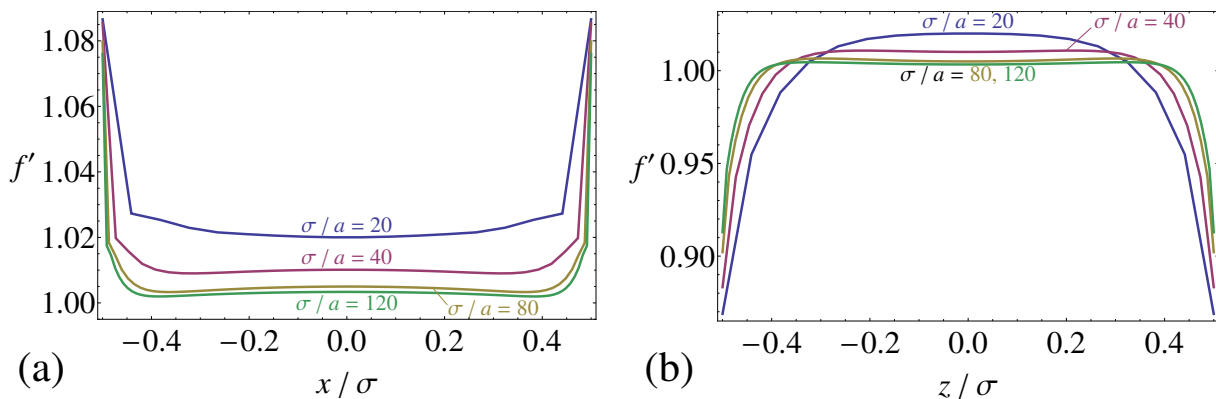


Figure 3.9: The local enhancement factor f' along a straight line in (a) the x -direction ($\perp \mathbf{E}_0$, illustrated in green in Fig. 3.8) and (b) the z -direction ($\parallel \mathbf{E}_0$, illustrated in yellow in Fig. 3.8), through the middle of a spherical cluster of atoms on a simple cubic lattice with lattice spacing $\tilde{a} = 2$, for sphere diameters $\sigma/a = 20, 40, 80$, and 120 , as a function of scaled coordinates x/σ (a) or z/σ (b).

3.6 Conclusions and Outlook

The enhancement factor of a cubic cluster of atoms on a simple cubic lattice at first glance seems to go to a well-defined asymptotic value. However, closer inspection reveals that, in fact, the enhancement factor starts decreasing again as the rib length increases, such that we were not able to determine the limiting value with certainty although, judging intuitively from the graph, we do not expect variations of much more than 0.1% for L -values higher than the ones considered here. The enhancement factor as a function of lattice spacing agrees excellently with results from continuum theory, strongly indicating that the CDM and continuum theory are equivalent. We note that for cubes, this agreement with continuum electrostatics is already excellent for a cube size of only $10 \times 10 \times 10$. For large cube sizes, the local enhancement factor in the interior of the cube scales in such a way that, as a function of relative coordinates, its behavior is independent of the cube size. The polarization charge seems relatively low, however, such that this variation can mostly be ascribed to the electric field varying near the edges of the cube, similar to continuum behavior.

For spheres, the results also indicate an equivalence between the CDM and continuum theory, but in this case the indication is somewhat less strong. The global enhancement factor was seen to decrease with increasing sphere size, reaching $f = 1.0017$ for the largest sphere studied, which is in good agreement with the result one would asymptotically expect, namely $f = 1$. From the graph, it seems entirely possible that the enhancement factor will continue to approach this value for large spheres. The local enhancement factor was constant throughout most of the interior of the sphere, in accordance with continuum theory. A certain nonzero penetration depth of the electric field into the sphere was observed, and it was not possible to determine whether this depth would become independent of the sphere size for large diameters, as we would expect from continuum theory. We note that the sphere is a somewhat problematic shape to model using a simple cubic lattice, which complicates the analysis and might influence the results somewhat.

For future study, it might therefore be worthwhile to investigate in what way the lattice type and orientation influence the resulting local and global enhancement factor. Such a study might also be of some experimental significance since, for experimentally achievable nanoparticles, the diameter of spherical particles could easily be as small as $\sigma/a \approx 20$, which is in the regime where f is still about 1% above the continuum expectation, while surface effects seen in the local enhancement factor are even stronger.

The Optimal Shape for Alignment in an External Electric Field: Bowls, Dumbbells, and Cuboids

Self-assembly and alignment of anisotropic colloidal particles are important processes that can be influenced by external electric fields. However, dielectric nanoparticles are generally hard to align this way because of their small size and low polarizability. In this work, we employ the Coupled Dipole Method to show that the minimum size parameter for which a particle may be aligned using an external electric field depends on the dimension ratio that defines the exact shape of the particle. We show, for rods, platelets, bowls, and dumbbells, that the optimal dimension ratio (the dimension ratio for which the size parameter that first allows alignment is minimal) depends on a nontrivial competition between particle bulkiness and anisotropy because more bulkiness implies more polarizable substance and thus higher polarizability, while more anisotropy implies a larger (relative) difference in polarizability.

4.1 Introduction

Self-assembly of nanoparticles is an interesting thermodynamic process in which particles spontaneously form highly ordered structures, with important technical applications in new materials and devices. In recent years, the technology of synthesizing anisotropic nanoparticles has made tremendous progress [13, 15], and has resulted in the synthesis and analysis of colloidal rods [14], bowls [17–20], and dumbbells [16]. Anisotropic particles are known to self-assemble into orientationally (and possibly positionally) ordered structures under the influence of their interparticle interactions [23–27, 29–31]. However, this process is often difficult to achieve in practice and hampered by slow dynamics. Several techniques can be employed to assist the self-assembly process, such as aligning the particles by introducing a substrate to the system [32, 33], employing a fluid flow [34], or applying external magnetic [35] or electric [36–39] fields. The fact that an external electric field can align an anisotropic particle is due to the particle’s anisotropic polarizability, which causes the particle’s potential energy to vary with its orientation in the field. Since the thermal Brownian motion competes with the tendency to align, the potential energy difference has to be high enough to overcome these fluctuations and substantially align the particle. For nanoparticles, this is difficult to achieve: because of their small size, they are generally only slightly polarizable and thus the difference in potential energy will, for accessible electric fields, be low. In this chapter, we investigate the conditions for alignment and we show that the minimum size for aligning a particle depends on the shape of the particle because of a nontrivial competition between particle bulkiness and anisotropy.

4.2 Theory

As in the previous chapters, we employ the Coupled Dipole Method to calculate the polarizability $\boldsymbol{\alpha}_c$ of a cluster of N Lorentz atoms, each with polarizability α_0 , placed on a lattice with dimensionless lattice constant $\tilde{a} = a/\alpha_0^{1/3}$, where a is the lattice constant in ordinary units. We only consider $\tilde{a} \gtrsim 1.7$ to prevent the polarization catastrophe [64, 93]. We investigate the same shapes as in Chapter 2, namely rods, platelets, bowls, and dumbbells, whose symmetries imply that $\boldsymbol{\alpha}_c$ only has two independent entries on the diagonal, α_{xx} and α_{zz} , as discussed in Chapter 2. If an external electric field \mathbf{E}_0 is applied, the difference between these entries leads to an orientational energy difference Δ , causing certain orientations to be preferred over others.

We note that within the theoretical framework of the CDM, the dipole couplings are the sole cause of the anisotropy of the cluster polarizability (where $\alpha_{zz} \neq \alpha_{xx}$). This can be seen by noting that one atom is considered to have an isotropic polarizability, $\alpha_0 \mathbf{I}$, and, thus, a cluster of N of these atoms would, if atom-atom interactions were ignored, have an isotropic polarizability $N\alpha_0 \mathbf{I}$. Hence, the magnitude of the polarization of the cluster would be independent of the orientation of the external electric field \mathbf{E}_0 . In contrast, in the CDM, where many-body effects *are* included in the calculation, the (diagonalized) cluster polarizability in general does *not* have equal entries on the diagonal and thus has an orientation-dependent polarizability.

As discussed in Chapter 2, the orientational energy difference induced by an external electric field is given by

$$\Delta = \frac{1}{2} (\alpha_{zz} - \alpha_{xx}) \mathbf{E}_0^2 \equiv \frac{1}{2} \Delta_f N \alpha_0 E_0^2, \quad (4.1)$$

with

$$\Delta_f \equiv \frac{(\alpha_{zz} - \alpha_{xx})}{N \alpha_0}.$$

The quantity Δ_f is the difference $f_{zz} - f_{xx}$ of the diagonal elements of the (3×3) enhancement factor $\mathbf{f}_c \equiv \boldsymbol{\alpha}_c / N \alpha_0$, which is a measure for how much the interactions between the point dipoles enhance or reduce the polarizability. From Chapter 2, we know that Δ_f is essentially independent of N and, thus, depends only on the particle's shape and on \tilde{a} but not on its overall size. This independence is approximate since, for small values of N , effects of the discretization employed by the CDM become appreciable. However, for the values of N that we employ, approximations for \mathbf{f}_c and Δ_f are very accurate, which is illustrated by the excellent agreement between values calculated using the CDM (see Chapter 2) and those calculated using continuum theory [86–90]. In Chapter 2, numerical values for Δ were presented for numbers of atoms N low enough that Δ could still be explicitly computed. In this chapter, we will use the independence of Δ_f of the cluster size to extrapolate to much larger N whilst keeping the shape of the cluster constant.

The angular distribution function $\psi(\theta)$ of a particle in solution, where θ is the angle between an applied electric field \mathbf{E}_0 and the particle's rotational symmetry axis, subject to Brownian motion due to the molecular medium at temperature T , is proportional to the Boltzmann factor,

$$\psi(\theta) = \frac{\exp(\beta \Delta \cos^2 \theta)}{4\pi \int_0^{\pi/2} d\theta \sin \theta \exp(\beta \Delta \cos^2 \theta)},$$

where $\beta = 1/k_B T$ is the inverse of the thermal energy. We can quantify the degree of orientational order of this particle by introducing the nematic order parameter

$$S(\beta \Delta) = \langle P_2(\cos \theta) \rangle = 4\pi \int_0^{\pi/2} d\theta \sin \theta \psi(\theta) P_2(\cos \theta),$$

where P_2 is the second Legendre polynomial and $\langle \cdot \rangle$ denotes the ensemble average. The distribution $\psi(\theta)$ for several values of Δ , and the order parameter $S(\beta \Delta)$, are plotted in Fig. 4.1.

From Fig. 4.1, it is clear that an externally applied electric field will only align a particle substantially if $\Delta \gtrsim k_B T$. The number of atoms N^* in the cluster for which $\Delta \approx k_B T$ is, via Eq. (4.1), given by

$$N^* = \frac{2k_B T}{\Delta_f \alpha_0 E_0^2}. \quad (4.2)$$

For given \tilde{a} , we can calculate N^* numerically by using the value of Δ_f as calculated within the CDM for (relatively) small clusters (with $N \approx 10^4$). This is accurate since, as noted before, Δ_f is essentially independent of N .

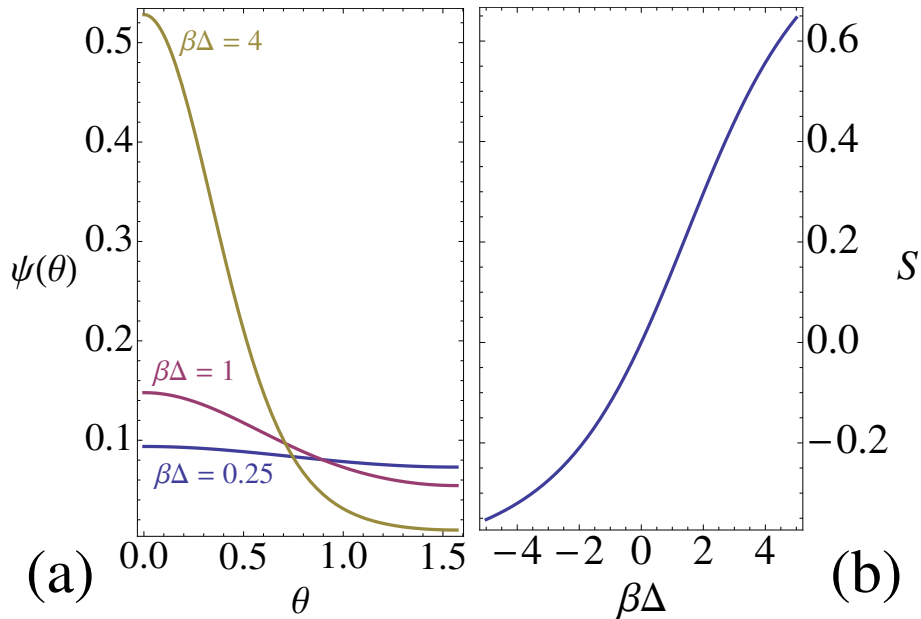


Figure 4.1: The angular distribution function $\psi(\theta)$ (a) and the nematic order parameter S (b) of an anisotropic particle with orientational energy $V_E(\theta) = -\Delta \cos^2 \theta$ in an external electric field \mathbf{E}_0 . Here, θ is the angle between the particle’s rotational symmetry axis and \mathbf{E}_0 and Δ is the energy difference of turning the particle from its least to its most favorable orientation.

4.3 Rods and Platelets

We model rods and platelets as $l \times l \times L$ cuboids of Lorentz atoms on a simple cubic lattice. The shape of the cuboid is determined by its shape parameter $r \equiv l/L$. For each r , we can calculate N^* [by making use of Eq. (4.2)] and, hence, the size parameter for which the cuboid satisfies $\Delta = k_B T$. This “size parameter” is, throughout this chapter, defined as the length of the particle when measured along the electric field if the particle is perfectly aligned^a. For rods, this is given by aL^* and for platelets by al^* , where L^* and l^* can be calculated from r and N^* by

$$L^* = \left(\frac{N^*}{r^2}\right)^{1/3}, \quad l^* = (N^* r)^{1/3}, \quad (4.3)$$

and a follows from $a = \tilde{a}\alpha_0^{1/3}$.

From our numerical data we find that Δ_f is largest for very anisotropic particles (see Chapter 2). This implies, via Eq. (4.2), that N^* is smallest for very anisotropic particles. However, when converting this N^* to a length such as L^* or l^* , a competing mechanism arises from the fact that more anisotropy means less bulkiness. For rods,

^aOther choices for the definition of size parameter are possible, with the condition that it, together with the shape parameter, fixes the dimensions of the particle. For example, one possibility would be to define the size parameter as the diameter of the particle’s circumscribed sphere. Qualitatively, this new definition does not cause any change to our results; quantitatively, we observe that the minima in Fig. 4.2 for rods shift to $l/L \approx 0.47$ and those for platelets to $L/l \approx 0.32$, while there is no change for bowls and dumbbells (since the size parameter remains σ and $\sigma + L$, respectively).

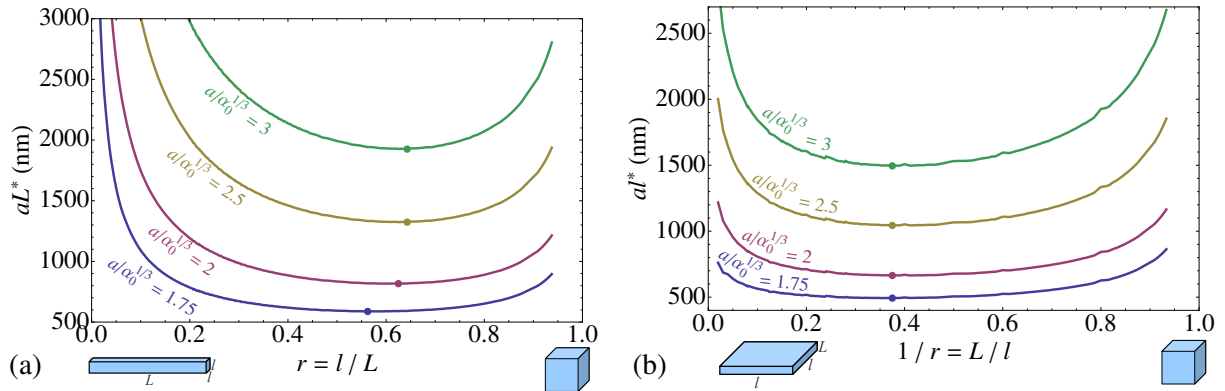


Figure 4.2: The length aL^* (a) and the width al^* (b) for which $l \times l \times L$ cuboidal rods and platelets, respectively, first become alignable by an electric field $E_0 = 100 \text{ V mm}^{-1}$, as a function of their shape (l/L and L/l , respectively), for several different lattice constants $\tilde{a} = a/\alpha_0^{1/3} = 1.75, 2, 2.5$ and 3 . The temperature is $T = 293 \text{ K}$, and the atomic polarizability is $\alpha_0 = 5.25 \text{ \AA}^3$. The dots denote the minima in the graphs.

we note that lowering r has two effects: on the one hand, it lowers N^* because more anisotropy enhances Δ_f ; on the other hand, it increases L^* via Eq. (4.3). Similarly, for platelets, higher anisotropy is achieved through raising r , while l^* rises with increasing r [see Eq. (4.3)]. In other words, fewer atoms “fit” in a highly anisotropic particle for a given L^* (for rods) or l^* (for platelets).

In Fig. 4.2 we plot L^* (for rods) and l^* (for platelets) as a function of the shape parameter $r = l/L$ (for rods) and $r^{-1} = L/l$ (for platelets), for several values of the lattice constant.^b The other parameters are the experimentally typical values of $T = 293 \text{ K}$, $E_0 = 100 \text{ V mm}^{-1}$, and $\alpha_0 = 5.25 \text{ \AA}^3$. For rods, we find a minimum L^* around $l/L \approx 0.62$; this dimension ratio thus defines the optimum shape for alignment of rods in an external electric field. For platelets, a minimum l^* is observed at $L/l \approx 0.38$. The locations of these minima do not depend strongly on the lattice constant. Additional numerical calculations, not shown here, confirm that this (approximate) independence also holds for $\tilde{a} > 3.0$. As could be expected^c, however, a lower lattice constant does imply a lower L^* or l^* .

4.4 Bowls and Dumbbells

The same analysis can be applied to clusters of other shapes. Here, we show results for bowl-shaped and dumbbell-shaped particles. As discussed in Chapter 2 and Fig. 2.3, the bowl shape is achieved by revolving a crescent around its symmetry axis [17]. Note that bowls with $d/\sigma = 0$ are hemispherical shells and bowls with $d/\sigma = 0.5$ are hemispheres.

^bThe chosen value for \tilde{a} corresponds to the following relative permittivities in vacuum: $\epsilon \approx 11.7$ for $\tilde{a} = 1.75$, $\epsilon \approx 4.2$ for $\tilde{a} = 2$, $\epsilon \approx 2.1$ for $\tilde{a} = 2.5$, and $\epsilon \approx 1.6$ for $\tilde{a} = 3$ [calculated using Eq. (2.22)].

^cThe reason that a lower lattice constant lowers L^* or l^* is two-fold: a lower lattice constant means that atoms interact more and hence will have a higher Δ_f ; at the same time it also means that the atom density is higher and thus smaller dimensions are needed to achieve a certain number of atoms.

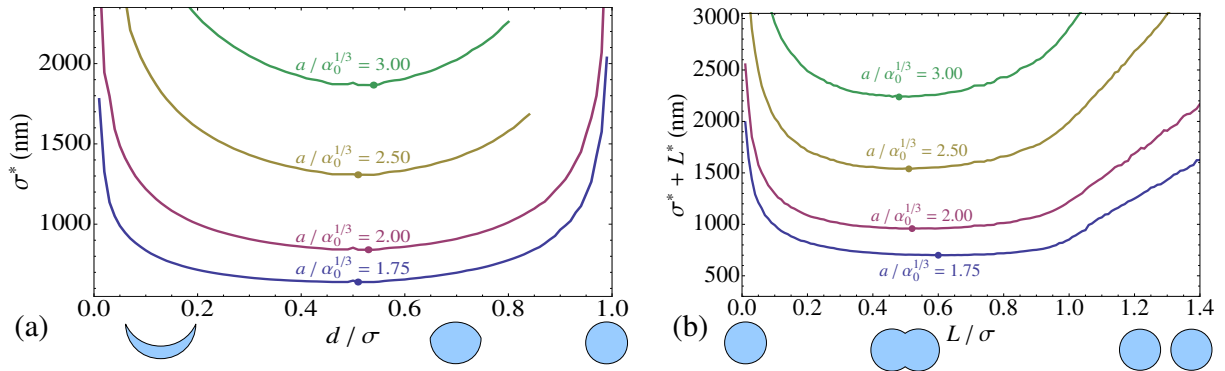


Figure 4.3: The size parameter σ^* (a) and $\sigma^* + L^*$ (b) for which colloidal bowls and dumbbells, respectively, first become alignable by an electric field $E_0 = 100 \text{ V mm}^{-1}$, as a function of their shape parameters d/σ and L/σ , respectively. Here, d is the thickness of a bowl and L is the separation of the two composing spheres of a dumbbell. The bowls and dumbbells are built up of atoms on a simple cubic lattice with dimensionless lattice spacings $a/\alpha_0^{1/3} = 1.75, 2, 2.5,$ and 3 . The temperature is $T = 293 \text{ K}$, and the atomic polarizability is $\alpha_0 = 5.25 \text{ \AA}^3$. The dots denote the minima in the graphs.

For $d/\sigma > 0.5$, instead of a bowl in the conventional meaning, we get a hemisphere with a protrusion on its flat side (the orange area in Fig. 2.3). “Bowls” with $d/\sigma = 1$ are spheres. The dumbbell shape has also been discussed in Chapter 2: we take two spheres of diameter σ at center-to-center distance L from each other and take as the shape of the dumbbell the region in which all points are either in one sphere or in the other, or in both. Thus, $L/\sigma = 0$ corresponds to a sphere, $L/\sigma = 1$ corresponds to two touching spheres, and $L/\sigma > 1$ refers to two separate spheres. Once the shape is determined, we intersect it with a simple cubic lattice grid with spacing a , resulting in a cluster of atoms of approximately the appropriate shape. Note that the size parameter, using the definition mentioned earlier, is given by σ for bowls and $\sigma + L$ for dumbbells.

As in the case of rods and platelets, extrapolation [Eq. (4.2)] has to be used to determine the atom number N^* for which $\Delta \gtrsim k_B T$. Furthermore, since we no longer have a straightforward relation to determine the size parameter (σ^* or $\sigma^* + L^*$) from a given N^* , we use extrapolation of the phenomenological dependence of N on σ ($N \propto \sigma^3$) to estimate σ^* . For dumbbells, we subsequently add L^* (which can be calculated from L/σ and σ^*) to gain the correct size parameter. The result is plotted in Fig. 4.3.

For bowls [Fig. 4.3(a)], we observe that the optimal shape is located around $d/\sigma \approx 0.52$, corresponding to a slightly protruded hemisphere. Note that for $d/\sigma > 0.5$, the bowl shape construction used in this work no longer produces a bowl in the traditional sense of the word. Hence, the optimally alignable “traditional” bowl is as bulky as possible: a hemisphere.

For dumbbells [Fig. 4.3(b)], the minima lie around $L/\sigma \approx 0.51$. Thus, as in the case of rods, the optimum size ratio for dumbbells lies between the maximally anisotropic and bulky configurations (two touching spheres and one sphere, respectively): two comfortably overlapping spheres.

4.5 Conclusion

Using the linear dependence of Δ on N , we estimated for rods, platelets, bowls, and dumbbells the number of atoms and hence the spatial dimensions required for Δ to be of the order of the thermal energy, as a function of the aspect ratio of the cluster. This is relevant because, as we showed, $\Delta \approx k_B T$ is the lowest orientational energy difference that can cause a particle to significantly align in an external electric field. The dimensions found, for an electric field strength of $E_0 = 100 \text{ V mm}^{-1}$, are typically of the order of $1 \text{ }\mu\text{m}$ along the longest dimension of the colloid, indicating that dielectric nanoparticles are not easily aligned in this external field. We note that $N^* \propto E_0^{-2}$ and all the size parameters are $\propto N^{1/3}$, such that we expect the size parameter required for alignment to scale as $E_0^{-2/3}$. This means, for example, that increasing the field strength tenfold would decrease the required size by a factor of approximately 4.6, which would put these particles in the nanoparticle regime (using the definition that the *smallest* dimension should be less than 100 nm). We also note that particles of strongly coupled materials (i.e., low \tilde{a} , achievable for example through a high dielectric constant mismatch between the particle and solvent) have a lower required size, such that nanoparticles consisting of those materials are more easily aligned by an electric field.

We showed that the dependence of the minimum size of an alignable particle on the shape ratio of the particle is nontrivial, as it is *not* in general true that, for alignment, the more anisotropic the particle the better, nor are bulkier particles always better: for all the particle shapes studied here, the optimum shape lies in-between. We note here that, for lower values of \tilde{a} (strong coupling), the graphs of Figs. 4.2 and 4.3 are very flat, such that a broad range of dimension ratios can be considered near-optimal. Interestingly, the graphs are more strongly dependent on the shape when the coupling is weak (high \tilde{a}). Apparently, with weak coupling, it is more important (for alignment) that the particle has exactly the right shape. We also note that, apart from being independent of the field strength (which only affects the height of the graphs and not their shape), the found optimum shapes are also independent of the material that the particle is made of, since the (horizontal) position of the minima in the graphs does not depend strongly on \tilde{a} .

Can Nonadditive Dispersion Forces Explain Chain Formation of Nanoparticles?

We study to what extent dielectric nanoparticles prefer to self-assemble into linear chains or into more compact structures. To calculate the Van der Waals (VdW) attraction between the clusters, we use the Coupled Dipole Method (CDM), which treats each atom in the nanoparticle as an inducible oscillating point dipole. The VdW attraction then results from the full many-body interactions between the dipoles. For non-capped nanoparticles we calculate in which configuration the VdW attraction is maximal. We find that in virtually all cases we studied, many-body effects only result in metastable (local) potential minima at the linear configuration, as opposed to global minima, and that these metastable minima are in most cases rather shallow compared to the thermal energy. In this chapter, we also compare the CDM results with those from Hamaker-de Boer and Axilrod-Teller theory to investigate the influence of the many-body effects and the accuracy of these two widely used approximate methods.

5.1 Introduction

In recent years, the self-assembly of colloidal nanoparticles has received a large amount of attention. Many procedures have been proposed to achieve the desired highly ordered structures, e.g., by using systems with substrates or templates [33], applying external electric or magnetic fields [35–39] to particles with anisotropic response to these fields, or using a fluid flow [34] to align the particles. One of the most widely used techniques, however, is the design and manipulation of particle-particle interactions, which can result in spontaneous self-assembly. Since the synthesis of anisotropically shaped particles has improved significantly in the past decade [13, 15], it is possible to control the shape of the particles and rely on excluded-volume interactions (possibly with the use of a depletant) to achieve alignment [28, 94]. Alternatively, interaction design by controlling the relevant chemistry has also been successfully employed, for instance when synthesizing colloids with patches of different materials [8–10], or by using single-stranded DNA molecules as linkers [11, 12].

Spontaneous self-assembly of nanoparticles into linear chains has been observed experimentally. Various types of particles display this behavior. Observed systems include gold [95], PbSe [96–98], CdSe [96, 99–101], ZnSe [101], and CdTe [102, 103] nanoparticles. In the referenced papers, the behavior is attributed to the presence of a permanent dipole moment in the nanoparticles, although its origin is not entirely understood. Initial explanations attributed it to the intrinsic polar character of the wurtzite (CdSe) structure [99], but this does not explain why the same behavior is observed in the nanoparticles of other structures. Other suggested origins include the presence of trapped, surface-localized charges [101], and breaking of the nanoparticle’s central symmetry due to asymmetric arrangement of crystal facets [97].

More recent experimental [104, 105] as well as theoretical and simulational [105] studies suggest that the capping layer plays an important role in the self-assembly of particles into various structures, including chains. The underlying mechanism here is a competition of the attractions between the particle cores with the entropy loss from distorting the capping layer polymer chains when two or more particles are close together. The linear conformation of the chains is explained by migration of ligands when two particles attach, making the site diametrically opposite the first contact point the most attractive for attachment of a third particle [105]. A detailed simulation study of the influence of the type of capping layer on two- and three-body interactions between nanoparticles [106] indeed suggests, among other things, that, due to the influence of the capping layer, a linear configuration of particles is energetically preferred over a triangular structure. These studies thus provide a possible explanation for spontaneous chain formation that does not depend on the presence of a permanent dipole. In this chapter, we investigate a third option, namely the presence of nonpermanent, induced, fluctuating dipoles. These fluctuating dipoles are the origin of the Van der Waals (VdW) force between atoms and colloidal particles. This force is isotropic between two interacting atoms but becomes orientation-dependent when more atoms are considered, since the fluctuating dipoles, like permanent ones, prefer to lie head-to-toe as opposed to side-by-side. Thus, to investigate this effect, we cannot rely on pairwise interactions between atoms, but have to calculate the full, many-atom VdW interaction, for which the Coupled Dipole Method (CDM) is

ideal. It turns out, however, that in virtually all of the cases that we studied, many-body effects only result in metastable local potential minima at the linear configuration, whereas the global minimum occurs for compact clusters. Moreover, these metastable minima are usually rather shallow compared to the thermal energy. In most cases, the answer to the question asked in this chapter's title therefore seems to be "No." There are, however, extreme parameter regimes where linear configurations have the lowest energy.

The CDM, as mentioned before, employs large-matrix manipulation to calculate the eigenmodes of the system under study; the sum of these frequencies then yields the ground state energy. The CDM takes many-body effects into account and can therefore be expected to be more accurate than both Hamaker-de Boer theory [57, 58], which employs pairwise summation of atom-atom interactions, and a modification thereof, offered by Axilrod and Teller [107], which includes three-atom interactions. In this chapter, we will examine the accuracy of the latter two methods when compared to the CDM (which we will assume to be the "exact" result) for several many-atom systems.

At the time that the CDM was conceived of, it was infeasible to perform the large-scale numerical calculations associated with the required matrix manipulation, but computers of today can easily handle systems of at least $\mathcal{O}(10^4)$ atoms. Recently, the CDM has been employed to calculate interactions between, and also the polarizability of, nanoclusters of various sizes and shapes [64, 66–68, 70, 81, 83, 84]. Furthermore, the accuracy of the first-, second-, and third-order approximations of the CDM have been compared to the CDM itself in the context of graphitic nanostructures, yielding results similar to ours [70].

For reasons that will be explained shortly, the CDM is only valid for non-metallic particles made of a material that satisfies $a/\alpha_0^{1/3} \gtrsim 1.7$, where a is the lattice constant and α_0 the atomic polarizability associated with the material. Furthermore, all the calculations in this chapter are performed for particles in vacuum. To obtain results for particles in a medium, the atomic polarizability would have to be modified to a value that can be obtained by inserting the permittivity contrast between the particle and the medium into the Clausius-Mossotti relation [Eq. (1.3)].

5.2 Methods

5.2.1 The Coupled Dipole Method

In the absence of an external electric field, the Hamiltonian of N Lorentz atoms [Eq. (2.1)] reduces to

$$H = \frac{1}{2m_e} \sum_{i=1}^N \mathbf{k}_i^2 + \frac{m_e \omega_0^2}{2} \sum_{i,j=1}^N \mathbf{d}_i (\mathbf{I}\delta_{ij} - \alpha_0 \mathbf{T}_{ij}) \cdot \mathbf{d}_j, \quad (5.1)$$

where we used \mathbf{k}_i to denote the linear momentum of the i th electron and \mathbf{d}_i for its displacement from its nucleus. Like previously, m_e and ω_0 are the mass of the electron and the characteristic frequency of the Lorentz atoms, respectively, and α_0 is the atomic polarizability as given by Eq. (1.1). In this case completing the square is not necessary, as the Hamiltonian is already quadratic. The angular eigenfrequencies of this harmonic system, ω_k with $k = 1, 2, \dots, 3N$, depend solely on the dimensionless positions $\mathbf{r}_i/\alpha_0^{1/3}$ of

the dipoles and on ω_0 (or, equivalently via Eq. (1.1), α_0). For $N \lesssim 10^4$ it is numerically fairly straightforward to find these eigenfrequencies, and hence the quantum mechanical ground state energy [61–64, 66–68, 83]

$$U(\{\mathbf{r}_i/\alpha_0^{1/3}\}; \omega_0) = \frac{\hbar}{2} \sum_{k=1}^{3N} \omega_k, \quad (5.2)$$

where \hbar is the reduced Planck constant.

In this chapter, we are interested in the effective VdW interactions between nanoparticles composed of atomic dipoles. These nanoparticles are described as clusters of atomic dipoles arranged on a cubic lattice with lattice spacing a such that they form a cubic or an (approximately) spherical nanoparticle. We will only consider interactions between identical nanoparticles. If we assign each nanoparticle a center-of-mass-position \mathbf{R}_i , the spectrum of eigenfrequencies ω_k only depends on the atomic eigenfrequency ω_0 , the number of atoms in each nanoparticle, the dimensionless combinations \mathbf{R}_{ij}/a , where $\mathbf{R}_{ij} = \mathbf{R}_i - \mathbf{R}_j$, and the dimensionless lattice spacing

$$\tilde{a} \equiv a/\alpha_0^{1/3}.$$

Typical values of \tilde{a} are, in vacuum, $\tilde{a} = 2.64$ for hexane, $\tilde{a} = 2.05$ for silica, and $\tilde{a} = 1.75$ for sapphire [81]. For low values of \tilde{a} , we encounter a polarization catastrophe, where the interactions become so strong that they overcome the harmonic binding force between the nuclei and their electrons, and the material becomes a conductor. In the CDM, the catastrophe manifests itself by some of the frequencies ω_k becoming imaginary. For large numbers of atoms, the value at which the catastrophe occurs lies between $\tilde{a} \approx 1.70$ and $\tilde{a} \approx 1.75$, depending on the lattice type. For very low numbers of atoms, the interatomic distance is allowed to be somewhat smaller; e.g., in Sec. 5.3.1, we show a setup with three atoms where the CDM is valid for $\tilde{a} \gtrsim 1.44$.

To obtain the effective interaction energy $V_2^{(CDM)}(\mathbf{R}_1, \mathbf{R}_2)$ between two nanoparticles at position \mathbf{R}_1 and \mathbf{R}_2 , we subtract the ground state energy at infinite separation, which is the same as the energy of each nanoparticle if the other were absent:

$$\begin{aligned} V_2^{(CDM)}(\mathbf{R}_1, \mathbf{R}_2) &= U_2^{(CDM)}(\mathbf{R}_1, \mathbf{R}_2) - U_1^{(CDM)}(\mathbf{R}_1) - U_1^{(CDM)}(\mathbf{R}_2) \\ &= U_2^{(CDM)}(\mathbf{R}_1 - \mathbf{R}_2) - 2U_1^{(CDM)}. \end{aligned} \quad (5.3)$$

Here, $U_2^{(CDM)}(\mathbf{R}_1, \mathbf{R}_2)$ is the CDM-energy of the system that results from taking the positions of the atoms in the clusters at \mathbf{R}_1 and \mathbf{R}_2 and plugging them into Eq. (5.2), and $U_1^{(CDM)}(\mathbf{R}_i)$ is obtained by plugging only the positions of the atoms in cluster i into Eq. (5.2). In the second line, we have resolved some of the dependencies by noting that, in the case of two clusters, translational symmetry requires that $U_2^{(CDM)}(\mathbf{R}_1, \mathbf{R}_2) = U_2^{(CDM)}(\mathbf{R}_1 - \mathbf{R}_2)$ only depends on the relative cluster coordinates and that $U_1^{(CDM)}(\mathbf{R}_i) = U_1^{(CDM)}$ does not depend on the center-of-mass position of the particle. Note that, in this simplification, we also use the fact that the clusters are identical.

If the system consists of two “clusters” consisting each of only one atom with polarizability α_0 , separated by a distance r , calculation of the interaction can be done analytically

within the CDM. When we Taylor-expand the result up to quadratic order for large interatomic distance, we find that the r^0 and r^{-3} terms of the expansion vanish and that we are left with only an r^{-6} term:

$$V_2^{(CDM)}(r) \simeq -\frac{3}{4}\hbar\omega_0\frac{\alpha_0^2}{r^6} \quad (r \gg \alpha_0^{1/3}). \quad (5.4)$$

This is the VdW interaction energy between two atoms.

For three clusters, the effective interaction energy is the sum of the effective interaction energies $V_2^{(CDM)}(\mathbf{R}_i, \mathbf{R}_j)$, plus the three-body term

$$\begin{aligned} V_3^{(CDM)}(\mathbf{R}_1, \mathbf{R}_2, \mathbf{R}_3) &= U_3^{(CDM)}(\mathbf{R}_1, \mathbf{R}_2, \mathbf{R}_3) - V_2^{(CDM)}(\mathbf{R}_1, \mathbf{R}_2) \\ &\quad - V_2^{(CDM)}(\mathbf{R}_2, \mathbf{R}_3) - V_2^{(CDM)}(\mathbf{R}_1, \mathbf{R}_3) \\ &\quad - U_1^{(CDM)}(\mathbf{R}_1) - U_1^{(CDM)}(\mathbf{R}_2) - U_1^{(CDM)}(\mathbf{R}_3) \\ &= U_3^{(CDM)}(\mathbf{R}_1, \mathbf{R}_2, \mathbf{R}_3) - U_2^{(CDM)}(\mathbf{R}_1 - \mathbf{R}_2) \\ &\quad - U_2^{(CDM)}(\mathbf{R}_2 - \mathbf{R}_3) - U_2^{(CDM)}(\mathbf{R}_1 - \mathbf{R}_3) \\ &\quad + 3U_1^{(CDM)}. \end{aligned} \quad (5.5)$$

Here, $U_3^{(CDM)}(\mathbf{R}_1, \mathbf{R}_2, \mathbf{R}_3)$ is obtained by plugging the atom positions of all three clusters into Eq. (5.2), and the second equality is obtained by using Eq. (5.3) and resolving the dependencies, as in the two-body case.

5.2.2 The Hamaker-de Boer Potential

A widely used method for calculating the interaction energy in a colloidal system is to sum the London potential between pairs of fluctuating dipoles. Given a set of atoms with locations $\{\mathbf{r}_i\}$ (where $i = 1, \dots, N$), the total Hamaker-de Boer (HdB) interaction energy is given by

$$U^{(HdB)}(\{\mathbf{r}_i\}) = \sum_{(ij)} v^{(L)}(r_{ij}), \quad (5.6)$$

where r_{ij} is the distance between atoms i and j and $v^{(L)}(r_{ij})$ is the London interaction energy between these atoms, given by

$$v^{(L)}(r) = -\frac{A}{r^6}, \quad (5.7)$$

where A is a constant determined by the two atoms' ionization energies and r is the distance between the atoms. When dealing with clusters of atoms, $U^{(HdB)}(\{\mathbf{r}_i\})$ will contain interactions not only between pairs of atoms in different clusters but also between pairs of atoms in the same cluster. Since we are only interested in the interaction energy between the clusters, we subtract the latter from their total energy to obtain the HdB inter-cluster interaction energy $V_2^{(HdB)}(\mathbf{R}_1, \mathbf{R}_2)$. For two clusters located at \mathbf{R}_1 and \mathbf{R}_2 , respectively, we have, similarly to Eq. (5.3),

$$\begin{aligned} V_2^{(HdB)}(\mathbf{R}_1, \mathbf{R}_2) &= U_2^{(HdB)}(\mathbf{R}_1, \mathbf{R}_2) - U_1^{(HdB)}(\mathbf{R}_1) - U_2^{(HdB)}(\mathbf{R}_2) \\ &= U_2^{(HdB)}(\mathbf{R}_1 - \mathbf{R}_2) - 2U_1^{(HdB)}. \end{aligned}$$

Here, $U_2^{(HdB)}(\mathbf{R}_1, \mathbf{R}_2)$ is obtained by considering the atoms of both cluster 1 and 2 for Eq. (5.6), while $U_1^{(HdB)}(\mathbf{R}_i)$ is obtained by only considering the atoms of cluster i . For three clusters, it turns out that $V_3^{(HdB)}$ (defined similarly to $V_3^{(CDM)}$) vanishes because only atomic pair interactions are considered.

The constant A to be used in Eq. (5.7) can be calculated in various ways. In this chapter, we intend to compare the HdB method to the CDM, and we therefore require that the long-range interaction energy between two atoms be equal when calculated using Eq. (5.7) and when using CDM (Eq. (5.4)). Comparing Eq. (5.4) with Eq. (5.7), we find

$$A = \frac{3}{4}\hbar\omega_0\alpha_0^2. \quad (5.8)$$

This is in agreement with, for example, the results in Ref. [108], Eq. (5), if $u_1 = \hbar\omega_0$ is inserted into that equation. Note that $\hbar\omega_0$ is the energy cost of ionizing the harmonic (Drude) oscillator, as expected.

5.2.3 The Axilrod-Teller Potential

The HdB potential only includes pair interactions and ignores any many-body interactions. In 1943, Axilrod and Teller approximated the three-body contribution to the atomic interaction energy[107],

$$v^{(AT)}(r_i, r_j, r_k) = B \frac{1 + 3 \cos \theta_i \cos \theta_j \cos \theta_k}{r_{ij}^3 r_{jk}^3 r_{ki}^3}, \quad (5.9)$$

where $\cos \theta_i = \hat{\mathbf{r}}_{ij} \cdot \hat{\mathbf{r}}_{ik}$, and B is, according to Ref. [108] with $u_1 = \hbar\omega_0$, given by

$$B = \frac{9}{16}\hbar\omega_0\alpha_0^3.$$

We note that Eq. (5.9), like Eq. (5.7), is a good approximation only for sufficiently large distances. The total Axilrod-Teller (AT) potential energy is the HdB potential energy, extended by a summation over dipole triplets,

$$U^{(AT)}(\{\mathbf{r}_i\}) = U^{(HdB)}(\{\mathbf{r}_i\}) + \sum_{(ijk)} v^{(AT)}(r_i, r_j, r_k), \quad (5.10)$$

and the interaction energy between clusters of dipoles can be defined in the usual way, i.e., by Eqs. (5.3) and (5.5), where the superscript (CDM) is replaced by (AT), and $U_1^{(AT)}$, $U_2^{(AT)}(\mathbf{R}_i, \mathbf{R}_j)$ and $U_3^{(AT)}(\mathbf{R}_i, \mathbf{R}_j, \mathbf{R}_k)$ are now calculated using Eq. (5.10).

As far as we are aware, there is no closed expression for the CDM potential energy of three dipoles in an arbitrary configuration and, therefore, it is in general not possible to compare the expression of the AT potential energy to that of the Taylor expansion of the CDM potential energy, as we did in the case of two dipoles. However, for the special case of an atomic triplet where $r_{12} = r_{23}$ (i.e., the distance between the first and the second dipole is equal to that between the second and the third), we show in Appendix C that the AT potential equals the first two nonzero terms of this Taylor expansion of the CDM potential energy.

5.2.4 A Note on Notation

In this chapter, we only consider setups where a number of clusters (usually two) are stationary, while an extra cluster is moved. For computational simplicity we will therefore consider the stationary clusters as one, so that we only calculate $V_2^{(CDM)}$, $V_2^{(HdB)}$, and $V_2^{(AT)}$ between the moving and the stationary clusters. In the case of three clusters, we have also analyzed the system when considered as three independent clusters and calculated $V_3^{(CDM,HdB,AT)}$ plus the three cluster pair interactions $V_2^{(CDM,HdB,AT)}$. As expected, the resulting interaction energy plots are the same, albeit shifted by a constant. Since every interaction energy we calculate in this chapter is a $V_2^{(CDM,HdB,AT)}$, we can ease the notation: from now on, we denote the interaction energy of the moving cluster with respect to the stationary ones by V_{CDM} , V_{HdB} , and V_{AT} .

5.3 Chains versus Compact Clusters

5.3.1 Atomic Chains and Clusters

Before discussing nanoparticles that are each composed of many atoms, we first consider N single atoms fixed on a straight line, separated by a lattice constant a . We consider an $N + 1$ -th atom near the end of the chain, such that the vector separating this atom from the last atom in the chain has length a and makes an angle θ with the line. This is illustrated in Fig. 5.1 for $N = 2$ (note that $r = a$ in the case of single dipoles). We calculate the CDM, HdB, and AT interaction energies $V_{CDM}(\theta)$, $V_{HdB}(\theta)$, and $V_{AT}(\theta)$, respectively, between the $N + 1$ -th atom and the cluster formed by the N atoms on the line, as a function of the angle θ , in order to study the most favorable (lowest energy) position of the additional atom. Here θ varies from $\theta = 0$, corresponding to the linear configuration, to $\theta = 2\pi/3$, corresponding to an equilateral triangle of the three end-particles of the chain. It is not *a priori* clear which of these configurations is more stable: the orientational dependence of the dipole-dipole interaction favors a linear arrangement and hence $\theta = 0$, but the $1/r^3$ decay of dipolar interactions favors small distances between the particles and hence $\theta = 2\pi/3$. If $V(0) < V(2\pi/3)$, the linear chain is more stable while, otherwise, a dense globule is favored.

In Fig. 5.2, we plot $V_{CDM}(\theta)$, $V_{HdB}(\theta)$, and $V_{AT}(\theta)$ for $N = 2, 3$ and 10, with $\alpha_0 = 5.25 \text{ \AA}$ (such that $\omega_0 = \sqrt{\frac{e^2}{m_e \alpha_0}} = 6.9 \times 10^{15} \text{ s}^{-1}$) for the dimensionless lattice spacings $\tilde{a} = 2.0$ and $\tilde{a} = 1.7$, the latter corresponding to stronger coupling. Note that we represent the interaction energies in units of $k_B T$, where k_B is the Boltzmann constant and $T = 293 \text{ K}$.

Concentrating first on V_{CDM} (solid lines) only, we note that for both $\tilde{a} = 2.0$ and $\tilde{a} = 1.7$, the configuration where the final three particles form an equilateral triangle is stable, by typically $1.5k_B T$ for $\tilde{a} = 2.0$ and by $4k_B T$ for $\tilde{a} = 1.7$. However, the insets also clearly show that, for all cases, a broad local minimum at $\theta = 0$ is separated from the global minimum at $\theta = 2\pi/3$ by a maximum at $\theta \approx 0.32\pi$ for $\tilde{a} = 2.0$ and at $\theta \approx 0.42\pi$ for $\tilde{a} = 1.7$. The barrier between the local and global minimum depends on the coupling parameter \tilde{a} : it is much smaller than $k_B T$ in the weak coupling case of $\tilde{a} = 2.0$, while it grows to almost $1k_B T$ for $N = 10$ and $\tilde{a} = 1.7$. Hence, in both cases, we expect

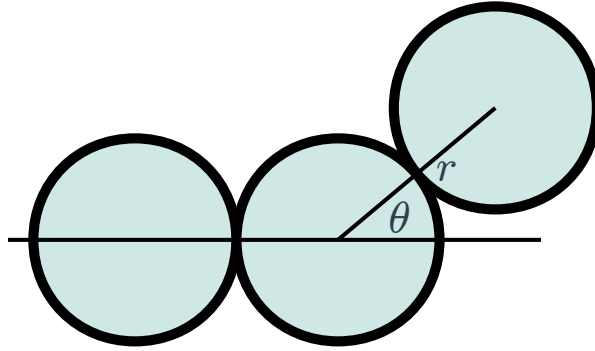


Figure 5.1: The angle θ is defined as the angle between the line connecting the first two particles and the line connecting the last two particles. The distance between two successive particles is r . The situation here depicted is for $N = 2$.

thermal fluctuations to allow for relatively fast crossing of this barrier, such that the linear configurations should be short-lived at best.

When comparing the results of the CDM to those of the HdB and AT methods, there are several things to note. First of all, the accuracy of the approximation is dependent on the interatomic distance: at weaker coupling, $\tilde{a} = 2.0$, they are much more accurate than at stronger coupling, $\tilde{a} = 1.7$. We note, furthermore, that the accuracy is also dependent on θ , higher values of which (more compact clusters) tend to produce a slightly better agreement. Comparing the HdB and the AT, we note, first of all, that AT seems to approximate the features of the CDM graph better than the HdB method, exhibiting a local minimum at $\theta = 0$, a barrier at $\theta \approx 0.3\pi$, and a global minimum at $\theta = 2\pi/3$, whereas the HdB method yields a monotonically decreasing function with its minimum at $\theta = 2\pi/3$. In passing, we can therefore note that many-body effects are clearly responsible for creating a local minimum at the linear configuration. In terms of absolute numbers, the accuracy depends on θ : AT produces better results for low angles, while the HdB method actually beats AT for high angles. Both HdB and AT underestimate the effect of adding a dipole to the chain: the graphs for the various values of N are very close together for HdB and AT, while the CDM produces clearly separated graphs.

From a theoretical perspective, it is interesting to investigate the behavior of $V_{CDM}(\theta)$ for values of \tilde{a} that are lower (i.e., stronger coupling) than the aforementioned value of 1.7. For (large) lattices of atoms, the CDM fails for such low \tilde{a} , since some of the eigenfrequencies ω_k become imaginary. In the specific case of three dipoles forming a configuration as in Fig. 5.1, however, the lower limit is $\tilde{a} \approx 1.435194$. In Fig. 5.3(a), we show what happens to $V_{CDM}(\theta)$ when \tilde{a} is lowered to this value. The HdB and AT approximations, $V_{HdB}(\theta)$ and $V_{AT}(\theta)$, respectively, are not considered here since, for low \tilde{a} , they become increasingly inaccurate. We clearly see that both the potential well at $\theta = 2\pi/3$ (the triangular configuration) and the one at $\theta = 0$ (the linear configuration) deepen as \tilde{a} is lowered, but that the $\theta = 0$ well deepens more. Below the value $\tilde{a} \approx 1.44332$, the well at the linear configuration becomes the deeper of the two. We note that, when compared with the aforementioned lower limit, the range of values for \tilde{a} for which a linear configuration is favorable is extremely narrow. Note, however, that the barrier between the metastable and the stable configurations grows significantly with decreasing \tilde{a} , being

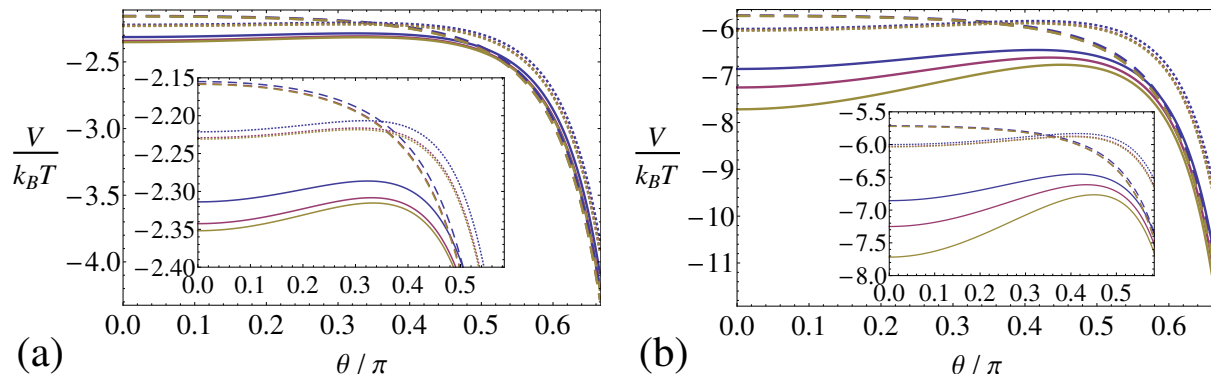


Figure 5.2: Angular dependence of the interaction potential $V(\theta)/k_B T$, where $T = 293$ K, of adding a particle to the end of a string of N particles at $r = a$ (see Fig. 5.1), for dimensionless lattice constant $\tilde{a} = 2.0$ (a) and $\tilde{a} = 1.7$ (b), and for $N = 2$ (blue), $N = 3$ (red), and $N = 10$ (yellow). The results of three calculation methods are shown: the Coupled Dipole Method (solid lines), the Hamaker-de Boer method (dashed lines), and the Axilrod-Teller method (dotted lines). The inset shows a magnification of the small-angle part of $V(\theta)$.

approximately $4k_B T$ at $\tilde{a} = 1.5$ and $14k_B T$ at $\tilde{a} \approx 1.44$, which could cause long-lived linear triplets. This is also visible in Fig. 5.3(b), where the depths Δ of the wells at $\theta = 0$ and $\theta = 2\pi/3$ are plotted as a function of \tilde{a} .

It should be noted that, throughout this subsection, we have varied the dimensionless dipole-dipole distance $\tilde{a} = a/\alpha_0^{1/3}$ by fixing α_0 and varying a . Another option is to fix a and vary α_0 instead. This affects the results, because ω_k/ω_0 depends on \tilde{a} only, and hence the eigenfrequencies ω_k (and, thus, V_{CDM}) are proportional to $\omega_0 \propto \alpha_0^{-1/2}$. Therefore, the shape of the graphs in Fig. 5.3(b), where \tilde{a} is the variable, becomes different, and the relative height of the various graphs of V_{CDM} (Figs. 5.2(a) and (b), and 5.3(a)) with different \tilde{a} change. However, as it turns out, these changes are not significant enough to warrant reporting here (for the parameters of interest), and the same qualitative conclusions apply.

Additional comparisons between the CDM, HdB, and AT approaches are presented in Appendix C.

5.3.2 Clusters and Chains of Spherical Nanoclusters

We now focus on chains of spherical nanoparticles. We perform these calculations with spherical nanoparticles made from silica atoms ($\alpha_0 = 5.25 \text{ \AA}$), which are positioned on a face-centered cubic (fcc) lattice with $\tilde{a} = 2.0$. To create a single nanoparticle of radius R we start by placing the silica atoms on the grid and then remove all those located further than a distance R away from the origin. Hence we obtain an approximately spherical cluster with radius R . Furthermore, we use the same definition for r and θ as given in Fig. 5.1 for the single particles. Now we fix $r = 2R + a$ and proceed in the same manner as above to calculate the interaction energy between a cluster consisting of two spheres and a third sphere as a function of the angle θ . It is again not *a priori* clear which is the more stable orientation: the orientational dependence of the dipole-dipole attraction will

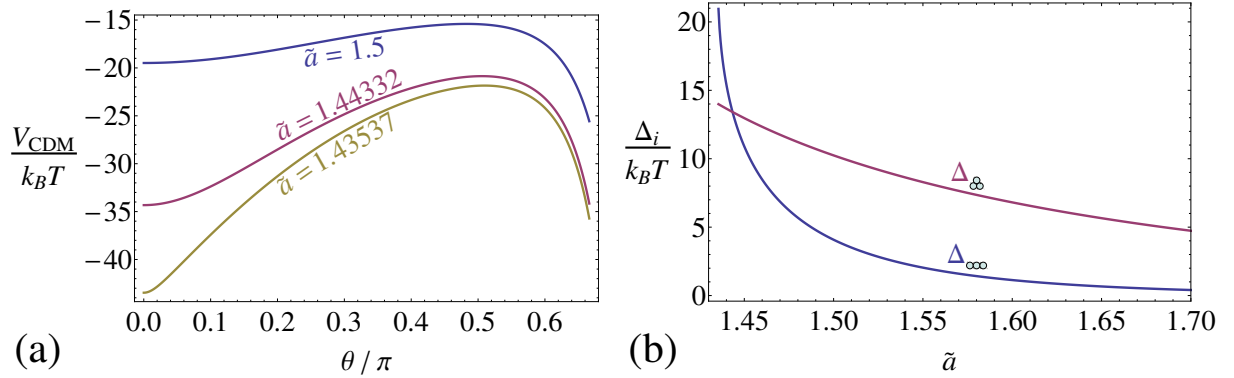


Figure 5.3: (a): The CDM interaction energy V_{CDM} , in room temperature ($T = 293$ K) $k_B T$ units, of adding a third dipole with polarizability $\alpha_0 = 5.25 \text{ \AA}^3$ to a chain of two, under an angle θ (defined in Fig. 5.1). The dimensionless dipole-dipole distance is $\tilde{a} = r/\alpha_0^{1/3} = 1.50$ (blue line), 1.44332 (red line), and 1.43573 (yellow line). (b): The well depth Δ , defined as the difference in interaction energy at the well's configuration and the maximal interaction energy (here located at around $\theta \approx 0.5\pi$) of the linear ($\theta = 0$) configuration (blue) and the triangular ($\theta = 2\pi/3$) configuration (red).

favor a linear arrangement ($\theta = 0$), whereas the $1/r^3$ decay will favor the small distances between the particles ($\theta = 2\pi/3$).

The resulting angle-dependence of the potential is, for $R = 3.85a$ ($N_c = 321$ particles in each cluster), given in Fig. 5.4 for CDM, HdB, and AT. Also shown is the result when we use Hamaker's famous expression for the interaction energy between a pair of spheres [58],

$$V_{\text{Hamaker}}(r, \sigma) = -\frac{\pi^2 \rho^2 A}{12} \left(\frac{\sigma^2}{r^2 - \sigma^2} + \frac{\sigma^2}{r^2} + 2 \log \left[\frac{r^2 - \sigma^2}{r^2} \right] \right), \quad (5.11)$$

where σ is the diameter of the spheres, r is the center-to-center distance between the spheres (given above), A is the London-VdW constant, in our case given by Eq. (5.8), and ρ is the number density of atoms in the sphere, which can be obtained by noting that, for an fcc lattice with $a/\alpha_0^{1/3} = 2$,

$$\rho = \frac{2}{\sqrt{2}a^3} = \frac{1}{4\sqrt{2}\alpha_0},$$

so that $\pi^2 \rho^2 A \approx 42k_B T$ at room temperature. Since our clusters are not exactly spherical and the outer atoms are never exactly a distance R away from the sphere center, the value to use for σ is nontrivial. We derive it by considering the dependence of the mean square displacement $\langle r'^2 \rangle_{\text{ball}}$ of mass inside a solid sphere, with homogeneous mass density ρ , on its diameter d ,

$$\langle r'^2 \rangle_{\text{ball}} = \frac{\int d\mathbf{r}' \rho r'^2}{\int d\mathbf{r}' \rho} = \frac{4\pi \int_{r=0}^{d/2} dr' r'^4}{4\pi \int_{r=0}^{d/2} dr' r'^2} = \frac{3}{20} d^2,$$

where r' is the distance of a mass element $\rho d\mathbf{r}'$ from the center of the sphere. We now assume that the mean square displacement of atoms inside our spherical atom clusters, $\langle r_i^2 \rangle_c = \frac{1}{N_c} \sum_{i=1}^{N_c} r_i^2$, where r_i is the distance of atom i from the center of the sphere, obeys

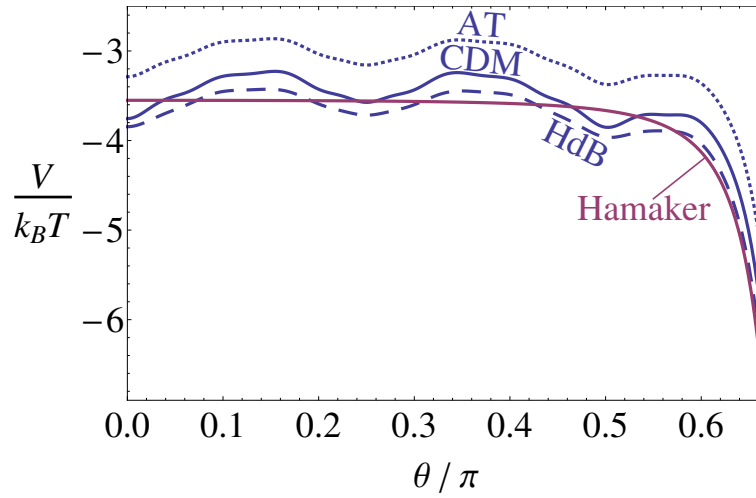


Figure 5.4: Interaction potential for three spherical nanoclusters of radius $R = 3.85a$, giving 321 silica particles each, with dimensionless lattice spacing $\tilde{a} = 2.0$, as a function of the angle θ between the line connecting the first and second and the line connecting the second and third cluster. The results of four calculation methods are shown: the Coupled Dipole Method (solid blue lines), the Hamaker-de Boer method (dashed blue lines), the Axilrod-Teller method (dotted blue lines), and the result from Hamaker’s formula Eq. (5.11) (the solid red line).

the same relationship, $\langle r_i^2 \rangle_c = \frac{3}{20} \sigma^2$, such that

$$\sigma = \sqrt{\frac{20}{3N_c} \sum_{i=1}^{N_c} r_i^2}.$$

The numerical value for our clusters with $R = 3.85a$ turns out to be

$$\sigma \approx 7.55a \approx 0.98 \times 2R.$$

The results of the CDM, HdB, and AT methods are similar to those observed for the atomic chains above, i.e. there is a local minimum at $\theta = 0$, when all three nanoclusters line up, while the global minimum is in the triangle orientation ($\theta = 2\pi/3$). The difference between the local minimum at $\theta = 0$ and the global minimum at $\theta = 2\pi/3$ is of the order of $3k_B T$. The main difference with the atomic chain are the additional wells at $\theta \approx 0.25\pi$ and $\theta \approx 0.5\pi$, separated by barriers of the order of $0.5k_B T$. This structure is caused by the relatively small size of the spherical nanoclusters (only 321 particles each), which renders the surfaces of the clusters not very smooth, causing the edges of the particles to “coincidentally” be closer to each other for some values of θ than for others. Surprisingly, the AT approximation, in this case, gives worse results than the HdB approximation.

The graph obtained from $V_{\text{Hamaker}}(r, \sigma)$ is quite accurate in shape and displays a very good quantitative agreement with the HdB approximation. This is remarkable because, for values of σ so close to r , the effective interaction energy depends strongly on σ . The graph does not contain local minima since, in this method, the spheres are assumed to consist of a continuous, homogeneous material, and the atoms are not individually modeled.

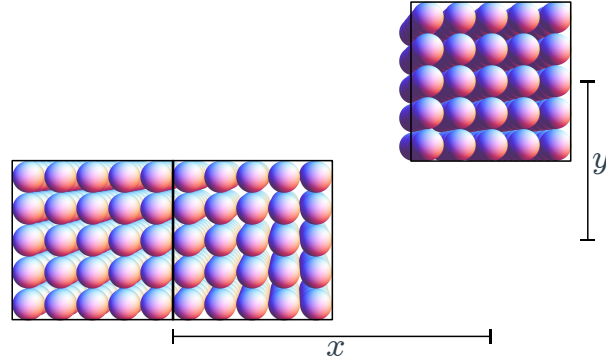


Figure 5.5: Orientation of the system of interest for three cubic clusters of which two are lined up and the third is a distance (x, y) away.

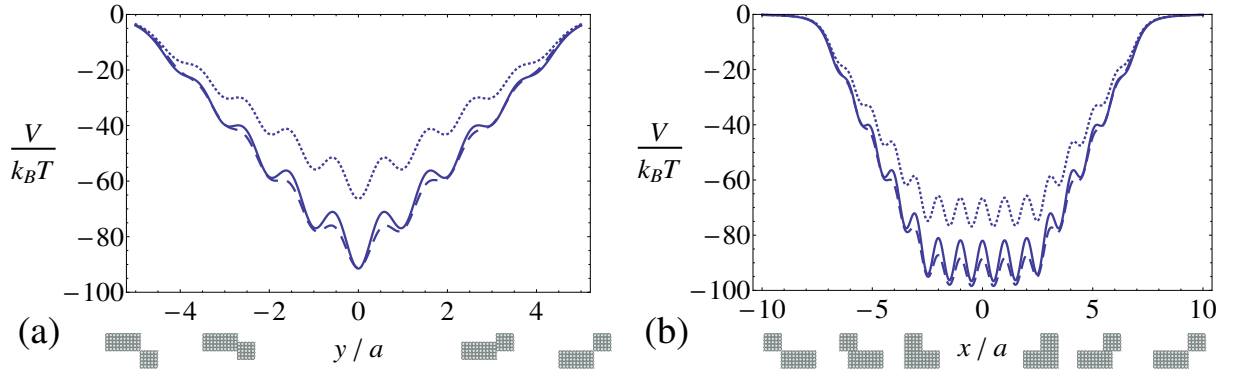


Figure 5.6: Interaction potential for three cubic clusters of 125 particles each with lattice spacing $a = 2.0\alpha_0^{1/3}$, (a) as function of the y -coordinate of the third cluster for fixed $x = 7.5a$ and (b) as function of the x -coordinate of the third cluster for fixed $y = 5a$. The results of three calculation methods are shown: the Coupled Dipole Method (solid lines), the Hamaker-de Boer method (dashed lines), and the Axilrod-Teller method (dotted lines).

5.3.3 Clusters and Chains of Cubic Nanoclusters

Next, we consider $L \times L \times L$ cubic nanoparticles of $N_c = L^3$ atoms on a cubic lattice with lattice spacing a . Similarly to the case above, we focus on a configuration of three particles: two lined up and close together, forming essentially a single $2L \times L \times L$ particle, with a third particle in its vicinity. We present results for clusters with $L = 5$. For the cubic particles of interest we will use Cartesian coordinates instead of the polar coordinates used before, with the x -direction parallel to the chain and y - and z -directions perpendicular, as illustrated in Fig. 5.5.

Here we consider two cases, both for coupling constant $\tilde{a} = 2.0$. First we vary y for fixed $x = 7.5a$, such that the third particle can (just) slide “vertically” past the other two on the right side. Note that this means that when $y = 0$, all three clusters lie on the same line and are touching (i.e., this corresponds to the $\theta = 0$ orientation of the spherical clusters). Secondly, we fix $y = 5a$ and vary x , such that the third particle slides “horizontally” along x on top of the other two particles.

The results are plotted in Fig. 5.6. Fig. 5.6(a) shows the potential $V(x = 7.5a, y)$ for the first, “vertical” case, revealing local minima at (roughly) $y/a \approx 0, \pm 0.96, \pm 1.93$, and ± 2.89 , while a “pseudo-minimum” (inflection point) occurs at $y/a \approx \pm 3.82$. These correspond to alignment of horizontal sheets of atoms in the three $5 \times 5 \times 5$ nanoclusters; we interpret the small deviation from perfect alignment (which occurs at $y/a = 0, \pm 1, \pm 2$, etc.) as a finite-size effect. The global minimum in Fig. 5.6(a) occurs for the linear chain characterized by $y = 0$. The energy barriers between adjacent local minima vary from roughly $5.9k_B T$ between $y/a = \pm 0.96$ and $y/a = 0$, and $2.7k_B T$ from $y/a = \pm 1.93$ to $y/a = \pm 0.962$, to vanishingly small barriers for $y/a \geq 3$. As a consequence, one could expect (temporary) trapping in local minima at $y/a = \pm 0.96$ and ± 1.93 . Fig. 5.6b shows the potential $V(x, y = 5a)$ for the second, “horizontal” case. Again, we observe local minima, near where vertical sheets of atoms align, in this case for $x/a \approx \pm 0.50, \pm 1.50, \pm 2.48, \pm 3.45, \pm 4.43, \pm 5.38$. The six deepest ones (with $|x/a| < 2.5$) are essentially degenerate and separated by barriers of about $15k_B T$. We note that the minima occur closer to perfect alignment when the third cube is near the middle: here, the effect of the edges of the first two cubes is smallest. For $|x/a| \gtrsim 7/2$, we can still make out the points where either 4, 3, 2, or 1 sheet(s) align(s).

Combining the information of Figs. 5.6(a) and 5.6(b) reveals that the global minimum, for these $5 \times 5 \times 5$ clusters, occurs in the vicinity of the “triangular” configuration, since $V(x = a/2, y = 5a) \approx -97k_B T$, whereas the deepest linear-chain minimum is $V(x = 7.5a, y = 0) = -91k_B T$, the difference being about $6k_B T$. One should realize, however, that the barrier(s) separating the two configurations are of the order of $100k_B T$, such that a chain, once formed, could essentially exist forever. It thus appears that the main difference between the attachment potential of atomic triplets (treated in an earlier section) and the $5 \times 5 \times 5$ triplets here is the existence of local minima separated by barriers due to the underlying atomic structure of the latter. These results are qualitatively similar to those of $3 \times 3 \times 3$ and $7 \times 7 \times 7$ particles.

We note again that the HdB approximation gives better results than the AT approximation, although the latter seems to better approximate the height of the inter-well barriers. We note that both the shape of the graphs, which feature local minima induced by the atomic structure, as well as the qualitative conclusion that HdB is more accurate than AT, are similar to those presented in Ref. [70]. For this setup, we also calculated the net force on the third (“moving”) particle by considering the gradient of V , but no interesting conclusions could be drawn from these calculations, except that the accuracy of the HdB and AT approximations remained roughly the same.

5.4 Summary and Conclusion

In this chapter, we have addressed the question of whether nonadditive dispersion forces can explain chain formation of nanoparticles. We have done this using the Coupled Dipole Method (CDM), where we model the nanoparticles as built up out of atoms and take into account all their many-body interactions. We have studied configurations of single atoms and spherical and cube-shaped atomic clusters. For almost all of these systems, we have found a local minimum of the potential energy at the linear configuration, but a global

minimum at the triangular one, making the latter thermodynamically favorable. For single dipoles, the energy difference between the two configurations is generally several $k_B T$ and the barrier between the two only of the order of, at most, one $k_B T$, such that we do not expect linear configurations to be stable. For a small parameter subspace with strong coupling we did find a stable linear configuration, which could indicate that strongly polarizable particles (most of which the CDM is unable to model due to the polarization catastrophe) indeed have a stable minimum at the linear configuration due to dipole-dipole coupling. This is speculative, however, since the result was obtained for point dipoles whereas real particles have nonvanishing dimensions and, furthermore, only a small coupling region that the CDM could still handle displayed the stable linear configuration, such that judgments about the majority of the stronger-coupling regime are not based on quantitative evidence. For spherical clusters of dipoles, we found only a stable triangular configuration. For cubes, although the triangular configuration is the overall minimum, the energy barrier between the linear and triangular configuration is so large that, once formed, we expect either configuration to essentially exist forever. However, this conclusion could have been reached using a Hamaker-de Boer (HdB) approach as well, such that we have to conclude that it is the shape, rather than coupled dipoles, that causes the local minimum at the linear configuration.

In many of the studied cases we have also investigated how accurate the Hamaker-de Boer (HdB) and Axilrod-Teller (AT) methods of calculating the interaction energy are when compared to the result given by the CDM. From the studied cases we can conclude that for strings of single dipoles, many-body effects are significant, especially when the coupling is strong. For the clusters consisting of many dipoles (i.e., spheres and cubes), we found that the HdB method performs very well and, in fact, much better than the AT method. A possible explanation for this is that, while both approaches are only exact when (dimensionless) dipole-dipole distances are large, the AT method might be more sensitive to dipoles being close together; and in a cluster of dipoles, each dipole has many nearby neighbors. More research is required to test this hypothesis. For spheres, we compared our results with Hamaker's expression, which is obtained by integrating the Van der Waals interaction over the volume of two spheres.

In the work by Schapotschnikow *et al.* [106], where simulation methods are used to arrive at an effective three-body interaction energy between triplets of nanoparticles stabilized by capping layers, it is suggested that linear chains are the overall most favorable orientation. In our work, we find that the CDM, which includes many-body VdW interactions between atoms but ignores steric interactions between the capping layers, shows that many-body linear chains are metastable, whereas the two-body HdB method exhibits no local minimum at the linear configuration. Still, in the CDM, the triangular configuration is overall more favorable, and the linear configuration is not stable enough to predict stable linear chains in a Brownian environment. From this we can conclude, as already suggested by Schapotschnikow *et al.*, that an important role in explaining chain formation could be played by effective three-body interactions between the particles' capping layers that make triangular configurations unfavorable. Many-atom VdW interactions, while not strong enough by themselves to make linear chains favorable, do provide a local minimum at this configuration, making it the most favorable configuration if triangular ones are excluded by steric interactions. This could provide an explanation for spontaneous chain

formation that does not include permanent dipole moments. It would be of interest to include steric interactions in our calculations in the manner employed by Schapotschnikow *et al.*, or, using the CDM, allowing for many-body interactions between ligand segments even during the simulation steps, thus calculating a full, many-body, effective average interaction energy. This is left for future study.

Maarten Verdult is acknowledged for his part in the work presented in this chapter. Even though his original data was lost, his work served as the backbone around which this chapter was later fleshed out.

The Self-Consistent Electric Field-Induced Dipole Interaction Energy of Particles in an External Electric Field: Spheres, Cubes, and Rods

When calculating the electric field-induced interaction between inducible dipoles, the dipole moments of these inducible dipoles are often taken to be equal to their polarizability multiplied by the external electric field. However, this approach is not exact, since it does not take into account the fact that particles with a dipole moment affect the local electric field experienced by the other particles. We employ the Coupled Dipole Method to calculate the electric-field-induced dipole pair interaction self-consistently: that is, we take into account many-body effects on the individual induced dipole moments. We present an analytical expression for the self-consistent electric field-induced interaction of two inducible dipoles. We also calculate interactions of particles with nonvanishing dimensions by splitting them up into self-consistently inducible dipole chunks of polarizable matter. For point dipoles, spheres, cubes, and rods, we discuss the differences and commonalities between our self-consistent approach and the aforementioned approach of pre-assigning dipole moments to either the point dipoles or, in the case of spatially extended particles, to the chunks making up the particle.

6.1 Introduction

Electric field-induced self-assembly of colloidal particles is an area with tremendous potential for technical applications. Unsurprisingly, therefore, experimental studies in which electric fields are used to orientationally and/or positionally organize particles are commonplace today [36–39, 109–111], as are simulation studies in this area [112–116]. The simultaneous progress in particle synthesis [13, 15] continues to increase the diversity of systems suitable for electric-field induced assembly. Nowadays, particles of many sizes, materials, and anisotropic shapes can be synthesized and the problem of theoretically describing the interaction of these anisotropic particles with the electric field and with each other under the influence of the electric field becomes less and less trivial. In fact, as we will show in this work, even the dipolar interaction between a pair of spherical particles is nontrivial.

We can roughly distinguish two processes by which an electric field can induce organization in a system of colloids that possess no permanent dipole, namely individual alignment and interparticle interactions. Individual alignment occurs if a particle has an anisotropic polarizability causing a potential-energy minimum at orientation(s) where the induced dipole moment is strongest. Interparticle interactions are the result of interactions between the induced dipole moments of two or more particles and are often crucial for electric field-induced formation of spatially ordered structures.

Theoretically, these interactions have often been described by assigning a permanent dipole moment, equal to the particle polarizability multiplied by the applied electric field, to each particle and then making use of the well-known expression for the interaction energy between two electric point dipoles [51]. This approach, which we will refer to as the “single permanent dipoles” (SPD) approach, is nonexact for two different reasons. The first is that a particle has a finite size and its polarization will therefore be spread out over its volume instead of concentrated in a point. This problem can be overcome by splitting up the particle into a sufficiently large number of “chunks” of matter, assigning to each chunk a (smaller) polarization, and then summing the interactions between all chunk pairs [117]. We dub this approach the “cluster of permanent dipoles” (CPD) approach. The second nonexactness arises because we neglected the influence that the particles have on each other’s induced dipole moment. Since each particle that gains a dipole moment produces an electric field, it will affect the local electric field experienced by all other particles, which is therefore no longer equal to the external (applied) electric field. Calculating each particle’s (or particle chunk’s) dipole moment turns out to be a system of linear equations that can be solved self-consistently within the framework of the Coupled Dipole Method (CDM) [61, 62, 81, 83].

The CDM was proposed by Renne and Nijboer in the 1960s to self-consistently calculate the eigenmodes of a system of inducible dipoles using large-matrix manipulation and, by summing the frequencies of these eigenmodes, to calculate the Van der Waals (VdW) interaction energy between clusters of atoms [61, 62, 64, 66–68]. Discrete dipoles have also been used for scattering calculations within the Discrete Dipole Approximation, which involves an incident oscillating electric field [71–74]. By considering a permanent electric field instead, the polarizability of particles of various shapes has been investigated as well [81, 83], resulting, where comparison was possible, in good agreement with polariz-

ability calculations using continuum theory [86–90]. However, to our knowledge, prior to our 2011 publication [83] a permanent electric field had never been included in the CDM’s Hamiltonian and, as a consequence, the dipole-dipole interaction between particles in an external electric field has not been calculated self-consistently until now.

To fit in with our naming scheme, we shall dub the approach that utilizes the CDM the “cluster of self-consistent dipoles” (CSCD) approach. In the case where each “cluster” in fact consists of only one dipole and hence the CDM is applied to only two interacting dipoles, we reserve a separate name and acronym: the “single self-consistent dipoles” (SSCD) approach. The reason for this distinction is that in the special case of two interacting dipoles, the set of linear equations can be solved analytically such that, for the SSCD, we use an analytical expression instead of numerical linear algebra algorithms. To our knowledge, this expression, presented in Sec. 6.3, has not been presented before. The widely used SPD approach turns out to be the dominant long-distance approximation of our new (SSCD) expression.

In this Chapter, we first introduce the CDM in Sec. 6.2 and generalize its formulation somewhat to allow for the description of systems split up into chunks of matter that are not necessarily of atomic proportions. Although we provide the tools for calculating VdW interactions, in this work we concentrate on the results for electric field-induced interactions. In Sec. 6.4 we compare our numerical results for the electric field-induced interaction energy for various particle shapes, namely spheres, cubes, and rods, using the various calculation techniques discussed above; i.e., the SPD approach, the CPD approach, the SSCD approach, and the CSCD approach (which we deem to be the “exact” result if the number of dipoles is large enough). We also vary the number of dipoles per cluster to investigate how many dipoles are required for an accurate description of the interaction energy. We find that the accuracy of the various approaches depends mainly on the degree of anisotropy in the particle shape, with the SSCD approach performing well for spheres and cubes, even better than the CPD approach. For rods, however, both single dipole approaches (SSCD and SPD) are severely lacking in accuracy and the cluster approaches (CSCD and CPD) give better results. Here, an approach that uses clusters of a very small number of self-consistent dipoles turns out to give very good accuracy. As for the question of how many dipoles are enough to accurately describe the electric field-induced interaction, we find that the answer depends strongly on the particle shape, with cubes and rods generally needing a smaller number of dipoles than spheres do. The reason might be that a spherical shape is hard to approximate using identical chunks whereas, for cubes and rods (which are described as cuboids), this is trivial even with a very low number of chunks.

6.2 The CDM

In previous work [61, 62, 83–85], when considering physical systems using the CDM, the atoms were usually assumed to consist of a nucleus and one electron bound to it by a harmonic force. In such a model, the charges making up the induced dipole are $\pm e$, where e is the elementary charge, and the mass of the vibrating part of the atom is the electron mass m_e . If the harmonic force is defined to have the characteristic frequency ω_0 , the

atomic polarizability then follows by [51, 93]

$$\alpha_0 = \frac{e^2}{m_e \omega_0^2}. \quad (6.1)$$

The Hamiltonian H of a system of N of these atoms, in an external electric field \mathbf{E}_0 can be written as

$$H(\{\mathbf{d}_i\}, \{\mathbf{k}_i\}) = \frac{1}{2m_e} \sum_{i=1}^N \mathbf{k}_i^2 + \frac{e^2}{2\alpha_0} \sum_{i=1}^N \mathbf{d}_i \cdot (\mathbf{I}\delta_{ij} - \alpha_0 \mathbf{T}_{ij}) \cdot \mathbf{d}_j - e \sum_{i=1}^N \mathbf{d}_i \cdot \mathbf{E}_0. \quad (6.2)$$

Here, \mathbf{I} is the 3×3 identity matrix, \mathbf{k}_i is the momentum of the electron associated with atom i , and \mathbf{d}_i is this electron's distance vector to the atom nucleus. The matrix \mathbf{T}_{ij} is the dipole tensor

$$\mathbf{T}_{ij} = \begin{cases} (3\mathbf{r}_{ij}\mathbf{r}_{ij}/r_{ij}^2 - \mathbf{I})/r_{ij}^3 & \text{if } i \neq j, \\ \mathbf{0} & \text{if } i = j, \end{cases}$$

where $\mathbf{r}_{ij} = \mathbf{r}_i - \mathbf{r}_j$, $r_{ij} = |\mathbf{r}_{ij}|$ and $\mathbf{0}$ is a 3×3 matrix filled with zero's. We note here that by a canonical transformation $(\{\mathbf{d}_i\}, \{\mathbf{k}_i\}) \rightarrow (\{\mathbf{p}_i\}, \{\mathbf{k}'_i\})$, where $\mathbf{p}_i = e\mathbf{u}_i$ and $\mathbf{k}'_i = m_e \dot{\mathbf{p}}_i/e^2$, we could write the Hamiltonian (6.2) such that only the atomic properties α_0 and e^2/m_e would be input parameters. For simplicity, we will continue to use $(\{\mathbf{d}_i\}, \{\mathbf{k}_i\})$ as coordinates, but we note that the CDM thus depends on only two atomic properties (α_0 and e^2/m_e).

We wish to model systems where the ‘‘atoms’’ in fact represent ‘‘chunks’’ of matter instead of physical atoms. For this purpose, we generalize the three atomic properties: the charge of oscillator i becomes q_i , its mass m_i , and the polarizability becomes α_i , which we choose to be a 3×3 tensor in order to allow for anisotropic ‘‘chunk’’ polarizabilities. In terms of these quantities, the Hamiltonian reads

$$H(\{\mathbf{d}_i\}, \{\mathbf{k}_i\}) = \frac{1}{2} \sum_{i=1}^N \mathbf{k}_i \cdot \mathbf{m}_i^{-1} \cdot \mathbf{k}_i + \frac{1}{2} \sum_{i=1}^N \mathbf{d}_i \cdot \mathbf{q}_i \cdot (\alpha_i^{-1} \delta_{ij} - \mathbf{T}_{ij}) \cdot \mathbf{q}_j \cdot \mathbf{d}_j - \sum_{i=1}^N (\mathbf{q}_i \cdot \mathbf{d}_i) \cdot \mathbf{E}_0,$$

where we defined the matrices $\mathbf{m}_i \equiv m_i \mathbf{I}$ and $\mathbf{q}_i \equiv q_i \mathbf{I}$. We now introduce $3N$ -dimensional vectors \mathcal{K} , \mathcal{D} and \mathcal{E}_0 , which are built up out of the \mathbf{k}_i , \mathbf{d}_i , and copies of \mathbf{E}_0 , respectively. Furthermore, we define the $3N \times 3N$ -dimensional matrices $\mathcal{M} \equiv \text{diag}(\{\mathbf{m}_i\})$, $\mathcal{Q} \equiv \text{diag}(\{\mathbf{q}_i\})$, $\mathcal{A} \equiv \text{diag}(\{\alpha_i\})$, and, lastly, \mathcal{T} , built up out of all the \mathbf{T}_{ij} . In terms of these quantities, the Hamiltonian reads

$$H(\mathcal{D}, \mathcal{K}) = \frac{1}{2} \mathcal{K} \cdot \mathcal{M}^{-1} \cdot \mathcal{K} + \frac{1}{2} \mathcal{D} \cdot \mathcal{Q} \cdot (\mathcal{A}^{-1} - \mathcal{T}) \cdot \mathcal{Q} \cdot \mathcal{D} - (\mathcal{Q} \cdot \mathcal{D}) \cdot \mathcal{E}_0,$$

and, since all the matrices involved are symmetric, the square can be completed such that

$$H = H_0 + U_E.$$

Here, H_0 is the Hamiltonian of a set of shifted harmonic oscillators,

$$H_0 = \frac{1}{2} \mathcal{K} \cdot \mathcal{M}^{-1} \cdot \mathcal{K} + \frac{1}{2} (\mathcal{D} - \mathcal{D}_0) \cdot \mathcal{Q} \cdot (\mathcal{A}^{-1} - \mathcal{T}) \cdot \mathcal{Q} \cdot (\mathcal{D} - \mathcal{D}_0),$$

with \mathcal{D}_0 a (time-independent) $3N$ -dimensional vector that describes the shift of the equilibrium positions, satisfying the equation

$$\left(\mathcal{A}^{-1} - \mathcal{T}\right) \cdot \mathcal{Q} \cdot \mathcal{D}_0 = \mathcal{E}_0. \quad (6.3)$$

The constant potential energy shift due to the electric field reads

$$U_E \equiv -\frac{1}{2} \mathcal{E}_0 \cdot \left(\mathcal{A}^{-1} - \mathcal{T}\right)^{-1} \cdot \mathcal{E}_0. \quad (6.4)$$

We switched the Hamiltonian variable \mathcal{D} to $\mathcal{D} - \mathcal{D}_0$, which is allowed since \mathcal{K} is also $\mathcal{D} - \mathcal{D}_0$'s conjugate momentum.

The equations of motion that follow from the Hamilton equations can be combined into:

$$\frac{\partial^2 (\mathcal{D} - \mathcal{D}_0)}{\partial t^2} = -\mathcal{M}^{-1} \mathcal{Q} \cdot \left(\mathcal{A}^{-1} - \mathcal{T}\right) \cdot \mathcal{Q} \cdot (\mathcal{D} - \mathcal{D}_0), \quad (6.5)$$

which describes oscillatory modes about the shifted equilibrium of the form

$$\mathcal{D} - \mathcal{D}_0 = \mathcal{C}_k \exp [i\Omega_k t], \quad (6.6)$$

where \mathcal{C}_k is a $3N$ -dimensional vector of constants and Ω_k is an angular frequency. Substituting Eq. (6.6) into Eq. (6.5), we arrive at the eigenvalue equation

$$\Omega_k^2 \mathcal{C}_k = \mathcal{S} \cdot \mathcal{C}_k, \quad (6.7)$$

where we defined the $3N \times 3N$ matrix

$$\mathcal{S} \equiv \mathcal{M}^{-1} \cdot \mathcal{Q} \cdot \left(\mathcal{A}^{-1} - \mathcal{T}\right) \cdot \mathcal{Q}. \quad (6.8)$$

Because of the dimensions of \mathcal{S} , Eq. (6.7) has $3N$ solutions labeled by $k = 1, 2, \dots, 3N$, each corresponding to a mode frequency Ω_k . It is worthwhile to note that it can be shown that the eigenvalues of \mathcal{S} are also the eigenvalues of the matrix $\mathcal{S}_{sym} = \mathcal{M}^{-1/2} \cdot \mathcal{Q} \cdot \left(\mathcal{A}^{-1} - \mathcal{T}\right) \cdot \mathcal{Q} \cdot \mathcal{M}^{-1/2}$, albeit with different eigenvectors. This gives a computational advantage since \mathcal{S}_{sym} is symmetric, whereas \mathcal{S} may not be. As a further note, if we had chosen to use the $(\{\mathbf{p}_i\}, \{\mathbf{k}'_i\})$ coordinate system, we would have obtained $\mathcal{S}' = \mathcal{F} \cdot \left(\mathcal{A}^{-1} - \mathcal{T}\right)$, or $\mathcal{S}'_{sym} = \mathcal{F}^{1/2} \cdot \left(\mathcal{A}^{-1} - \mathcal{T}\right) \cdot \mathcal{F}^{1/2}$, where $\mathcal{F} = \text{diag} \left(\left\{ \frac{q_i^2}{m_i} \mathbf{I} \right\} \right)$. \mathcal{S}' and \mathcal{S}'_{sym} have the same eigenvalues as \mathcal{S} and \mathcal{S}_{sym} .

As mentioned, the CDM depends on the fractions q_i^2/m_i of the CDM-“atoms”. For physical atoms, these quantities could be obtained from ω_0 , but if our “atoms” represent multiple physical atoms, it is not *a priori* clear which reasonable value to choose for q_i^2/m_i . In Sec. 6.3 we show, using the example of pair interaction between particles in the simplified case where each chunk is identical, that the chunks’ characteristic frequency $\omega_d = q_d^2/m_d \alpha_d$ should in fact equal the characteristic frequency ω_0 of the material we wish to model.

From a quantum mechanical point of view, the sum of the normal mode frequencies is the ground-state potential energy U_0 of the Hamiltonian H_0 ,

$$U_0 = \frac{1}{2} \hbar \sum_{k=1}^{3N} \Omega_k, \quad (6.9)$$

where \hbar is the reduced Planck constant. This energy U_0 stems from the zero-point motion of the harmonic oscillators and contains the VdW interaction energy of the system.

Re-examining the trial solution of Eq. (6.6), we note that the equilibrium (“average”) electron-nucleus distance is not zero, but \mathcal{D}_0 . Physically, this means that each chunk’s (ground state) electron cloud is shifted by a distance given by its associated 3-dimensional vectors contained in \mathcal{D}_0 , such that average position of the electrons no longer coincides with their nucleus. This gives rise to an average chunk dipole moment $\mathcal{P} = \mathcal{Q} \cdot \mathcal{D}_0$ that satisfies, from Eq. (6.3),

$$(\mathcal{A}^{-1} - \mathcal{T}) \cdot \mathcal{P} = \mathcal{E}_0. \quad (6.10)$$

Thus, in terms of \mathcal{P} , the electrostatic energy U_E as defined in Eq. (6.4) is

$$U_E = -\frac{1}{2} \mathcal{P} \cdot \mathcal{E}_0, \quad (6.11)$$

which is consistent with the form of the energy of an induced dipole in an electric field; note that the factor $\frac{1}{2}$ arises from the fact that the dipole is induced, not permanent [51]. We can simplify Eq. (6.11) further by reverting to 3-dimensional vectors:

$$U_E = -\frac{1}{2} \mathbf{p}_{tot} \cdot \mathbf{E}_0,$$

where \mathbf{p}_{tot} is the total polarization of the N chunks:

$$\mathbf{p}_{tot} = \sum_{i=1}^N \mathbf{p}_i,$$

where \mathbf{p}_i is the polarization of chunk i . As a final step, we note that, as long as \mathbf{E}_0 is spatially homogeneous, it turns out that \mathbf{p}_{tot} can always be written in terms of a 3×3 matrix and the applied electric field:

$$\mathbf{p}_{tot} = \boldsymbol{\alpha} \cdot \mathbf{E}_0.$$

We call the matrix $\boldsymbol{\alpha}$ the polarizability matrix of the atom cluster. Mathematically, it is given by $\boldsymbol{\alpha} = \sum_{ij} \mathbf{B}_{ij}$, where \mathbf{B}_{ij} are 3×3 blocks of the matrix $(\mathcal{A}^{-1} - \mathcal{T})^{-1}$. However, since matrix inversion is computationally more expensive than finding the solution to a linear system such as Eq. (6.10), it is in practice more feasible to infer $\boldsymbol{\alpha}$ by calculating the three \mathbf{p}_{tot} ’s that result from applying the electric field in each of the three Cartesian directions. In terms of $\boldsymbol{\alpha}$, U_E can be written as

$$U_E = -\frac{1}{2} \mathbf{E}_0 \cdot \boldsymbol{\alpha} \cdot \mathbf{E}_0. \quad (6.12)$$

Closely related to the polarizability matrix is the enhancement factor matrix, which we define as

$$\mathbf{f} = \left(\sum_{i=1}^N \boldsymbol{\alpha}_i \right)^{-1} \boldsymbol{\alpha}.$$

The enhancement factor quantifies the influence of chunk-chunk interactions on the overall polarizability, since $\sum_{i=1}^N \boldsymbol{\alpha}_i$ is the polarizability one would expect if one were to ignore

these interactions. Note that if each chunk has the same isotropic polarizability $\alpha_i = \alpha_0 \mathbf{I}$, the enhancement factor reduces to $\alpha_i/N\alpha_0$, which is the familiar expression used in previous chapters and in Ref. [81].

The energies U_0 and U_E of Eqs. (6.9) and (6.12) are total potential energies and, thus, contain the interactions between all atoms, including each atom's self-energy, i.e., the energy that the atom would have if there were no other atoms in the system. In this work, we are mainly interested in interactions between colloidal particles, which we treat as clusters of atoms. To obtain the interaction energy between two clusters of atoms, we calculate, for a given separation and orientation of the clusters, the total potential energies U_0 and U_E and subsequently subtract the energy that the clusters would have if their separation were infinite. This is equivalent to subtracting each cluster's self-energy, i.e. the cluster's energy as if there were no other clusters. We can write the two-cluster interaction energy $V_0^{(2)}$ as [85]

$$V_0^{(2)} = U_0^{(2)} - U_{0,1}^{(1)} - U_{0,2}^{(1)};$$

$V_E^{(2)}$ has a similar expression. Here, $U_0^{(2)}$ is the total potential energy of this system of two clusters of atoms and $U_{0,1}^{(1)}$ and $U_{0,2}^{(1)}$ are the self-energy of cluster 1 and 2, respectively. In this work, we only consider pair interactions and intend to compare the results of various calculation techniques. For clarity, we therefore now modify the notation somewhat, so that the pair interaction between clusters of atoms with self-consistent dipole moments will from now on be referred to as $V_{0,X}^{(\text{CSCD})}$ (for VdW) and $V_{E,X}^{(\text{CSCD})}$ (for electric field-induced interaction), where we replace “X” by the cluster type that we are considering (i.e., “sphere”, “cube”, or “rod”). The pair interaction in the special case where the “clusters” of atoms in fact consist of only one atom each, is denoted by $V_0^{(\text{SSCD})}$ (for VdW) and $V_E^{(\text{SSCD})}$ (for electric field-induced interaction).

6.3 Identical Inducible Dipoles with Isotropic Polarizability

We now turn our attention to the specific case of two identical colloidal particles, each with polarizability α_p . For simplicity, we assume α_p to be isotropic; that is, $\alpha_p = \alpha_p \mathbf{I}$, where α_p is a scalar constant. We note that rods do not have an isotropic polarizability; we shall indicate how we deal with this complication in Sec. 6.4.4. The particles are separated by a distance r and an external electric field \mathbf{E}_0 is applied such that \mathbf{E}_0 makes an angle θ with the line connecting the particle centers. We will use our theoretical framework to derive expressions for calculating the interaction energy between these two particles by modeling each as a cluster of $N_{d/p}$ inducible dipoles, each with isotropic polarizability $\alpha_d = \alpha_d \mathbf{I}$, with α_d a scalar constant. We also discuss the special case where each cluster consists of only a single inducible dipole, and derive an analytical expression for the interaction energy in this case. The interaction energy has two parts, namely a VdW part, which is present even in the absence of an external electric field, and an electrostatic part, which is the result of the interaction between the induced dipole moments of the particles. We

will discuss application of the CDM to both interaction energies but, for the numerical results, we will focus only on the electrostatic interaction.

For both interaction energies, the polarizability of the dipoles composing the clusters has to be tuned such that the polarizability α_c (α_d) of the cluster of dipoles is close to the desired polarizability α_p . We do this by finding the root of the function $\alpha_c(\alpha_d) - \alpha_p$ using Ridder's bracketing algorithm [118]. In the special case that each cluster consists of only one dipole, we can simply set $\alpha_d = \alpha_p$.

6.3.1 Van der Waals Interaction

Apart from their polarizability α_d , two more quantities associated with the chunks composing the particles are relevant for VdW interaction, namely the oscillator's mass m_d and charge q_d associated with each chunk. In the aforementioned case where each dipole chunk has the same isotropic polarizability α_d , \mathcal{S} , as defined in Eq. (6.8), simplifies to

$$\mathcal{S} = \omega_d^2 [\mathcal{I} - \alpha_d \mathcal{T}], \quad (6.13)$$

where ω_d is given by

$$\omega_d^2 = \frac{q_d^2}{m_d \alpha_d},$$

in analogy with Eq. (6.1).

In the simple case that each particle is modeled as a single dipole, we have $\alpha_d = \alpha_p$, and since \mathcal{S} has dimensions of only 6×6 we can, without loss of generality, assume a coordinate system and analytically calculate \mathcal{T} and its eigenvalues. Summing their square roots, we arrive at a total (ground state) potential energy

$$U_0^{(\text{SSCD})} = \frac{1}{2} \hbar \omega_d \left[\sqrt{1 + 2\tilde{r}^{-3}} + 2\sqrt{1 + \tilde{r}^{-3}} + 2\sqrt{1 - \tilde{r}^{-3}} + \sqrt{1 - 2\tilde{r}^{-3}} \right],$$

where $\tilde{r} = r/\alpha_d^{1/3}$ is the dimensionless distance between the particles. We note that U_0 becomes complex-valued for $\tilde{r} < 2^{1/3}$, which is indicative of a polarization catastrophe occurring for those distances [64, 93]. The energy of the system for $\tilde{r} \rightarrow \infty$ is $3\hbar\omega_d$, which we subtract from U_0 to obtain the interaction energy between the particles:

$$V_0^{(\text{SSCD})} = U_0 - 3\hbar\omega_d.$$

Expanding $V_0^{(\text{SSCD})}$ to second order for small \tilde{r}^{-3} , and substituting back $\alpha_d = \alpha_p$, we arrive at the expression

$$V_0^{(\text{SSCD})} \simeq -\frac{3}{4} \hbar \omega_d \frac{\alpha_p^2}{r^6} \quad (\alpha_p r^{-3} \ll 1), \quad (6.14)$$

which is the Van der Waals interaction. For single atoms, $\omega_d = \omega_0$, where ω_0 is the characteristic atomic frequency associated with the atoms. Moreover, for large distances, Eq. (6.14) is expected to hold for clusters composed of multiple atoms as well, and the interaction energy should scale quadratically with the amount of matter (i.e., the number

of atoms) involved. This leads us to conclude that, for any number of composing atoms, ω_d in Eq. (6.14) should satisfy

$$\omega_d = \omega_0.$$

We can reason in the inverse direction as well. Suppose we start with the problem of modeling the Van der Waals interaction between two particles with polarizability α_p . This can be done by dividing up the particle in a number of dipoles $N_{d/p}$ and, as mentioned, carefully tuning their α_d such that the resulting clusters have exactly the polarizability α_p . If we perform the calculation with various dipole numbers $N_{d/p}$, we expect each approximation to yield the same result at large distances, that is, Eq. (6.14) is independent of $N_{d/p}$. Since we have made sure that α_p is the same for each calculation, it follows that ω_d should also be independent of $N_{d/p}$. In this thought experiment, we can moreover choose $N_{d/p}$ as large as we like, and can therefore make it equal to the number of physical atoms in the particles (in practice, this would be computationally infeasible for most realistic particle sizes given the available computer power). In that case, since each dipole now represents a single physical atom, we know that ω_d should equal the characteristic atomic frequency ω_0 so, since ω_d is independent of $N_{d/p}$, it should have this value for any $N_{d/p}$. Thus, the dipoles in our model should have the characteristic frequency of the atoms that they are meant to represent.

This is a convenient solution to the problem of setting a correct q_d^2/m_d for the dipoles: if we want to know ω_d (which, since α_d is known, is equivalent to knowing the fraction q_d^2/m_d), we can suffice with calculating $e/\sqrt{m_e\alpha_0}$, where α_0 is the material's atomic polarizability.

6.3.2 Induced-Dipole Interaction

The electrostatic interaction energy is conceptually more straightforward to calculate, because it does not involve the problematic quantities m_d and q_d . In fact, the interaction energy depends only on the inverse of the matrix $(\mathcal{A}^{-1} - \mathcal{T})$. This inverse can in principle be calculated analytically for any number of dipoles, but this calculation already becomes infeasible when the number of dipoles exceeds two. Therefore, if the number of dipoles per particle $N_{d/p} > 1$, we solve Eq. (6.10) numerically for \mathcal{P} and take its inner product with \mathcal{E}_0 [Eq. (6.11)] (this circumvents having to calculate $\boldsymbol{\alpha}$). On the other hand, if each particle is modeled as a single dipole ($N_{d/p} = 1$), we can simply plug $\alpha_d = \alpha_p$ into the expressions that follow.

For two inducible dipoles in the electric field \mathbf{E}_0 , the potential energy is

$$U_E^{(\text{SSCD})} = \alpha_d E_0^2 \frac{\tilde{r}^3 (-\tilde{r}^3 + 2 - 3 \cos^2 \theta)}{(\tilde{r}^3 - 2)(\tilde{r}^3 + 1)},$$

where $\tilde{r} = r/\alpha_d^{1/3}$ is the dimensionless distance between the dipoles. The energy at infinite separation is $-\alpha_d E_0^2$, which is reasonable physically, since both particles in this case are induced dipoles with dipole moment $\alpha_d E_0$ and, thus, they each have energy $-\frac{1}{2}\alpha_d E_0^2$. Subtracting the energy at infinite separation from U_E , we arrive at the interaction energy

$$V_E^{(\text{SSCD})}(\tilde{r}, \theta) = \alpha_d E_0^2 \frac{\tilde{r}^3 - 2 - 3\tilde{r}^3 \cos^2 \theta}{(\tilde{r}^3 - 2)(\tilde{r}^3 + 1)}. \quad (6.15)$$

This is the self-consistent interaction energy between a pair of inducible point dipoles in an external electric field where, by “self consistent”, we mean that the dipoles have a dipole moment equal to their polarizability α_d multiplied by the local electric field (the external electric field plus the electric field due to the other dipole). A simpler and more commonly used method for calculating the interaction energy of two inducible dipoles in an electric field is to impose upon each dipole a “permanent dipole” moment $\alpha_d \mathbf{E}_0$ and use this setup to calculate the well-known dipole-dipole interaction energy [51], resulting in

$$V_E^{(\text{SPD})}(\tilde{r}, \theta) = \alpha_d E_0^2 \frac{1 - 3 \cos^2 \theta}{\tilde{r}^3}. \quad (6.16)$$

As it turns out, $V_E^{(\text{SPD})}(\tilde{r}, \theta)$ is exactly the first-order approximation of $V_E^{(\text{SSCD})}(\tilde{r}, \theta)$ for small \tilde{r}^{-3} : Taylor expanding Eq. (6.15) yields

$$\frac{V_E^{(\text{SSCD})}(\tilde{r}, \theta)}{E_0^2 \alpha_d} \simeq \frac{V_E^{(\text{SPD})}(\tilde{r}, \theta)}{E_0^2 \alpha_d} - \frac{1 + 3 \cos^2 \theta}{\tilde{r}^6} + \mathcal{O}\left([\tilde{r}^{-3}]^3\right).$$

We note that the first correction term is always negative, indicating that $V_E^{(\text{SSCD})}(\tilde{r}, \theta)$ has a larger attractive region than $V_E^{(\text{SPD})}(\tilde{r}, \theta)$. Indeed, the angle $\theta_0^{(\text{SSCD})}$ at which $V_E^{(\text{SSCD})}(\tilde{r}, \theta_0^{(\text{SSCD})}) = 0$ is given by

$$\theta_0^{(\text{SSCD})}(\tilde{r}) = \arccos \sqrt{\frac{\tilde{r}^3 - 2}{3\tilde{r}^3}},$$

whereas this angle for $V_E^{(\text{SPD})}(\tilde{r}, \theta)$ is the limit $\theta_0^{(\text{SSCD})}(\tilde{r} \rightarrow \infty)$, which is the well-known “magic” angle $\theta_0^{(\text{SPD})} = \arccos \sqrt{1/3} \approx 54.7^\circ$. We note that $\theta_0^{(\text{SSCD})}(\tilde{r})$ increases as \tilde{r} decreases, with as limiting value $\theta_0^{(\text{SSCD})}(\tilde{r} \downarrow 2^{1/3}) = \pi/2$, indicating an attractive interaction for all angles except $\pi/2$. This limiting case coincides with the occurrence of the aforementioned polarization catastrophe: $V_E^{(\text{SSCD})}(\tilde{r} \downarrow 2^{1/3}, \theta)$ diverges for all θ except $\theta = \theta_0^{(\text{SSCD})}$ (in which case the limiting value is $\alpha_d E_0^2/3$). We deem the values produced by $V_E^{(\text{SSCD})}$ for $\tilde{r} < 2^{1/3}$ unphysical. A further difference between $V_E^{(\text{SSCD})}(\tilde{r}, \theta)$ and $V_E^{(\text{SPD})}(\tilde{r}, \theta)$ is the relative strength of the attraction and repulsion for $\theta = 0$ and $\theta = \pi/2$. The ratio between these two is a constant in the SPD approach, $V_E^{(\text{SPD})}(\tilde{r}, 0)/V_E^{(\text{SPD})}(\tilde{r}, \pi/2) = -2$, but in the self-consistent (SSCD) case it is given by

$$\frac{V_E^{(\text{SSCD})}(\tilde{r}, 0)}{V_E^{(\text{SSCD})}(\tilde{r}, \pi/2)} = -2 \frac{\tilde{r}^3 + 1}{\tilde{r}^3 - 2}. \quad (6.17)$$

For large distances, Eq. (6.17) goes to the constant -2 , while for $\tilde{r} \downarrow 2^{1/3}$ it goes to $-\infty$, which reflects the fact that $V_E^{(\text{SSCD})}(\tilde{r} \downarrow 2^{1/3}, 0)$ diverges but $V_E^{(\text{SSCD})}(\tilde{r} \downarrow 2^{1/3}, \pi/2)$ does not.

Fig. 6.1 is a contour plot of $V_E^{(\text{SSCD})}(\tilde{r}, \theta)$ as a function of the location of the second dipole, with the first being kept at the origin. Also plotted in the same figure are the contours of $V_E^{(\text{SPD})}(\tilde{r}, \theta)$, as well as the line denoting the 54.7° magic angle. In this case, trivially, the $V_E^{(\text{SPD})}(\tilde{r}, \theta) = 0$ contour coincides with this line. We see that for small

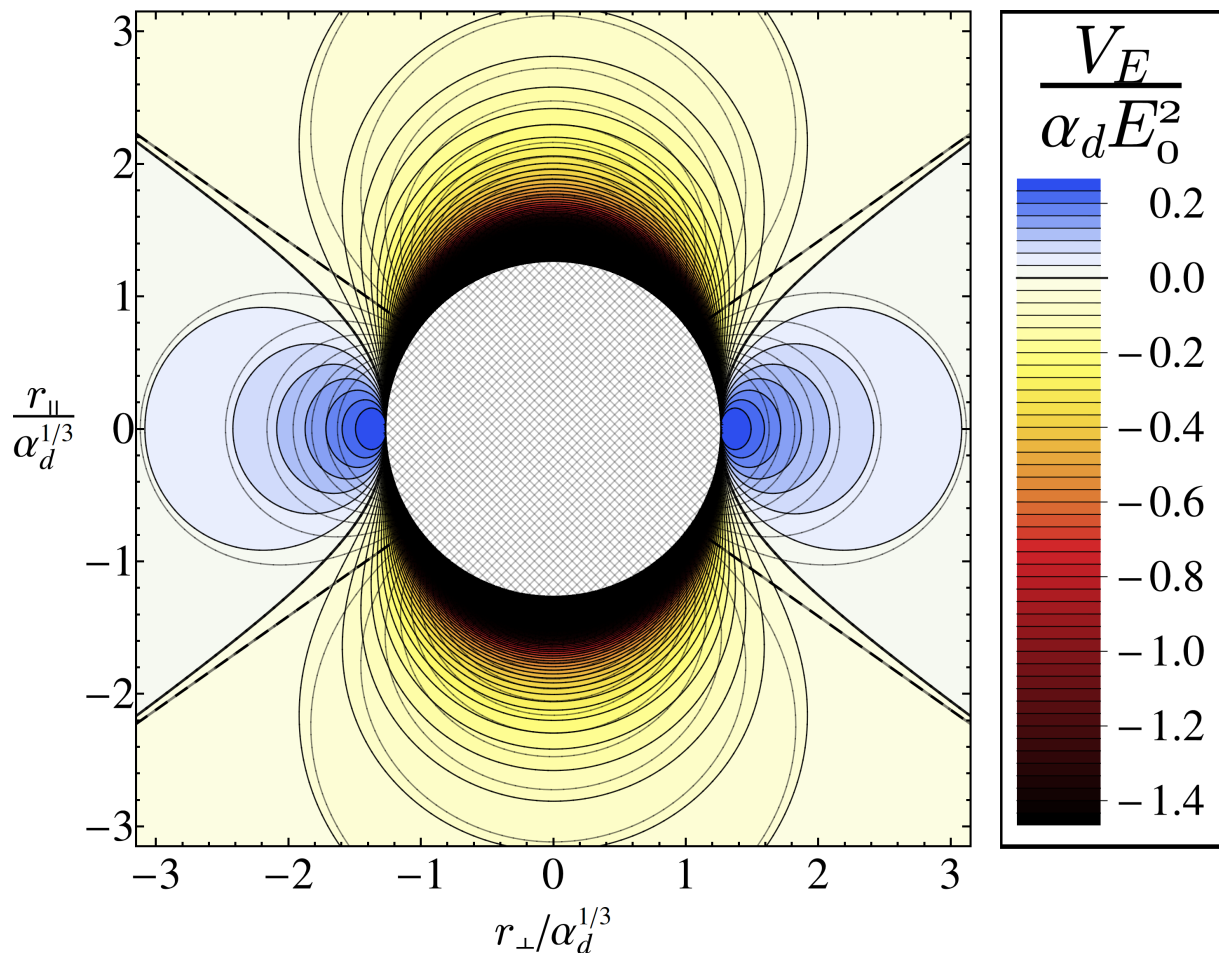


Figure 6.1: Contour plot of the interaction energy $V_E^{(\text{SSCD})}/\alpha_d E_0^2$, as given in Eq. (6.15), of a pair of inducible point dipoles with polarizability α_d subject to an external electric field \mathbf{E}_0 that points along r_\parallel (the vertical axis of the plot), as a function of the location (r_\perp, r_\parallel) of the second inducible dipole. The dipole moments are calculated self-consistently, taking into account the influence that the inducible point dipoles have on each other's dipole moments. The contour lines of the function $V_E^{(\text{SPD})}/\alpha_d E_0^2$ of Eq. (6.16), which is the result of the single permanent dipole (SPD) approach where each dipole has a fixed dipole moment equal to $\alpha_d \mathbf{E}_0$, are shown as see-through lines. The hatched area is excluded from the plot: at distances $r/\alpha_d^{1/3} \leq 2^{1/3} \approx 1.26$, a polarization catastrophe occurs and $V_E^{(\text{SSCD})}(\tilde{r}, \theta)/\alpha_d E_0^2$ is no longer valid.

separation, the $V_E^{(\text{SPD})}(\tilde{r}, \theta)$ contours are very different in shape and location than their $V_E^{(\text{SSCD})}(\tilde{r}, \theta)$ counterparts. For large separation, the contours start to coincide more, as expected, since the first-order approximation dominates the Taylor series for large distances.

It is also possible to analytically calculate the interaction energy of particles with anisotropic polarizability. The simplest example of such particles are particles with a diagonal polarizability matrix with only two independent entries, α_{xx} and α_{zz} . All particles with at least a 4-fold rotational symmetry axis have a polarizability of this form; examples include rods, dumbbells, platelets, and bowls. In the following, we assume that the electric field is pointing in the z -direction and that both particles are perfectly aligned with it. Thus, the Cartesian coordinate system is defined by the electric field direction and not the symmetry axis of the particles. In fact, rods and dumbbells align their rotational symmetry axis along the electric field (i.e., in the z -direction), whereas bowls and platelets align their rotational symmetry axis perpendicular to the electric field (i.e., in the x - y plane) [83], meaning that for rods and dumbbells, $\alpha_{yy} = \alpha_{xx}$, but for bowls and platelets, $\alpha_{yy} = \alpha_{zz}$. However, as the value of α_{yy} turns out to be irrelevant for the mathematical expression of the interaction energy, the result is valid in both cases. Keeping the first particle at the origin and parametrizing the position of the second by the distance r and the polar angle θ (the angle between the electric field and the line connecting the particles), the interaction energy is

$$V_{E, \text{anisotropic}}^{(\text{SSCD})}(\tilde{r}, \theta, \eta_\alpha) = E_0^2 \alpha_{zz} \frac{(\tilde{r}^3 - 2\eta_\alpha - 3\tilde{r}^3 \cos^2 \theta)}{(\tilde{r}^3 + 1)(\tilde{r}^3 - 2\eta_\alpha) - 3(1 - \eta_\alpha)\tilde{r}^3 \cos^2 \theta}, \quad (6.18)$$

where $\tilde{r} = r/\alpha_{zz}^{1/3}$ and $\eta_\alpha = \alpha_{xx}/\alpha_{zz}$, which always satisfies $\eta_\alpha < 1$. This function is plotted for $\eta_\alpha = 0.44$ in Fig. 6.2, along with the contours of its first-order approximation, which equals $V_E^{(\text{SPD})}(\tilde{r}, \theta)$ with $\alpha_d = \alpha_{zz}$.^a The plot looks similar to the one that was shown in Fig. 6.1, albeit squished together along the horizontal (r_\perp -)axis.

6.4 Interaction between Cluster Pairs

6.4.1 Methods

We now proceed to numerically calculate the induced-dipole interaction energy between pairs of clusters of atoms, which we model to represent micron-sized particles. Before presenting the numerical results, we discuss the applied methods in practical terms, which are the same for each cluster shape we consider. First, we set a desired particle size and use it, together with the number of dipoles $N_{d/p}$ to be used to model a particle and the lattice type, to infer the lattice spacing a of the dipoles. Having thus fixed the positions of the dipoles, we proceed to tune the dipoles' polarizability α_d such that the polarizability α_c of the cluster of dipoles is close to the desired polarizability α_p of the particle we wish to model.

^aThe choice of $\eta_\alpha = 0.44$ was made because it coincides with the observed η_α of the particular rod-shaped particles that we consider in Sec. 6.4.4.

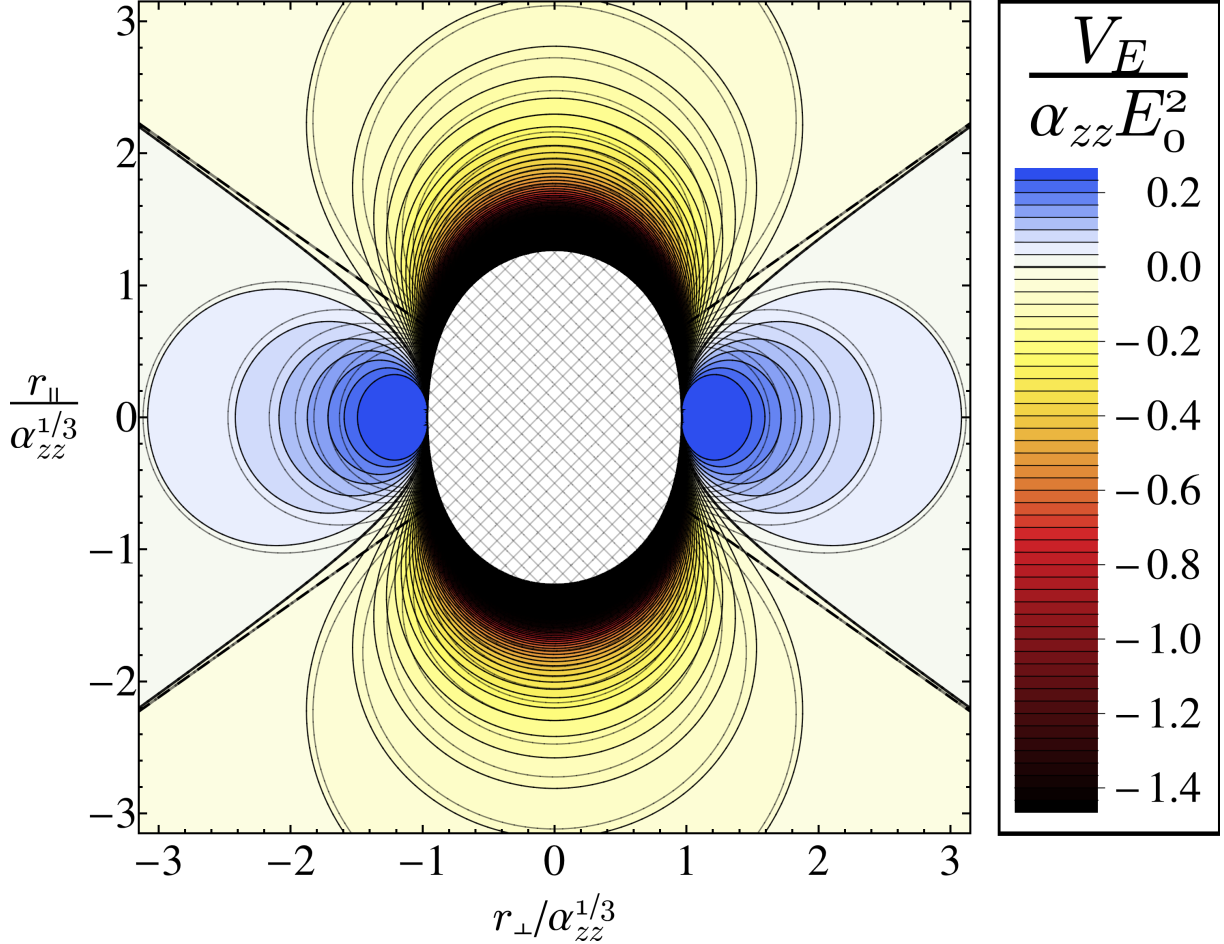


Figure 6.2: Contour plot of the interaction energy $V_E^{(\text{SSCD})}/\alpha_{zz}E_0^2$, as given in Eq. (6.18), of a pair of inducible point dipoles, each with anisotropic polarizability $\boldsymbol{\alpha}_d = \text{diag}(\alpha_{xx}, \alpha_{yy}, \alpha_{zz})$ satisfying $\alpha_{xx}/\alpha_{zz} = 0.44$, subject to an external electric field \mathbf{E}_0 pointing in the z -direction, as a function of the location of the second inducible dipole relative to the first in the x - z plane. Note that restricting ourselves to this plane makes the value of α_{yy} irrelevant for the value of $V_E^{(\text{SSCD})}$. The dipole moments are calculated self-consistently, taking into account the influence that the inducible point dipoles have on each other's dipole moments. The contour lines (see-through) of the function $V_E^{(\text{SPD})}/\alpha_d E_0^2$ of Eq. (6.16), which is the result of the single permanent dipole (SPD) approach where each dipole has a fixed dipole moment equal to $\alpha_{zz}\mathbf{E}_0$, are shown as well. The hatched area, within which a polarization catastrophe occurs and $V_E^{(\text{SSCD})}$ is no longer valid, is excluded from the plot.

In choosing the polarizability α_p , it is important to beware of the polarization catastrophe. As α_d increases, the dimensionless lattice spacing $\tilde{a} = a/\alpha_d^{1/3}$ decreases, and α_c increases until, for a certain \tilde{a} , the polarization catastrophe occurs, with α_c diverging into a $(\tilde{a} - \tilde{a}_{\text{cat.}})^{-1}$ -like peak, where $\tilde{a}_{\text{cat.}}$ is the dimensionless lattice spacing at which the polarization catastrophe occurs. For $\tilde{a} < \tilde{a}_{\text{cat.}}$, the function α_c is characterized by many of these divergences, with ranges between the divergences where α_c seems well-behaved but where the values for computed physical quantities like $V_E^{(2)}$ cannot be trusted. Another point of interest is that the exact value of $\tilde{a}_{\text{cat.}}$ is dependent on the number of dipoles in the system and their arrangement with respect to each other. Therefore, even though the first divergence in theory makes it possible to create a cluster of dipoles with an arbitrarily high cluster polarizability (by choosing an α_d such that \tilde{a} is only just above $\tilde{a}_{\text{cat.}}$), when two of these clusters are allowed to interact, the location of the catastrophe may shift to higher \tilde{a} such that the system's dimensionless lattice spacing becomes $\tilde{a} < \tilde{a}_{\text{cat.}}$. This could easily remain unnoticed, since α_c is well-behaved between its divergences, but the numerical results are not reliable in this case. Therefore, it is prudent to choose α_c such that the resulting α_d is low enough and, thus, \tilde{a} is high enough to be comfortably above $\tilde{a}_{\text{cat.}}$.

Having thus determined the properties of the dipoles and the lattice, we place a copy (or, in the case of the misaligned clusters of subsection 6.4.5, a rotated copy) of the cluster at a certain relative position of the cluster and numerically compute the total electrostatic potential energy $U_E^{(2)}$ and each cluster's self energy $U_{E,1}^{(1)}$ and $U_{E,2}^{(1)}$ (these are equal in the case of identical clusters that are not rotated with respect to each other), and subtract this from $U_E^{(2)}$ to gain the interaction energy $V_E^{(\text{CSCD})}$ at that relative position. We then modify the relative position to calculate a new $V_E^{(\text{CSCD})}$, and repeat this process until the desired sample points have been run through. To generate a contour plot, we additionally have to interpolate in order to gain approximate values for locations between sample points. This occasionally creates slight artifacts in the plots and so, generally, features in the plots smaller than the distance between the sample points should be ignored. The interpolation method is always a 2nd-order spline, chosen because it smooths out the function the best (judged by eye).

We can contrast the CDM's self-consistent manner (i.e., the CSCD approach) of calculating the induced-dipole interaction energy with the more usually applied method, in which each dipole is assigned a permanent dipole $\mathbf{p}_d = \alpha_p \mathbf{E}_0 / N_{d/p}$, and the total interaction energy can be calculated by summing over pairs of dipoles that are not in the same cluster:

$$V_E^{(\text{CPD})} = \frac{\alpha_p^2 E_0^2}{N_{d/p}^2} \sum_{(ij)} \frac{1 - 3 \cos^2 \theta_{ij}}{r_{ij}^3},$$

where r_{ij} is the length of the vector $(\mathbf{r}_i - \mathbf{r}_j)$, θ_{ij} is the angle between $\tilde{\mathbf{r}}_{ij}$ and \mathbf{E}_0 , and the sum, as mentioned, is assumed to run over the appropriate pairs (there are $N_{d/p}^2/2$ of these pairs).

In the next subsections, we will be comparing numerical results of various methods of calculation. Apart from qualitative comparisons, we also wish to compare the methods in a quantitative way. Suppose we wish to compare a numerically computed function

$g(r_{\perp}, r_{\parallel})$ to another function $h(r_{\perp}, r_{\parallel})$. We can then define a relative deviation

$$\sigma[g, h] = \sqrt{\frac{\int_S d\mathbf{r} [g(r_{\perp}, r_{\parallel}) - h(r_{\perp}, r_{\parallel})]^2}{\int_S d\mathbf{r} [h(r_{\perp}, r_{\parallel})]^2}}, \quad (6.19)$$

where S is some integration area and $d\mathbf{r} = dr_{\perp} dr_{\parallel}$ is an infinitesimal area element, as a measure of how “wrong” g is, compared to h . If g is very close to h for all locations in S , $\sigma[g, h]$ will be much smaller than unity, whereas $\sigma[g, h]$ will be of the order of, or greater than, unity if g is off by amounts that are of the same order as h itself. Of course, $\sigma[g, h]$ has some limitations, such as the fact that, even if g is wrong in only a small area, it may still receive a high $\sigma[g, h]$ if its discrepancy in this area is large enough. $\sigma[g, h]$ also does not work well if h has divergences that g does not. For example, if S is taken to be an infinite plane of which a disk of radius R around the origin is excluded, $\sigma[V_E^{(\text{SPD})}, V_E^{(\text{SSCD})}]$ goes to unity as $R/\alpha_d^{1/3} \downarrow 2^{1/3}$. We can therefore not use σ to compare $V_E^{(\text{SSCD})}$ and $V_E^{(\text{SPD})}$, because the obtained value would depend strongly on R . However, most of the results that follow do not contain such divergences, such that σ is a useful comparison tool.

As a last remark before moving on to the numerical results, we note that even though, from the theory, $\alpha_p E_0^2$ is a naturally occurring unit of measure for V_E , we have chosen to measure the interaction energy in the familiar units of $k_B T$ at room temperature ($T = 293$ K) instead, and have chosen specific experimental parameters, including an electric field strength of $E_0 = 300$ V mm $^{-1}$, in order to gain numerical values for the energy. Since V_E is exactly quadratic in E_0 , the obtained numbers can be straightforwardly adapted to other electric field strengths. Moreover, we note that V_E is an extensive quantity, that is, if we multiply all distances by a value $\lambda^{1/3}$ and, simultaneously, the polarizability of the particles α_p by λ , the resulting interaction potential is scaled by the same factor. To see this, we note that the polarizability of the system is $\alpha = N\alpha_d \mathbf{f}(\{\mathbf{r}_i/\alpha_d^{1/3}\})$, where \mathbf{f} is the enhancement factor of the system, only dependent on the dimensionless coordinates $\{\mathbf{r}_i/\alpha_d^{1/3}\}$ of the inducible point dipoles. Multiplying the dipole chunk polarizability α_d by λ and the coordinates \mathbf{r}_i by $\lambda^{1/3}$, we note that the dimensionless coordinates, and hence the enhancement factor of the system, remain invariant. Less trivially, we note that the enhancement of each individual particle (cluster of dipole chunks) also remains the same, such that we must have $\alpha_p \propto \alpha_d$ (for constant $\{\mathbf{r}_i/\alpha_d^{1/3}\}$). We note that our scaling scheme has kept the polarizability per unit volume of the particles constant. A less trivial dependence appears when we scale α_p or the dimensions of the particle individually. In general, we can say that, the lower the particles’ polarizability per unit volume, the closer the CSCD interaction energy gets to the CPD interaction energy, which scales quadratically in α_p .

6.4.2 Numerical Results for Spheres

For spheres of diameter l , we put the dipoles on an fcc lattice and remove any dipoles that are more than a distance $l/2$ away from the origin. If $N_{d/p}$ is large enough, this will produce

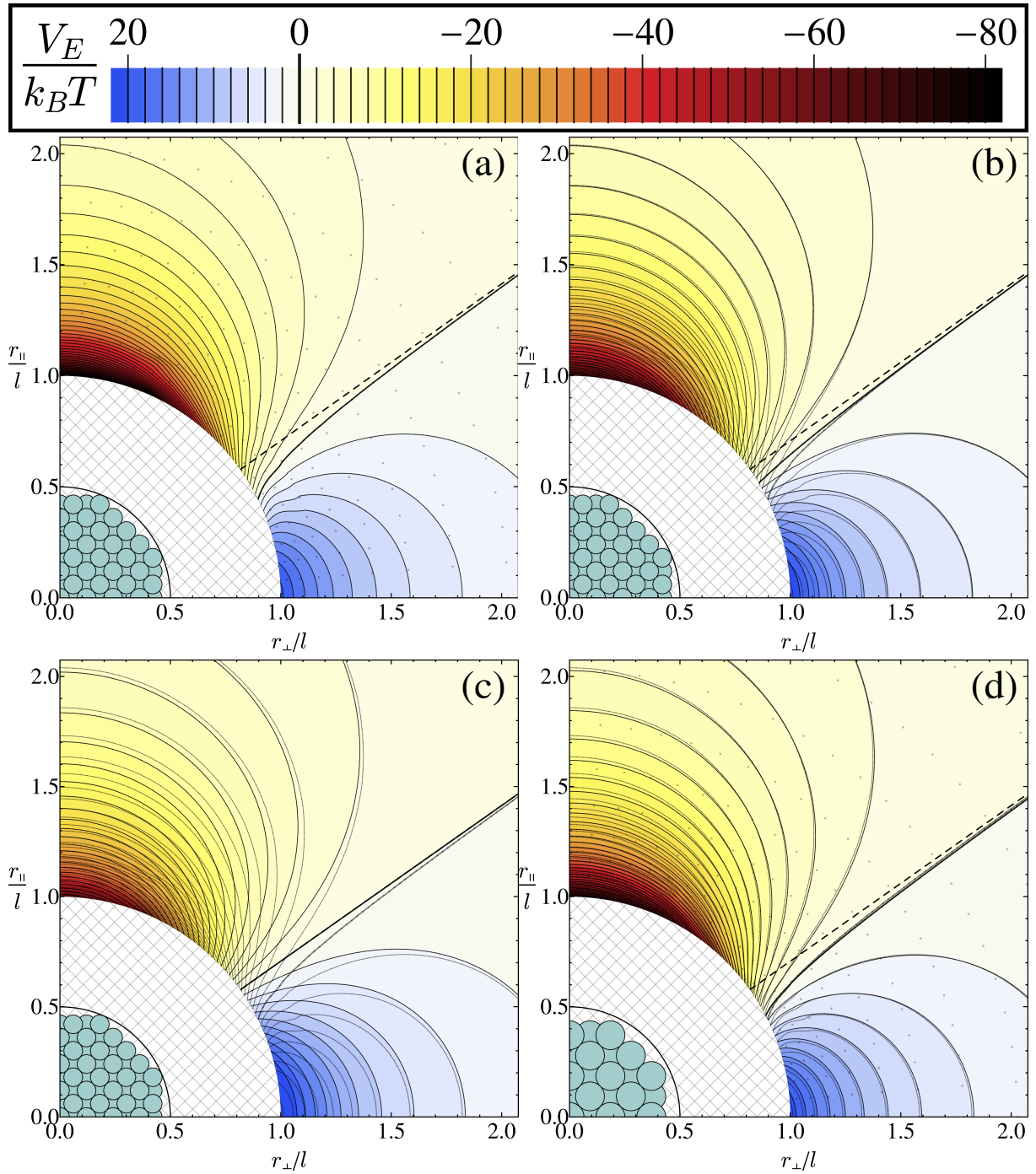


Figure 6.3: The interaction energy $V_E/k_B T$, at $T = 293$ K, of spherical particles with diameter $l = 1 \mu\text{m}$ and polarizability $\alpha_p = 0.1 \mu\text{m}^3$, in an external electric field $E_0 = 300 \text{ V mm}^{-1}$ along the r_{\parallel} -axis, as a function of the location of the second particle with respect to the first, calculated using (a) CSCD with 959 dipole chunks per sphere, (b) SSCD, (c) SPD, and (d) CSCD with 225 dipole chunks per sphere (each approach is discussed in the text). Each plot uses the same contour lines and color coding provided in the legend. The dashed lines represent the 54.7° “magic angle”. The contour lines of (a) are reproduced as see-through lines in panels (b-d). A cross-section of the 959-chunk sphere is displayed in the center of panels (a-c), and that of a 225-chunk sphere in panel (d). The hatched area, within which the spheres overlap, is excluded from the plots. The dots in panels (a) and (d) represent the sample points at which the interaction energy was explicitly calculated.

	σ	$\frac{V_{E,min}}{k_B T}$	$\frac{V_{E,max}}{k_B T}$
CSCD	0	-81.2	20.5
SSCD	0.15	-61.8	22.5
SPD	0.28	-49.4	24.7
CSCD(225)	0.086	-67.12	21.3

Table 6.1: Numerical quantities associated with the various calculation techniques for the interaction energy between two spheres, as plotted in Fig. 6.3. $V_{E,min}$ and $V_{E,max}$ refer, respectively, to the minimum and maximum value achieved by the calculation technique mentioned in the leftmost column. σ is the relative deviation, as defined in Eq.(6.19), where h is always $V_{E,sphere}^{(CSCD)}$ and g is the V_E associated with the technique given in the leftmost column. The last entry, ‘‘CSCD(225)’’, refers to the CSCD approach with spheres composed of 225 dipole chunks each, instead of 959.

an approximately spherical cluster shape, while if it is smaller, the resulting cluster will be more faceted. In Fig. 6.3(a), we plot the interaction energy $V_{E,sphere}^{(CSCD)}$ between a pair of spheres as a function of the position of the second sphere, with the first being kept at the origin. The spheres have a diameter $l = 1 \mu\text{m}$ and a polarizability $\alpha_p = 0.1 \mu\text{m}^3$. The number of dipoles in each sphere is $N_{d/p} = 959$ (i.e., there are 1918 dipoles in the system), the electric field is $E_0 = 300 \text{ V mm}^{-1}$, and the energy is scaled with the thermal energy at room temperature ($T = 293 \text{ K}$). In Table 6.1, we give the maximum and minimum of the interaction energy for the various approaches, and also give the relative deviation σ of each approach compared to the CSCD approach. As integration area for σ , we use a disk of radius $2.075l$ (which is also the plotted range), with an excluded region that is a disk of radius l around the origin.

In Fig. 6.3(b), we plot the single self-consistent dipole potential $V_E^{(SSCD)}$, while the contour lines of $V_{E,sphere}^{(CSCD)}$ are shown in the same plot. We note that the single-dipole approximation $V_E^{(SSCD)}$ is remarkably accurate, especially at angles perpendicular to the electric field. The accuracy also increases with the distance between the spheres, a distance of $2l$ already exhibiting an excellent agreement for all angles. The approximation is worst near the zero-contour, i.e. the boundary between the attractive and repulsive regions of the plot. While both calculation methods predict a θ_0 greater than the magic angle of 54.7° (also denoted in the plot), the $V_E^{(SSCD)}$ result seems to consistently underestimate θ_0 , its zero-contour at contact being about halfway between the zero-contour of $V_{E,sphere}^{(CSCD)}$ and the 54.7° -line. From Table 6.1, we see that the SSCD approach gives a good approximation for the maximum repulsion but underestimates the maximum attraction strength.

In Fig 6.3(c), we judge the accuracy of $V_E^{(SPD)}$ by plotting it together with the contour lines of $V_{E,sphere}^{(CSCD)}$. We note that the contour lines of $V_E^{(SPD)}$ coincide less well with those of $V_{E,sphere}^{(CSCD)}$ than do the contour lines of $V_E^{(SSCD)}$ in every region of the plot. From Table 6.1, we see that the SPD approach underestimates attractions even more than the SSCD does, while also overestimating repulsions. Its σ -value is almost a factor 2 higher than that of the SSCD approach.

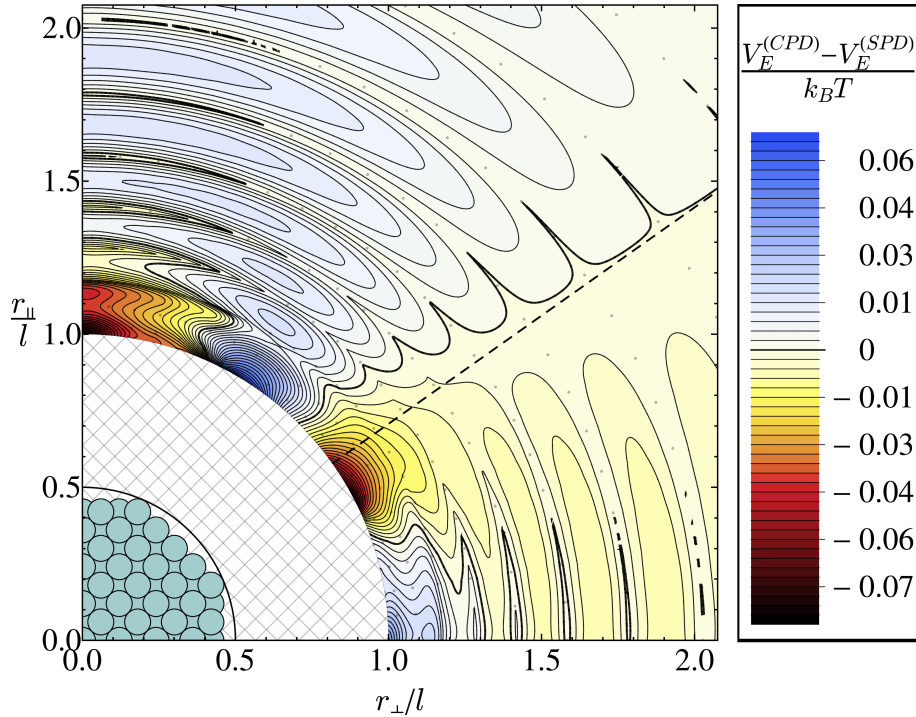


Figure 6.4: A comparison of the SPD and CPD approaches for calculating the sphere interaction energy of Fig. 6.3. Plotted is the difference between the CPD and the SPD result, in units of $k_B T$.

Next, we compare our calculations using $N_{d/p} = 959$ spheres with those using $N_{d/p} = 225$ spheres. In Fig. 6.3(d), we plot $V_{E,\text{sphere}}^{(\text{CSCD})}$ for $N_{d/p} = 225$, while showing the contours of $V_{E,\text{sphere}}^{(\text{CSCD})}$ with $N_{d/p} = 959$ in the same figure. We see that the agreement is in general very good for large distances and depends on θ . The agreement is bad for $\theta = 0$ at close distances but improves as θ increases, with the best agreement at roughly $\theta \approx \pi/4$ for close distances and $\theta \approx \pi/6$ for large distances. For values of θ beyond the zero-contour, the agreement gradually deteriorates again but remains much better than the $\theta = 0$ case at close distance. This approach yields a σ -value that is about half of that of the SSCD approach, but still underestimates attractions.

When we compare $V_{E,\text{sphere}}^{(\text{CPD})}$ to the single permanent dipole approximation $V_E^{(\text{SPD})}$, it turns out that, perhaps surprisingly, the contours coincide so well that it makes more sense to show the comparison by a difference plot ($V_{E,\text{sphere}}^{(\text{CPD})} - V_E^{(\text{SPD})}$), which is done in Fig. 6.4. For the experimental values chosen, the difference between $V_{E,\text{sphere}}^{(\text{CPD})}$ and $V_E^{(\text{SPD})}$ is much smaller than $k_B T$ for all values of r and θ , and $\sigma[V_E^{(\text{SPD})}, V_{E,\text{sphere}}^{(\text{CPD})}] \approx 0.00095$. This implies that modeling a sphere by a number of dipoles and using the permanent dipole approximation to calculate the interaction energy is equivalent to simply modeling it as one dipole, i.e., using $V_E^{(\text{SPD})}$. We note, though, that both approximations are more or less wrong, depending on r and θ , and that $V_E^{(\text{SSCD})}$ is a better approximation than both, while it is only slightly more complicated to compute than $V_E^{(\text{SPD})}$.

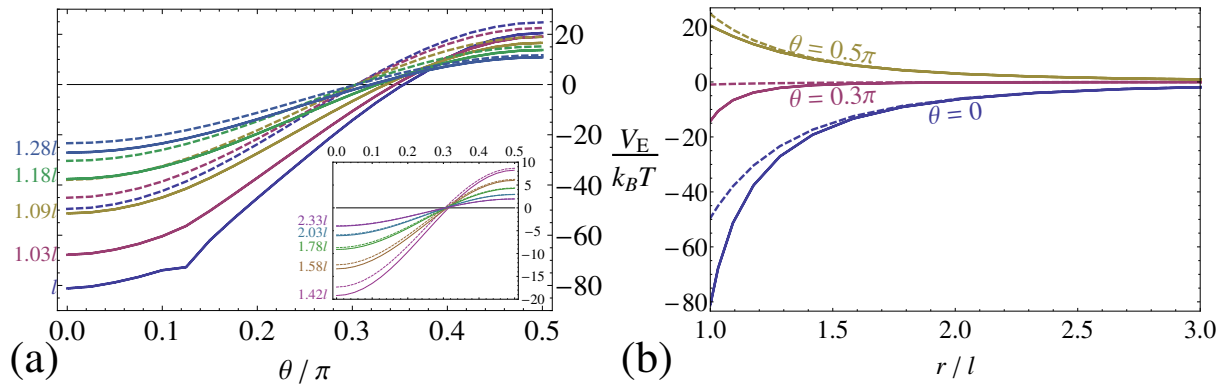


Figure 6.5: The sphere interaction energy $V_{E,\text{sphere}}^{(\text{CSCD})}$ (solid lines) and $V_{E,\text{sphere}}^{(\text{CPD})}$ (dashed lines) of the setup described in Fig. 6.3, (a) as a function of the angle θ between the electric field and the line connecting the sphere centers, for various center-to-center distances (indicated to the left, as multiples of the sphere diameter $l = 1 \mu\text{m}$), and (b) as a function of the center-to-center distance r , for various angles θ , indicated in the plot.

To gain more quantitative data, we also plot $V_{E,\text{sphere}}^{(\text{CSCD})}$ and $V_{E,\text{sphere}}^{(\text{CPD})}$ as a function of θ for various r in Fig. 6.5(a), and as a function of r for various θ in Fig. 6.5(b). We again note the bad agreement for small distances; e.g., from Fig. 6.5(a) we see that, at contact and at $\theta = 0$, $V_{E,\text{sphere}}^{(\text{CPD})}$ underestimates the interaction energy by about a factor 1.6, corresponding to about $30k_B T$ for the experimental values used. $V_{E,\text{sphere}}^{(\text{CPD})}$ also underestimates the angle at which the crossover from attraction to repulsion occurs, as noted before. The agreement becomes better as the distance increases, as evident by the curves coinciding more and the crossover being more localized to 54.7° in the inset graph. In Fig. 6.5(b), the interaction energy is plotted as a function of r for $\theta = 0, 0.3\pi$ (an angle close to the magic angle) and 0.5π . As expected, $V_{E,\text{sphere}}^{(\text{CPD})}$ at $\theta = 0.3\pi$ is almost exactly zero for all distances, whereas its $V_{E,\text{sphere}}^{(\text{CSCD})}$ counterpart displays a significant attraction for close distances, up to roughly $14k_B T$.

In conclusion, for spheres, it seems unnecessary to use the SPD (or CPD) approach, since the SSCD approach gives a better result and is not (significantly) more expensive computationally. The CSCD approach with 225 chunks per sphere gives a better approximation than the SSCD approach but is also more computationally expensive and still underestimates attractions at close distances, making it impractical for most applications. For spheres, the SSCD approach is therefore usually to be preferred over the other approaches.

6.4.3 Numerical Results for Cubes

We now turn our attention to cubic-shaped particles with a rib length of $l = 1 \mu\text{m}$, which we model by a simple cubic lattice of $N_{d/p} = n_l \times n_l \times n_l$ dipoles. The lattice spacing a is given by $a = 1 \mu\text{m}/n_l$. We fix the particle polarizability at $\alpha_p = 0.2 \mu\text{m}^3$, about twice that of the sphere, a value chosen because the cubes have about twice as much volume as the spheres. In Table 6.2, we give some relevant quantities associated with each calculation

technique plotted in Figs. 6.6 and 6.7. In the case of cubes, the integration area used in the calculation of σ is given by $|r_\perp|, |r_\parallel| < 2.6l$.

In Fig. 6.6(a), we plot $V_{E,\text{cube}}^{(\text{CSCD})}$. We first note that the interaction strength is higher than that of the spheres, presumably due to the fact that the cubes have a higher polarizability but also due to their shape, which allows the cubes to bring many of their surface dipoles very close together.

In Fig. 6.6(b) we plot $V_E^{(\text{SSCD})}$ with the appropriate α_p while also showing the contours of $V_{E,\text{cube}}^{(\text{CSCD})}$. We see differently shaped contour lines and different levels of agreement between the two functions for the attractive and repulsive regions of the plot. In the attractive region, the contour lines of $V_{E,\text{cube}}^{(\text{CSCD})}$ are flattened and seem to “wrap” around the corner of the cube and $V_E^{(\text{SSCD})}$, which does not account for any anisotropy and thus does not display these features, does not agree well with $V_{E,\text{cube}}^{(\text{CSCD})}$, especially for small distances. As can be seen from Table 6.2, the SSCD overestimates the attraction at close distances. In the repulsive region of the plot, however, the contour lines of $V_{E,\text{cube}}^{(\text{CSCD})}$ are much more rounded and coincide better with $V_E^{(\text{SSCD})}$, although the latter underestimates the repulsion at larger distances and overestimates it at smaller distances, as can also be seen from Table 6.2.

The $V_E^{(\text{SPD})}$ approximation is evaluated by plotting it together with the contour lines of $V_{E,\text{cube}}^{(\text{CSCD})}$, in Fig. 6.6(c). The question of whether $V_E^{(\text{SSCD})}$ or $V_E^{(\text{SPD})}$ is a better approximation has a mixed answer. The contour lines of $V_E^{(\text{SSCD})}$ follow the shape of the contours of $V_{E,\text{cube}}^{(\text{CSCD})}$ better around the boundary between the attractive and repulsive region, but $V_E^{(\text{SPD})}$ better approximates the attractions at small and large distances and repulsions at larger distances, while $V_E^{(\text{SSCD})}$ does better for the repulsions at close distance (see also Table 6.2). SPD’s value for σ is of the same order of magnitude, but slightly smaller than that of SSCD.

Interestingly, splitting up the cube into $10 \times 10 \times 10$ permanent dipoles does not improve the approximation. In Fig. 6.6(d) we plot $V_{E,\text{cube}}^{(\text{CPD})}$ with the contour lines of $V_{E,\text{cube}}^{(\text{CSCD})}$. Some notable discrepancies are the fact that the zero-contour is bent in the wrong direction with respect to the 54.7° line. Furthermore, the contour lines in the repulsive region do not bend “inward” enough, whereas the ones in the attractive region bend inward too much. Away from the corners (near $\theta = 0$ and $\pi/2$), $V_{E,\text{cube}}^{(\text{CPD})}$ makes up for these faults somewhat by being a better approximation for the maximum attraction strength than $V_{E,\text{cube}}^{(\text{SSCD})}$ and a better approximation for the maximum repulsion than $V_{E,\text{cube}}^{(\text{SPD})}$. Still, with its σ in the same ballpark as those of the latter two but with a significantly higher computational cost, the CPD should not be the preferred approach for cubes. The difference between $V_{E,\text{cube}}^{(\text{CPD})}$ and $V_E^{(\text{SPD})}$ (not shown explicitly) is much larger in this case than in the case of spheres, giving discrepancies of up to about $30k_B T$ at close distance.

A major downside of $V_{E,\text{cube}}^{(\text{CSCD})}$ is that it is computationally expensive to calculate due to the high number of dipoles per particle ($N_{d/p} = 1000$). In Fig. 6.7(a) we plot $V_{E,\text{cube}}^{(\text{CSCD})}$ ($L = 5$) and the contours of $V_{E,\text{cube}}^{(\text{CSCD})}$ ($L = 10$), the former being the outcome of the calculation if the number of dipoles is reduced by a factor of 8 (2 in each dimension). Surprisingly, the accuracy of $V_{E,\text{cube}}^{(\text{CSCD})}$ ($L = 5$) is very good; much better than the accuracy

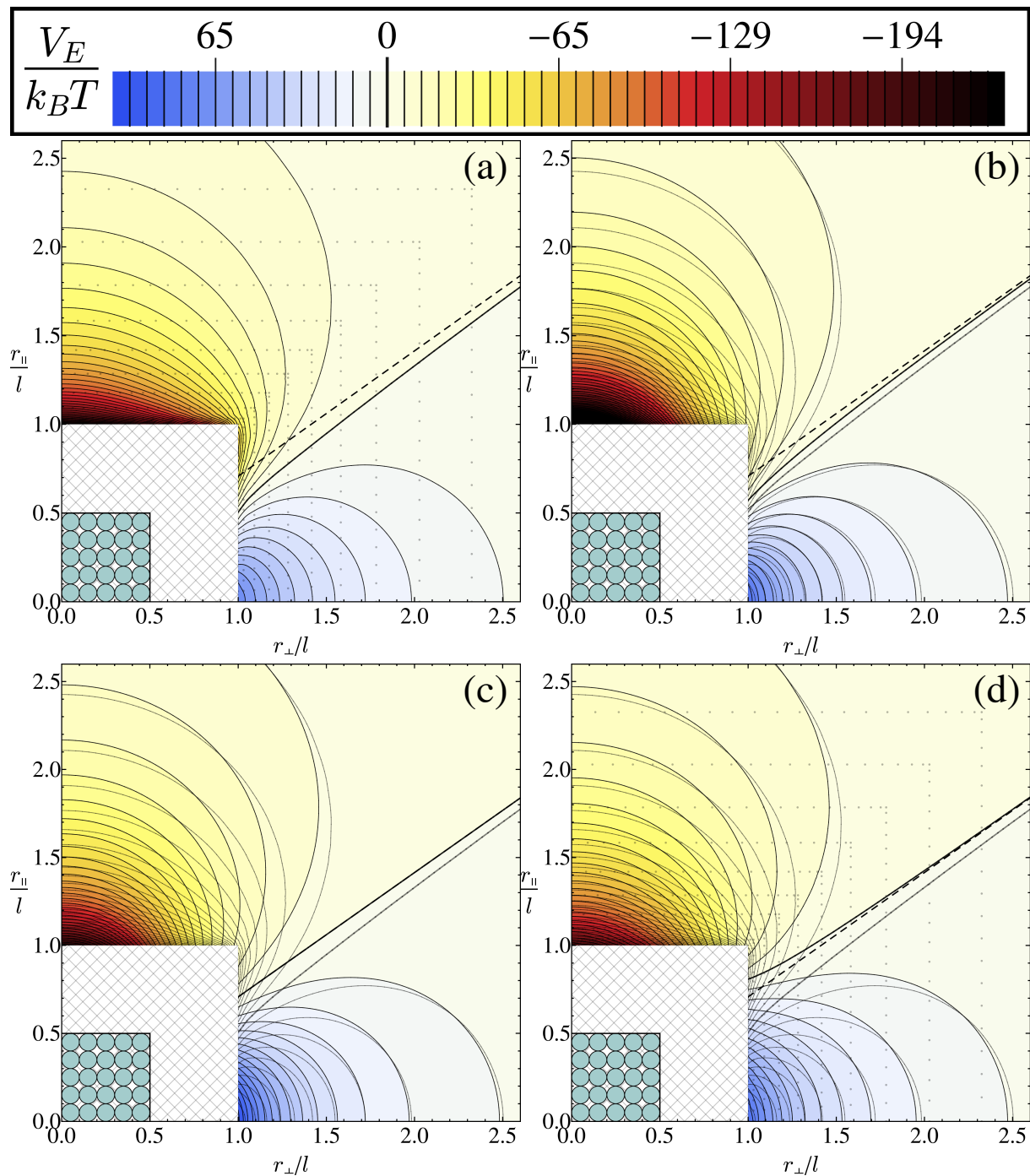


Figure 6.6: The interaction energy $V_E/k_B T$, at $T = 293$ K, of cubic particles with rib length $l = 1 \mu\text{m}$ and polarizability $\alpha_p = 0.2 \mu\text{m}^3$ in an external electric field $E_0 = 300 \text{ V mm}^{-1}$ along the r_{\parallel} -axis, as a function of the location of the second cube with respect to the first, calculated using (a) CSCD with 1000 dipole chunks per cube, (b) SSCD, (c) SPD, and (d) CPD (each approach is discussed in the text). Each plot uses the same contour lines and color coding provided in the legend. The dashed lines represent the 54.7° “magic angle”. The contour lines of (a) are reproduced as see-through lines in panels (b-d). A cross-section of the 1000-chunk cube is displayed in the center of the plots. The hatched area, within which the cubes overlap, is excluded from the plots. The dots in panels (a) and (d) represent the sample points at which the interaction energy was explicitly calculated.

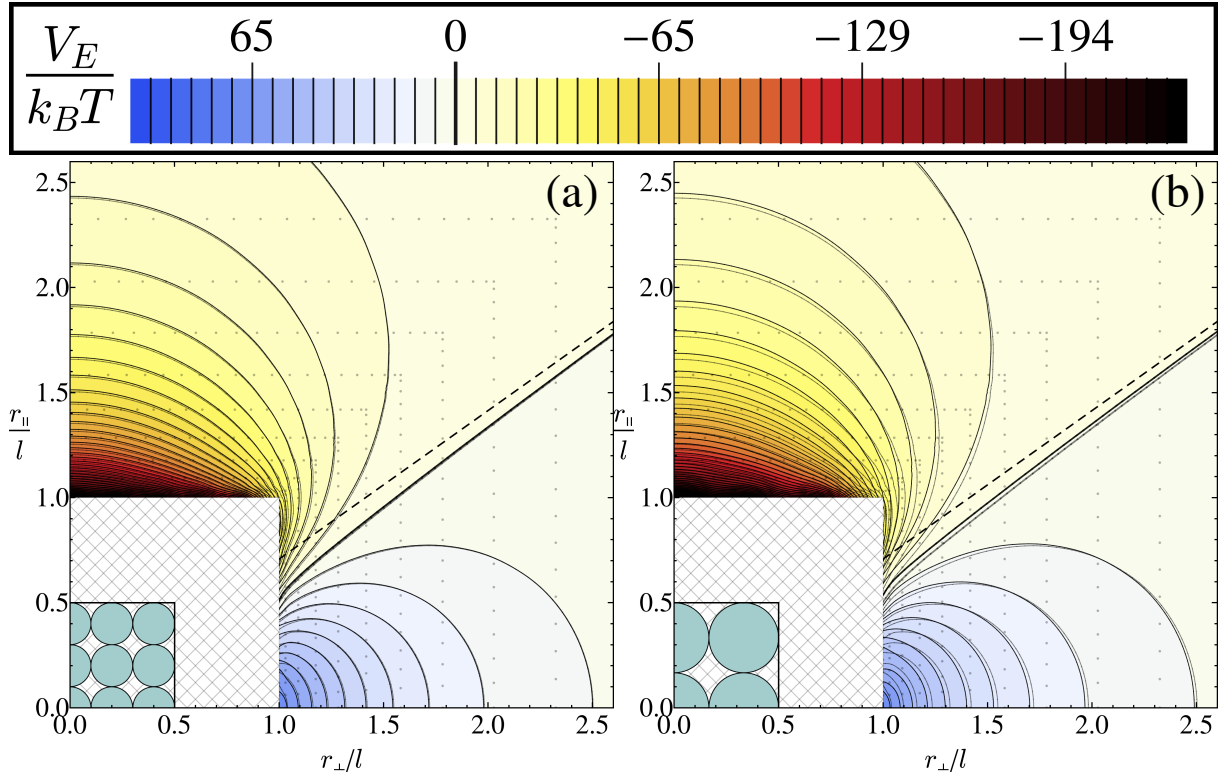


Figure 6.7: The interaction energy of the same setup as in Fig. 6.6, but now calculated using the CSCD approach with (a) 125 and (b) 27 dipole chunks per cube. As in Fig. 6.6(b-d), the contour lines resulting from the CSCD approach with 1000 chunks are displayed in the same plots. Cross-sections of the 125- and 27-dipole cubes are displayed in the center of panels (a) and (b), respectively.

	σ	$\frac{V_{E,min}}{k_B T}$	$\frac{V_{E,max}}{k_B T}$
CSCD	0	-234.7	70.9
SSCD	0.29	-329.6	82.4
SPD	0.24	-197.8	98.9
CPD	0.25	-171.0	85.5
CSCD(125)	0.028	-252.8	71.0
CSCD(27)	0.086	-282.7	70.5

Table 6.2: Numerical quantities associated with the various calculation techniques for the interaction energy between two cubes, as plotted in Figs. 6.6 and 6.7. $V_{E,min}$ and $V_{E,max}$ refer, respectively, to the minimum and maximum value achieved by the calculation technique mentioned in the leftmost column. σ is the relative deviation, as defined in 6.19, where h is always $V_{E,cube}^{(CSCD)}$, and g is the V_E associated with the technique given in the leftmost column. The approaches labeled as “CSCD(125)” and “CSCD(27)” refer to the CSCD approach with $5 \times 5 \times 5$ and $3 \times 3 \times 3$ dipoles per cube, respectively.

of the $N_{d/p} = 225$ sphere versus the $N_{d/p} = 959$ one. As can be seen from the values in Table 6.2, the 125-dipole cube has a low σ and approximates the maximum and minimum well.

Inspired by the good agreement between the $L = 5$ cube and the $L = 10$ cube, we also investigate a cube with an even smaller number of dipoles. In Fig. 6.7(b), we plot $V_{E,\text{cube}}^{(\text{CSCD})}$ ($L = 3$) together with the contours of $V_{E,\text{cube}}^{(\text{CSCD})}$. The agreement is significantly worse than that of the $L = 5$ case, with the $L = 3$ contour lines lying somewhere in-between those of the $L = 10$ case and the single dipole case. However, its σ is still a factor 4 lower than the SSCD, SPD, and CPD techniques, so it may be useful as a relatively cheap alternative to using 125 dipoles per cube.

We have seen that for cubes, neither the SSCD nor the SPD approach gave very good results, the former significantly overestimating attractions and somewhat overestimating repulsions, and the latter underestimating attractions and significantly overestimating repulsions. The CPD at first seems to be a compromise solution, underestimating attractions somewhat more than the SPD does, but giving a better result for repulsions. However, the CPD approach does not have a better σ -value and it comes at the cost of computational speed, making any gain probably not worth it for most applications. If accuracy is required, more can be gained by using the CSCD approach with smaller cubes. These overestimate attractions somewhat, but are very accurate for repulsions.

6.4.4 Numerical Results for Rods

We model rods as $N_{d/p} = n_t \times n_t \times n_l$ cuboids of dipoles on a simple cubic lattice. The shape of the rod is controlled by the parameter n_t/n_l , which we fix at 0.2. Because this particle has different dimensions in different Cartesian directions, its polarizability matrix is no longer proportional to the identity matrix, but has different values on the diagonal. For a $5 \times 5 \times 25$ rod, it turns out that $\alpha_t \approx 0.44\alpha_l$, where α_t is the polarizability in the transverse direction and α_l is the polarizability in the longitudinal direction. For a $3 \times 3 \times 15$ rod, we have $\alpha_t \approx 0.43\alpha_l$, i.e., the proportionality is almost identical to the one for the $5 \times 5 \times 25$ rod, which is in line with expectations since the enhancement factor is only weakly dependent on the number of dipoles and instead depends mainly on the particle shape [83]. For an even smaller rod, $1 \times 1 \times 5$, the ratio is $\alpha_t \approx 0.40\alpha_l$. We choose α_d such that $\alpha_l = 0.3 \mu\text{m}^3$, and choose the length of the rod to be $l = 3 \mu\text{m}$, such that its volume is $1.08 \mu\text{m}^3$. As for cubes and spheres, we calculate the relative deviation σ , with an integration area given by $|r_\perp|, |r_\parallel| < 1.72l$, and list the result in Table 6.3.

In Fig. 6.8(a), we plot $V_{E,\text{rod}}^{(\text{CSCD})}$ for $n_L = 25$. Qualitatively, we see that the contours seem stretched out in the longitudinal direction with respect to the case of cubes. As with cubes, the zero-contour meets the excluded region near the tips of the particle, meaning that in the case of rods, $\theta_0 < 54.7^\circ$, contrary to the case of cubes and spheres.

In Fig. 6.8(b) we plot $V_{E,\text{anisotropic}}^{(\text{SSCD})}(\tilde{r}, \theta, \eta_\alpha)$ (where $\eta_\alpha \approx 0.44$) with the contours of $V_{E,\text{rod}}^{(\text{CSCD})}$ visible in the same graph. We note that the agreement is very bad at the distances plotted. Qualitatively, we note that the contours of $V_{E,\text{anisotropic}}^{(\text{SSCD})}$ seem far more focused on the center than those of $V_{E,\text{rod}}^{(\text{CSCD})}$, suggesting that the source of the disagreement is the fact that with the former we try to describe a spatially anisotropic particle as a point dipole.

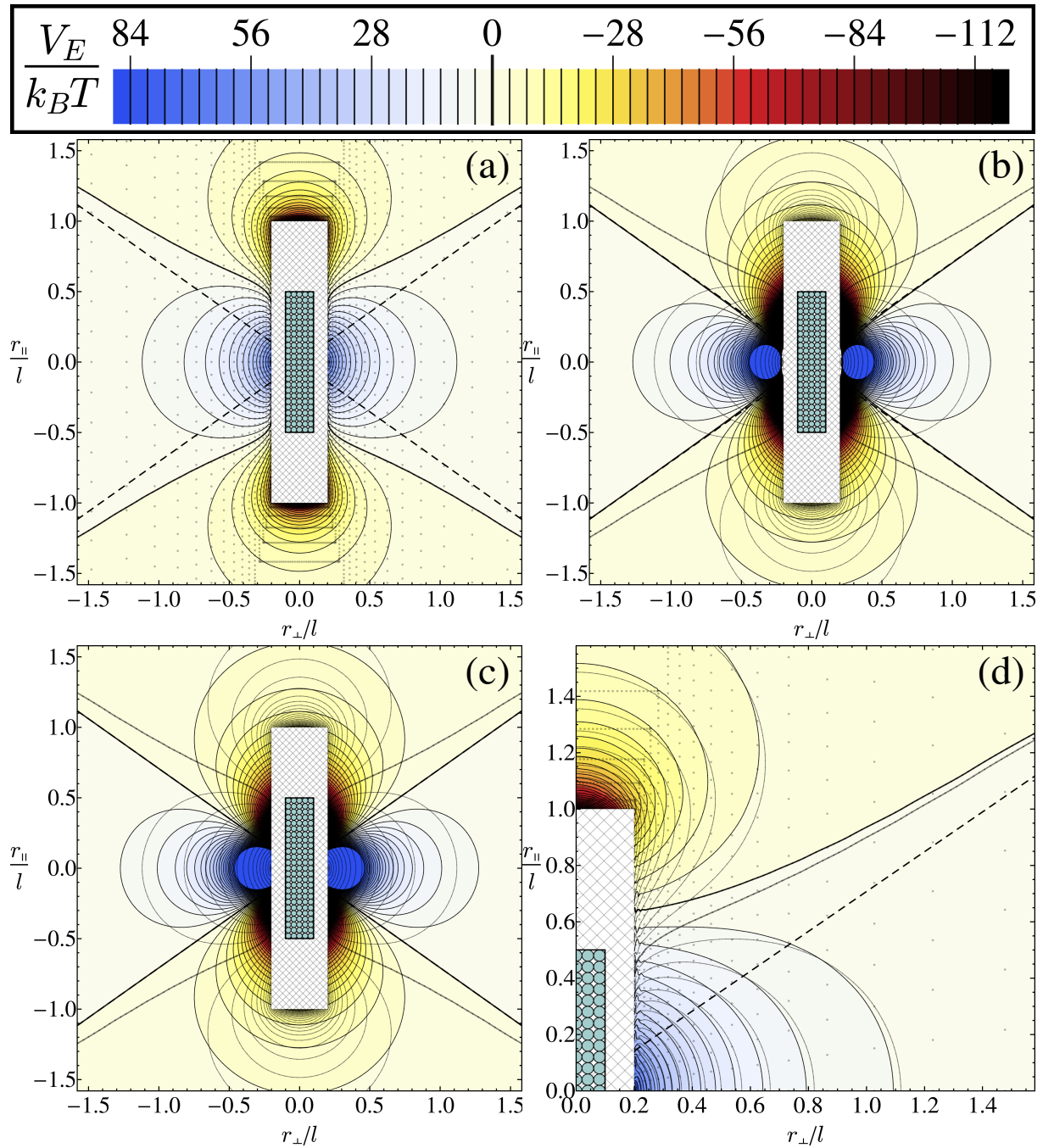


Figure 6.8: The interaction energy $V_E/k_B T$, at $T = 293$ K, of rods with length $l = 3 \mu\text{m}$, aspect ratio 0.2, and longitudinal polarizability $\alpha_l = 0.3 \mu\text{m}^3$, in an external electric field $E_0 = 300 \text{ V mm}^{-1}$ along the r_{\parallel} -axis, as a function of the location of the second rod with respect to the first, calculated using (a) CSCD with 625 dipole chunks per rod, (b) SSCD, (c) SPD, and (d) CPD (each approach is discussed in the text). Each plot uses the same contour lines and color coding provided in the legend. The dashed lines represent the 54.7° “magic angle”. The contour lines of (a) are reproduced as see-through lines in panels (b-d). A cross-section of the 625-chunk rod is displayed in the center of the plots. The hatched area, within which the rods overlap, is excluded from the plots. The dots in panels (a) and (d) represent the sample points at which the interaction energy was explicitly calculated.

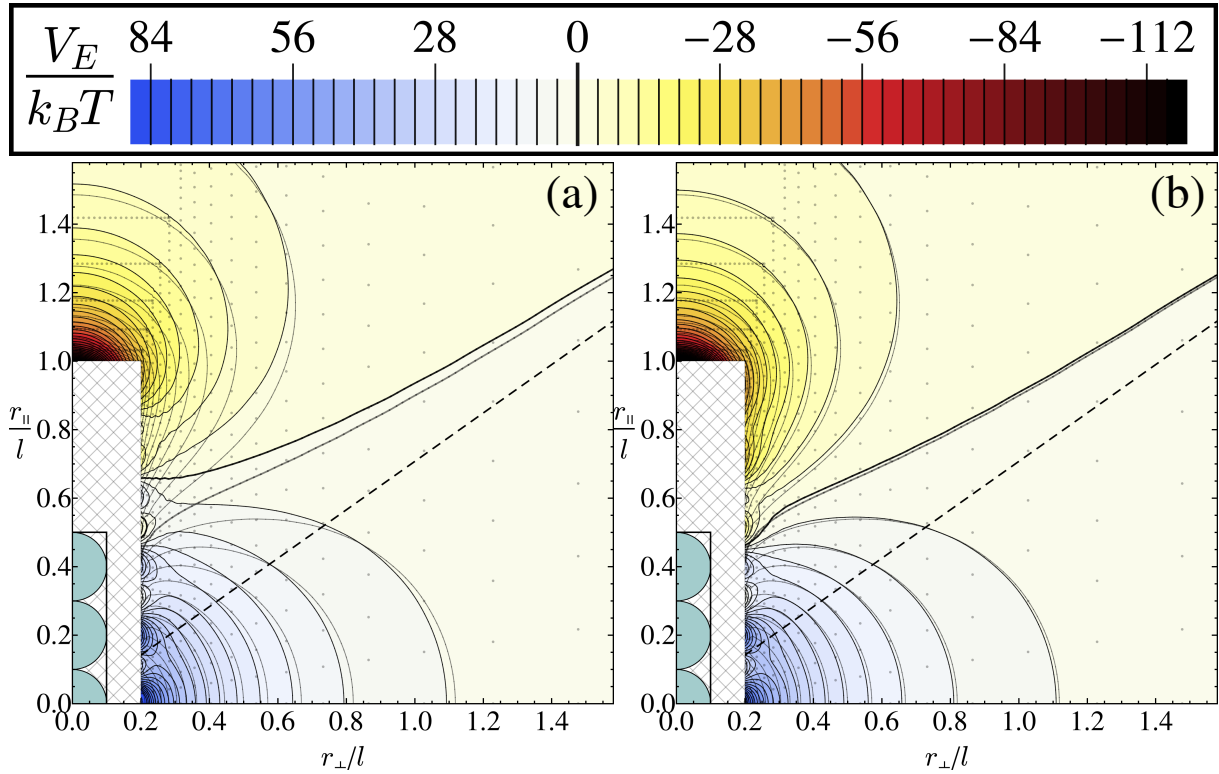


Figure 6.9: The interaction energy of the same setup as in Fig. 6.8, but now calculated using 5 dipole chunks per rod in (a) the CPD and (b) the CSCD approach. As in Fig. 6.8(b-d), the contour lines resulting from the CSCD approach with 625 chunks are displayed in the same plots. Cross-sections of the 5-dipole rods are displayed in the center of the plots.

The function could not be calculated at locations close to the origin, since these points lie inside the forbidden region of $V_{E, \text{anisotropic}}^{(\text{SSCD})}$. Plotted in Fig. 6.8(c) is a comparison between $V_{E, \text{rod}}^{(\text{CSCD})}$ and $V_E^{(\text{SPD})}$, which displays a similarly bad agreement. Note that in both of these plots, the minimum of the potential is no longer located at the tip of the rod but near the center instead, such that both the SSCD and the SPD predict that two dipolar rods to prefer to lie side-by-side instead of head-to-toe, which is clearly unphysical. Due to the problematic nature of both these functions, σ could not be evaluated for $V_{E, \text{anisotropic}}^{(\text{SSCD})}$ and is very large for $V_E^{(\text{SPD})}$, and hence neither was included in Table 6.3.

In Fig. 6.8(d), we plot $V_{E, \text{rod}}^{(\text{CPD})}$ for $n_l = 25$, together with the contours of $V_{E, \text{rod}}^{(\text{CSCD})}$ (also for $n_l = 25$). The agreement is much better than in panels (b) and (c), such that we zoom in on the upper right quadrant in order to be able to make out the differences better. We see a similar type of disagreement as the one we saw for cubes: the zero-contour, although this time on the correct side of the 54.7° line, gets bent too much to small angles and, in general, $V_{E, \text{rod}}^{(\text{CPD})}$ seems to underestimate attractions. We notice that $V_{E, \text{rod}}^{(\text{CPD})}$'s contours bend inwards too much in the attractive region, and do not bend enough in the repulsive region. Repulsions at high θ are about right, except for close distances, where, as can be seen from Table 6.3, the CPD approach overestimates repulsions.

	σ	$\frac{V_{E,min}}{k_B T}$	$\frac{V_{E,max}}{k_B T}$
CSCD	0	-108.6	68.4
CPD	0.23	-124.0	85.9
CPD(5)	0.25	-123.3	105.8
CSCD(5)	0.15	-147.0	87.9

Table 6.3: Numerical quantities associated with the various calculation techniques for the interaction energy between a pair of rods, as plotted in Figs. 6.8 and 6.9. $V_{E,min}$ and $V_{E,max}$ refer, respectively, to the minimum and maximum value achieved by the calculation technique mentioned in the leftmost column. σ is the relative deviation, as defined in 6.19, where h is always $V_{E,rod}^{(CSCD)}$, and g is the V_E associated with the technique given in the leftmost column. The approaches labeled as “CSCD(5)” and “CPD(5)” refer to the CSCD and CPD approach, respectively, with $1 \times 1 \times 5$ per rod, respectively.

After drastically reducing the number of dipoles to $1 \times 1 \times 5$, we note that $V_{E,rod}^{(CPD)}$'s accuracy remains the same, as illustrated in Fig. 6.9(a), where $V_{E,rod}^{(CPD)}$ for $n_L = 5$ is plotted together with $V_{E,rod}^{(CSCD)}$ for $n_L = 25$. From Table 6.3 we can confirm that the accuracy is similar, although the CPD with $n_L = 5$ overestimates repulsions at close distances.

The best agreement for the $n_l = 5$ case is reached when we plot $V_{E,rod}^{(CSCD)}$ for $n_l = 25$ with the contours of $V_{E,rod}^{(CSCD)}$ for $n_l = 5$, in Fig. 6.9(b). We note a good agreement, especially considering the low number of dipole chunks. As can be seen in Table 6.3, while this approximation overestimates the maximum attraction, its σ is somewhat lower than the other two reviewed approximations, such that it is the best approximation found for rods.

We see that in the case of rods, to gain any good results, we need to use a technique that employs multiple chunks per rod. The cheapest of these is the CPD approach with 5 dipoles per rod. This approach, however, significantly overestimates repulsions and, if more accuracy is required, the SSCD with 5 chunks will provide improvement. Increasing the number of dipole chunks in the CPD approach will not improve the accuracy much.

6.4.5 Numerical Results for Misaligned Particles

So far, we have only considered the interaction energy between aligned cubes and rods. For rods, the reason for this choice is that, if the electric field is strong enough, even a single rod will align along the field due to its anisotropic polarizability. However, situations where misaligned rods interact may still occur, for example if the electric field is weaker. Cubes do not individually align in an electric field [83] and therefore interaction between misaligned cubes seems plausible.

Investigating the interaction between misaligned clusters, however, causes the practical problem that the parameter space becomes very large, making it impossible to discuss all the possible orientations here. We therefore restrict ourselves to particles that are “as misaligned as possible”. For rods, this means that we rotate one rod with respect to the other by a 90° angle around an axis perpendicular to the rod. Thus, in our plots, the rod at the origin is still pointing in the direction of the electric field (along the $r_{||}$ -axis of the

plots), but the rod being moved is lying horizontally (along the r_{\perp} -axis of the plots). For cubes, we first rotate the second particle by a 45° angle around the axis parallel to r_{\perp} , and subsequently by an angle equal to $\arctan(\sqrt{2}/2)$ around the axis perpendicular to both r_{\perp} and r_{\parallel} . This way, we obtain a setup where, if the line connecting the centers of the particle is either approximately perpendicular or parallel to the electric field, a corner of the second cube is turned towards a face of the first.

The particles considered in this subsection are the same as the cubes and rods considered above; i.e., cubes with a rib length of $1 \mu\text{m}$ and a polarizability of $0.2 \mu\text{m}^3$, and rods with an aspect ratio of $n_t/n_l = 0.2$, a length of $3 \mu\text{m}$, and a polarizability in the longitudinal direction of $0.3 \mu\text{m}^3$.

Misaligned Rods

An analytical expression for the self-consistent interaction energy of point dipoles with anisotropic polarizabilities $\text{diag}(\alpha_t, \alpha_t, \alpha_l)$ and $\text{diag}(\alpha_l, \alpha_t, \alpha_t)$, where, for rods, α_t and α_l are the transverse and longitudinal polarizabilities, respectively, such that $\alpha_t < \alpha_l$, is given in Appendix D. Taylor-expanding this expression to first order, we gain the SPD variant,

$$\begin{aligned} V_{E, \text{misal.}}^{(\text{SPD})}(\tilde{r}, \theta, \eta_{\alpha}) &= E_0^2 \alpha_l \frac{\eta_{\alpha} - 3\eta_{\alpha} \cos^2 \theta}{\tilde{r}^3} \\ &= E_0^2 \alpha_t \alpha_l \frac{1 - 3 \cos^2 \theta}{r^3}, \end{aligned} \quad (6.20)$$

where $\eta_{\alpha} = \alpha_t/\alpha_l$. Eq. (6.20) is also the expression to be used for the pair interactions composing the CPD approach. Alternatively, we can continue to use Eq. (6.16) with $\alpha_d = \alpha_l/N_{d/p}$ for the pair interactions and multiply the end result by α_t/α_l . We note here that to gain α_t/α_l , we have to use the CDM, which causes the SPD and CPD methods to no longer be entirely independent of the CDM. For our rods, $\alpha_t/\alpha_l \approx 0.44$, such that excluding this extra factor would make the CPD a very bad approximation. As previously, we calculate the relative deviation σ with an integration area given by $|r_{\perp}|, |r_{\parallel}| < 1.38l$, and list the result in Table 6.4.

In Fig. 6.10(a), we plot $V_{E, \text{misal. rod}}^{(\text{CSCD})}$ as a function of the location of the second rod. One feature we note are the flattened contour lines in the attractive region at small distances, which correspond to the second rod “sliding” over the first which, if the ends are relatively far away, does not change the interaction energy significantly. Another feature is the fact that the zero-contour starts out coinciding almost exactly with the 54.7° -line, but at longer distances bends towards higher θ . At even larger distances, the line does go back to 54.7° . Lastly, we also note the extreme inward bending of the contour line closest to contact in the repulsive region. We speculate that if r_{\parallel} is somewhat above zero and the rods are touching, a significant part of the stationary rod, the “lower” part, is located such that its dipolar interaction with the tip of the moving rod is attractive (because the dipole moments of the interacting chunks lie approximately head-to-toe), such that the overall interaction becomes less repulsive. If the second rod is moved somewhat away, however, the angle between the line connecting the lower part of the stationary rod and the tip of the second rod becomes larger and the interaction between these parts becomes less attractive or even repulsive, making the overall interaction more repulsive.

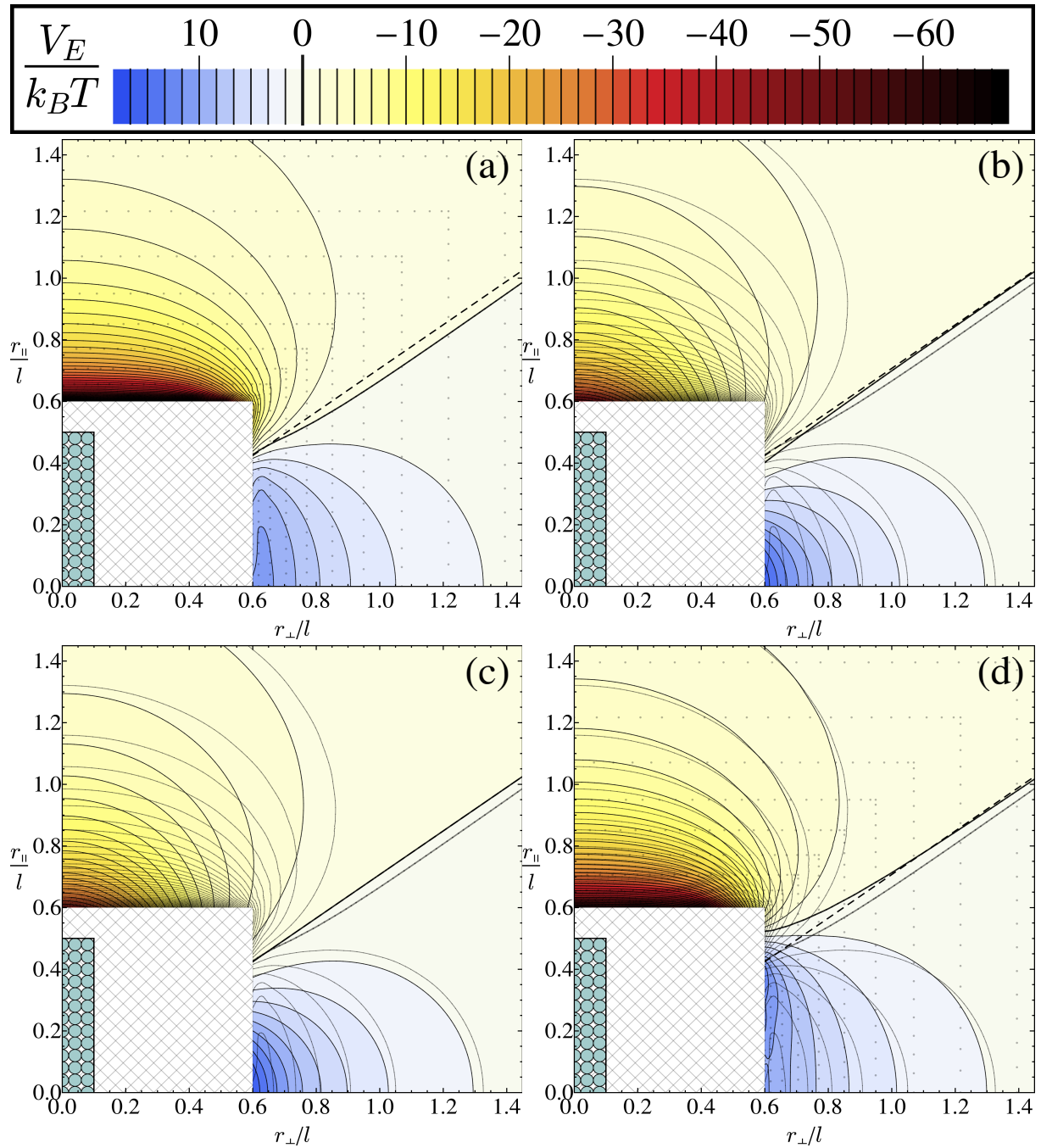


Figure 6.10: The interaction energy $V_E/k_B T$, at $T = 293$ K, of “misaligned” rods (explained in the text) with length $l = 3 \mu\text{m}$, aspect ratio 0.2, and longitudinal polarizability $\alpha_l = 0.3 \mu\text{m}^3$, in an external electric field $E_0 = 300 \text{ V mm}^{-1}$ along the r_{\parallel} -axis, as a function of the location of the second rod with respect to the first, calculated using (a) CSCD with 625 dipole chunks per rod, (b) SSCD, (c) SPD, and (d) CPD (each approach is discussed in the text). Each plot uses the same contour lines and color coding provided in the legend. The dashed lines represent the 54.7° “magic angle”. The contour lines of (a) are reproduced as see-through lines in panels (b-d). A cross-section of the 625-chunk rod is displayed in the center of the plots. The hatched area, within which the rods overlap, is excluded from the plots. The dots in panels (a) and (d) represent the sample points at which the interaction energy was explicitly calculated.

	σ	$\frac{V_{E,min}}{k_B T}$	$\frac{V_{E,max}}{k_B T}$
CSCD	0	-69.4	10.2
SSCD	0.49	-35.2	15.8
SPD	0.51	-32.7	16.3
CPD	0.15	-53.9	13.1*
CSCD(5)	0.071	-71.3	13.5
CSCD(5, mod)	0.12	-78.6	14.9
CSCD(135)	0.018	-69.5	11.1
CSCD(135, mod)	0.018	-71.2	11.4

Table 6.4: Numerical quantities associated with the various calculation techniques for the interaction energy between two misaligned rods (where the second rod is rotated by a 90° angle with respect to the first), as plotted in Figs. 6.10 and 6.11. $V_{E,min}$ and $V_{E,max}$ refer, respectively, to the minimum and maximum value achieved by the calculation technique mentioned in the leftmost column. σ is the relative deviation, as defined in 6.19, where h is always $V_{E,misaligned\ rod}^{(CSCD)}$, and g is the V_E associated with the technique given in the leftmost column. The approaches labeled as “CSCD(5)” and “CSCD(135)” refer to the CSCD approach with $1 \times 1 \times 5$ and $3 \times 3 \times 15$ dipole chunks per rod, respectively. The “CSCD(5, mod)” and “CSCD(135, mod)” techniques are the same except that, at the end of the calculation, the interaction energy is multiplied by a correction factor. The maximum value predicted by the CPD (marked by an asterisk) is attained not at $r_{\parallel} = 0$ but at $r_{\parallel} \approx 0.38l$. The value of the interaction energy predicted by the CPD at location $(r_{\perp}, r_{\parallel}) = (0.6, 0)l$ is approximately $10.8k_B T$.

In Fig. 6.10(b), we plot $V_{E, misal. rod}^{(SSCD)}$ together with the contour lines of $V_{E, misal. rod}^{(CSCD)}$. The agreement is fair for larger distances but becomes bad at low distance. As is also clear from Table 6.4, at close distances the SSCD underestimates attractions and overestimates repulsions.

In Fig. 6.10(c), we plot $V_{E, misal. rod}^{(SPD)}$ together with the contour lines of $V_{E, misal. rod}^{(CSCD)}$. We note that this plot looks very similar to the one for $V_{E, misal. rod}^{(SSCD)}$. This is not very surprising, because, due to the misaligned nature of the rods, the center-to-center distance is always relatively large such that the SSCD and SPD agree well. The numerical quantities listed in Table 6.4 are also very similar when comparing the SSCD and SPD approaches.

Fig. 6.10(d) displays $V_{E, misal. rod}^{(CPD)}$, again with the contour lines of $V_{E, misal. rod}^{(CSCD)}$. Here we see a behavior similar to the one observed with cubes: the zero-contour bends towards the attractive region, the contours in the attractive region bend inwards too much, and, on the repulsive side, the contours do not bend inwards enough. We also note that the CPD predicts the strongest repulsions at locations where the center of the second rod is almost at the same r_{\parallel} as the tip of the first rod. The CPD approach does a better job at predicting the maximum attraction and repulsion strength than the SPD and SSCD approach, as can be seen in Table 6.4, and is therefore rewarded with a σ that is lower by more than a factor 3. We note here that, while not shown explicitly, our numerical results show that the CPD with $1 \times 1 \times 5$ chunks per rod has a similar accuracy as the CPD with $5 \times 5 \times 25$ chunks per rod.

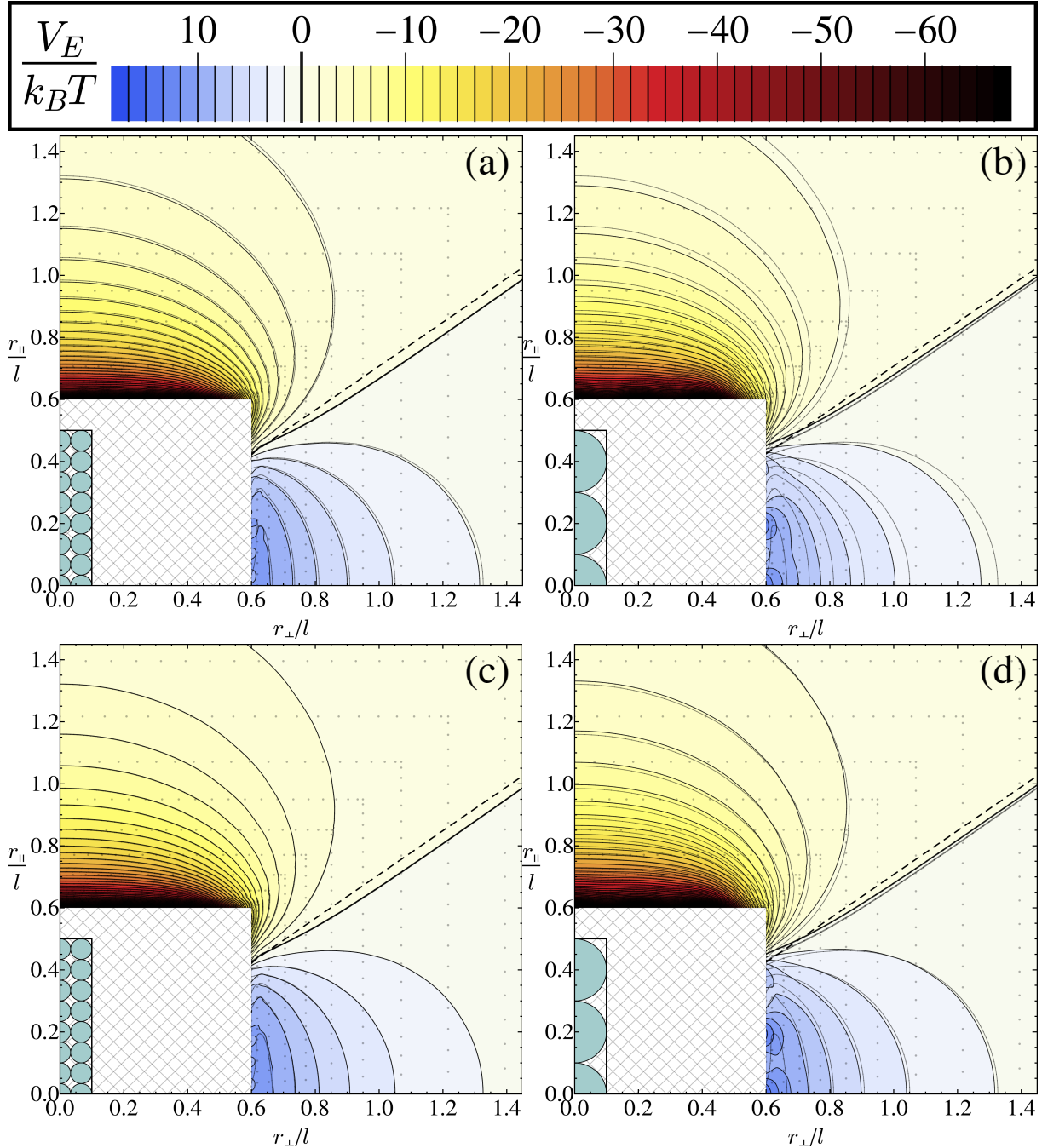


Figure 6.11: The interaction energy of the same setup as in Fig. 6.10, but now calculated using the CSCD approach with (a) 135 and (b) 5 dipole chunks per rod. In (c) and (d), the interaction energies of (a) and (b), respectively, were multiplied by a constant correction factor. As in Fig. 6.10(b-d), the contour lines resulting from the CSCD approach with 625 chunks are displayed in the same plots. Cross-sections of the 135- and 5-dipole rods are displayed in the center of panels (a) and (c), and (b) and (d), respectively.

In Fig. 6.11, we investigate the accuracy when reducing the number of dipole chunks per rod. In Fig. 6.11(a), we plot the interaction energy for $V_{E, \text{misal. rod}}^{(\text{CSCD})}(n_l = 5)$ with $1 \times 1 \times 5$ dipoles per rod, together with the contour lines of $V_{E, \text{misal. rod}}^{(\text{CSCD})}(n_l = 25)$ (i.e., the $5 \times 5 \times 25$ rod used in Fig. 6.10(a)). From the plot it appears as if the agreement is not very good; much worse than was the case for aligned rods with 5 dipoles per rod. However, the numerical values of Table 6.4 contradict this assessment, showing a σ twice as low as the one for CPD and a good approximation of the interaction energy at close distances.

If we do not reduce the number of dipole chunks as dramatically, the agreement becomes better. In Fig. 6.11(b), we plot the interaction energy $V_{E, \text{misal. rod}}^{(\text{CSCD})}(n_l = 15)$, which corresponds to a $3 \times 3 \times 15$ rod, together with the contour lines of $V_{E, \text{misal. rod}}^{(\text{CSCD})}(n_l = 25)$. Clearly, the agreement is much better, which can also be seen from the fact that σ has decreased almost by a factor 4 and that the maximum attraction and repulsion are even closer to those of $V_{E, \text{misal. rod}}^{(\text{CSCD})}(n_l = 25)$ (see Table 6.4). We note that in both Figs. 6.11(a) and 6.11(b), we see some “bumps” in the interaction energy, which is due to the discretization.

The relatively good agreement of the CPD of Fig. 6.10(d) was achieved by using the correct fraction α_t/α_l as an overall multiplier of the interaction energy. We note, in contrast, that this fraction is slightly different for $n_l = 5$ and $n_l = 15$ rods than for $n_l = 25$ rods. It is not hard to see that therefore, at large distances, the results of the low- $N_{d/p}$ CSCD approaches are off by approximately a factor 0.40/0.44 for $n_l = 5$ rods and 0.43/0.44 for $n_l = 15$ rods (the ratios α_t/α_l , as mentioned, being 0.40, 0.43, and 0.44 for $n_l = 5, 15$ and 25, respectively). Dividing the results by these factors significantly improves their accuracy as perceived from the plots, as can be seen in Figs. 6.11(c) and (d), which plot the “modified” interaction energies $V_{E, \text{misal. rod}}^{(\text{CSCD, mod})}(n_l = 5)$ and $V_{E, \text{misal. rod}}^{(\text{CSCD, mod})}(n_l = 15)$, respectively, both with the contour lines of $V_{E, \text{misal. rod}}^{(\text{CSCD})}(n_l = 25)$. We see that the contour lines of $V_{E, \text{misal. rod}}^{(\text{CSCD, mod})}(n_l = 5)$ now lie very close to those of $V_{E, \text{misal. rod}}^{(\text{CSCD})}(n_l = 25)$, while those of $V_{E, \text{misal. rod}}^{(\text{CSCD, mod})}(n_l = 15)$ are almost indistinguishable from those of $V_{E, \text{misal. rod}}^{(\text{CSCD})}(n_l = 25)$. Still, at contact, our approximation has become worse, and σ has even increased somewhat in the case of $n_l = 5$ rods. This is entirely due to the discrepancies at close distance: if we integrate only over an area that does not include the smaller relative distances, the σ -values quickly become much better in the modified than in the unmodified case.

In conclusion, we see that for misaligned rods, similarly to aligned ones, the single-dipole approaches SSCD and SPD do not give good results and we therefore need to split up the particles into multiple chunks. Using the CPD will give fair results and is cheap if not many dipoles are used (which, as mentioned, has little influence on accuracy). However, the CPD has the problematic property that the location of maximum repulsion is situated in the wrong place. If more accuracy is needed, the CSCD with 5 dipoles seems the best option. If long-range interactions are more important than short-range ones, it is advisable to include the extra correction factor mentioned, but this will negatively affect the accuracy at (very) short range.

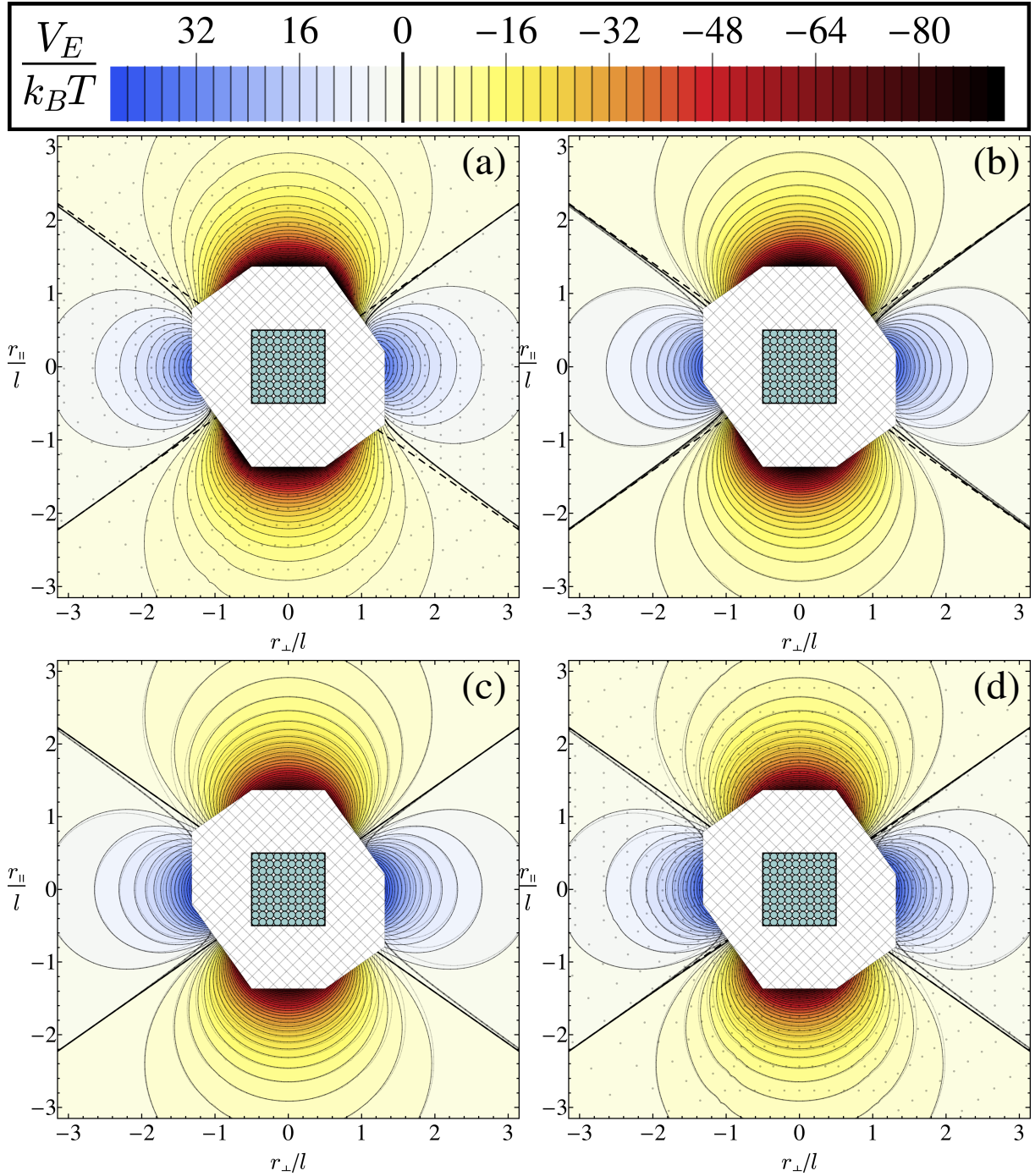


Figure 6.12: The interaction energy $V_E/k_B T$, at $T = 293$ K, of “misaligned” cubes (explained in the text) with rib length $l = 1 \mu\text{m}$ and polarizability $\alpha_l = 0.2 \mu\text{m}^3$, in an external electric field $E_0 = 300 \text{ V mm}^{-1}$ along the r_{\parallel} -axis, as a function of the location of the second cube with respect to the first, calculated using (a) CSCD with 1000 dipole chunks per rod, (b) SSCD, (c) SPD, and (d) CPD (each approach is discussed in the text). Each plot uses the same contour lines and color coding provided in the legend. The dashed lines represent the 54.7° “magic angle”. The contour lines of (a) are reproduced as see-through lines in panels (b-d). A cross-section of the 1000-chunk cube is displayed in the center of the plots. The hatched area, within which the cubes overlap, is excluded from the plots. The dots in panels (a) and (d) represent the sample points at which the interaction energy was explicitly calculated.

Misaligned Cubes

In Fig. 6.12(a), we plot the interaction energy $V_{E, \text{misal. cube}}^{(\text{CSCD})}$ that is the result of an CSCD calculation with $10 \times 10 \times 10$ cubes. Apart from the differently-shaped excluded region, the plot looks similar to the ones shown for spheres, showing a similarly expanded attractive region. However, we note that the plot has lost one of its symmetries: instead of being invariant under 90° rotations, it is now only invariant under 180° degree rotations. This is not only due to the shape of the excluded region but also because the shape of the contour lines is slightly different. For instance, the zero-contours to the upper left and lower right take much longer to close in on their respective 54.7° lines than the zero-contours to the upper right and lower left. Another difference with the spherical plots is that repulsions seem to be somewhat stronger relative to the attractions, which can also be seen from Table 6.5, where the minimum and maximum value for the interaction energy are listed for each calculation approach, as well as each approach's value of σ , which is calculated using an integration area defined by $|r_\perp|, |r_\parallel| < 3.15l$.

When comparing the CSCD result with the SSCD result by plotting $V_{E, \text{misal. cube}}^{(\text{SSCD})}$ with the contour lines of $V_{E, \text{misal. cube}}^{(\text{CSCD})}$, as done in Fig. 6.12(b), we note, first of all, a rather good agreement. The only areas where the SSCD is off is close to the lower left and upper right edges of the excluded region, where the CSCD zero-contours bend inwards more. We note that, because the SSCD result is 4-fold symmetric, we can also more clearly make out the asymmetries in the CSCD result. Examining the values in Table 6.5, we note that the SSCD approximates the attraction and repulsion strengths at contact rather well, such that it has a low σ -value.

In Fig. 6.12(c), we plot the result from the SPD approach, $V_{E, \text{misal. cube}}^{(\text{SPD})}$, again together with the contour lines of $V_{E, \text{misal. cube}}^{(\text{CSCD})}$. As could be expected, the SPD does not capture the behavior of the contour lines near the zero-contours well. However, as is clear from Table 6.5, it also gives a bad approximation for the maximum attraction. Its approximation for the repulsion is somewhat better but still further off than the SSCD approximation. The overall σ -rating is therefore a factor two higher than that of the SSCD result.

In Fig. 6.12(d), we also examine $V_{E, \text{misal. cube}}^{(\text{CPD})}$, i.e., the result from the CPD approach. Both by eye and by the values in Table 6.5, we can see that the CPD certainly does not improve the approximation but rather makes it somewhat worse.

In Figs. 6.13(a) and 6.12(b), we examine the accuracy of CSCD approaches with low numbers of dipole chunks per cube ($5 \times 5 \times 5$ and $3 \times 3 \times 3$, respectively). In both plots, the contour lines of the CSCD approaches with low dipole numbers almost exactly coincide with those of the CSCD with $10 \times 10 \times 10$ dipole chunks, showing that their accuracy is very good. This is confirmed by the values in Table 6.5, which shows small values for σ and good agreement with the maximum and minimum interaction energy.

In conclusion, we note that for misaligned cubes, while all the approximations did relatively well, the self-consistent approaches clearly outperformed their permanent-dipole counterparts. In particular, the SSCD did remarkably well, especially considering its relatively weak performance for aligned cubes. The CSCD approaches with low dipole numbers also did very well but we note that, because of the SSCD's excellent performance, the former seem necessary (for rotated cubes) only if a high level of precision is required.

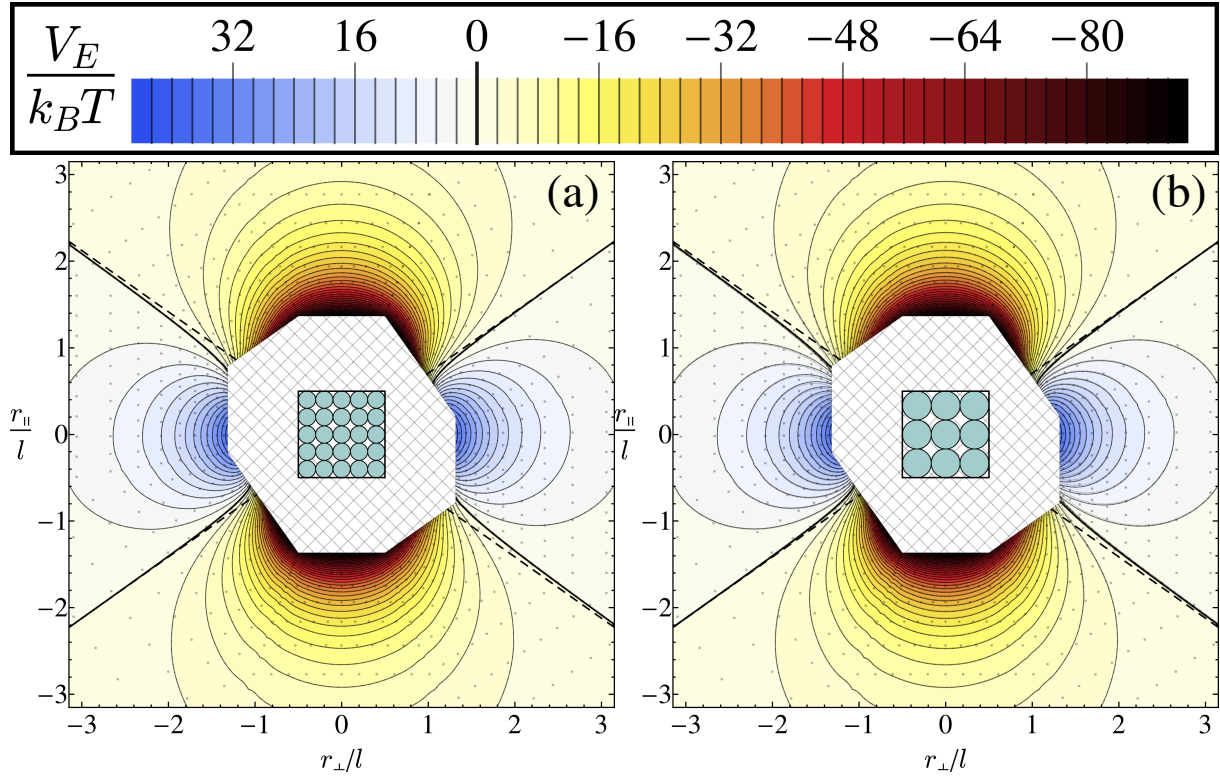


Figure 6.13: The interaction energy of the same setup as in Fig. 6.12, but now calculated using the CSCD approach with (a) 125 and (b) 27 dipole chunks per cube. As in Fig. 6.12(b-d), the contour lines resulting from the CSCD approach with 1000 chunks are displayed in the same plots. Cross-sections of the 125- and 27-dipole cubes are displayed in the center of panels (a) and (b), respectively.

	σ	$\frac{V_{E,min}}{k_B T}$	$\frac{V_{E,max}}{k_B T}$
CSCD	0	-95.2	36.0
SSCD	0.071	-92.0	39.8
SPD	0.18	-77.6	43.3
CPD	0.19	-74.9	41.2
CSCD(125)	0.0092	-94.6	36.2
CSCD(27)	0.022	-94.3	36.1

Table 6.5: Numerical quantities associated with the various calculation techniques for the interaction energy between two misaligned cubes (where the second cube is rotated such that, at polar angles $\theta = 0$ and $\pi/2$, one of its corners points into a face of the first cube), as plotted in Figs. 6.12 and 6.13. $V_{E,min}$ and $V_{E,max}$ refer, respectively, to the minimum and maximum value achieved by the calculation technique mentioned in the leftmost column. σ is the relative deviation, as defined in 6.19, where h is always $V_{E, misal. cube}^{(CSCD)}$, and g is the V_E associated with the technique given in the leftmost column. The approaches labeled as “CSCD(125)” and “CSCD(27)” refer to the CSCD approach with $5 \times 5 \times 5$ and $3 \times 3 \times 3$ dipoles per cube, respectively.

6.5 Conclusion

We have introduced and generalized the Coupled Dipole Method (CDM) to include polarizable matter chunks that are not necessarily of atomic proportions. We used the CDM to derive an expression for the self-consistent interaction energy for two inducible point dipoles. We compared this result to the commonly used method of pre-assigning dipole moments to calculate the interaction energy. We found that the expression derived for the latter method is a first-order Taylor approximation in r^{-3} of the “full” expression obtained using the self-consistent method.

We then proceeded to numerically evaluate the accuracy of various techniques for calculating the electric-field interaction energy of various particle shapes. The techniques considered were the SPD, where the particles are treated as point dipoles with pre-assigned dipole moments, the SSCD, where the particles are still treated as point dipoles but have self-consistent dipole moments, the CPD, where the particles are split up into chunks with pre-assigned dipole moments, and the CSCD, where the chunks instead have self-consistent dipole moments, calculated using the CDM. The particle shapes considered were spheres, cubes, and rods. For cubes and rods we considered the case where the particles are aligned with respect to each other and the electric field, and the case where the particles were “as misaligned as possible”. For each shape and technique, the CSCD with the most dipole chunks was considered to be the “exact” result and the other techniques were judged according to their agreement with it.

We found that, for spheres, the SSCD approach does better than the other techniques, except the CSCD approach with a reduced number of dipoles. However, the latter is computationally expensive for the limited improvement it provides. The SPD and the CPD were found to give almost identical results, such that, if the permanent dipole approximation is used, there is no point in splitting up the sphere into multiple chunks. For aligned cubes, neither the SSCD, SPD, nor CPD gave very satisfactory results. In this case, the SPD and CPD approaches do not give identical results, but the CPD approach is not more accurate than the SPD, such that, if using a permanent dipole approach, splitting up a cube into multiple chunks is not advisable. If using a self-consistent dipole approach, however, splitting up the cube into multiple chunks does improve the accuracy significantly, with a $3 \times 3 \times 3$ cube already giving decently accurate results (when compared to a $10 \times 10 \times 10$ cube). For misaligned cubes, the SSCD did better than the SPD and CPD (where, again, the latter is not more accurate than the former). Rods are the only particle studied for which the CPD is worthwhile. In fact, splitting up the rod into multiple chunks is absolutely crucial for gaining accurate results, regardless of whether a permanent or a self-consistent dipole approach is used. However, if using the CPD, the lowest possible number of chunks that gives the correct aspect ratio should be preferred, because splitting up the rod into more chunks does not improve the accuracy of the CPD. For the CSCD, we saw good agreement even if using the lowest possible number of chunks.

Speculating on the effects of using the interaction energy obtained from the SSCD approach instead of the result from the usual SPD for simulations, we note that the SSCD approach in general gives stronger attractions and weaker repulsions, especially at close distances. Therefore, it seems not unreasonable to assume that the SSCD would result in a widening of the parameter regime for which crystal phases such as body-centered

tetragonal and body-centered orthorhombic lattices, which are based on shifted strings, are stable. On the other hand, because repulsions are weaker, it becomes less important for a string to be shifted exactly half a unit cell with respect to its neighbors. As a consequence, we might also see more stable string fluids, where the particles form strings in the direction of the electric field, but where the strings are positionally disordered with respect to each other. Another interesting direction of research might be to study one of the interaction energies resulting from the CSCD or CPD [119]. The most obvious particle shape to investigate this for is the rod, since the effect of splitting up this particle into multiple chunks is significant even if the number of chunks is low, given the very bad agreement between the single dipole approaches (SSCD and SPD) and the CSCD result and the comparatively good accuracy of the cluster approaches (CPD and CSCD with a low number of chunks).

We note here that the SSCD and CSCD approaches, though they use self-consistent dipole moments, have, in this chapter, only been used to study interactions between particle pairs in the absence of other particles. It is of interest to investigate what effect the presence of other particles would have on these interactions; in other words, to study the many-body interactions between polarizable particles in an external electric field. This might be done in simulations, although the large-matrix manipulation involved in the CDM would make such simulations rather cumbersome, but the many-body effects might also be investigated by, for example, simply studying the interaction between a pair of particles in the presence of a third particle. This is left for future study.

Miscellaneous

We discuss three studies with a promising basis for further research. We first study the density of states of chains of Lorentz atoms, and investigate whether specific modes might be responsible for the interaction between two of these chains. We also derive theoretically a density of states function that agrees with the numerical results. Next, we discuss modes in interacting squares of Lorentz atoms and investigate what type of modes is responsible for the energy difference when moving one square with respect to the other. The results indicate that the responsible modes are those that concentrate their amplitude of vibration near the gap between the squares. However, we also show that “ordinary” modes can transform into such surface modes and vice versa, such that it does not appear to be possible to predict which modes will become surface modes. Lastly, we discuss the interaction of an inducible dipole and a chain of inducible dipoles (a rod) with a conducting plate under the influence of an electric field. To this end, we extend the CDM somewhat to include image dipoles, which are similar to image charges.

7.1 Introduction

The three sections of this chapter correspond to three separate studies. Sec. 7.2 describes a study into the density of states of dipole polymers: i.e., it addresses the question of which mode frequencies are more and which are less prevalent in chains of Lorentz atoms. It also investigates the effect of a second nearby polymer, which could potentially have allowed us to identify modes that change the most and, hence, contribute most to the interaction energy. Unfortunately, no such modes could be identified. We proceed to theoretically calculate the density of state function of an infinite dipole chain.

Sec. 7.3 studies in detail the modes of interacting squares of Lorentz atoms, looking at what distinguishes modes that contribute more to the interaction energy from modes that contribute less. It is found that modes that are localized near the gap between the squares contribute most but, unfortunately, since the modes develop as a function of distance, any mode can transform into such a surface mode and it is not clear how to predict which modes will do so.

Sec. 7.4 investigates the effect of a conducting plate near coupled Lorentz atoms. It shows that the method of image charge (in our case, image dipoles) can readily be extended to the CDM, such that the interaction between an electric field-induced dipole and the conducting plate can be easily calculated. We derive an expression for a single dipole interacting with its image and proceed to also investigate the interaction of rods with their images. We find that, under certain circumstances, rods near a metal plate lie down on the latter's surface if an electric field is applied in the direction perpendicular to the plate.

7.2 Density of States of Dipole Polymers

In this section, we present a study into the density of states of “dipole polymers”, i.e., straight chains of Lorentz atoms. Calculations on dipole cubes have also been performed but these will not be presented here. The work was inspired by the desire to speed up the process of calculating Van der Waals interactions between clusters of atoms. One possibility for speed increase, we reasoned, could possibly be provided by calculating only a few eigenfrequencies of the dipole clusters instead of all of them. If we were to find only a small number of “interaction modes” (i.e., modes that change their frequency significantly as a result of moving one cluster with respect to the other) while the rest of the modes do not significantly contribute to the interaction (i.e., change their frequency significantly), then we would have to compute only the interaction modes for a good estimate of the interaction energy. We will find, however, that it is not the case that only certain modes change. It seems more accurate to say that many modes change their frequency and predicting which one will change most appears to be impossible. We will first present numerical calculations on finite polymers. We found densities of states that do not look overly complicated, which inspired us to theoretically calculate a density of state function $D(\omega)$ for an infinite polymer in Sec. 7.2.1.

Numerically calculating the density of states for a set of N dipoles is conceptually very straightforward. The Hamiltonian in terms of $3N \times 3N$ vectors of the system is

$$H = \frac{\mathcal{K}^2}{2m} + \frac{1}{2}m\omega_0^2\mathcal{D}^2 + \mathcal{D} \cdot \mathcal{T} \cdot \mathcal{D},$$

where \mathcal{T} is the $3N \times 3N$ matrix built up of 3×3 matrices \mathbf{T}_{ij} , which are given by

$$\mathbf{T}_{ij} = (1 - \delta_{ij}) \frac{e^2}{2r_{ij}^3} \left(\mathbf{I} - 3 \frac{\mathbf{r}_{ij}\mathbf{r}_{ij}}{r_{ij}^2} \right).$$

The eigenfrequencies ω_k are now found by simply calculating the eigenvalues λ_k of \mathcal{T} , and hence

$$\omega_k = \omega_0 \sqrt{1 + \alpha_0 \lambda_k},$$

where

$$\alpha_0 = \frac{e^2}{m_e \omega_0^2}$$

is the atomic polarizability. The eigenfrequencies can then be binned and plotted as a histogram displaying how many of the ω_k are in the range $(\omega, \omega + \Delta\omega)$, where $\Delta\omega$ is the bin width.

Finite Polymers

In Fig. 7.1 the density of states for an $L = 3000$ polymer with $a/\alpha_0^{1/3} = 2$ is displayed. Some interesting properties of the histogram include: the fact that the ω are limited to a quite narrow range around ω_0 ; the profound peaks in the histogram, apparently denoting certain preferred frequencies (resonance); the apparent discontinuities in the plot; the low frequency ‘‘tail’’; and the fact that, on both edges of the nonzero part of the histogram, the number of ω ’s per bin rises before suddenly dropping to zero. We can also calculate the mean of all the found frequencies. For any L , this lies very close to ω_0 . For example, for the $L = 3000$ case, the mean is $0.991344 \times \omega_0$.

The general shape of the plot is only weakly dependent on the number of dipoles; for example, Fig. 7.2 displays the histogram for an $L = 10$ polymer. This plot already shares many of its properties with the $L = 3000$ histogram, such as the limited range of found ω ’s, the low-frequency tail, and the two middle peaks. In this case, the mean of the frequencies is $0.992299 \times \omega_0$.

We can also calculate the density of states for two polymers. The result for two $L = 1500$ polymers lying head-to-toe, separated by a gap of width $r/a = 50$, is displayed in figure 7.3. This histogram is almost indistinguishable from that for a single polymer.^a No significant difference in the shape of the histogram is expected (and, indeed, observed) for different distances because, for larger distances, the polymers look more and more like two single polymers, such that the resulting histogram will simply be the sum of two individual $L = 1500$ histograms, which are very similar to the $L = 3000$ case because, as mentioned, the shape hardly depends on the number of dipoles (i.e., two $L = 1500$

^aVisible by eye, in fact, are some slight differences in the relative height of the bins at frequencies near $\omega \approx 0.75\omega_0$, just below the resonance at $\omega \approx 0.88\omega_0$ and just above $\omega \approx \omega_0$.

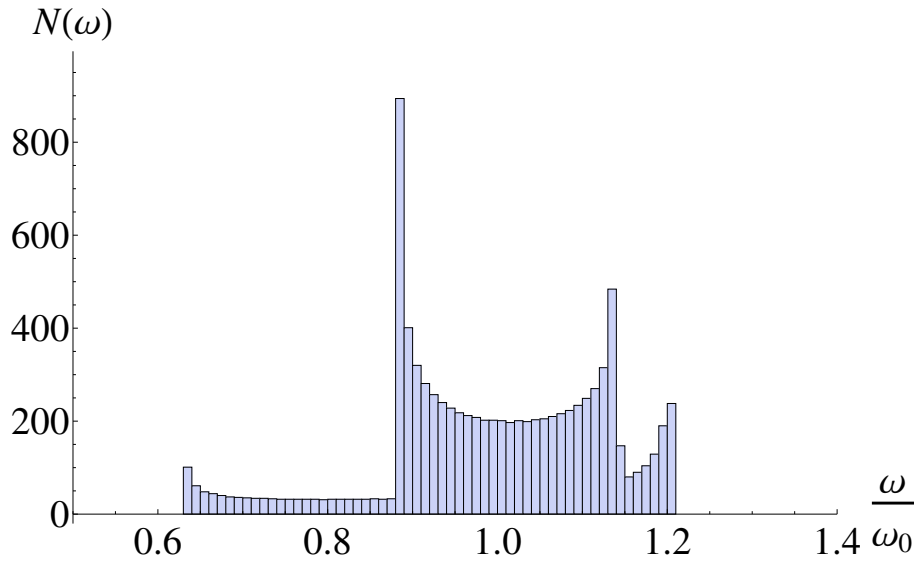


Figure 7.1: Histogram displaying the number of modes $N(\omega)$ with a frequency between $\omega \pm \frac{1}{2}\Delta\omega$, where $\Delta\omega = 0.01\omega_0$, as a function of ω , for an $L = 3000$ chain of dipoles with lattice constant $a = 2\alpha_0^{1/3}$.

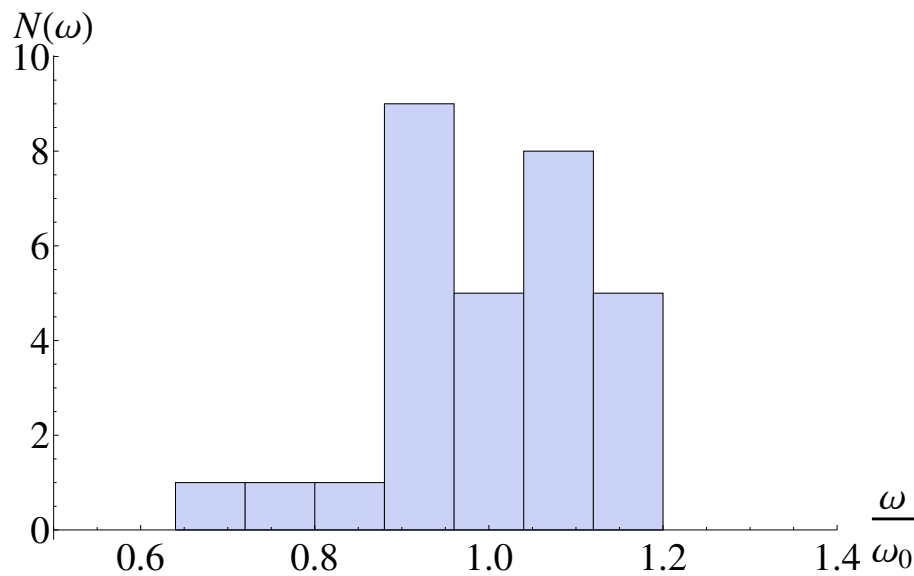


Figure 7.2: Histogram displaying the number of modes $N(\omega)$ with a frequency between $\omega \pm \frac{1}{2}\Delta\omega$, where $\Delta\omega = 0.08\omega_0$, as a function of ω , for an $L = 10$ chain of dipoles with lattice constant $a = 2\alpha_0^{1/3}$.

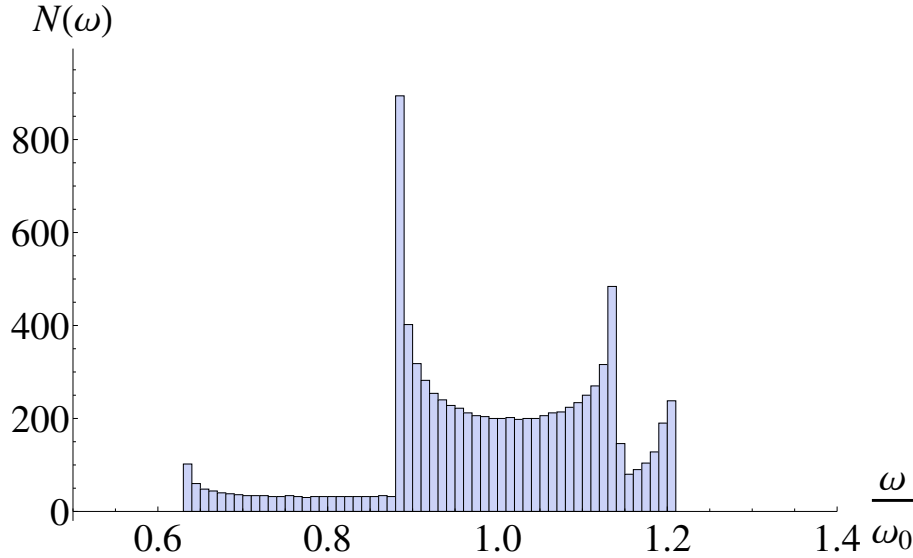


Figure 7.3: Histogram displaying the number of modes $N(\omega)$ with a frequency between $\omega \pm \frac{1}{2}\Delta\omega$, where $\Delta\omega = 0.01\omega_0$, as a function of ω , for two $L = 1500$ polymers with lattice constant $a = 2\alpha_0^{1/3}$ lying head-to-toe, separated by a distance $r/a = 50$.

histograms summed together give a $L = 3000$ histogram); for smaller distances, the two polymers simply look more and more like a single polymer with $L = 3000$ dipoles. Therefore, it is not possible to single out certain frequency ranges where much change happens as a result of moving the polymers with respect to each other and, thus, it does not seem that only a small number of modes is responsible for the change in interaction energy when the polymer is displaced. From similar calculations done for cubes, we note the same behavior: the change of shape of the histograms happens over the whole range, not only in a small subrange.

7.2.1 Theoretical Calculation for an Infinite Polymer

Because the ω -dependence of the density of states looks relatively simple (as compared to, for example, cubes, for which the density of states looks very capricious), we can try to calculate the density of states for an infinite polymer. The Hamiltonian of the system is the total energy:

$$H = \sum_i \frac{\mathbf{k}_i^2}{2m_e} + \sum_i \frac{m_e \omega_0^2 \mathbf{d}_i^2}{2} + \sum_{ij} \mathbf{d}_i \cdot \mathbf{T}_{ij} \cdot \mathbf{d}_j,$$

where \mathbf{k}_i is the momentum of the electron associated with atom i and \mathbf{d}_i is the deviation from the equilibrium position of the electron at position i . Choosing the coordinate system such that the dipole chain is directed in the x -direction, the interaction matrix \mathbf{T}_{ij} can

be written in terms of each dipole's x -position $x_i = ai$ as

$$\begin{aligned}\mathbf{T}_{ij} &= \frac{\alpha_0 m_e \omega_0^2}{2|x_i - x_j|^3} \left(\begin{pmatrix} 1 & 0 & 0 \\ 0 & 1 & 0 \\ 0 & 0 & 1 \end{pmatrix} - \frac{3}{|x_i - x_j|^2} \begin{pmatrix} (x_i - x_j)^2 & 0 & 0 \\ 0 & 0 & 0 \\ 0 & 0 & 0 \end{pmatrix} \right) \\ &= \frac{\alpha_0 m_e \omega_0^2}{2|x_i - x_j|^3} \begin{pmatrix} -2 & 0 & 0 \\ 0 & 1 & 0 \\ 0 & 0 & 1 \end{pmatrix},\end{aligned}$$

for $i \neq j$, and for $i = j$ we set

$$\mathbf{T}_{ij} = \mathbf{0}.$$

Hamilton's equations of motion are

$$\frac{\partial H}{\partial \mathbf{k}_i} = \dot{\mathbf{d}}_i, \quad \frac{\partial H}{\partial \mathbf{d}_i} = -\dot{\mathbf{k}}_i.$$

Substituting our Hamiltonian, we obtain

$$\begin{aligned}\mathbf{k}_i &= m_e \dot{\mathbf{d}}_i, \\ m_e \omega_0^2 \mathbf{d}_i + 2 \sum_j \mathbf{T}_{ij} \cdot \mathbf{d}_j &= -\dot{\mathbf{k}}_i,\end{aligned}$$

which can be combined into

$$m_e \omega_0^2 \mathbf{d}_i + 2 \sum_j \mathbf{T}_{ij} \cdot \mathbf{d}_j = -m_e \ddot{\mathbf{d}}_i.$$

We now insert a wave solution of the form

$$\mathbf{d}_i = \begin{pmatrix} u_x \exp(ik_{x,i}x_i - i\omega_{x,i}(k_{x,i})t) \\ u_y \exp(ik_{y,i}x_i - i\omega_{y,i}(k_{y,i})t) \\ u_z \exp(ik_{z,i}x_i - i\omega_{z,i}(k_{z,i})t) \end{pmatrix},$$

where $u_{x,i}$, $u_{y,i}$, and $u_{z,i}$ are the wave amplitudes, $k_{x,i}$, $k_{y,i}$, $k_{z,i}$ are the wave numbers, and $\omega_{x,i}$, $\omega_{y,i}$, and $\omega_{z,i}$ are the frequencies in each Cartesian direction, which are allowed to be different for different i . Because the matrix \mathbf{T}_{ij} is diagonal in our case, the resulting equations decouple into the dispersion relations

$$\begin{aligned}\frac{\omega_{x,i}^2(k)}{\omega_0^2} &= 1 - 2\alpha_0 \sum_{j \neq i} \frac{1}{|x_i - x_j|^3} \exp[ik(x_j - x_i)], \\ \frac{\omega_{y,i}^2(k)}{\omega_0^2} &= 1 + \alpha_0 \sum_{j \neq i} \frac{1}{|x_i - x_j|^3} \exp[ik(x_j - x_i)], \\ \frac{\omega_{z,i}^2(k)}{\omega_0^2} &= 1 + \alpha_0 \sum_{j \neq i} \frac{1}{|x_i - x_j|^3} \exp[ik(x_j - x_i)],\end{aligned}$$

where we dropped the subscript of the k 's because the equations are decoupled, such that k is only a dummy variable in each. Note that $\omega_{y,i}(k)$ and $\omega_{z,i}(k)$ have the same expression,

which makes intuitive sense because the y - and z -direction are equivalent in this problem. For further simplification, we eliminate the i -dependence by assuming periodic boundary conditions, such that each dipole is identical. Thus, we ignore boundary effects but note that they are negligible for large N : numerical calculations shows that a ring of $N = 3000$ dipoles produces almost exactly the same density of state histogram as is shown in Fig. 7.1 for a straight chain of $N = 3000$ dipoles.

We use a variable substitution $m = i - j$ in the sum, such that it takes the form

$$\begin{aligned} \sum_{j \neq i} \frac{1}{|x_i - x_j|^3} \exp(x_j - x_i) &= \sum_{m \neq 0} \frac{1}{a^3 |m|^3} \exp(ikx_{-m}) \\ &= \sum_{m \neq 0} \frac{\exp(-iakm)}{a^3 |m|^3} \\ &= \frac{2}{a^3} \sum_{m=1}^{\infty} \frac{\cos(akm)}{m^3}, \end{aligned}$$

where we used $x_m = am$. Unfortunately, the sum does not have a closed analytical form, but it *can* be expressed in so-called polylogarithmic functions, allowing for its fast numerical evaluation. We continue by defining

$$f(ak) \equiv 2 \sum_{m=1}^{\infty} \frac{\cos(akm)}{m^3},$$

such that our dispersion relations become

$$\begin{aligned} \tilde{\omega}_x(ak) &= \sqrt{1 - 2\tilde{a}^{-3}f(ak)}, \\ \tilde{\omega}_y(ak) &= \sqrt{1 + \tilde{a}^{-3}f(ak)}, \\ \tilde{\omega}_z(ak) &= \sqrt{1 + \tilde{a}^{-3}f(ak)}, \end{aligned}$$

where $\tilde{\omega}_{x,y,z} = \omega_{x,y,z}/\omega_0$ is a dimensionless frequency and $\tilde{a} = a/\alpha_0^{1/3}$ is the dimensionless lattice constant. The dispersion relations are plotted in Fig. 7.4(a). In a moment, it will become clear that the derivative of the ω 's to k is also of importance. The mathematical expressions for these derivatives are

$$\begin{aligned} \frac{\partial \tilde{\omega}_x(ak)}{\partial ak} &= -\frac{\tilde{a}^{-3}f'(ak)}{\sqrt{1 - 2\tilde{a}^{-3}f(ak)}}, \\ \frac{\partial \tilde{\omega}_y(ak)}{\partial ak} &= \frac{\tilde{a}^{-3}f'(ak)}{2\sqrt{1 + \tilde{a}^{-3}f(ak)}}, \\ \frac{\partial \tilde{\omega}_z(ak)}{\partial ak} &= \frac{\tilde{a}^{-3}f'(ak)}{2\sqrt{1 + \tilde{a}^{-3}f(ak)}}, \end{aligned}$$

with

$$f'(ak) = -2 \sum_{m=1}^{\infty} \frac{\sin(akm)}{m^2}.$$

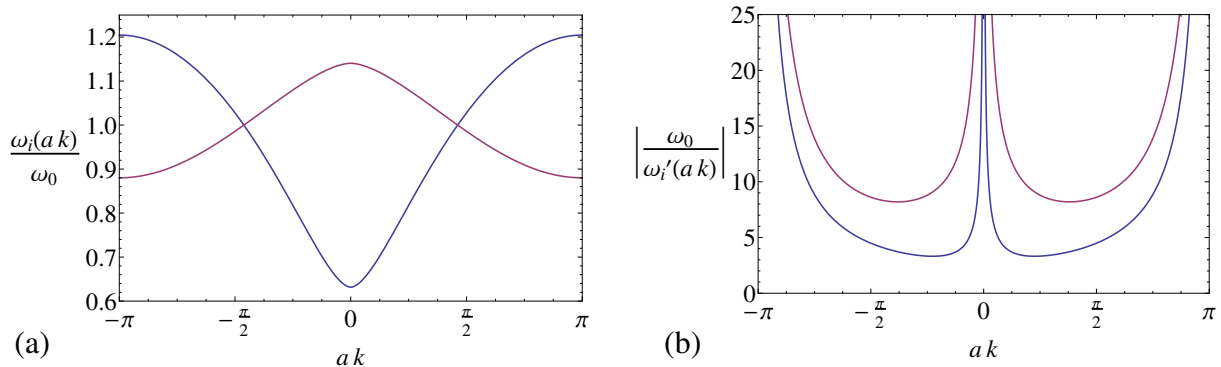


Figure 7.4: The dispersion relation $\omega_i(ak)/\omega_0$ (a), where $i = x$ (blue) or $i = y$ (red) and the absolute value of the inverse of its derivative (b) for an infinite dipole chain with lattice constant $a = 2\alpha_0^{1/3}$ and periodic boundary conditions.

We plot the absolute value of the inverse of these derivatives in Fig 7.4(b). We note that, physically, the maximum $k = \pi/\lambda$ allowed in the problem is the one where the wave length λ is minimal. It makes physical sense to choose $\lambda_{min} = a$, so $ak \in [-\pi, \pi]$.

To calculate a density of states $D(\omega)$ from the dispersion relation, we suppose that $D(\omega)$ satisfies an equation that looks like

$$D(\omega) d\omega = c(k) dk,$$

i.e., for each infinitesimal interval $d\omega$ there is an interval dk that corresponds to this interval, and the number of solutions (modes) $D(\omega) d\omega$ in the interval should be equal to the number of solutions $c(k) dk$ in the corresponding interval. It seems logical that the k inserted on the right-hand side should be the k that produces the requested ω on the left-hand side. However, this is problematic, since we see from the dispersion relations that multiple k might produce the same ω and, moreover, we have not one but three dispersion relations and each might produce the frequency that we are looking for. We therefore modify our equation to

$$D(\omega) = \sum_{i \in \{x, y, z\}} \sum_{j=1}^{N_i(\omega)} \left| \frac{\partial \omega}{\partial k} \right|_{k=k_j(\omega)}^{-1},$$

where $k_{i,j}(\omega)$ are the solutions (for k) to the equation

$$\omega_i(k) = \omega,$$

where $i \in \{x, y, z\}$ and $j \in [1, N_i(\omega)] \cap \mathbb{N}$, where $N_i(\omega)$ is the number of such solutions. Graphically, we might imagine drawing a horizontal line in Fig. 7.4(a) at the height associated with the ω that we want to calculate $D(\omega)$ for. Then, for each intersection of our horizontal line with one of the functions $\omega_i(k)$ ($i \in \{x, y, z\}$), we calculate $|\partial \omega_i / \partial k|^{-1}$ (plotted in Fig. 7.4(b)) at the intersection point. Finally, we sum each of these $|\partial \omega_i / \partial k|^{-1}$ to obtain $D(\omega)$. We see that, thus, ω 's where $|\partial \omega_i / \partial k|^{-1}$ is large (in other words, ω 's at heights where an intersecting $\omega_i(k)$ is nearly level) will get a higher $D(\omega)$. Note

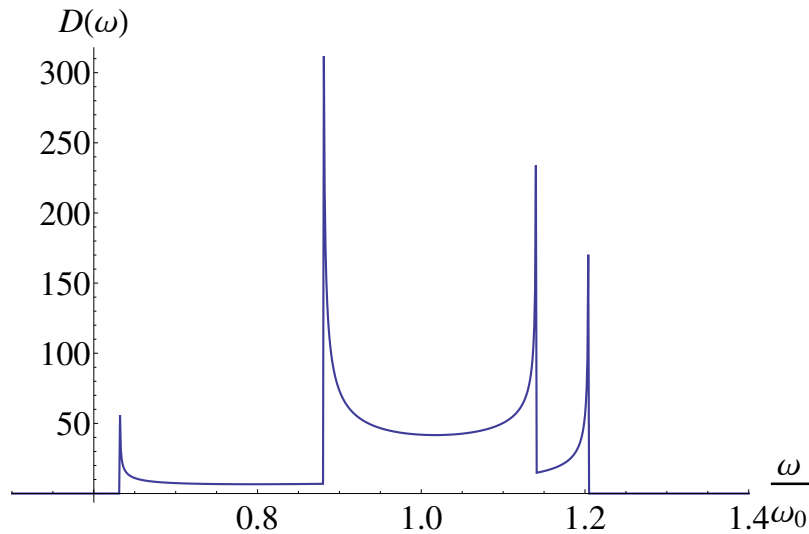


Figure 7.5: The density of states $D(\omega)$ of an infinite chain of dipoles with lattice constant $a = 2\alpha_0^{1/3}$ and periodic boundary conditions.

that we take the absolute value of $\partial\omega_i/\partial k$ because negative contributions to $D(\omega)$ seem unphysical.

The resulting $D(\omega)$ of the infinite chain is plotted in Fig. 7.5. We note that $D(\omega)$ bears a very strong qualitative resemblance to the histogram plotted in Fig. 7.1, including the low-frequency tail and the peaks at $\omega \approx 0.63\omega_0$, $\omega \approx 0.88\omega_0$, $\omega \approx 1.14\omega_0$, and $\omega \approx 1.20\omega_0$.

7.2.2 Summary and Conclusion

Creating a density of states histogram is rather straightforward for any cluster shape and, for dipole polymers, the histogram looks relatively simple. However, the original goal of finding out which frequencies, if any, are responsible for interaction between clusters was not reached: it appears that all frequencies shift as the polymers are moved with respect to each other, rather than only a select few frequencies. We proceeded with the theoretical exercise of finding a density of state function, as opposed to a histogram of numerical data. In this, it appears that we have succeeded, since the obtained function displays all the features of the numerically calculated histograms: the support of the function, the location of the resonances, and the relative height in the ranges in-between are all correct. We note that we also know, mathematically, why these resonances happen: because $\omega(ak)$ is level at those frequencies. Interpreting $\partial\omega/\partial k$ as the propagation speed (group velocity) of our wave solution, it thus seems that resonances occur for standing waves, which seems physically reasonable.

7.3 Modes in Interacting Square Plates

In this section, we will investigate the behavior of vibrational modes in two interacting 20×20 squares of dipoles. This study was inspired by a 1968 publication by Van Kampen

et al. [120], in which the Van der Waals force between two half-spaces separated by a gap is calculated by considering only vibrational surface solutions of the Poisson equation, i.e., the bulk modes are disregarded as they are independent of the gap. If only surface modes contribute to the interaction energy, this could possibly lead to a quicker algorithm for calculating Van der Waals forces within the CDM, since not all eigenvalues would need to be calculated. In this section, we will visualize the evolution of the vibrational modes as a function of the distance between two clusters of atoms. We will not consider half-spaces (because their infinite size makes them impossible to study numerically using the CDM), nor will we consider three-dimensional clusters (because the modes become hard to visualize in that case). Instead, we will restrict ourselves to the relatively simple case of two 2-dimensional clusters, namely two 20×20 square lattices of 400 Lorentz atoms each (so that the total number of dipoles $N = 800$). The lattice constant of these square lattices is given by $\tilde{a} = a/\alpha_0^{1/3} = 2$, where a is the lattice constant in ordinary units and $\alpha_0^{1/3}$ is the atomic polarizability. As usual, we denote the characteristic frequency of the Lorentz atoms by ω_0 . Starting with the two squares touching (such that they effectively form a 40×20 square lattice), we slowly move one away from the other and study the evolution of individual modes.

7.3.1 Methods

To compute the modes for a given setup, our computer algorithm needs to be modified only slightly. Whereas, before, we were only interested in the eigenvalues of the $(\mathcal{I} - \alpha_0\mathcal{T})$ matrix, we now require the program to also output the corresponding eigenvectors. These eigenvectors represent the amplitude of the oscillation of each dipole in the mode of interest and, by plotting the amplitudes of a given mode in 2D, we can study the spatial properties of an eigenvector, e.g., we can see whether the eigenvector represents vibrations of all the dipoles or of only a small subset of dipoles. The only problem here is that the collection of these eigenvectors ($3N = 2400$ vectors of $3N = 2400$ values each) for the various distances considered can take up significant storage space, so using a simple data compression algorithm is advisable, but apart from this detail, computing modes is relatively straightforward.

The most significant problem comes after the calculation and is posed by tracking the modes as a function of distance. By default, the computed modes are ordered according to the magnitude of their eigenvalues. Since these eigenvalues change as a function of distance, the order of the modes changes and tracking a single mode through each successive step in distance becomes a nontrivial task. The solution to this problem is to take very small steps in distance and, for each step, identify modes that bear the largest resemblance to each other. In mathematical terms, if a certain setup characterized by a distance d outputs a collection of eigenvectors (modes) $\{\mathcal{U}_1, \mathcal{U}_2, \dots, \mathcal{U}_{2400}\}$ and the successive setup with distance $d + \Delta d$ (with Δd sufficiently small) outputs the collection $\{\mathcal{V}_1, \mathcal{V}_2, \dots, \mathcal{V}_{2400}\}$, we could calculate the square distance between each pair of these $3N$ -dimensional vectors, $(\mathcal{U}_i - \mathcal{V}_j)^2$ for each i and j , and identify each \mathcal{U}_i with the \mathcal{V}_j for which this square distance is smallest. Since the eigenvectors are normalized, however, this boils down to calculating their inner products $\mathcal{U}_i \cdot \mathcal{V}_j$ and identifying vector pairs with the largest inner product. In practice, the inner product indeed turns out to be a very good measure for the cor-

relation between two vectors. On the other hand, calculating all the inner products by using ordinary computer algorithms turns out to be a lengthy process, but one that can be sped up tremendously by using the parallel capabilities of a graphics card. In terms of matrices build up from the eigenvectors, the matrix product

$$\begin{pmatrix} - & \mathcal{V}_1 & - \\ - & \mathcal{V}_2 & - \\ & \vdots & \\ - & \mathcal{V}_{2400} & - \end{pmatrix} \begin{pmatrix} | & | & \dots & | \\ \mathcal{U}_1 & \mathcal{U}_2 & \dots & \mathcal{U}_{2400} \\ | & | & \dots & | \end{pmatrix}$$

produces a matrix with all the inner products. Since graphics cards excel at multiplying matrices, this problem is ideal for graphics card calculations, which we therefore used to infer all the correlations.

The results of these calculations can be visualized by plotting, in a movie, the spatial configuration of each mode as a function of distance as well as the frequency associated with the mode and the variance of the square norm of the polarization of each dipole,

$$\sigma_{\mathbf{d}^2}^2 = \frac{1}{N} \sum_{i=1}^N (\mathbf{d}_i^2 - \mu_{\mathbf{d}^2})^2,$$

with

$$\mu_{\mathbf{d}^2} = \frac{1}{N} \sum_{i=1}^N \mathbf{d}_i^2 = \frac{1}{800},$$

and where the last equality follows because the eigenvector that contains the \mathbf{d}_i is normalized and $N = 800$. The quantity $\sigma_{\mathbf{d}^2}^2$ can be expected to be a measure for the degree to which the mode is localized.

7.3.2 Results

The number of output modes is 2400. This is a huge number to study, so we will restrict ourselves to some examples that, in our view, reflect some interesting physics. Furthermore, exactly one third of the modes vibrates in the direction orthogonal to the plates. We will disregard these modes and only focus on the in-plane vibrations.

First of all, let us investigate the frequencies of all the modes collectively. Since it is infeasible to plot 2400 frequencies as a function of distance, we only plot, in Fig. 7.6, the difference $\Delta\omega$ between the maximum and minimum frequency associated with a mode over the distances considered, as a function of the value of this frequency ω at contact. Clearly, there is no specific frequency band for which there is more variation than for other bands. Furthermore, the number of frequencies for which no, or very little, variation occurs at all seems to be low compared to the number of frequencies that do change significantly.

The most obvious mode to study first would be the one that changes most, which is located (when the plates are touching) at $\omega \approx 1.099\omega_0$. Snapshots of this mode for various distances are displayed in Fig. 7.7. One property that immediately catches our attention is that the frequency of this mode decreases as a function of distance r_x . Since the energy associated with a mode is simply $\hbar\omega_k$, this means that this mode actually contributes a

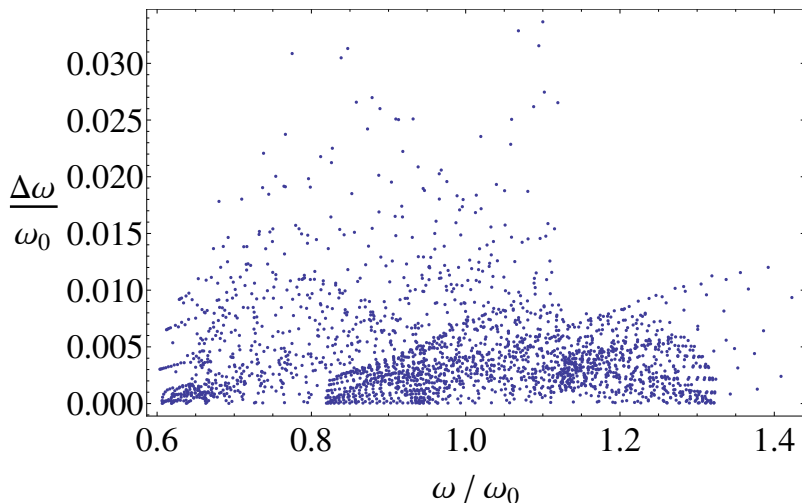


Figure 7.6: The difference $\Delta\omega/\omega_0$ between the maximum and minimum frequency achieved by each normal mode in a system of two interacting parallel-oriented 20×20 squares of coupled Lorentz atoms, with center-to-center distances between the squares in the range $20 \leq r_x/a \lesssim 26.3155$. Here, ω_0 is the characteristic frequency of the atoms, a is the lattice constant of the square lattices, and $\Delta\omega/\omega_0$ is plotted as a function of the value of the mode’s initial frequency ω/ω_0 .

repelling force to the total force (which is attractive). The mode starts out nonlocalized. This means that part of the mode is at the surface, which explains the mild change in frequency at small distances. At $r_x/a \approx 20.09$, the mode transforms into a surface mode, with virtually all of its amplitude near the facing edges of the squares. This lasts until $r_x/a \approx 20.34$, when the mode abruptly collapses back into a nonlocal mode, which does not change significantly afterwards. We note that the plotted variance seems to do well when it comes to describing the localization of the mode.

In Fig. 7.8, we plot the strongest attractive mode (where by “attractive” we mean that its frequency change is positive, and by “strongest” we mean that its frequency change is largest), located at contact at $\omega \approx 0.847\omega_0$. This mode starts out much the same as the mode that we discussed above, a nonlocal mode with a significant contribution at the facing square edges and a nonlevel ω , although in this case the dependence is stronger and results in a change in ω of about $0.007\omega_0$, which is already above what most modes achieve (see Fig. 7.6). At $r_x/a \approx 20.32$, the mode undergoes a transformation, first displaying two vertical “bands” across each square (not shown), and then, around $r_x/a \approx 20.377$, transforming into a surface mode (in this frame, the vertical bands are still vaguely visible), which becomes very localized after this frame (not shown). However, from around $r_x/a \approx 20.57$, the vibrations near edges other than the ones near the gap become stronger, to the point were, near $r_x/a \approx 20.92$, the mode seems to be more localized near the edges that do not face than near the edges that do face the gap. After this frame, the mode develops a bulk component again, and does not change significantly afterwards.

Not all modes that develop into surface modes do so only once in the studied distance interval. In Fig. 7.9, we show an example of a mode (initially located at $\omega \approx 0.803\omega_0$)

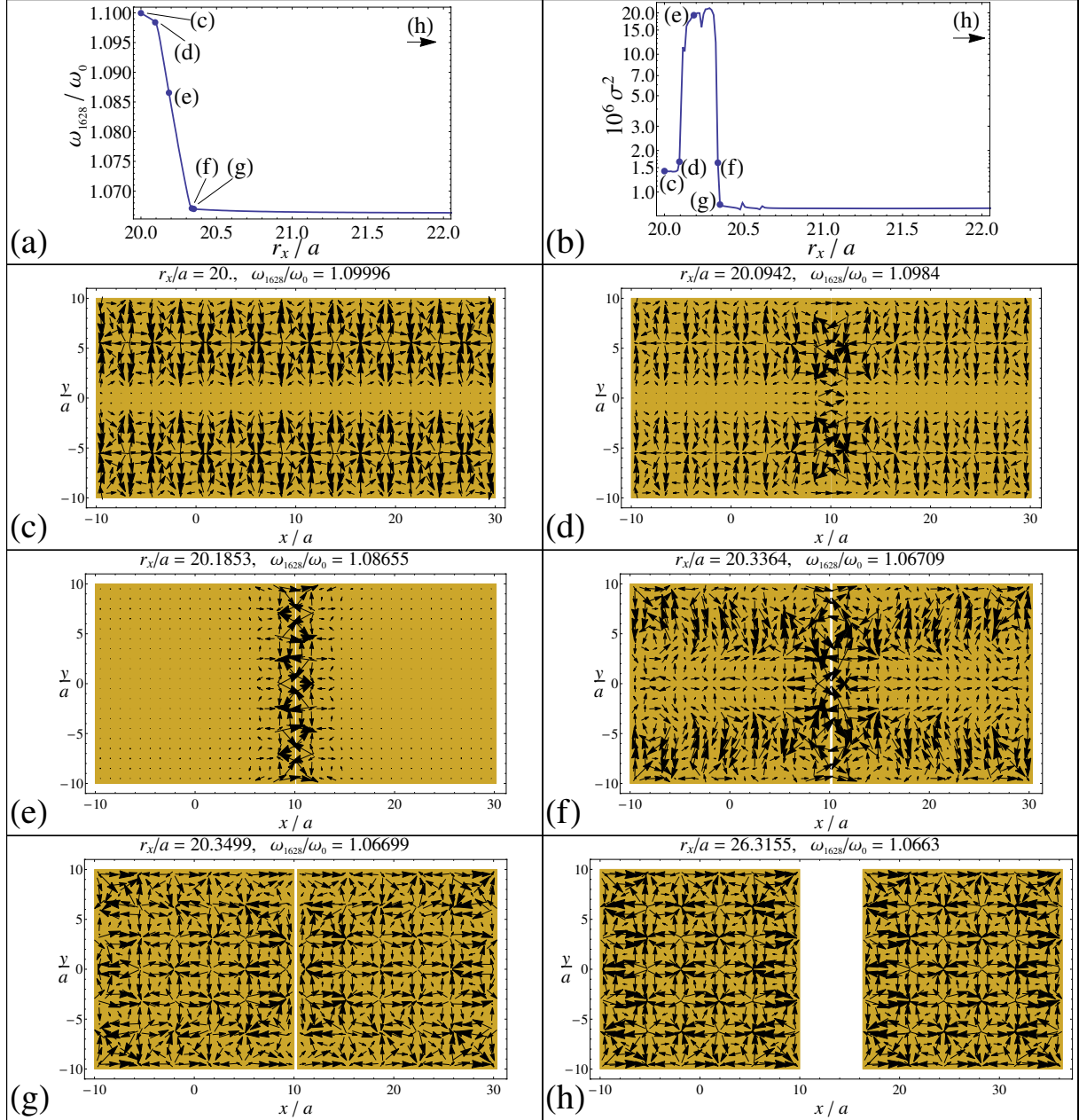


Figure 7.7: Snapshots of the normal mode identified by index $i = 1628$ (frequency at contact: $\omega/\omega_0 \approx 1.09996$). (a, b): The dependence of this mode's frequency ω_{1628}/ω_0 (a) and the variance σ^2 of the square norm of each dipole's amplitude (b) on the distance r_x/a between the squares, with labels (c)-(h) referring to the snapshots given in panels (c) through (h). (c-h): snapshots of the amplitudes of each dipole for various distances r_x/a , plotted as black vector arrows, with larger arrows indicating a larger (relative) magnitude of the amplitude. The vectors are placed at the locations of the dipole with which they are associated while, in yellow, an outline of the squares comprising the dipoles is given.

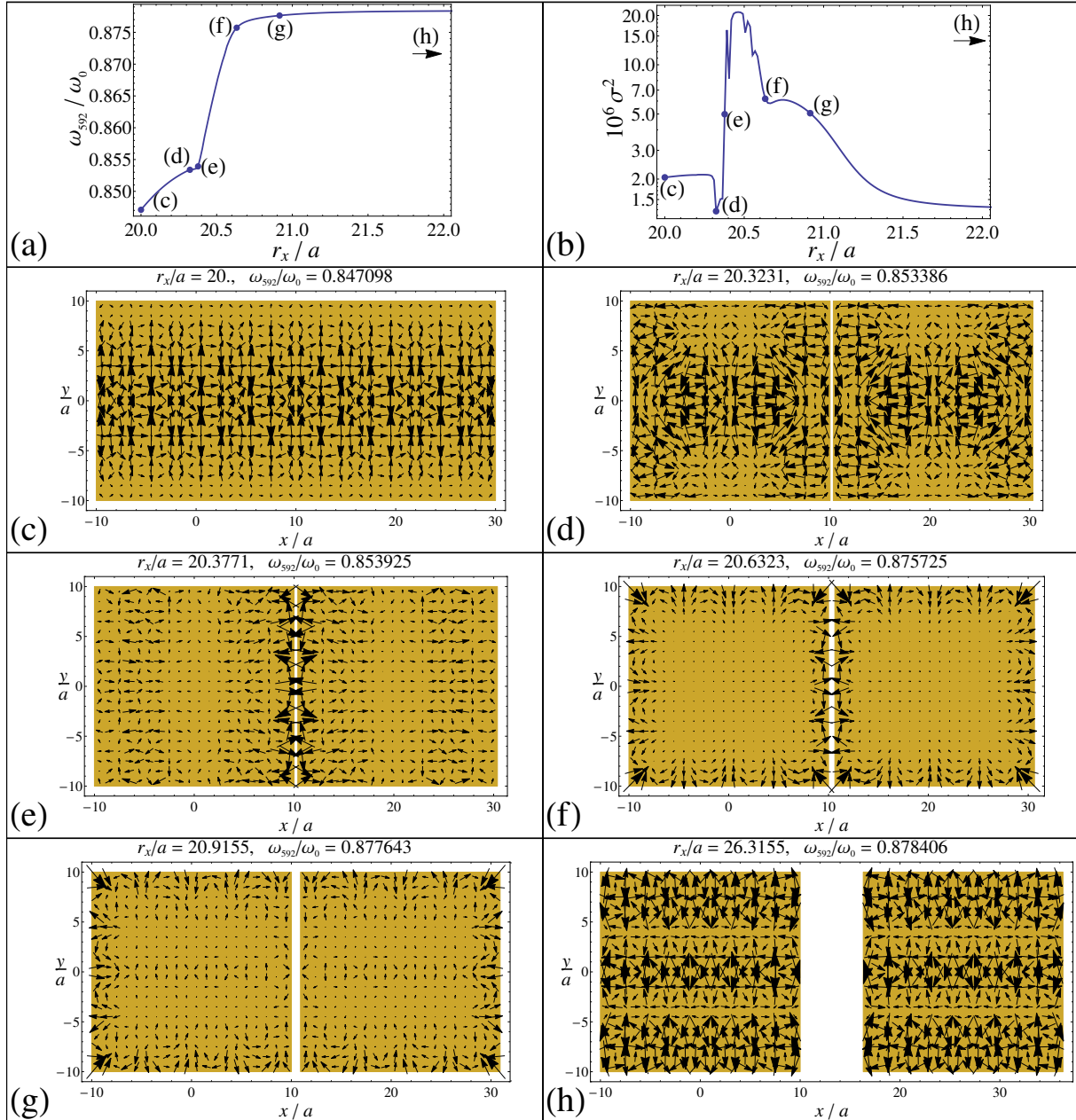


Figure 7.8: Snapshots of the normal mode identified by index $i = 592$ (frequency at contact: $\omega/\omega_0 \approx 0.847098$). (a, b): The dependence of this mode's frequency ω_{592}/ω_0 (a) and the variance σ^2 of the square norm of each dipole's amplitude (b) on the distance r_x/a between the squares, with labels (c)-(h) referring to the snapshots given in panels (c) through (h). (c-h): snapshots of the amplitudes of each dipole for various distances r_x/a , plotted as black vector arrows, with larger arrows indicating a larger (relative) magnitude of the amplitude. The vectors are placed at the locations of the dipole with which they are associated while, in yellow, an outline of the squares comprising the dipoles is given.

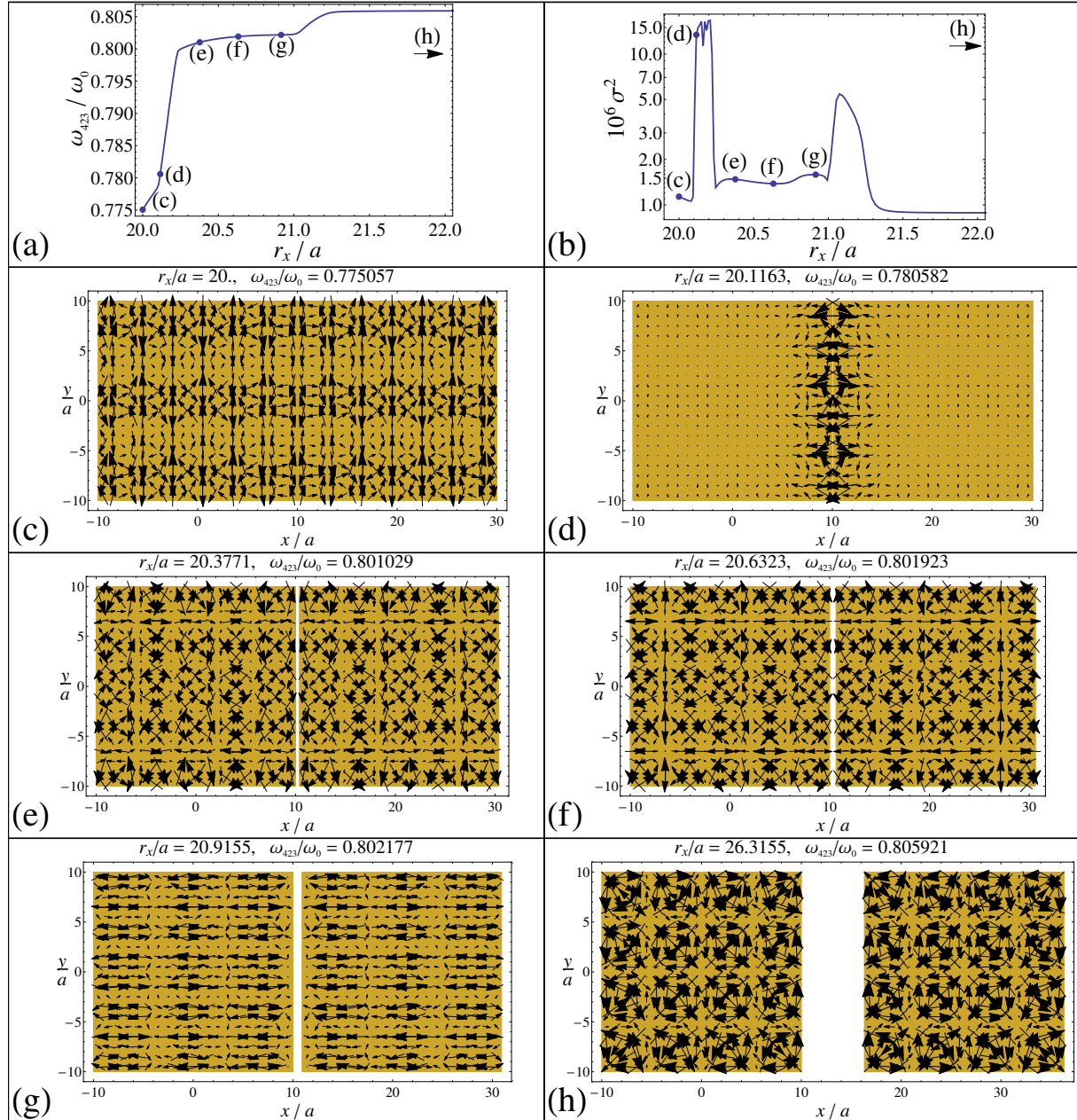


Figure 7.9: Snapshots of the normal mode identified by index $i = 423$ (frequency at contact: $\omega/\omega_0 \approx 0.775057$). (a, b): The dependence of this mode's frequency ω_{423}/ω_0 (a) and the variance σ^2 of the square norm of each dipole's amplitude (b) on the distance r_x/a between the squares, with labels (c)-(h) referring to the snapshots given in panels (c) through (h). (c-h): snapshots of the amplitudes of each dipole for various distances r_x/a , plotted as black vector arrows, with larger arrows indicating a larger (relative) magnitude of the amplitude. The vectors are placed at the locations of the dipole with which they are associated while, in yellow, an outline of the squares comprising the dipoles is given.

that becomes a surface mode twice. The mode starts out much the same as the previous two modes studied, but with a rather steep ω -dependence. It soon develops into a surface mode at around $r_x/a \approx 20.105$ (shown is the fully developed surface mode at a somewhat longer distance), which collapses at around $r_x/a \approx 20.234$; the mode shape that ensues is shown. This gradually changes, around $r_x/a \approx 20.786$, from a vibration in many directions to a mainly horizontal vibration. Then, at $r_x/a \approx 21.075$, the mode abruptly becomes a surface mode for the second time, although it seems somewhat less localized than the first time. The mode then gradually decays into the bulk mode shown in the last frame.

Not all modes that develop into surface modes near the gap do so at small r_x/a . Shown in Fig. 7.10 is the mode that starts out at $\omega \approx 1.050\omega_0$ as a bulk mode across both squares, which results in a strong component near the gap. Almost as soon as the squares become separated, however, the mode splits into two and the surface component vanishes. At around $r_x/a \approx 20.42$, the mode transforms into a surface mode concentrated not near the gap but on the lower and upper edges of the squares. This lasts until $r_x/a \approx 20.54$ and is accompanied by a strong dependence of ω on distance. Then follows a region where the mode is a bulk mode again, with almost level ω , until around $r_x/a \approx 21.41$, where it finally becomes a surface mode concentrated near the gap. This subsequently very gradually transforms into the mode shown in the last frame: a mode concentrated at all of the edges of both squares. Thus, we see that modes can also become surface modes in the long-range limit. Note that for this mode, ω and $\sigma_{\mathbf{d}^2}^2$ are plotted over a longer distance range.

7.3.3 Summary and Conclusion

We have succeeded in tracking the modes as a function of the distance between the squares. Plotting the change of frequency of each mode as a function of the mode's starting frequency did not result in any identifiable pattern by which it could be predicted which modes will change their frequency the most. We then proceeded to plot the amplitudes of several in-plane modes as a function of the distance between the squares. From snapshots of the resulting movies, it is clear that modes that have a surface component near the gap between the squares contribute most to the change in energy when the squares are moved. However, it was found that most modes are surface modes only temporarily, which seemingly makes it impossible to predict which modes will be important for the interaction energy. The situation is complicated further by the fact that the contributions to the interaction energy of some modes are opposite in sign to those of other modes. We have seen that the variance of the square amplitude of each dipole is a good measure of the degree of localization of the mode, but it does not provide information regarding whether or not the localization is near the gap between the squares, and a more specialized parameter would be appropriate. Such a parameter would also help to objectively quantify whether a mode is a "gap-surface" mode because, in this section, we have judged this mostly by eye. We note also that, in this section, we have ignored modes that vibrate in the direction perpendicular to the squares, which should be rectified in future study, because these modes make up a third of all the modes. Further directions for future study would be to link the results in this section to those in Sec. 7.2, perhaps deriving a density

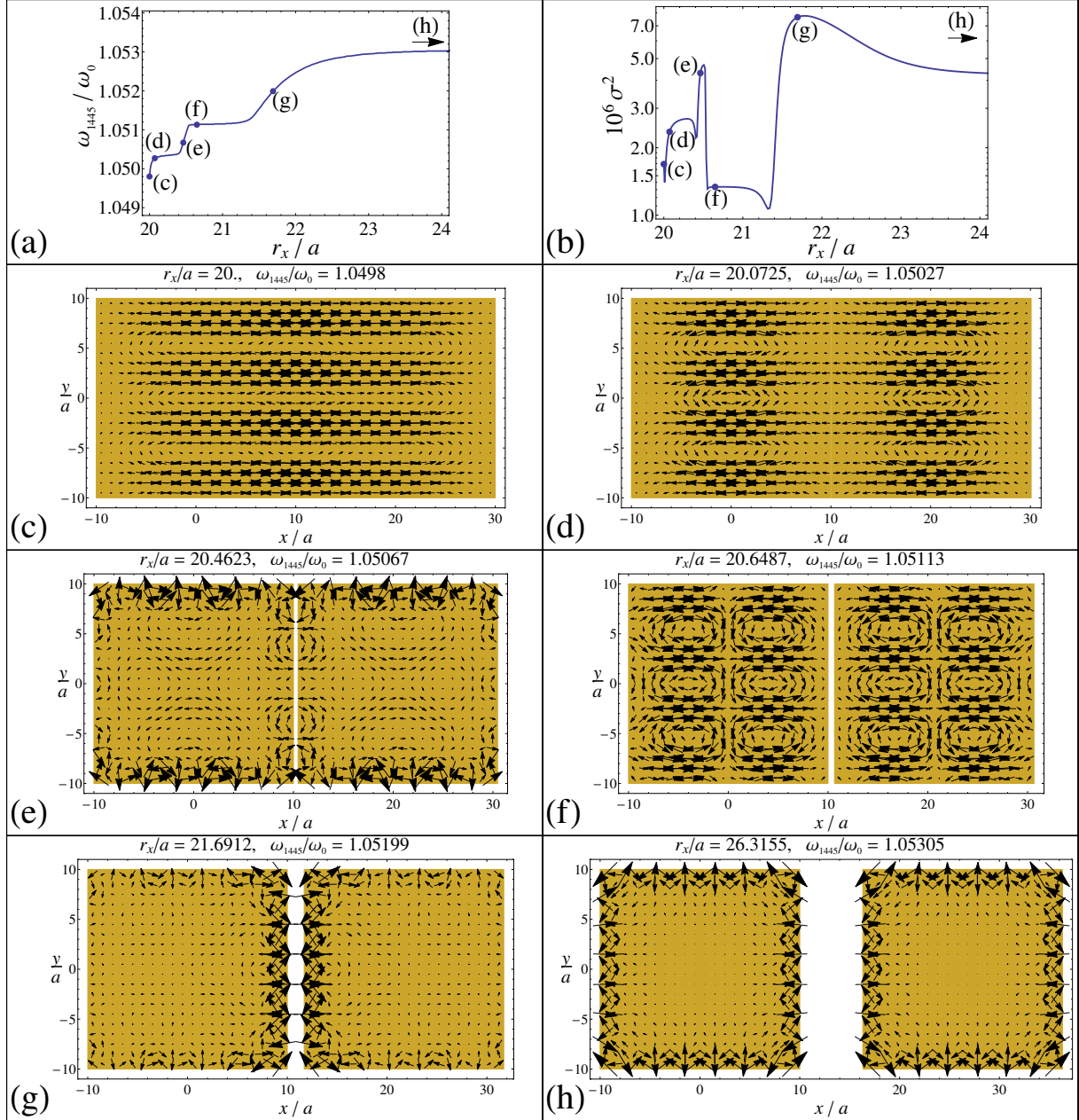


Figure 7.10: Snapshots of the normal mode identified by index $i = 1445$ (frequency at contact: $\omega/\omega_0 \approx 1.04980$). (a, b): The dependence of this mode's frequency ω_{1445}/ω_0 (a) and the variance σ^2 of the square norm of each dipole's amplitude (b) on the distance r_x/a between the squares, with labels (c)-(h) referring to the snapshots given in panels (c) through (h). (c-h): snapshots of the amplitudes of each dipole for various distances r_x/a , plotted as black vector arrows, with larger arrows indicating a larger (relative) magnitude of the amplitude. The vectors are placed at the locations of the dipole with which they are associated while, in yellow, an outline of the squares comprising the dipoles is given.

of states function for infinite squares or investigating the amplitudes of the modes of the polymers in a similar fashion as in this section.

7.4 Coupled Dipoles near a Conducting Plate

In this section, we discuss what happens when dielectric particles are placed near a conducting plate and an electric field is applied. In particular, we will investigate the potential energy of rods in such a setup as a function of the location and orientation of the rod.

7.4.1 Theory

The method of image charges is a useful application of the uniqueness theorem of electrostatics, which states that a volume containing a given charge distribution and a given set of boundary conditions will have a uniquely defined electric field inside it. This means that even if two systems are different outside a certain volume of interest, if the boundary conditions on the surface of the volume and the charge distribution inside the volume are the same, so will the electric field inside the volume be. Thus, if we encounter an electrostatic problem that seems difficult to solve, it is sometimes possible to instead solve a different, simpler problem that has the same boundary conditions and in this way find the solution to the more difficult problem as well.

The most well-known example of the method of image charges is the one where we are asked to calculate the force on a point charge q a distance d from a conducting half-space at zero potential. This problem may at first seem hard to solve: since the field inside a conductor is zero, the conducting plate will accumulate a charge distribution at its surface to exactly compensate for the electric field due to the charge q and this charge distribution will subsequently exert a force on the point charge. We can solve this problem by looking at a different setup. In a system where we have a charge q and a charge $-q$ separated by a distance $2r$, the plane in the middle (i.e., a distance r from both charges) will have zero potential. Thus, in these two problems, the half-space that contains the charge q has the same charge distribution (a single point charge q) and boundary condition (zero potential at its edge), hence the electric field in the half-space that contains q is the same in both problems. Thus, the force on the charge q in both problems would be $-q^2/4r^2$ (in CGS). Note that the solutions in the *other* half-space, i.e., the one that in the original problem contains the conductor and in the simplified problem contains charge $-q$, will *not* be the same.

It is not hard to see that we can apply the method of image charges to any charge distribution near a planar conductor. By placing image charges with opposite sign and a mirrored position on the “conductor side” of the dividing plane, we can always ensure that the potential on the surface of the half-space of interest is zero. By picturing electric dipoles as a pair of charges of opposite sign a certain distance apart, we can also work out what an image dipole should look like; explicitly, if the surface of the conductor is in the x - y plane and we have a point dipole \mathbf{d} at location \mathbf{r} , the image dipole should have a

dipole moment \mathbf{d}' and location \mathbf{r}' given by

$$\mathbf{d}' = \begin{pmatrix} -1 & 0 & 0 \\ 0 & -1 & 0 \\ 0 & 0 & 1 \end{pmatrix} \mathbf{d}, \quad \mathbf{r}' = \begin{pmatrix} 1 & 0 & 0 \\ 0 & 1 & 0 \\ 0 & 0 & -1 \end{pmatrix} \mathbf{r}. \quad (7.1)$$

We now proceed to incorporate image charges in the CDM. Given a set of N inducible dipoles indexed by $i = 1, 2, \dots, N$, we include a set of corresponding image dipoles indexed by $i = -1, -2, \dots, -N$, such that each dipole \mathbf{d}_i located at \mathbf{r}_i has an image dipole \mathbf{d}_{-i} located at \mathbf{r}_{-i} . The “real” dipoles still follow the relation $\mathbf{d}_i = \alpha_0 \mathbf{E}_i$, where \mathbf{E}_i is the local electric field at \mathbf{r}_i , whereas the image dipoles gain a dipole moment not due to any external electric field: instead, their dipole moments are supposed to follow from \mathbf{d}_i by Eq. (7.1). For positive i , we now have that the electric field at site i is given by the external electric field plus the contributions from the real as well as the image dipoles:

$$\mathbf{E}_i = \mathbf{E}_0 + \sum_{j=-N}^N \mathbf{T}_{ij} \cdot \mathbf{d}_j \quad (i > 0),$$

where \mathbf{T}_{ij} is the dipole-dipole tensor if $i \neq j$, and $\mathbf{T}_{ii} = \mathbf{0}$. We now plug in the proportionality of \mathbf{d}_i with \mathbf{E}_i and rearrange the terms,

$$\mathbf{d}_i - \alpha_0 \sum_{j=-N}^N \mathbf{T}_{ij} \cdot \mathbf{d}_j = \alpha_0 \mathbf{E}_0 \quad (i > 0),$$

and then eliminate the part of the sum that runs over negative indices:

$$\mathbf{d}_i - \alpha_0 \sum_{j=1}^N \mathbf{S}_{ij} \cdot \mathbf{d}_j = \alpha_0 \mathbf{E}_0 \quad (i > 0), \quad (7.2)$$

where

$$\mathbf{S}_{ij} \equiv \left[\mathbf{T}_{ij} + \mathbf{T}_{i,-j} \begin{pmatrix} -1 & 0 & 0 \\ 0 & -1 & 0 \\ 0 & 0 & 1 \end{pmatrix} \right]. \quad (7.3)$$

Eq. (7.2) can be solved in exactly the same manner as done in previous chapters, with the only difference that the 3×3 interaction matrices are somewhat modified. Once the collection of \mathbf{d}_i is found, the potential energy of the system follows easily by

$$U_E = -\frac{1}{2} \sum_{i=1}^N \mathbf{d}_i \cdot \mathbf{E}_0,$$

where we take note not to sum over negative indices, since the image dipoles do not experience an electric field (and are, furthermore, not actually physically “real” objects).

7.4.2 Results and Discussion

A simple example system is one where an inducible dipole with polarizability α_0 is a distance r away from a conducting half-space, and an electric field of strength E_0 is

applied in the direction perpendicular to the surface of the half-space, here defined as the z -direction. The interaction energy of this problem can be found analytically. \mathbf{S}_{ij} [as defined in Eq. (7.3)] has to be calculated only for $i = j = 1$, meaning that its first term vanishes; the remaining term gives

$$\mathbf{S}_{11} = \frac{\alpha_0}{8r^3} \begin{pmatrix} 1 & 0 & 0 \\ 0 & 1 & 0 \\ 0 & 0 & 2 \end{pmatrix}.$$

Inverting $\mathbf{I} - \mathbf{S}_{11}$ and multiplying by $\alpha_0 E_0 \hat{z}$ gives

$$\mathbf{p}_1 = \frac{\alpha_0 E_0}{1 - \alpha_0/4r^3} \hat{z}.$$

Taking the dot product with $-\frac{1}{2}E_0\hat{z}$ gives us U_E , from which we subtract $U_E(r \rightarrow \infty) = -\frac{1}{2}\alpha_0 E_0^2$ to gain the interaction energy

$$V_E = -\frac{1}{2} \frac{\alpha_0 E_0^2}{4\tilde{r}^3 - 1},$$

where $\tilde{r} = r/\alpha_0^{1/3}$ is a dimensionless distance. We plot $V_E / (\frac{1}{2}\alpha_0 E_0^2)$ in Fig 7.11. For long distances, the interaction energy goes as

$$V_E \simeq -\frac{1}{8} \frac{\alpha_0 E_0^2}{\tilde{r}^3} \quad (\tilde{r} \gg 1),$$

while at short distances, the interaction is enhanced by the -1 term in the numerator. At distances $\tilde{r}^3 \leq 1/4$ ($r/\alpha_0^{1/3} \lesssim 0.63$), the system undergoes a polarization catastrophe and the result is no longer valid.

Motivated by recent (unpublished) experiments [121], we now turn our attention to rods, which we model as strings of Lorentz atoms. We will discuss here the example of a single rod of length $3.3 \mu\text{m}$ and width $0.55 \mu\text{m}$, which we model as a string of 6 inducible dipoles, spaced a distance of $a_0 = 0.55 \mu\text{m}$ apart. Each inducible dipole is given a polarizability of $0.030 \mu\text{m}^3$, which results in the rod having a longitudinal polarizability of $0.62 \mu\text{m}^3$ and a transverse polarizability of $0.135 \mu\text{m}^3$. We then place the tip of the rod a distance r from the x - y plane and orient it such that it makes an angle θ with the z -axis. The setup is depicted in Fig. 7.12, from which it can be seen that the smallest allowed distance between the tip dipole and the plate is $a_0/2$, such that we define a gap length $h = r - a_0/2$, which vanishes if the rod is touching the plate. From the figure, we also see that the maximum allowed θ is $\pi/2$. We apply an electric field of $E_0 = 300 \text{ V/mm}$ in the z -direction and calculate the potential energy of the rod. We then subtract the energy that the rod would have if it were an infinite distance away from the plate and oriented in the direction of the electric field ($\theta = 0$) to gain the interaction energy of the rod with the plate. The result is plotted in Fig. 7.13 for several gap sizes h as a function of θ .

Clearly, the situation where the rod is pointing in the \hat{z} -direction is the most favorable and, furthermore, the rod feels an attraction to the plate because a lower distance results in a lower potential energy. For small distances, however, we also observe a local minimum

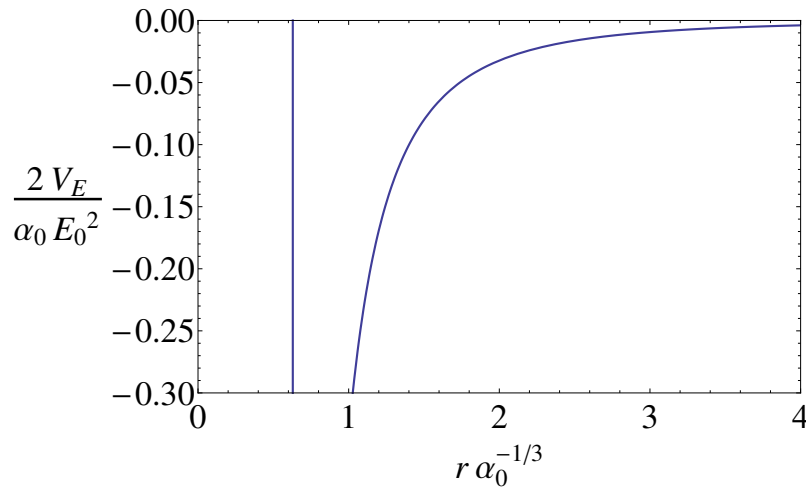


Figure 7.11: The interaction energy $V_E / \left(\frac{1}{2}\alpha_0 E_0^2\right)$ of an inducible dipole with polarizability α_0 with a conducting half-space at zero potential, as a function of the dimensionless distance $r\alpha_0^{-1/3}$ between the dipole and the half-space, in the presence of an external electric field of magnitude E_0 pointing perpendicular to the half-space.

at $\theta = \pi/2$, where the rod is oriented in the x - y plane. For the chosen parameters, this local minimum at contact is about $30k_B T$ deep, such that a rod, once caught in this situation, can lie flat on the conducting plate almost indefinitely. Moreover, starting from a sample of more or less randomly oriented rods and no electric field, one expects any rod touching the plate and oriented such that $\theta \gtrsim 0.476\pi$ to be pulled into the lying-down position once the electric field is turned on, the mentioned value being the maximum of the $h = 0$ graph of Fig. 7.13. The height of the graph depends quadratically on the electric field strength, such that higher field strengths create deeper potential minima and barriers, while lower field strengths make them more shallow, meaning that stronger electric fields will be better able to retain rods in the local potential minimum, where they are lying down. The local minimum at $\theta = \pi/2$ quickly becomes less shallow if the gap length is increased, being already mostly negligible at $h = 0.33 \mu\text{m}$. Simultaneously, the maximum shifts to higher θ with increasing gap lengths, suggesting that a smaller percentage of rods will be trapped in the local minimum even for arbitrarily high electric fields. However, since the gap lengths are smaller than the rod length, it can be expected that, when the electric field is turned on, the motion of the rod towards the plate and a resulting shift of the local maximum to smaller θ will play a significant role. For instance, a rod starting at $h = 0.165 \mu\text{m}$ and $\theta = 0.48\pi$ starts out with an angle smaller than the angle at which the maximum occurs for the given gap length, meaning that, if its distance to the plate does not change, it is most likely to eventually end up in the global minimum at $\theta = 0$. However, if the rod moves towards the plate much quicker than it orients itself along the field, it may end up touching the plate before rotating significantly and fall into the $\theta = \pi/2$ minimum after all.

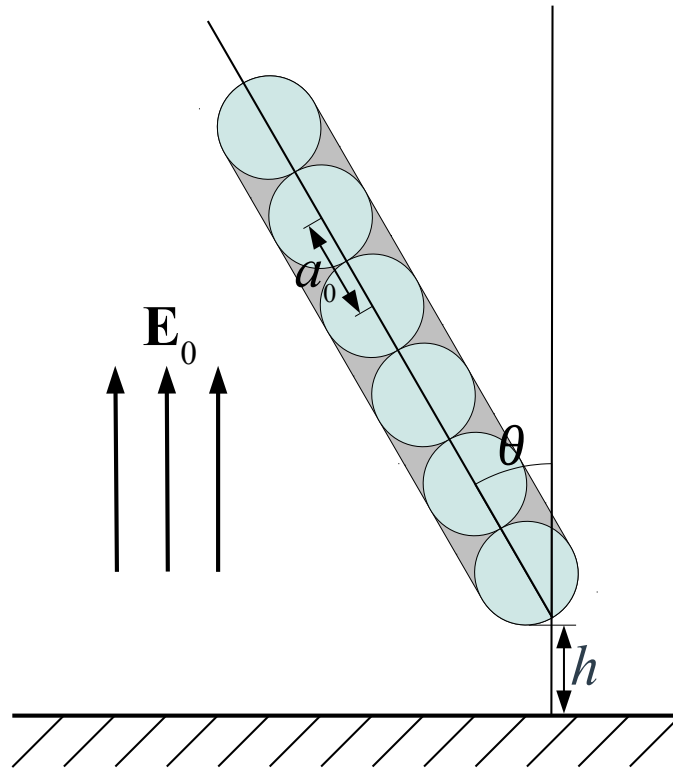


Figure 7.12: Depiction of the setup for which the electrostatic interaction energy is calculated and plotted in Fig. 7.13. A “rod”, consisting of a chain of six inducible point dipoles a distance a_0 away from each other, is positioned near a conducting half-space at zero potential, while an electric field \mathbf{E}_0 is applied normal to the surface of the half-space. The rod’s position and orientation are defined by the distance h between its tip and the surface of the conducting half-space and the angle θ between the director of the rod and the line normal to the surface of the half-space.

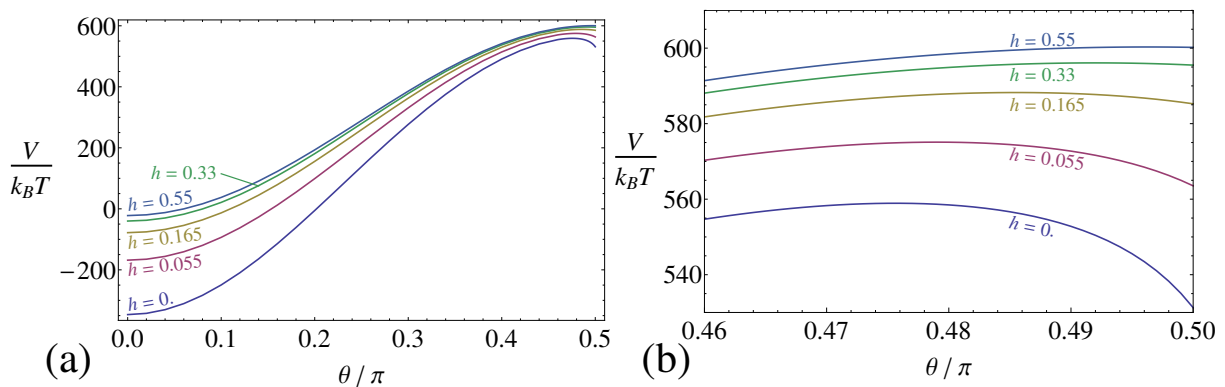


Figure 7.13: (a): Interaction energy between the rod depicted in Fig. 7.12 and the conducting half-space, with an applied electric field strength of $E_0 = 300 \text{ V/mm}$ at room temperature, as a function of the angle θ between the rod director and the line normal to the surface of the half-space, for gap lengths $h = 0 \mu\text{m}$, $0.055 \mu\text{m}$, $0.165 \mu\text{m}$, $0.33 \mu\text{m}$, and $0.55 \mu\text{m}$. (b): A close-up of the local minimum observed at high θ (i.e., rods lying flat on the surface of the conductor).

7.4.3 Summary and Conclusion

We have seen that the CDM can be rather straightforwardly extended to include image dipole interaction. We have derived an analytical expression for the interaction of a single induced dipole with its image. We then proceeded to investigate the case of rods near a conducting surface and concluded that, when an electric field is applied, rods experience a local minimum near the orientation where they lie down flat on the surface. This minimum becomes more shallow if the distance between the rod and the plate is increased, and if the electric field is reduced. We note that the setup we investigated was rather specific, such that, for future study, it would be interesting to investigate other cluster shapes and polarizabilities. Furthermore, we studied only a single particle: it would be interesting to also study the effect of multiple particles near a conducting plate, which could include many-body interactions.

A

Proof that the Cluster Polarizability is a Symmetric Matrix

In this appendix, we prove that the polarizability of a cluster of Lorentz atoms with equal atomic polarizability is a symmetric matrix, as asserted in Chapter 2.

A.1 Introduction

In this appendix, we prove that a cluster of N Lorentz atoms has a symmetric polarizability matrix $\boldsymbol{\alpha}_c$ if each Lorentz atom has the same polarizability α_0 . We also assume the applied electric field to be homogeneous, which, as we shall see, is a requirement for a quantity such as $\boldsymbol{\alpha}_c$ to be well-defined.

Our starting point will be the equation for the $3N$ -dimensional vector \mathcal{P} , which contains the individual polarizations \mathbf{p}_i of each Lorentz atom, from Eq. (2.11),

$$\mathcal{P} = (\mathcal{I} + \alpha_0 \mathcal{T})^{-1} \alpha_0 \boldsymbol{\mathcal{E}}_0, \quad (\text{A.1})$$

where \mathcal{I} is the $3N \times 3N$ identity matrix, $\boldsymbol{\mathcal{E}}_0$ is a $3N$ -dimensional vector containing N copies of the applied electric field \mathbf{E}_0 , and \mathcal{T} is a $3N \times 3N$ matrix containing all the dipolar tensors \mathbf{T}_{ij} , which describe the dipole-dipole interaction between atom i and j [see Eq. (2.2)]. As shown already in Chapter 2, under Eq. (2.13), the cluster polarizability can always be written as a $3N \times 3N$ matrix. Explicitly, dividing $(\mathcal{I} + \alpha_0 \mathcal{T})^{-1}$ into 3×3 blocks \mathbf{Y}_{ij} , we have

$$\boldsymbol{\alpha}_c = \alpha_0 \sum_{i,j} \mathbf{Y}_{ij}. \quad (\text{A.2})$$

Note that the structure of $(\mathcal{I} + \alpha_0 \mathcal{T})^{-1}$ plays no role in the reasoning leading to A.2, apart from the fact that we assume $(\mathcal{I} + \alpha_0 \mathcal{T})^{-1}$ and, hence, $\boldsymbol{\alpha}_c$, to exist. We do require that \mathbf{E}_0 not depend on the location, such that $\boldsymbol{\mathcal{E}}_0$ will be a vector with repeating elements.

A.2 Proof of the Symmetry of the Polarizability Matrix

To prove that $\boldsymbol{\alpha}_c$ is symmetric, we do need to look at the structure of $(\mathcal{I} + \alpha_0 \mathcal{T})^{-1}$. First, note that if we assert

$$\mathbf{Y}_{ij} = \mathbf{Y}_{ji}^T, \quad (\text{A.3})$$

we have

$$\begin{aligned} \boldsymbol{\alpha}_c &= \alpha_0 \sum_{i=1}^N \left[\mathbf{Y}_{ii} + \sum_{j=1}^{i-1} (\mathbf{Y}_{ij} + \mathbf{Y}_{ji}) \right] \\ &= \alpha_0 \sum_{i=1}^N \left[\mathbf{Y}_{ii} + \sum_{j=1}^{i-1} (\mathbf{Y}_{ij} + \mathbf{Y}_{ij}^T) \right]. \end{aligned}$$

The obtained expression is clearly symmetric, since \mathbf{Y}_{ii} is symmetric (this follows from the assertion of Eq. A.3), and an expression of the form $(\mathbf{Y}_{ij} + \mathbf{Y}_{ij}^T)$ is always symmetric. Thus, we see that we sum a number of symmetric matrices, leading to a symmetric result.

A.2.1 Proof of the Assertion $\mathbf{Y}_{ij} = \mathbf{Y}_{ji}^T$.

To complete the proof, we still have to prove the assertion of Eq. (A.3). This proof now follows. First of all, we define the matrix $\mathcal{S} \equiv (\mathcal{I} + \alpha_0 \mathcal{T})$, and call its 3×3 subblocks \mathbf{S}_{ij} .

Note that the \mathbf{S}_{ij} matrices have the same symmetry properties as \mathbf{T}_{ij} , namely $\mathbf{S}_{ij} = \mathbf{S}_{ji}$ and $\mathbf{S}_{ij} = \mathbf{S}_{ij}^T$.

Our aim is now the following. Given is a $3N \times 3N$ dimensional matrix S , built up from 3×3 symmetric matrices \mathbf{S}_{ij} , for which also $\mathbf{S}_{ij} = \mathbf{S}_{ji}$, as follows:

$$\mathcal{S} = \begin{pmatrix} \mathbf{S}_{11} & \mathbf{S}_{12} & \dots & \mathbf{S}_{1N} \\ \mathbf{S}_{21} & \mathbf{S}_{22} & \dots & \mathbf{S}_{2N} \\ \vdots & \vdots & \ddots & \vdots \\ \mathbf{S}_{N1} & \mathbf{S}_{N2} & \dots & \mathbf{S}_{NN} \end{pmatrix}.$$

We want to show that the inverse of this matrix, \mathcal{S}^{-1} , is built up from 3×3 blocks \mathbf{Y}_{ij} , which obey $\mathbf{Y}_{ij} = \mathbf{Y}_{ji}^T$. To do this, we are going to use induction in combination with the following identity for the inverse of a matrix built up from blocks \mathbf{A} , \mathbf{B} , \mathbf{C} , and \mathbf{D} (see, e.g., Ref. [122]):

$$\begin{pmatrix} \mathbf{A} & \mathbf{B} \\ \mathbf{C} & \mathbf{D} \end{pmatrix}^{-1} = \begin{pmatrix} \mathbf{A}^{-1} + \mathbf{A}^{-1}\mathbf{B}(\mathbf{D} - \mathbf{C}\mathbf{A}^{-1}\mathbf{B})^{-1}\mathbf{C}\mathbf{A}^{-1} & -\mathbf{A}^{-1}\mathbf{B}(\mathbf{D} - \mathbf{C}\mathbf{A}^{-1}\mathbf{B})^{-1} \\ -(\mathbf{D} - \mathbf{C}\mathbf{A}^{-1}\mathbf{B})^{-1}\mathbf{C}\mathbf{A}^{-1} & (\mathbf{D} - \mathbf{C}\mathbf{A}^{-1}\mathbf{B})^{-1} \end{pmatrix}. \quad (\text{A.4})$$

We start with an $N = 2$ matrix, $\mathcal{S}(2)$. According to Eq. (A.4), we have

$$\begin{aligned} \mathcal{S}^{-1}(2) &= \begin{pmatrix} \mathbf{S}_{11} & \mathbf{S}_{12} \\ \mathbf{S}_{21} & \mathbf{S}_{22} \end{pmatrix}^{-1} = \\ &= \begin{pmatrix} \mathbf{S}_{11}^{-1} + \mathbf{S}_{11}^{-1}\mathbf{S}_{12}(\mathbf{S}_{22} - \mathbf{S}_{21}\mathbf{S}_{11}^{-1}\mathbf{S}_{12})^{-1}\mathbf{S}_{21}\mathbf{S}_{11}^{-1} & -\mathbf{S}_{11}^{-1}\mathbf{S}_{12}(\mathbf{S}_{22} - \mathbf{S}_{21}\mathbf{S}_{11}^{-1}\mathbf{S}_{12})^{-1} \\ -(\mathbf{S}_{22} - \mathbf{S}_{21}\mathbf{S}_{11}^{-1}\mathbf{S}_{12})^{-1}\mathbf{S}_{21}\mathbf{S}_{11}^{-1} & (\mathbf{S}_{22} - \mathbf{S}_{21}\mathbf{S}_{11}^{-1}\mathbf{S}_{12})^{-1} \end{pmatrix}. \end{aligned}$$

We can easily check, using the symmetries of \mathbf{S}_{ij} , that

$$\begin{aligned} \mathbf{Y}_{11}(2) &= \mathbf{S}_{11}^{-1} + \mathbf{S}_{11}^{-1}\mathbf{S}_{12}(\mathbf{S}_{22} - \mathbf{S}_{21}\mathbf{S}_{11}^{-1}\mathbf{S}_{12})^{-1}\mathbf{S}_{21}\mathbf{S}_{11}^{-1} = \mathbf{Y}_{11}^T(2), \\ \mathbf{Y}_{22}(2) &= (\mathbf{S}_{22} - \mathbf{S}_{21}\mathbf{S}_{11}^{-1}\mathbf{S}_{12})^{-1} = \mathbf{Y}_{22}^T(2), \\ \mathbf{Y}_{12}(2) &= -\mathbf{S}_{11}^{-1}\mathbf{S}_{12}(\mathbf{S}_{22} - \mathbf{S}_{21}\mathbf{S}_{11}^{-1}\mathbf{S}_{12})^{-1} = \mathbf{Y}_{21}^T(2), \end{aligned}$$

and hence

$$\mathbf{Y}_{ij}(2) = \mathbf{Y}_{ji}^T(2).$$

Even though not strictly necessary for the proof to work, we are also going to explicitly discuss the $N = 3$ case, because it clarifies some notation that will be used in the case of

general N . We define the blocks of the matrix to be as follows:

$$\begin{aligned} \mathcal{S}(3) &= \begin{pmatrix} \mathbf{S}_{11} & \mathbf{S}_{12} & \mathbf{S}_{13} \\ \mathbf{S}_{21} & \mathbf{S}_{22} & \mathbf{S}_{23} \\ \mathbf{S}_{31} & \mathbf{S}_{32} & \mathbf{S}_{33} \end{pmatrix} \\ &= \begin{pmatrix} \begin{bmatrix} \mathbf{S}_{11} & \mathbf{S}_{12} \\ \mathbf{S}_{21} & \mathbf{S}_{22} \\ \mathbf{S}_{31} & \mathbf{S}_{32} \end{bmatrix} & \begin{bmatrix} \mathbf{S}_{13} \\ \mathbf{S}_{23} \\ \mathbf{S}_{33} \end{bmatrix} \end{pmatrix} \\ &\equiv \begin{pmatrix} \mathcal{S}(2) & \mathcal{B}(2) \\ \mathcal{C}(2) & \mathbf{S}_{33} \end{pmatrix}. \end{aligned}$$

The inverse of this matrix is, according to Eq. (A.4),

$$\mathcal{S}^{-1}(3) = \begin{pmatrix} \mathcal{S}^{-1}(2) + \mathcal{S}^{-1}(2) \mathcal{B}(2) \mathbf{K}(2) \mathcal{C}(2) \mathcal{S}^{-1}(2) & -\mathcal{S}^{-1}(2) \mathcal{B}(2) \mathbf{K}(2) \\ -\mathbf{K}(2) \mathcal{C}(2) \mathcal{S}^{-1}(2) & \mathbf{K}(2) \end{pmatrix},$$

where we have defined^a

$$\mathbf{K}(2) \equiv (\mathbf{S}_{33} - \mathcal{C}(2) \mathcal{S}^{-1}(2) \mathcal{B}(2))^{-1}.$$

We see that we have four blocks in the matrix for which we have to prove our assertion. First of all, we note that $\mathcal{B}(2) = \mathcal{C}^T(2)$. With this, the symmetry of the lower right (3×3) block is trivial to show,

$$\begin{aligned} \mathbf{K}^T(2) &= \left[(\mathbf{S}_{33} - \mathcal{C}(2) \mathcal{S}^{-1}(2) \mathcal{B}(2))^{-1} \right]^T \\ &= \left(\mathbf{S}_{33}^T - \mathcal{B}^T(2) [\mathcal{S}^{-1}]^T(2) \mathcal{C}^T(2) \right) \\ &= \left(\mathbf{S}_{33} - \mathcal{C}(2) [\mathcal{S}^{-1}](2) \mathcal{B}(2) \right) \\ &= \mathbf{K}(2), \end{aligned}$$

hence the block is symmetric. For the upper right and lower left blocks, we note that

$$-\mathcal{S}^{-1}(2) \mathcal{B}(2) \mathbf{K}(2) = - \begin{pmatrix} \mathbf{Y}_{11}(2) \mathbf{S}_{13} \mathbf{K}(2) + \mathbf{Y}_{12}(2) \mathbf{S}_{23} \mathbf{K}(2) \\ \mathbf{Y}_{21}(2) \mathbf{T}_{13} \mathbf{K}(2) + \mathbf{Y}_{22}(2) \mathbf{T}_{23} \mathbf{K}(2) \end{pmatrix},$$

while

$$\begin{aligned} -\mathbf{K}(2) \mathcal{C}(2) \mathcal{S}^{-1}(2) &= - \left(\mathbf{K}(2) \mathbf{S}_{31} \mathbf{Y}_{11}(2) + \mathbf{K}(2) \mathbf{S}_{32} \mathbf{Y}_{21}(2), \right. \\ &\quad \left. \mathbf{K}(2) \mathbf{S}_{31} \mathbf{Y}_{12}(2) + \mathbf{K}(2) \mathbf{S}_{32} \mathbf{Y}_{22}(2) \right). \end{aligned}$$

^aThe matrix $\mathbf{M}(2) \equiv \mathbf{S}_{33} - \mathcal{C}(2) \mathcal{S}^{-1}(2) \mathcal{B}(2)$ is called the Schur complement of $\mathcal{S}(2)$, and it has to be invertible for our proof to work. Note, however, that $\det[\mathcal{S}(3)] = \det[\mathcal{S}(2)] \det[\mathbf{S}_{33} - \mathcal{C}(2) \mathcal{S}^{-1}(2) \mathcal{B}(2)] = \det[\mathcal{S}(2)] \det[\mathbf{M}(2)]$, such that, if $\mathbf{M}(2)$ is *not* invertible (i.e., $\det[\mathbf{M}(2)] = 0$), then $\mathcal{S}(3)$ is also not invertible, meaning that α_c does not exist, contrary to the assumption made at the start. Therefore, $\mathbf{M}(2)$ must be invertible and hence $\mathbf{K}(2)$ exists.

For our assertion [Eq. (A.3)] to hold true, we must thus have

$$\begin{aligned} \mathbf{Y}_{11}(2) \mathbf{S}_{13} \mathbf{K}(2) + \mathbf{Y}_{12}(2) \mathbf{S}_{23} \mathbf{K}(2) &= [\mathbf{K}(2) \mathbf{S}_{31} \mathbf{Y}_{11}(2) + \mathbf{K}(2) \mathbf{S}_{32} \mathbf{Y}_{21}(2)]^T, \\ \mathbf{Y}_{21}(2) \mathbf{S}_{13} \mathbf{K}(2) + \mathbf{Y}_{22}(2) \mathbf{S}_{23} \mathbf{K}(2) &= [\mathbf{K}(2) \mathbf{S}_{31} \mathbf{Y}_{12}(2) + \mathbf{K}(2) \mathbf{S}_{32} \mathbf{Y}_{22}(2)]^T. \end{aligned}$$

Both are easily shown to be true if we use $\mathbf{S}_{ij}^T = \mathbf{S}_{ij} = \mathbf{S}_{ji}$ and the result from the $N = 2$ case, $\mathbf{Y}_{ij}(2) = \mathbf{Y}_{ji}^T(2)$. The last block to prove our assertion for is the upper left block. Of this block, only the second term is important since the first term has been shown to already obey our assertion. It follows that our task is to examine the expression

$$\mathcal{L}(2) \equiv \mathcal{S}^{-1}(2) \mathcal{B}(2) \mathbf{K}(2) \mathcal{C}(2) \mathcal{S}^{-1}(2).$$

We define 3×3 matrices $\mathbf{L}_{ij}(2)$ of which $\mathcal{L}(2)$ is built up. Furthermore we define $\mathcal{G}(2)$, representing all the factors in $\mathcal{L}(2)$ to the right of $\mathcal{S}^{-1}(2)$:

$$\begin{aligned} \mathcal{G}(2) &\equiv \mathcal{B}(2) \mathbf{K}(2) \mathcal{C}(2) \mathcal{S}^{-1}(2) \\ &= \begin{pmatrix} \mathbf{S}_{13} \\ \mathbf{S}_{23} \end{pmatrix} \left(\mathbf{K}(2) (\mathbf{S}_{31} \mathbf{Y}_{11}(2) + \mathbf{S}_{32} \mathbf{Y}_{21}(2)), \mathbf{K}(2) (\mathbf{S}_{31} \mathbf{Y}_{12}(2) + \mathbf{S}_{32} \mathbf{Y}_{22}(2)) \right) \\ &= \begin{pmatrix} \mathbf{S}_{13} \mathbf{K}(2) (\mathbf{S}_{31} \mathbf{Y}_{11}(2) + \mathbf{S}_{32} \mathbf{Y}_{21}(2)) & \mathbf{S}_{13} \mathbf{K}(2) (\mathbf{S}_{31} \mathbf{Y}_{12}(2) + \mathbf{S}_{32} \mathbf{Y}_{22}(2)) \\ \mathbf{S}_{23} \mathbf{K}(2) (\mathbf{S}_{31} \mathbf{Y}_{11}(2) + \mathbf{S}_{32} \mathbf{Y}_{21}(2)) & \mathbf{S}_{23} \mathbf{K}(2) (\mathbf{S}_{31} \mathbf{Y}_{12}(2) + \mathbf{S}_{32} \mathbf{Y}_{22}(2)) \end{pmatrix}. \end{aligned}$$

We see that $\mathcal{G}(2)$ is built up from matrices $\mathbf{G}_{ij}(2)$, where

$$\mathbf{G}_{ij}(2) = \sum_{l=1}^2 \mathbf{S}_{i3} \mathbf{K}(2) \mathbf{S}_{3l} \mathbf{Y}_{lj}(2).$$

Therefore, since $\mathcal{L}(2) = \mathcal{S}^{-1}(2) \mathcal{G}(2)$, we have for the $\mathbf{L}_{ij}(2)$:

$$\begin{aligned} \mathbf{L}_{ij}(2) &= \sum_{k=1}^2 \mathbf{Y}_{ik}(2) \mathbf{G}_{kj}(2) \\ &= \sum_{k=1}^2 \sum_{l=1}^2 \mathbf{Y}_{ik}(2) \mathbf{S}_{k3} \mathbf{K}(2) \mathbf{S}_{3l} \mathbf{Y}_{lj}(2), \end{aligned}$$

and for their transpose:

$$\begin{aligned} \mathbf{L}_{ij}^T(2) &= \sum_{k=1}^2 \sum_{l=1}^2 \mathbf{Y}_{lj}^T(2) \mathbf{S}_{3l} \mathbf{K}(2) \mathbf{S}_{k3} \mathbf{Y}_{ik}^T(2) \\ &= \sum_{k=1}^2 \sum_{l=1}^2 \mathbf{Y}_{jl}(2) \mathbf{S}_{3l} \mathbf{K}(2) \mathbf{S}_{k3} \mathbf{Y}_{ki}(2) \\ &= \sum_{l=1}^2 \sum_{k=1}^2 \mathbf{Y}_{jk}(2) \mathbf{S}_{3k} \mathbf{K}(2) \mathbf{S}_{l3} \mathbf{Y}_{li}(2), \end{aligned}$$

where in the last equality we replaced the dummy indices k and l . Since $\mathbf{S}_{3k} = \mathbf{S}_{k3}$ and $\mathbf{S}_{l3} = \mathbf{S}_{3l}$, we thus see that

$$\mathbf{L}_{ij}(2) = \mathbf{L}_{ji}^T(2).$$

Thus, the upper left block of $\mathcal{S}^{-1}(3)$ obeys our assertion, and hence we have shown that for the entire matrix $\mathcal{S}^{-1}(3)$,

$$\mathbf{Y}_{ij}(3) = \mathbf{Y}_{ji}^T(3).$$

To be exhaustively complete, we now move on to the induction step. We suppose $\mathbf{Y}_{ij}(n) = \mathbf{Y}_{ji}^T(n)$, and show that it then follows that $\mathbf{Y}_{ij}(n+1) = \mathbf{Y}_{ji}^T(n+1)$. To save some space, we define $m \equiv n+1$. Our matrix $\mathcal{S}(m)$ has the following form:

$$\mathcal{S}(m) = \begin{pmatrix} \mathcal{S}(n) & \mathcal{B}(n) \\ \mathcal{C}(n) & \mathbf{S}_{mm} \end{pmatrix}.$$

I.e., the expression for $\mathcal{B}(n)$ is

$$\mathcal{B}(n) = \begin{pmatrix} \mathbf{S}_{1m} \\ \vdots \\ \mathbf{S}_{nm} \end{pmatrix},$$

and similarly for $\mathcal{C}(n)$. The inverse of the matrix $\mathcal{S}(m)$ is

$$\mathcal{S}^{-1}(m) = \begin{pmatrix} \mathcal{S}^{-1}(n) + \mathcal{S}^{-1}(n) \mathcal{B}(n) \mathbf{K}(n) \mathcal{C}(n) \mathcal{S}^{-1}(n) & -\mathcal{S}^{-1}(n) \mathcal{B}(n) \mathbf{K}(n) \\ -\mathbf{K}(n) \mathcal{C}(n) \mathcal{S}^{-1}(n) & \mathbf{K}(n) \end{pmatrix},$$

where

$$\mathbf{K}(n) = \left(\mathbf{S}_{mm} - \mathcal{C}(n) \mathcal{S}^{-1}(n) \mathcal{B}(n) \right)^{-1},$$

which is a symmetric matrix because $\mathcal{B}(n) = \mathcal{C}^T(n)$. This immediately implies that the lower right block obeys the assertion. The off-diagonal blocks also obey our assertion, because

$$-\mathcal{S}^{-1}(n) \mathcal{B}(n) \mathbf{K}(n) = - \begin{pmatrix} \sum_{k=1}^n \mathbf{Y}_{1k}(n) \mathbf{S}_{km} \mathbf{K}(n) \\ \vdots \\ \sum_{k=1}^n \mathbf{Y}_{nk}(n) \mathbf{S}_{km} \mathbf{K}(n) \end{pmatrix}$$

and

$$-\mathbf{K}(n) \mathcal{C}(n) \mathcal{S}^{-1}(n) = \left(\sum_{k=1}^n \mathbf{K}(n) \mathbf{S}_{mk} \mathbf{Y}_{k1}(n), \dots, \sum_{k=1}^n \mathbf{K}(n) \mathbf{S}_{mk} \mathbf{Y}_{kn}(n) \right),$$

the blocks of which are each other's transpose, that is, for the transpose of block i of $-\mathcal{S}^{-1}(n) \mathcal{B}(n) \mathbf{K}(n)$ we have:

$$\begin{aligned} \left[\sum_{k=1}^n \mathbf{Y}_{ik}(n) \mathbf{S}_{km} \mathbf{K}(n) \right]^T &= \sum_{k=1}^n \mathbf{K}^T(n) \mathbf{S}_{km}^T \mathbf{Y}_{ik}^T(n) \\ &= \sum_{k=1}^n \mathbf{K}(n) \mathbf{S}_{mk} \mathbf{Y}_{ki}(n), \end{aligned}$$

which is equal to block i of $-\mathbf{K}(n) \mathcal{C}(n) \mathcal{S}^{-1}(n)$. Here we made use of the induction assumption $\mathbf{Y}_{ij}(n) = \mathbf{Y}_{ji}^T(n)$ and of the symmetries in the \mathbf{S}_{ij} . Only the upper left block of $\mathcal{S}^{-1}(m)$ is left for us to examine, of which only the second term is of interest,

$$\begin{aligned} \mathcal{L}(n) &\equiv \mathcal{S}^{-1}(n) \mathcal{B}(n) \mathbf{K}(n)^{-1} \mathcal{C}(n) \mathcal{S}^{-1}(n) \\ &\equiv \mathcal{S}^{-1}(n) \mathcal{G}(n). \end{aligned}$$

The matrix $\mathcal{G}(n)$ is now built up from blocks $\mathbf{G}_{ij}(n)$ given by

$$\mathbf{G}_{ij}(n) = \sum_{l=1}^n \mathbf{S}_{im} \mathbf{K}(n) \mathbf{S}_{ml} \mathbf{Y}_{lj}(n),$$

where we made use of the expressions for $\mathcal{B}(n)$ and $\mathcal{C}(n)$. Thus, the 3×3 blocks in $\mathcal{L}(n)$ have the following form:

$$\begin{aligned} \mathbf{L}_{ij}(n) &= \sum_{k=1}^n \mathbf{Y}_{ik}(n) \mathbf{G}_{kj}(n) \\ &= \sum_{k=1}^n \sum_{l=1}^n \mathbf{Y}_{ik}(n) \mathbf{S}_{km} \mathbf{K}(n) \mathbf{S}_{ml} \mathbf{Y}_{lj}(n), \end{aligned}$$

and therefore their transpose is

$$\begin{aligned} \mathbf{L}_{ij}^T(n) &= \sum_{k=1}^n \sum_{l=1}^n \mathbf{Y}_{lj}^T(n) \mathbf{S}_{ml} \mathbf{K}(n) \mathbf{S}_{km} \mathbf{Y}_{ik}^T(n) \\ &= \sum_{k=1}^n \sum_{l=1}^n \mathbf{Y}_{jl}(n) \mathbf{S}_{ml} \mathbf{K}(n) \mathbf{S}_{km} \mathbf{Y}_{ki}(n) \\ &= \sum_{l=1}^n \sum_{k=1}^n \mathbf{Y}_{jk}(n) \mathbf{S}_{mk} \mathbf{K}(n) \mathbf{S}_{lm} \mathbf{Y}_{li}(n) \\ &= \mathbf{L}_{ji}(n). \end{aligned}$$

Therefore, the upper left block of $\mathcal{S}^{-1}(m)$ obeys $\mathbf{Y}_{ij}(n) = \mathbf{Y}_{ji}^T(n)$. It follows that for the entire matrix $\mathcal{S}(m)$,

$$\mathbf{Y}_{ij}(m) = \mathbf{Y}_{ji}^T(m).$$

Thus, we have done the following:

- We have proven that the assertion holds for $N = 2$ and for $N = 3$,
- We have proven that if the assertion holds for $N = n$, it must then also hold for $N = n + 1$.

Therefore, we conclude that the assertion must hold for all $N \geq 2$.^b

^bOf course, trivially, the assertion is also true for $N = 0$ and $N = 1$.

B

Exploiting Spatial Symmetries in Large Cubes and Spheres

In this appendix, we show explicitly how to exploit spatial symmetries in the CDM, making it possible to calculate the polarizability of very large cubes and spheres, as done in Chapter 3.

In Chapter 3, it is mentioned that one of the ways to simplify the problem of finding the polarizability α_c of a cluster of N Lorentz atoms of polarizability α_0 is to exploit the symmetries of the cluster. In particular, cubic and spherical cluster of atoms on a simple cubic lattice are invariant under 90° rotations around a Cartesian axis.

In this appendix, we use a slightly different notation to index the atoms of the cluster. Instead of using a single index i , we use three indices $\mathbf{n} = (n_x, n_y, n_z)$, counting atoms along each of the cubic lattice vectors, starting at the origin, which we always place in the center of the cluster. For example, if we consider a cube with an even number of atoms along each rib and with lattice spacing a , the atom at location $\mathbf{r} = (a/2, 0, 0)$ is denoted by $\mathbf{n} = (1, 0, 0)$, the one at $\mathbf{r} = (3a/2, 0, 0)$ by $(2, 0, 0)$, and the one at $\mathbf{r} = (-5a/2, a/2, -a/2)$ by $\mathbf{n} = (-3, 1, -1)$. The polarization of the atom at \mathbf{n} is denoted by $\mathbf{p}(\mathbf{n})$. Using this notation, Eq. (2.11) becomes, in terms of 3-dimensional objects,

$$\mathbf{p}(\mathbf{n}') + \alpha_0 \sum_{\mathbf{n}} \mathbf{T}(\mathbf{n}, \mathbf{n}') \cdot \mathbf{p}(\mathbf{n}) = \alpha_0 \mathbf{E}_0, \quad (\text{B.1})$$

where $\mathbf{T}(\mathbf{n}, \mathbf{n}')$ is the dipole tensor for the interaction between the atoms at \mathbf{n} and \mathbf{n}' . Assuming that the electric field is directed along the x -axis, the symmetries of the polarizations can be seen to be:

$$\begin{aligned} \mathbf{p}(-n_x, n_y, n_z) &= \begin{pmatrix} 1 & 0 & 0 \\ 0 & -1 & 0 \\ 0 & 0 & -1 \end{pmatrix} \mathbf{p}(n_x, n_y, n_z), \\ \mathbf{p}(n_x, -n_y, n_z) &= \begin{pmatrix} 1 & 0 & 0 \\ 0 & -1 & 0 \\ 0 & 0 & 1 \end{pmatrix} \mathbf{p}(n_x, n_y, n_z), \\ \mathbf{p}(n_x, n_y, -n_z) &= \begin{pmatrix} 1 & 0 & 0 \\ 0 & 1 & 0 \\ 0 & 0 & -1 \end{pmatrix} \mathbf{p}(n_x, n_y, n_z). \end{aligned}$$

From these, we can also infer that

$$\begin{aligned} \mathbf{p}(-n_x, -n_y, n_z) &= \begin{pmatrix} 1 & 0 & 0 \\ 0 & 1 & 0 \\ 0 & 0 & -1 \end{pmatrix} \mathbf{p}(n_x, n_y, n_z), \\ \mathbf{p}(-n_x, n_y, -n_z) &= \begin{pmatrix} 1 & 0 & 0 \\ 0 & -1 & 0 \\ 0 & 0 & 1 \end{pmatrix} \mathbf{p}(n_x, n_y, n_z), \\ \mathbf{p}(n_x, -n_y, -n_z) &= \begin{pmatrix} 1 & 0 & 0 \\ 0 & -1 & 0 \\ 0 & 0 & -1 \end{pmatrix} \mathbf{p}(n_x, n_y, n_z), \\ \mathbf{p}(-n_x, -n_y, -n_z) &= \mathbf{p}(n_x, n_y, n_z). \end{aligned}$$

We now assume that our cluster is a cube with an even number of atoms L along each rib. A sphere can be treated similarly, by noting that it is a cube of which the atoms

further than a certain distance from the origin have been removed. We can expand the sum in equation (B.1) as follows:

$$\begin{aligned}
\sum_{\mathbf{n}} \mathbf{T}(\mathbf{n}, \mathbf{n}') \cdot \mathbf{p}(\mathbf{n}) &= \sum_{n_x=1}^l \sum_{n_y=1}^l \sum_{n_z=1}^l [\mathbf{T}(\{n_x, n_y, n_z\}, \mathbf{n}') \cdot \mathbf{p}(n_x, n_y, n_z) \\
&+ \mathbf{T}(\{-n_x, n_y, n_z\}, \mathbf{n}') \cdot \mathbf{p}(-n_x, n_y, n_z) \\
&+ \mathbf{T}(\{n_x, -n_y, n_z\}, \mathbf{n}') \cdot \mathbf{p}(n_x, -n_y, n_z) \\
&+ \mathbf{T}(\{-n_x, -n_y, n_z\}, \mathbf{n}') \cdot \mathbf{p}(-n_x, -n_y, n_z) \\
&+ \mathbf{T}(\{n_x, n_y, -n_z\}, \mathbf{n}') \cdot \mathbf{p}(n_x, n_y, -n_z) \\
&+ \mathbf{T}(\{-n_x, n_y, -n_z\}, \mathbf{n}') \cdot \mathbf{p}(-n_x, n_y, -n_z) \\
&+ \mathbf{T}(\{n_x, -n_y, -n_z\}, \mathbf{n}') \cdot \mathbf{p}(n_x, -n_y, -n_z) \\
&+ \mathbf{T}(\{-n_x, -n_y, -n_z\}, \mathbf{n}') \cdot \mathbf{p}(-n_x, -n_y, -n_z)].
\end{aligned}$$

If we now use the symmetry relations, we can rewrite this as

$$\sum_{\mathbf{n}} \mathbf{T}(\mathbf{n}, \mathbf{n}') \cdot \mathbf{p}(\mathbf{n}) = \sum_{n_x=1}^l \sum_{n_y=1}^l \sum_{n_z=1}^l \mathbf{A}(\mathbf{n}, \mathbf{n}') \cdot \mathbf{p}(n_x, n_y, n_z),$$

where we defined the 3×3 matrix

$$\begin{aligned}
\mathbf{A}(\mathbf{n}, \mathbf{n}') &\equiv \mathbf{T}(\{n_x, n_y, n_z\}, \mathbf{n}') + \mathbf{T}(\{-n_x, -n_y, -n_z\}, \mathbf{n}') \\
&+ \{\mathbf{T}(\{n_x, -n_y, n_z\}, \mathbf{n}') + \mathbf{T}(\{-n_x, n_y, -n_z\}, \mathbf{n}')\} \begin{pmatrix} 1 & 0 & 0 \\ 0 & -1 & 0 \\ 0 & 0 & 1 \end{pmatrix} \\
&+ \{\mathbf{T}(\{-n_x, -n_y, n_z\}, \mathbf{n}') + \mathbf{T}(\{n_x, n_y, -n_z\}, \mathbf{n}')\} \begin{pmatrix} 1 & 0 & 0 \\ 0 & 1 & 0 \\ 0 & 0 & -1 \end{pmatrix} \\
&+ \{\mathbf{T}(\{-n_x, n_y, n_z\}, \mathbf{n}') + \mathbf{T}(\{n_x, -n_y, -n_z\}, \mathbf{n}')\} \begin{pmatrix} 1 & 0 & 0 \\ 0 & -1 & 0 \\ 0 & 0 & -1 \end{pmatrix}.
\end{aligned}$$

Thus, our set of linear equations becomes

$$\mathbf{p}(\mathbf{n}') + \alpha_0 \sum_{n_x=1}^l \sum_{n_y=1}^l \sum_{n_z=1}^l \mathbf{A}(\mathbf{n}, \mathbf{n}') \cdot \mathbf{p}(\mathbf{n}) = \alpha_0 \mathbf{E}_0.$$

We see that, in the sum, only $l^3 = L^3/8$ dipoles are referenced and that the problem can thus be solved self-consistently by only solving for these first l^3 dipoles. Afterwards, the rest of the polarizations can be inferred using the symmetry relations. We have gained a factor 1/8 in memory usage and this means that our cubes and spheres can now be twice as large in each dimension.

C

Additional Mathematical and Numerical Comparisons

In this appendix, we show a few more calculations relevant to Chapter 5. We derive an analytical expression for the interaction energy for three Lorentz atoms in the special case where the distance between the first and the second atom is the same as the distance between the second and the third. We investigate the accuracy of the Hamaker-de Boer and Axilrod-Teller approaches compared to this many-body expression.

For the atomic configuration described in Fig. 5.1 and subsection 5.3.1, it is possible to calculate the CDM interaction energy exactly. The eigenfrequencies of the system are given by

$$\omega_k = \omega_0 \sqrt{1 + \lambda_k},$$

where the λ_k are the nine eigenvalues of a 9×9 matrix. These can be expressed in terms of the functions

$$\begin{aligned} A_1(x) &= 1 + 512x^6 - 384x^8, \\ A_2(x) &= 192\sqrt{3}x^6 (2 - 3x^2)^2, \\ B_1(x) &= 1 + 128x^6 + 384x^8, \\ B_2(x) &= 1728\sqrt{3}x^8 (1 - x^2), \\ f_1(x) &= \frac{\sqrt{A_1^{3/2}(x) + A_2(x)}}{\sqrt{A_1^{3/2}(x) - A_2(x)}}, \\ f_2(x) &= \frac{\sqrt{B_1^{3/2}(x) + B_2(x)}}{\sqrt{B_1^{3/2}(x) - B_2(x)}} \end{aligned}$$

and

$$\begin{aligned} T_1(x) &= 3 + 2\sqrt{3A_1(x)} \cos \left[\frac{2}{3} \arctan(f_1(x)) \right], \\ T_{2,3}(x) &= 3 - \sqrt{3A_1(x)} \left(\cos \left[\frac{2}{3} \arctan(f_1(x)) \right] \right. \\ &\quad \left. \pm \sqrt{3} \sin \left[\frac{2}{3} \arctan(f_1(x)) \right] \right) \\ &= 3 - 2\sqrt{3A_1(x)} \cos \left[\frac{2}{3} \arctan(f_1(x)) \mp \frac{\pi}{3} \right], \\ T_4(x) &= -3 - 2\sqrt{3B_1(x)} \cos \left[\frac{2}{3} \arctan(f_2(x)) \right], \\ T_{5,6}(x) &= -3 + \sqrt{3B_1(x)} \left(\cos \left[\frac{2}{3} \arctan(f_2(x)) \right] \right. \\ &\quad \left. \pm \sqrt{3} \sin \left[\frac{2}{3} \arctan(f_2(x)) \right] \right) \\ &= -3 + 2\sqrt{3B_1(x)} \cos \left[\frac{2}{3} \arctan(f_2(x)) \mp \frac{\pi}{3} \right] \end{aligned}$$

by

$$\begin{aligned} \lambda_k(\tilde{r}, \theta) &= \frac{T_k \left(\cos \left[\frac{\theta}{2} \right] \right)}{24\tilde{r}^3 \cos^3 \left[\frac{\theta}{2} \right]} \quad (k = 1, \dots, 6), \\ \lambda_{7,8}(\tilde{r}, \theta) &= \frac{1 \pm \sqrt{1 + 512 \cos^6 \left[\frac{\theta}{2} \right]}}{16\tilde{r}^3 \cos^3 \left[\frac{\theta}{2} \right]}, \\ \lambda_9(\tilde{r}, \theta) &= -\frac{1}{8\tilde{r}^3 \cos^3 \left[\frac{\theta}{2} \right]}. \end{aligned}$$

Here, \tilde{r} is the dimensionless distance $r/\alpha_0^{1/3}$. The total CDM interaction energy $V_{CDM}(\tilde{r}, \theta)$ between the three dipoles is given by:

$$V_{CDM}(\tilde{r}, \theta) = \frac{1}{2} \hbar \omega_0 \left[\sum_{k=1}^9 \sqrt{1 + \lambda_k} - 9 \right].$$

This can be approximated for small λ_k (or, equivalently, large r/α_0) by a Taylor expansion of the square root:

$$V_{CDM} \simeq \frac{1}{2} \hbar \omega_0 \sum_{k=1}^9 \left(\frac{1}{2} \lambda_k - \frac{1}{8} \lambda_k^2 + \frac{1}{16} \lambda_k^3 \right).$$

It can be straightforwardly shown that $\sum_{k=1}^9 \lambda_k = 0$, while it can also be (less straightforwardly) calculated that

$$\begin{aligned} \sum_{k=1}^9 \lambda_k^2 &= \frac{3}{16 \tilde{r}^6 \cos^6 \left[\frac{\theta}{2} \right]} + \frac{24}{\tilde{r}^6}, \\ \sum_{k=1}^9 \lambda_k^3 &= \frac{9 \left(1 + 3 \cos^2 \left[\frac{\theta}{2} \right] - 6 \cos^4 \left[\frac{\theta}{2} \right] \right)}{4 \tilde{r}^9 \cos^3 \left[\frac{\theta}{2} \right]}. \end{aligned}$$

It follows that

$$\begin{aligned} \frac{1}{2} \hbar \omega_0 \sum_{k=1}^9 \left(-\frac{1}{8} \lambda_k^2 \right) &= \sum_{(ij)} v^{(L)}(r_{ij}), \\ \frac{1}{2} \hbar \omega_0 \sum_{k=1}^9 \left(\frac{1}{16} \lambda_k^3 \right) &= v^{(AT)}(r_i, r_j, r_k), \end{aligned}$$

as defined in Eqs. (5.7) and (5.10), thus confirming that, in this case, the London and AT approximations follow from a Taylor expansion of the CDM result.

The accuracy of the HdB and AT approximations depends on the angle θ , but also greatly on the interatomic distance r . In Fig. C.1, we illustrate this for the three-dipole case of Fig. 5.1 (section 5.3.1), for a few values of θ , by plotting the absolute difference Δ between V_{CDM} and V_{HdB} , V_{CDM} and V_{AT} , and V_{CDM} and V_{cHdB} , where V_{cHdB} is the result obtained by only considering pair interactions in CDM but not Taylor-expanding the result in \tilde{r}^{-3} (as is done for V_{HdB}). For large \tilde{r} , we observe that the AT approximation becomes the best of the three plotted methods; however, for smaller \tilde{r} , this is not always the case. The AT performs best for a straight line of dipoles ($\theta = 0$), but even here there is a region ($\tilde{r} \lesssim 1.8$) where it is beaten by V_{cHdB} . For $\theta = \pi/3$, V_{cHdB} outperforms V_{AT} up until $\tilde{r} \approx 3.75$. The straight-angled case ($\theta = \pi/2$) is interesting in that each of the three methods has a region where it has the best accuracy: V_{cHdB} for $\tilde{r} \lesssim 1.9$, V_L for $1.9 \lesssim \tilde{r} \lesssim 2.6$, and V_{AT} for $\tilde{r} \gtrsim 2.6$. In the case of the equilateral triangle ($\theta = 2\pi/3$), V_{HdB} beats V_{AT} in the region $\tilde{r} \lesssim 2.1$. We note that, with the exception of the straight-line case, AT only starts giving more accurate results than the other two methods in the regime $\tilde{r} > 2.1$, which was not considered in the main body of the present work.

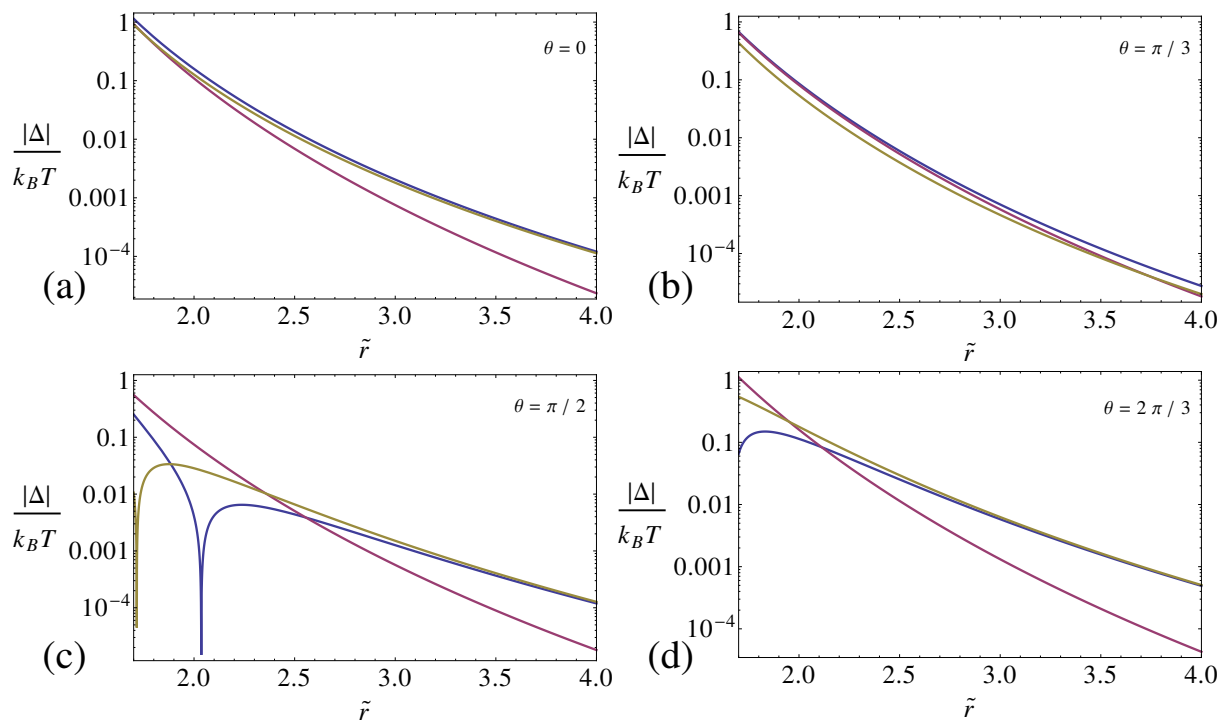


Figure C.1: The absolute difference $|\Delta|$ between V_{CDM} and V_{HdB} (blue), V_{CDM} and V_{AT} (red), and V_{CDM} and V_{cHdB} (yellow), corresponding, respectively, to Hamaker-de Boer, Axilrod-Teller and “corrected HdB” (or, rather, Hamaker-de Boer with unapproximated pair potentials) methods of approximation, for three dipoles positioned as in Fig. 5.1, as a function of the dimensionless distance $\tilde{r} = r/\alpha_0^{1/3}$ between the first two and the last two dipoles in the chain. We consider $\theta = 0$ (a), $\theta = \pi/3$ (b), $\theta = \pi/2$ (c), and $\theta = 2\pi/3$ (d).

D

Additional Analytical Expressions for the Self-Consistent Electric Field-Induced Dipolar Interaction Energy

In this appendix, we give two more analytical expressions for the self-consistent electric field-induced dipolar interaction energy between point dipoles, as discussed in Chapter 6. The first is an expression that is actually used in numerical calculations in Chapter 6 and gives the interaction energy between two anisotropically inducible dipoles that are rotated by a 90° angle with respect to each other. The second gives the interaction energy between point dipoles that have different, but isotropic polarizabilities.

In Chapter 6 (Sec. 6.4.5), we use an analytical expression for the interaction between a point dipole with polarizability $\alpha_1 = \text{diag}(\alpha_t, \alpha_{yy}, \alpha_l)$ and one with polarizability $\alpha_2 = \text{diag}(\alpha_l, \alpha_{yy}, \alpha_t)$ in an external electric field pointed in the z -direction. This expression is given in terms of the dimensionless dipole-dipole distance $\tilde{r} = r/\alpha_l^{1/3}$, the ratio $\eta_\alpha = \alpha_t/\alpha_l$, and the angle θ between the electric field and the line connecting the dipoles, by

$$V_{E,\text{misal.}}^{(\text{SSCD})}(\tilde{r}, \theta, \eta_\alpha) = \frac{\alpha_l E_0^2}{2} \frac{A(\tilde{r}, \theta, \zeta)}{B(\tilde{r}, \theta, \zeta)}, \quad (\text{D.1})$$

where

$$A(\tilde{r}, \theta, \zeta) = (\tilde{r}^6 - 4\eta_\alpha)(2\tilde{r}^3 - 1 - \eta_\alpha)\eta_\alpha - 3 \left[2\eta_\alpha(\tilde{r}^6 - 2\eta_\alpha) + \tilde{r}^3(1 + \eta_\alpha)(\eta_\alpha + 3(1 - \eta_\alpha)^2 \sin^2 \theta) \right] \tilde{r}^3 \cos^2 \theta$$

and

$$B(\tilde{r}, \theta, \zeta) = (\tilde{r}^6 - 4\eta_\alpha)(\tilde{r}^6 - \eta_\alpha) - 9\tilde{r}^6(1 - \eta_\alpha)^2 \cos^2 \theta \sin^2 \theta.$$

Note that these expressions do not depend on α_{yy} . The first-order Taylor expansion of Eq. (D.1) for small \tilde{r} yields Eq. (6.20). $V_{E,\text{misal.}}^{(\text{SSCD})}(\tilde{r}, \theta, \eta_\alpha)$ is, together with the contour lines of its permanent-dipole counterpart of Eq. (6.20), plotted in Fig. D.1 for $\eta \approx 0.44$.

We can also derive an expression for the interaction energy of a dipole with polarizability $\alpha_1 \mathbf{I}$ with one with polarizability $\alpha_2 \mathbf{I}$. The result is:

$$V_E^{(\text{SSCD})}(\tilde{r}, \theta, \zeta) = \frac{E_0^2 \alpha_1 \zeta}{2(\tilde{r}^6 - 4\zeta)(\tilde{r}^6 - \zeta)} \left[(\tilde{r}^6 - 4\zeta)(2\tilde{r}^3 - \zeta - 1) - 3\tilde{r}^3(2\tilde{r}^6 + \tilde{r}^3(\zeta + 1) - 4\zeta) \cos^2 \theta \right],$$

where $\zeta = \alpha_1/\alpha_2$, $\tilde{r} = r/\alpha_1^{1/3}$ and θ is, as before, the angle between the electric field and the line connecting the dipoles. The first-order Taylor approximation of this expression for small \tilde{r}^{-3} is

$$\begin{aligned} V_E^{(\text{SPD})}(\tilde{r}, \theta, \zeta) &= E_0^2 \alpha_1 \zeta \frac{1 - 3 \cos^2 \theta}{\tilde{r}^3} \\ &= E_0^2 \alpha_1 \alpha_2 \frac{1 - 3 \cos^2 \theta}{r^3}, \end{aligned}$$

which seems physically reasonable. $V_E^{(\text{SSCD})}(\tilde{r}, \theta, \zeta)$ is not applied in Chapter 6 but might be useful for future study.

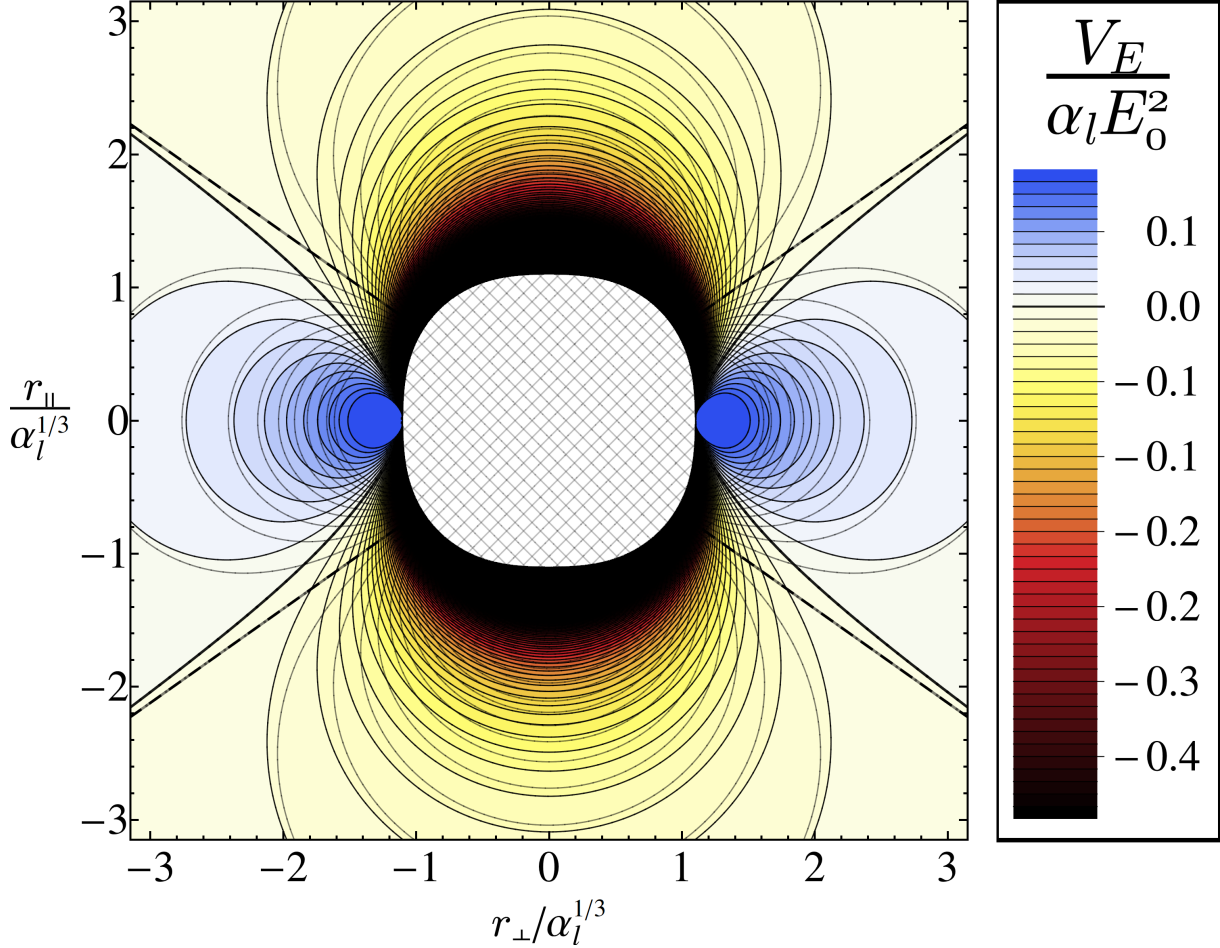


Figure D.1: The interaction energy $V_{E,\text{misal.}}^{(\text{SSCD})}/\alpha_l E_0^2$, as given in Eq. (D.1), of a pair of inducible point dipoles, the first with polarizability $\boldsymbol{\alpha}_1 = \text{diag}(\alpha_t, \alpha_{yy}, \alpha_l)$ and the second with polarizability $\boldsymbol{\alpha}_2 = \text{diag}(\alpha_l, \alpha_{yy}, \alpha_t)$, satisfying $\alpha_t/\alpha_l \approx 0.44$, subject to external electric field \mathbf{E}_0 pointing in the direction of r_\parallel , as a function of the location of the second inducible dipole relative to the first in the $r_\perp - r_\parallel$ plane. Note that restricting ourselves to this plane makes the value of α_{yy} irrelevant for the value of $V_{E,\text{misal.}}^{(\text{SSCD})}$. The dipole moments are calculated self-consistently, taking into account the influence that the inducible point dipoles have on each other's dipole moment. The contour lines of the function $V_{E,\text{misal.}}^{(\text{SPD})}/\alpha_d E_0^2$ of Eq. (6.20), which is the result if the dipole moments are instead fixed to values equal to $\alpha_l \mathbf{E}_0$ and $\alpha_t \mathbf{E}_0$, respectively, are shown as well. The hatched area, within which a polarization catastrophe occurs and $V_E^{(\text{SSCD})}$ is no longer valid, is excluded from the plot.

References

- [1] T. Graham, *Liquid diffusion applied to analysis*. Philosophical Transactions of the Royal Society of London, 151:183–224, 1861.
- [2] A. McNaught. *IUPAC compendium of chemical terminology*. Blackwell Science Inc. (Hoboken), 1997.
- [3] R. Brown, *A brief account of microscopical observations made in the months of June, July and August 1827 on the particles contained in the pollen of plants; and on the general existence of active molecules in organic and inorganic bodies*. Phil. Mag., 4:161, 1828.
- [4] A. Einstein, *Über die von der molekularkinetischen theorie der wärme geforderte bewegung von in ruhenden flüssigkeiten suspendierten teilchen*. Ann. Phys., 322(8):549–560, 1905.
- [5] J. Perrin, *Mouvement Brownien et réalité moléculaire*. Ann. Chim. Phys., 18:5, 1909.
- [6] John Dalton, *A new system of chemical philosophy*, 1808. An online version is located at <http://archive.org/details/newssystemofchemi01daltuoft>.
- [7] C. L. Pearson. *Handbook of Adhesive Technology*, chapter Animal Glues and Adhesives. Marcel Dekker, Inc., 2003.
- [8] G. Doppelbauer, E. Bianchi, and G. Kahl, *Self-assembly scenarios of patchy colloidal particles in two dimensions*. J. Phys.: Condens. Matter, 22(10):104105, 2010.
- [9] F. Romano and F. Sciortino, *Colloidal self-assembly: Patchy from the bottom up*. Nature Mater., 10(3):171–173, Mar. 2011.
- [10] Q. Chen, S. C. Bae, and S. Granick, *Directed self-assembly of a colloidal kagome lattice*. Nature, 469(7330):381–384, Jan. 2011.
- [11] A. Travesset, *Self-assembly enters the design era*. Science, 334(6053):183–184, 2011.
- [12] R. J. Macfarlane, B. Lee, M. R. Jones, N. Harris, G. C. Schatz, and C. A. Mirkin, *Nanoparticle superlattice engineering with dna*. Science, 334(6053):204–208, 2011.
- [13] S. C. Glotzer and M. J. Solomon, *Anisotropy of building blocks and their assembly into complex structures*. Nature Mater., 6(8):557–562, 2007.
- [14] L. Rossi, S. Sacanna, and K. P. Velikov, *Cholesteric colloidal liquid crystals from phytosterol rod-like particles*. Soft Matter, 7:64–67, 2011.
- [15] S.-M. Yang, S.-H. Kim, J.-M. Lima, and G.-R. Yi, *Synthesis and assembly of structured colloidal particles*. J. Mater. Chem., 18(19):2177–2190, 2008.
- [16] D. Nagao, C. M. van Kats, K. Hayasaka, M. Sugimoto, M. Konno, A. Imhof, and A. van Blaaderen, *Synthesis of hollow asymmetrical silica dumbbells with a movable inner core*. Langmuir, 26(7):5208–5212, 2010.
- [17] M. Marechal, R. J. Kortschot, A. F. Demirörs, A. Imhof, and M. Dijkstra, *Phase behavior and structure of a new colloidal model system of bowl-shaped particles*. Nano Lett., 10(5):1907–1911, 2010.
- [18] I. D. Hosein and C. M. Liddell, *Convectively assembled nonspherical mushroom cap-based colloidal crystals*. Langmuir, 23(17):8810–8814, 2007.

- [19] X. D. Wang, E. Graugnard, J. S. King, Z. L. Wang, and C. J. Summers, *Large-scale fabrication of ordered nanobowl arrays*. *Nano Lett.*, 4(11):2223–2226, 2004.
- [20] C. I. Zoldesi, C. A. van Walree, and A. Imhof, *Deformable hollow hybrid silica/siloxane colloids by emulsion templating*. *Langmuir*, 22(9):4343–4352, 2006.
- [21] A. Kuijk, A. van Blaaderen, and A. Imhof, *Synthesis of monodisperse, rodlike silica colloids with tunable aspect ratio*. *J. Am. Chem. Soc.*, 133(8):2346–2349, 2011.
- [22] A. Kuijk, D. V. Byelov, A. V. Petukhov, A. van Blaaderen, and A. Imhof, *Phase behavior of colloidal silica rods*. *Faraday Discuss.*, 159:181–199, 2012.
- [23] B. Nikoobakht, Z. L. Wang, and M. A. El-Sayed, *Self-assembly of gold nanorods*. *J. Phys. Chem. B*, 104(36):8635–8640, 2000.
- [24] D. Fava, Z. Nie, M. A. Winnik, and E. Kumacheva, *Evolution of self-assembled structures of polymer-terminated gold nanorods in selective solvents*. *Adv. Mater.*, 20(22):4318–4322, 2008.
- [25] E. L. Thomas, *The abcs of self-assembly*. *Science*, 286(5443):1307, 1999.
- [26] D. J. Kraft, W. S. Vlug, C. M. van Kats, A. van Blaaderen, A. Imhof, and W. K. Kegel, *Self-assembly of colloids with liquid protrusions*. *J. Am. Chem. Soc.*, 131:1182–1186, 2008.
- [27] I. D. Hosein, S. H. Lee, and C. M. Liddell, *Dimer-based three-dimensional photonic crystals*. *Adv. Funct. Mater.*, 20(18):3085–3091, 2010.
- [28] L. Onsager, *The effects of shape on the interaction of colloidal particles*. *Ann. N.Y. Acad. Sci.*, 51:627–659, 1949.
- [29] M. J. Solomon, *Directions for targeted self-assembly of anisotropic colloids from statistical thermodynamics*. *Curr. Opin. Colloid In.*, 16:158–167, 2011.
- [30] S. C. Glotzer, M. A. Horsch, C. R. Iacovella, Z. Zhang, E. R. Chan, and X. Zhang, *Self-assembly of anisotropic tethered nanoparticle shape amphiphiles*. *Curr. Opin. Colloid In.*, 10(5-6):287–295, 2005.
- [31] M. Grzelczak, J. Vermant, E. M. Furst, and L. M. Liz-Marzán, *Directed self-assembly of nanoparticles*. *ACS Nano*, 4(7):3591–3605, 2010.
- [32] D. V. Talapin, E. V. Shevchenko, C. B. Murray, A. Kornowski, S. Förster, and H. Weller, *Cdse and cdse/cds nanorod solids*. *J. Am. Chem. Soc.*, 126(40):12984–12988, 2004. PMID: 15469296.
- [33] S. Ahmed and K. M. Ryan, *Self-assembly of vertically aligned nanorod supercrystals using highly oriented pyrolytic graphite*. *Nano Lett.*, 7(8):2480–2485, 2007.
- [34] B. Sun and H. Siringhaus, *Surface tension and fluid flow driven self-assembly of ordered zno nanorod films for high-performance field effect transistors*. *J. Am. Chem. Soc.*, 128(50):16231–16237, 2006.
- [35] D. van der Beek, A. V. Petukhov, P. Davidson, J. Ferré, J. P. Jamet, H. H. Wensink, G. J. Vroege, W. Bras, and H. N. Lekkerkerker, *Magnetic-field-induced orientational order in the isotropic phase of hard colloidal platelets*. *Phys. Rev. E*, 73(4):041402, 2006.
- [36] K. M. Ryan, A. Mastroianni, K. A. Stancil, H. Liu, and A. P. Alivisatos, *Electric-field-assisted assembly of perpendicularly oriented nanorod superlattices*. *Nano Lett.*, 6(7):1479–1482, 2006.

- [37] K. Bubke, H. Gnewuch, M. Hempstead, J. Hammer, and M. L. H. Green, *Optical anisotropy of dispersed carbon nanotubes induced by an electric field*. Appl. Phys. Lett., 71(14):1906–1908, 1997.
- [38] A. F. Demirörs, P. M. Johnson, C. M. van Kats, A. van Blaaderen, and A. Imhof, *Directed self-assembly of colloidal dumbbells with an electric field*. Langmuir, 26(18):14466–14471, 2010.
- [39] P. A. Smith, C. D. Nordquist, T. N. Jackson, T. S. Mayer, B. R. Martin, J. Mbindyo, and T. E. Mallouk, *Electric-field assisted assembly and alignment of metallic nanowires*. Appl. Phys. Lett., 77(9):1399–1401, 2000.
- [40] Aristotle, *Metaphysics*, 4th century BC. An online version is located at <http://classics.mit.edu/Aristotle/metaphysics.html>.
- [41] B. Russell. *A History of Western Philosophy*. George Allen & Unwin Ltd., 1945.
- [42] G. S. Kirk and J. E. Raven. *The Presocratic Philosophers*. Cambridge University Press, 1957.
- [43] Diogenes Laërtius, *Lives and Opinions of Eminent Philosophers*, 3rd century AD. An online version is located at <http://archive.org/details/livesandopinions00dioguoft>.
- [44] Aristotle, *On the Soul*, 3rd century AD. An online version is located at <http://classics.mit.edu/Aristotle/soul.html>.
- [45] R. P. Feynman, R. B. Leighton, and M. Sands. *The Feynman Lectures on Physics*. Addison-Wesley, 6th edition, 1977.
- [46] M. Faraday. *Experimental researches in electricity*. J.M. Dent & Sons, 1922.
- [47] M. Faraday, *Experimental researches in electricity. eleventh series*. Phil. Trans. R. Soc. Lond., 128:1–40, 1838.
- [48] M. Faraday, *Experimental researches in electricity. twelfth series*. Phil. Trans. R. Soc. Lond., 128:83–123, 1838.
- [49] M. Faraday, *Experimental researches in electricity. thirteenth series*. Phil. Trans. R. Soc. Lond., 128:125–168, 1838.
- [50] M. Faraday, *Experimental researches in electricity. fourteenth series*. Phil. Trans. R. Soc. Lond., 128:265–282, 1838.
- [51] J. D. Jackson. *Classical Electrodynamics*. John Wiley & Sons, Inc., third edition, 1999.
- [52] R. Eisenschitz and F. London, *Über das verhältnis der van der waalsschen kräfte zu den homöopolaren bindungskräften*. Z. Phys., 60(7-8):491–527, 1930.
- [53] F. London, *Zur theorie und systematik der molekularkräfte*. Z. Phys., 63(3-4):245–279, 1930.
- [54] F. London, *The general theory of molecular forces*. Trans. Faraday Soc., 33:8b–26, 1937.
- [55] B. V. Derjaguin and L. Landau, *Theory of the stability of strongly charged lyophobic sols and of the adhesion of strongly charged particles in solutions of electrolytes*. Acta Physicochim. URSS., 14:633–662, 1941.
- [56] E. J. W. Verwey and J. T. G. Overbeek. *Theory of the stability of lyophobic colloids*. Elsevier Publishing Company, 1948.

- [57] J. H. de Boer, *The influence of van der waals' forces and primary bonds on binding energy, strength and orientation, with special reference to some artificial resins*. Trans. Faraday Soc., 32:10–37, 1936.
- [58] H. Hamaker, *The london–van der waals attraction between spherical particles*. Physica, 4(10):1058 – 1072, 1937.
- [59] E. M. Lifshitz, *The theory of molecular attraction forces between solid bodies*. Zh. Eksp. Teor. Fiz., 2:73, 1955.
- [60] G. Bimonte, *Making precise predictions of the casimir force between metallic plates via a weighted kramers-kronig transform*. Phys. Rev. A, 83:042109, Apr 2011.
- [61] M. Renne and B. Nijboer, *Microscopic derivation of macroscopic van der waals forces*. Chem. Phys. Lett., 1(8):317 – 320, 1967.
- [62] B. Nijboer and M. Renne, *Microscopic derivation of macroscopic van der waals forces. ii*. Chem. Phys. Lett., 2(1):35 – 38, 1968.
- [63] B. R. A. Nijboer and M. J. Renne, *On the van der waals interaction between dielectric media*. Phys. Nor., 5:243, 1971.
- [64] M. W. Cole and D. Velegol, *Van der waals energy of a 1-dimensional lattice*. Mol. Phys., 106(12-13):1587–1596, 2008.
- [65] I. E. Dzyaloshinskii, E. M. Lifshitz, and L. P. Pitaevskii, *The general theory of van der waals forces*. Adv. Phys., 10(38):165–209, 1961.
- [66] H.-Y. Kim, J. O. Sofo, D. Velegol, M. W. Cole, and A. A. Lucas, *van der waals forces between nanoclusters: Importance of many-body effects*. J. Chem. Phys., 124(7):074504, 2006.
- [67] S. M. Gatica, M. W. Cole, and D. Velegol, *Designing van der waals forces between nanocolloids*. Nano Lett., 5(1):169–173, 2005.
- [68] H.-Y. Kim, J. O. Sofo, D. Velegol, M. W. Cole, and A. A. Lucas, *Van der waals dispersion forces between dielectric nanoclusters*. Langmuir, 23(4):1735–1740, 2007.
- [69] M. W. Cole, D. Velegol, H.-Y. Kim, and A. A. Lucas, *Nanoscale van der waals interactions*. Mol. Simulat., 35(10-11):849–866, 2009.
- [70] Y. V. Shtogun and L. M. Woods, *Many-body van der waals interactions between graphitic nanostructures*. The Journal of Physical Chemistry Letters, 1(9):1356–1362, 2010.
- [71] E. M. Purcell and C. R. Pennypacker, *Scattering and absorption of light by nonspherical dielectric grains*. Astrophys. J., 186:705, 1973.
- [72] B. T. Draine, *The discrete-dipole approximation and its application to interstellar graphite grains*. Astrophys. J., 333:848, 1988.
- [73] C. F. Bohren and S. B. Singham, *Backscattering by nonspherical particles: a review of methods and suggested new approaches*. J. Geophys. Res., 96:5269, 1991.
- [74] B. T. Draine and P. J. Flatau, *Discrete-dipole approximation for scattering calculations*. J. Opt. Soc. Am. A, 11:1491, 1994.
- [75] P. C. Chaumet and C. Billaudeau, *Coupled dipole method to compute optical torque: Application to a micropropeller*. J. of Appl. Phys., 101(2):023106, 2007.
- [76] P. C. Chaumet and M. Nieto-Vesperinas, *Time-averaged total force on a dipolar sphere in an electromagnetic field*. Opt. Lett., 25(15):1065–1067, Aug 2000.

- [77] J. P. Gordon, *Radiation forces and momenta in dielectric media*. Phys. Rev. A, 8:14–21, Jul 1973.
- [78] P. C. Chaumet and M. Nieto-Vesperinas, *Optical binding of particles with or without the presence of a flat dielectric surface*. Phys. Rev. B, 64:035422, Jun 2001.
- [79] P. C. Chaumet, A. Rahmani, A. Sentenac, and G. W. Bryant, *Efficient computation of optical forces with the coupled dipole method*. Phys. Rev. E, 72:046708, Oct 2005.
- [80] M. Apostol, S. Ilie, A. Petrut, M. Savu, and S. Toba, *A generalization of the dipolar force*. J. of Appl. Phys., 112(2):024905, 2012.
- [81] H.-Y. Kim, J. O. Sofo, D. Velegol, M. W. Cole, and G. Mukhopadhyay, *Static polarizabilities of dielectric nanoclusters*. Phys. Rev. A, 72:053201, Nov 2005.
- [82] L. Rossi, S. Sacanna, W. T. M. Irvine, P. M. Chaikin, D. J. Pine, and A. P. Philipse, *Cubic crystals from cubic colloids*. Soft Matter, 7:4139–4142, 2011.
- [83] B. W. Kwaadgras, M. Verdult, M. Dijkstra, and R. van Roij, *Polarizability and alignment of dielectric nanoparticles in an external electric field: Bowls, dumbbells, and cuboids*. J. Chem. Phys., 135(13):134105, 2011.
- [84] B. W. Kwaadgras, M. Dijkstra, and R. van Roij, *Communication: Bulkiness versus anisotropy: The optimal shape of polarizable brownian nanoparticles for alignment in electric fields*. J. Chem. Phys., 136(13):131102, 2012.
- [85] B. W. Kwaadgras, M. W. J. Verdult, M. Dijkstra, and R. van Roij, *Can nonadditive dispersion forces explain chain formation of nanoparticles?* J. Chem. Phys., 138:104308, 2013.
- [86] A. Sihvola, *Dielectric polarization and particle shape effects*. J. Nanomater., 2007:45090, 2007.
- [87] A. Sihvola, P. Yla-Oijala, S. Jarvenpaa, and J. Avelin, *Polarizabilities of platonic solids*. IEEE T. Antenn. Propag., 52:2226 – 2233, 2004.
- [88] H. Kettunen, H. Wallen, and A. Sihvola, *Polarizability of a dielectric hemisphere*. J. Appl. Phys., 102:044105, 2007.
- [89] M. Pitkonen, *Polarizability of a pair of touching dielectric spheres*. J. Appl. Phys., 103:104910, 2008.
- [90] M. Pitkonen, *Polarizability of the dielectric double-sphere*. J. Math. Phys., 47:102901, 2006.
- [91] See <http://www.netlib.org/lapack/> for information and downloadable versions of LAPACK.
- [92] R. Barrett, M. Berry, T. F. Chan, J. Demmel, J. Donato, J. Dongarra, V. Eijkhout, R. Pozo, C. Romine, and H. v. d. Vorst. *Templates for the Solution of Linear Systems: Building Blocks for Iterative Methods*. SIAM, 1994.
- [93] C. Kittel. *Introduction to Solid State Physics*. John Wiley & Sons, Inc., seventh edition, 1996.
- [94] S. Sacanna, W. T. M. Irvine, P. M. Chaikin, and D. J. Pine, *Lock and key colloids*. Nature, 464(7288):575–578, Mar. 2010.
- [95] J. Liao, K. Chen, L. Xu, C. Ge, J. Wang, L. Huang, and N. Gu, *Self-assembly of length-tunable gold nanoparticle chains in organic solvents*. Appl. Phys. A Mater. Sci. Process., 76:541–543, 2003.

- [96] M. Klokkenburg, A. J. Houtepen, R. Koole, J. W. J. de Folter, B. H. Ern e, E. van Faassen, and D. Vanmaekelbergh, *Dipolar structures in colloidal dispersions of pbse and cdse quantum dots*. Nano Lett., 7(9):2931–2936, 2007.
- [97] K.-S. Cho, D. V. Talapin, W. Gaschler, and C. B. Murray, *Designing pbse nanowires and nanorings through oriented attachment of nanoparticles*. J. Am. Chem. Soc., 127(19):7140–7147, 2005.
- [98] A. J. Houtepen, R. Koole, D. Vanmaekelbergh, J. Meeldijk, and S. G. Hickey, *The hidden role of acetate in the pbse nanocrystal synthesis*. J. Am. Chem. Soc., 128(21):6792–6793, 2006.
- [99] S. A. Blanton, R. L. Leheny, M. A. Hines, and P. Guyot-Sionnest, *Dielectric dispersion measurements of cdse nanocrystal colloids: Observation of a permanent dipole moment*. Phys. Rev. Lett., 79:865–868, Aug 1997.
- [100] L.-s. Li and A. P. Alivisatos, *Origin and scaling of the permanent dipole moment in cdse nanorods*. Phys. Rev. Lett., 90:097402, Mar 2003.
- [101] M. Shim and P. Guyot-Sionnest, *Permanent dipole moment and charges in colloidal semiconductor quantum dots*. J. Chem. Phys., 111(15):6955–6964, 1999.
- [102] Z. Tang, N. A. Kotov, and M. Giersig, *Spontaneous organization of single cdte nanoparticles into luminescent nanowires*. Science, 297(5579):237–240, 2002.
- [103] Z. Tang, Z. Zhang, Y. Wang, S. C. Glotzer, and N. A. Kotov, *Self-assembly of cdte nanocrystals into free-floating sheets*. Science, 314(5797):274–278, 2006.
- [104] M. S. Nikolic, C. Olsson, A. Salcher, A. Kornowski, A. Rank, R. Schubert, A. Fr msdorf, H. Weller, and S. F rster, *Micelle and vesicle formation of amphiphilic nanoparticles*. Angew. Chem. Int. Ed., 48(15):2752–2754, 2009.
- [105] P. Akcora, H. Liu, S. K. Kumar, J. Moll, Y. Li, B. C. Benicewicz, L. S. Schadler, D. Acehan, A. Z. Panagiotopoulos, V. Pryamitsyn, V. Ganesan, J. Ilavsky, P. Thiyagarajan, R. H. Colby, and J. F. Douglas, *Anisotropic self-assembly of spherical polymer-grafted nanoparticles*. Nature Mater., 8:354, 2009.
- [106] P. Schapotschnikow and T. J. H. Vlugt, *Understanding interactions between capped nanocrystals: Three-body and chain packing effects*. J. Chem. Phys., 131(12):124705, 2009.
- [107] B. M. Axilrod and E. Teller, *Interaction of the van der waals type between three atoms*. J. Chem. Phys., 11(6):299–300, 1943.
- [108] M. A. van der Hoef and P. A. Madden, *A novel simulation model for three-body dispersion interactions*. J. Phys.: Condens. Matter, 8(47):9669, 1996.
- [109] A. Yethiraj and A. van Blaaderen, *A colloidal model system with an interaction tunable from hard sphere to soft and dipolar*. Nature, 421(6922):513–517, 2003.
- [110] H. R. Vutukuri, J. Stiefelhagen, T. Vissers, A. Imhof, and A. van Blaaderen, *Bonding assembled colloids without loss of colloidal stability*. Advanced Materials, 24(3):412–416, 2012.
- [111] K. Kang and J. K. G. Dhont, *Double-layer polarization induced transitions in suspensions of colloidal rods*. Europhys. Lett., 84:14005, 2008.
- [112] A.-P. Hynninen and M. Dijkstra, *Phase diagram of dipolar hard and soft spheres: Manipulation of colloidal crystal structures by an external field*. Phys. Rev. Lett., 94:138303, Apr 2005.

-
- [113] A.-P. Hynninen and M. Dijkstra, *Phase behavior of dipolar hard and soft spheres*. Phys. Rev. E, 72:051402, Nov 2005.
- [114] F. Smallenburg and M. Dijkstra, *Phase diagram of colloidal spheres in a biaxial electric or magnetic field*. J. of Chem. Phys., 132(20):204508, 2010.
- [115] F. Smallenburg, H. R. Vutukuri, A. Imhof, A. van Blaaderen, and M. Dijkstra, *Self-assembly of colloidal particles into strings in a homogeneous external electric or magnetic field*. J. Phys.: Condens. Matter, 24(46):464113, 2012.
- [116] D. Levesque and J.-J. Weis, *Stability of solid phases in the dipolar hard sphere system*. Molecular Physics, 109(23-24):2747–2756, 2011.
- [117] P. I. C. Teixeira, M. A. Osipov, and M. M. Telo da Gama, *Phase diagrams of aligned dipolar hard rods*. Phys. Rev. E, 57:1752–1760, Feb 1998.
- [118] W. H. Press, S. A. Teukolsky, W. T. Vetterling, and B. P. Flannery. *Numerical Recipes: The Art of Scientific Computing*. Cambridge University Press, third edition, 2007.
- [119] F. Smallenburg. *Clustering and self-assembly in colloidal systems*. PhD thesis, Utrecht University, Jan 2012.
- [120] N. V. Kampen, B. Nijboer, and K. Schram, *On the macroscopic theory of van der waals forces*. Phys. Lett. A, 26(7):307, 1968.
- [121] T. Coopmans, T. Besseling, and A. van Blaaderen. Private communication.
- [122] D. S. Bernstein. *Matrix Mathematics: Theory, Facts, and Formulas*. Princeton University Press, second edition, 2009.

Summary

In this thesis, we studied colloids and nanoparticles, which are particles of sizes below roughly $1\ \mu\text{m}$. Because these particles exhibit Brownian motion - erratic motion due to the constant bombardment by solvent molecules - they can efficiently sample phase space. Thus, due to the random “kicks” that characterize Brownian motion, a system of particles can overcome potential barriers and reach its thermal equilibrium position without getting stuck in local equilibria on the way there. Under the right conditions, this thermal equilibrium is an ordered structure and, in these cases, the random process of Brownian motion helps systems of particles to spontaneously assemble into states with a high degree of order. If such an assembly occurs as a result of only Brownian motion and interparticle interactions, we speak of “self-assembly”. In practice, self-assembly is not always feasible, or even desirable, and experimentalists often assist the assembly by, for example, applying external electric fields in order to align the particles, or to induce interparticle interactions that help the assembly.

External electric fields cause insulating matter to polarize, which means that its atoms’ electron clouds get shifted with respect to their nuclei, such that each atom becomes an induced electric dipole with a dipole moment dependent on the strength of the electric field. For small electric fields, an atom’s dipole moment is, in fact, exactly proportional to the local electric field at the site of the atom, where the proportionality constant between the atom’s dipole moment and the local electric field is the atomic polarizability. The polarization of a cluster of atoms (e.g., a colloid) is also linear with the applied electric field but, in this case, the polarizability of the cluster is a tensor. A polarized atom in turn creates an additional electric field in its surroundings, which is felt by all the other atoms and, in this way, multiple atoms can enhance or reduce each other’s polarization and calculating a cluster’s polarizability is therefore a many-body problem. The enhancement factor is defined as the ratio of the “full” cluster polarizability (i.e., taking into account interatomic interactions) to the cluster polarizability if interatomic interactions are ignored, and is thus a measure of the degree to which these interactions enhance or reduce the total polarizability.

In this thesis, we employed the Coupled Dipole Method (CDM) to calculate the polarizability of anisotropic (i.e., nonspherical) particles while taking into account the influence that the atoms exert on each other. As we have shown in this thesis, it is also possible to use the CDM to calculate the potential energy of a configuration of atoms in an external electric field, such that the orientational energy of single clusters as well as the interaction between multiple clusters induced by the external electric field can be calculated. The results of these calculations are described in this thesis.

We also studied the so-called London-Van der Waals force between various particles. This force is a result of the collective ground-state vibrations of the atoms’ dipole moments and is present even in the absence of an external electric field. In a way, it is therefore somewhat of a separate subject from induced polarization and the interaction between polarized particles, which are phenomena occurring only in the presence of an electric field. On the other hand, the London-Van der Waals force does share the property that

it involves interacting induced dipoles (albeit fluctuating ones) and the feature that, like polarizability, it can be calculated using the CDM.

In Chapter 2, we used the CDM to calculate the polarizability and enhancement factor tensor of cuboid-, bowl-, and dumbbell-shaped particles. Using a Hamiltonian approach, we were able to straightforwardly calculate the potential energy of the particles in an external electric field, such that we could investigate their alignment properties. For the various particles, we calculated the potential energy difference between perfect alignment and a perpendicular orientation as a function of the number of atoms composing the particle. We found that this relation is linear, which implies that the difference of the two independent enhancement factor elements is only dependent on the shape of the particle and the material that it is composed of. We found that, for rods and dumbbells, it is energetically favorable to align their rotational symmetry axis along the electric field, while platelets and bowls prefer to align this axis perpendicular to the electric field. Cubes, on the other hand, have no preferred orientation.

In Chapter 3, we focused on spherical and cubic particles, studying their global and local enhancement factor in detail. The global enhancement factor of cubes first increases as a function of the number of rib atoms, then reaches a maximum, and finally decreases again, seemingly decaying to the value predicted by continuum electrostatics. For large cubes, the local enhancement factor was found to vary only as a function of scaled coordinates inside the cube, such that the graphs for different cube sizes collapse on the same curve if the rib length is scaled out of the coordinates. For spheres, the global enhancement factor also seemed to decay to the value predicted by continuum electrostatics but, for the sphere sizes studied, did not come as close as was the case for cubes. The local enhancement factor of the spheres was found to be constant throughout the interior of the sphere, in accordance with continuum electrostatics. Some variation was found at and near the surface, but we were unable to determine whether this dependence would scale with the sphere size, as it did for cubes. In conclusion, using the discrete dipoles of the CDM, the sphere seemed a somewhat more problematic shape to model than the cube but, for both shapes, the CDM and continuum theory did seem to agree well for large cluster sizes. This is a promising result, since it suggests that solving problems for complex electrostatic arrangements could be possible using the CDM.

In Chapter 4, we exploited the linear relation between the orientational energy difference and the atom number in order to extrapolate quantities found for small clusters to much larger clusters. In this way, we could calculate, for typical experimental parameters, the size for which the orientational energy first becomes of the order of the thermal energy, i.e., for which particle size alignment by an electric field first becomes possible. The answer to this question depends on the shape of the particle, but also on the definition of “size”. If it is meant to refer to the number of atoms (or, equivalently, the volume of the particle), it turns out that the more anisotropic the particle, the smaller the size (number of atoms) required for alignment. However, a very anisotropic particle, even though it contains a low number of atoms, may still be very large (e.g., larger than colloidal scales) along one or two of its dimensions. As it turns out, if we define “size” as the length of a particle when measured along the direction of the electric field while the particle is perfectly lined up (i.e., it is in its most favorable orientation), the dependence of the required size for alignment on the particle shape is nontrivial. This is because of a competition be-

tween particle anisotropy, which leads to a high orientational energy difference per atom, and particle bulkiness, which allows more atoms to fit in a particle with a certain size (according to the last-mentioned definition), thus increasing the polarizability and, hence, the orientational energy difference. For each particle type (cuboid, bowl, and dumbbell), we determined the “optimal shape,” i.e., the shape for which the required size parameter for alignment is smallest. The answer was in each case found to lie more or less halfway between extreme anisotropy and extreme bulkiness.

We subsequently turned our attention to interparticle interactions, starting with Van der Waals (VdW) interactions in Chapter 5. In the absence of an electric field, we investigated whether particles, under the influence of only their VdW interactions, prefer to form strings or more compact structures. This is a nontrivial question, since the former could be favorable because dipoles (even fluctuating ones) prefer to lie head-to-toe, while the latter could be favored because it minimizes the distance between pairs of particles. It turned out that, although a local minimum arises at the linear configuration, compact structures are energetically preferred in almost all circumstances. The only setup for which a linear configuration was stable was that of three very strongly interacting inducible point dipoles. We noted that it is not unreasonable to suppose that linear chains are also preferable for interaction strengths higher than the CDM can handle, i.e., beyond the polarization catastrophe.

In Chapter 6, we generalized the CDM somewhat to allow for Lorentz atoms that are not necessarily of atomic proportions. Subsequently, we studied the other type of interparticle interaction that can be calculated using the CDM: the induced dipolar interaction between particles in an external electric field. We gave a formula for the interaction energy between a pair of inducible point dipoles in an external electric field, taking into account the effect one dipole has on the other’s dipole moment. We compared this expression to its first-order Taylor approximation, which turned out to be the result one gets when treating the electric field-induced dipoles as permanent. We then proceeded to calculate the interaction energy of cluster pairs of various shapes in an external electric field, namely spheres, cubes, and rods, and compared the results given by the CDM to those given by various other calculation techniques, in the end arriving at a number of recommendations on which calculation technique to use in which situation.

Chapter 7 contains three separate studies. In the first of these, we investigated the density of states of a straight chain of Lorentz atoms by plotting the number of modes in each frequency interval. We found that the range of frequencies is limited to between 0.6 and 1.2 times the characteristic frequency of the composing Lorentz atoms, and that certain frequencies are preferred over others. We then investigated how this distribution changes when a second chain of atoms is allowed to interact with the first, in order to discover whether certain frequency ranges contribute more to VdW interaction than others. Unfortunately, we were not able to distinguish a pattern indicating which frequencies change and which do not. We proceeded instead to theoretically calculate the density of states of an infinite chain of Lorentz atoms, the result of which agrees well with the numerical results for finite chains.

In the second study of Chapter 7, we investigated the amplitude of vibration of individual modes on interacting squares of Lorentz atoms, and visualized the evolution of the modes as a function of the distance between the squares. As suspected, mainly modes

concentrated near the opposing edges of the squares turned out to contribute to the interaction. However, it was found that as, a function of distance, a mode can transform from an ordinary to a surface mode and vice versa. Therefore, if a mode is found to be a surface mode (and is thus an interacting mode) at one distance, it is not guaranteed that it will still be a surface mode at another distance, such that we again were unable to make predictions about which modes will contribute most to VdW interaction.

In the last study of Chapter 7, we turned our attention to induced dipoles in the presence of a conducting plate. We slightly modified the CDM to include “image dipoles” (in analogy with image charges) and calculated the interaction of a single inducible dipole as well as a chain (rod) of these dipoles with the conducting plate when an external electric field is applied normal to the plate. For the single dipole case, we were able to derive an analytical expression while, for the rod, we found from numerical calculations that, at short distances from the plate, the rod is in a local minimum when lying flat on the plate, although the global minimum is still at the orientation where the rod is aligned with the electric field. This implies that in a system of rods with random orientation near a conducting plate, if an electric field perpendicular to the plate is switched on, and this field is strong enough, a certain percentage of rods near the plate will be captured in this local minimum and will lie flat on the plate, while the rest will align with the electric field.

Samenvatting

In dit proefschrift hebben we colloïden en nanodeeltjes bestudeerd: deeltjes met een grootte beneden ruwweg $1\ \mu\text{m}$. Deze deeltjes ondergaan Brownse beweging - onregelmatige beweging teweeg gebracht door het continue bombardement van de moleculen in het oplosmiddel - en kunnen daardoor hun faseruimte efficiënt verkennen. Door de willekeurige duwtjes die typerend zijn voor Brownse beweging kan een deeltjessysteem dus potentiaalbarrières overwinnen en zijn thermisch evenwicht bereiken zonder vast te komen zitten in een metastabiel evenwicht. In de juiste omstandigheden is het thermisch evenwicht een geordende structuur, en in deze gevallen helpt de willekeurige Brownse beweging systemen zich spontaan te schikken in een toestand met een hoge mate van orde. Als zo'n assemblage zich voordoet als gevolg van alleen Brownse beweging en interactie tussen de deeltjes spreken we van zelfassemblage. In de praktijk is zelfassemblage niet altijd realiseerbaar, of zelfs gewenst, en experimentatoren helpen de assemblage vaak een handje, bijvoorbeeld door externe elektrische velden aan te leggen om de deeltjes in een bepaalde richting te laten wijzen of om interacties tussen de deeltjes teweeg te brengen die de assemblage bevorderen.

Externe elektrische velden zorgen dat isolerende materie polariseert. Dat betekent dat de elektronenwolken van de atomen verschoven worden ten opzichte van hun nucleus, zodat elk atoom een geïnduceerde elektrische dipool wordt met een dipoolmoment afhankelijk van de elektrische veldsterkte. Voor lage veldsterktes is het dipoolmoment van een atoom zelfs precies evenredig met het lokale elektrische veld op de locatie van het atoom. De evenredigheidsconstante tussen het dipoolmoment van het atoom en het lokale elektrische veld heet de atoompolariseerbaarheid. Ook de polarisatie van een cluster van atomen (bijvoorbeeld een colloïde) is lineair evenredig met het aangelegde elektrische veld, maar in dit geval is de polariseerbaarheid van het cluster een tensor. Een gepolariseerd atoom brengt op zijn beurt een extra elektrisch veld teweeg in zijn omgeving, hetgeen gevoeld wordt door alle andere atomen. Op deze manier kunnen meerdere atomen dus elkaars polarisatie versterken of verzwakken en het uitrekenen van een clusterpolarisatie is daarom een veeldeeltjesprobleem. De versterkingsfactor is gedefinieerd als de verhouding tussen de 'volledige' clusterpolariseerbaarheid (die rekening houdt met wisselwerkingen tussen atomen) en de clusterpolariseerbaarheid als interatomaire interacties genegeerd worden. Hij meet dus in hoeverre deze interacties de totale polariseerbaarheid versterken of verzwakken.

In dit proefschrift hebben we de Coupled Dipole Method (CDM) gebruikt om de polariseerbaarheid van anisotrope (dat wil zeggen niet-bolvormige) deeltjes te berekenen waarbij we rekening hielden met de invloed die de atomen op elkaar uitoefenen. Zoals we lieten zien in dit proefschrift is het ook mogelijk om de CDM te gebruiken om de potentiële energie van een configuratie van atomen in een extern elektrisch veld uit te rekenen, zodat de oriëntationele energie van enkele clusters alsook de interactie tussen meerdere clusters geïnduceerd door het externe elektrische veld berekend kan worden; de resultaten hiervan staan beschreven in dit proefschrift.

We hebben ook de zogenaamde London-Vanderwaalskracht tussen verscheidene deeltjes bestudeerd. Deze kracht is het gevolg van de collectieve grondtoestandsvibraties van de dipoolmomenten van de atomen en bestaat zelfs in afwezigheid van een extern elektrisch veld. Zodoende is het dus min of meer een afzonderlijk onderwerp van geïnduceerde polarisatie en de interactie tussen gepolariseerde deeltjes, welke fenomenen zich alleen voordoen in de aanwezigheid van een elektrisch veld. Met de interactie tussen gepolariseerde deeltjes deelt de London-Vanderwaalskracht echter wel de eigenschap dat interagerende geïnduceerde dipolen (ofschoon fluctuerend) erbij betrokken zijn, alsook het kenmerk dat hij uitgerekend kan worden met behulp van de CDM.

In Hoofdstuk 2 gebruikten we de CDM om de polariseerbaarheid en versterkingsfactor van balk-, kom-, en dumbbellootvormige deeltjes uit te rekenen. Met behulp van de Hamiltoniaan van het systeem waren we in staat eenvoudig de potentiële energie van de deeltjes in een extern elektrisch veld te berekenen, zodat we eigenschappen met betrekking tot het richten van deze deeltjes konden onderzoeken. Voor verscheidene deeltjes hebben we het verschil in potentiële energie uitgerekend tussen de oriëntatie waarbij het deeltje perfect gericht is door het elektrisch veld en een oriëntatie loodrecht hierop, als functie van het aantal atomen in het deeltje. We ontdekten dat deze relatie lineair is, hetgeen erop wijst dat het verschil tussen de twee onafhankelijke versterkingsfactorelementen alleen afhangt van de vorm van het deeltje en het materiaal waar het deeltje uit bestaat. We vonden ook dat het voor staven en dumbbells energetisch voordelig is om hun rotatiesymmetrieas te richten naar het elektrisch veld, terwijl platen en kommen deze as liever loodrecht op het elektrisch veld richten. Kubussen hebben helemaal geen voorkeursoriëntatie.

In Hoofdstuk 3 richtten we onze aandacht op bolvormige en kubusvormige deeltjes en bestudeerden we hun globale en lokale versterkingsfactor grondig. De globale versterkingsfactor van kubussen wordt eerst groter als functie van het aantal atomen op de rib, bereikt een maximum en wordt dan weer kleiner, schijnbaar afvallend naar de waarde voorspeld door continuümelektrostatica. Voor grote kubussen bleek de lokale versterkingsfactor alleen te variëren als functie van geschaalde coördinaten in de kubus, zodat de grafieken voor verschillende kubusgrootten op dezelfde curve vallen als de riblengte uit de coördinaten wordt geschaald. Voor bollen leek de globale versterkingsfactor ook af te vallen naar de waarde die continuümelektrostatica voorspelt, maar kwam voor de bestudeerde bolgroottes niet zo dichtbij als het geval was voor kubussen. De lokale versterkingsfactor van de bollen bleek binnenin constant, hetgeen in overeenstemming is met continuümelektrostatica. We vonden wel wat variatie op en nabij het oppervlak van de bol, maar we konden niet bepalen of deze afhankelijkheid voor grote bollen zou meeschalen met de bolgrootte, zoals het geval was bij kubussen. We kunnen dus concluderen dat, gebruik makend van de discrete dipolen van de CDM, de bolvorm ietwat problematischer te modelleren was dan de kubus maar dat voor beide vormen de CDM en continuümtheorie goed overeenkomen voor grote clusters. Dit is een hoopgevend resultaat omdat het erop wijst dat het oplossen van problemen voor complexe elektrostatiche opstellingen mogelijk zou kunnen zijn met behulp van de CDM.

In Hoofdstuk 4 maakten we gebruik van het lineaire verband, gevonden in Hoofdstuk 2, tussen het oriëntationele-energieverschil en het aantal atomen, om grootheden gevonden voor kleine clusters te extrapoleren naar veel grotere clusters. Op deze manier konden we voor typische experimentele parameters de deeltjesgrootte uitrekenen waarvoor het

oriëntationele-energieverschil voor het eerst van de orde van grootte van de thermische energie wordt, dat wil zeggen, voor welke deeltjesgrootte het voor het eerst mogelijk wordt het deeltje te richten met een elektrisch veld. Het antwoord op deze vraag hangt af van de vorm van het deeltje, maar ook van de gebruikte definitie van ‘grootte’. Als met deze term het aantal atomen bedoeld wordt (gelijkwaardig aan deze definitie is de inhoud van het deeltje) dan blijkt: hoe anisotroper het deeltje, hoe kleiner de grootte (aantal atomen) noodzakelijk voor het richten. Een zeer anisotroop deeltje kan echter zeer grote (groter dan colloïdaal) fysieke afmetingen hebben gemeten langs één of twee richtingen, ook al is het aantal atomen klein. Als we de ‘grootte’ definiëren als de lengte van het deeltje gemeten langs de richting van het elektrisch veld terwijl het deeltje perfect gericht is naar het elektrisch veld (dus als het deeltje de meest gunstige oriëntatie heeft), blijkt dat het verband tussen de benodigde grootte voor het richten van het deeltje en de vorm van het deeltje niet meer triviaal is. Dan ontstaat namelijk rivaliteit tussen een hoge anisotropie, hetgeen leidt tot een hoog verschil in oriëntationele energie per atoom, en een grote dikte, hetgeen ervoor zorgt dat meer atomen in een deeltje met een bepaalde grootte (volgens de laatstgenoemde definitie) passen, waardoor de polariseerbaarheid en dus het oriëntationele-energieverschil verhoogd wordt. Voor elk deeltjestype (balk, kom en dumbbell) hebben we bepaald wat de ‘optimale vorm’ is, namelijk de vorm waarvoor de benodigde grootte (volgens de laatstgenoemde definitie) voor het richten van het deeltje zo klein mogelijk is. Het antwoord lag voor elk deeltjestype min of meer halverwege tussen extreme anisotropie en extreem grote dikte.

Vervolgens richtten we ons op wisselwerkingen tussen deeltjes, beginnend met de Vanderwaalsinteracties (VdW) in Hoofdstuk 5. In afwezigheid van een elektrisch veld onderzochten we of deeltjes onder invloed van alleen hun Vanderwaalsinteracties liever kettingen vormen of compactere structuren. Dit is geen triviale vraag aangezien kettingen gunstiger zouden kunnen zijn omdat dipolen (zelfs fluctuerende) liever kop-staart liggen, terwijl de compactere structuren gunstiger zouden kunnen zijn omdat ze de afstand tussen deeltjesparen minimaliseren. Hoewel een lokaal minimum zich voordoet bij de lineaire configuratie, bleken compacte structuren bijna altijd energetisch gunstiger te zijn. De enige situatie waarvoor we een stabiele lineaire configuratie vonden was er één met drie zeer sterk interagerende induceerbare puntdipolen. We merkten op dat het niet onredelijk is om te veronderstellen dat lineaire kettingen ook de voorkeur hebben bij interactiesterktes hoger dan ondersteund door de CDM, dus voorbij de polarisatiecatastrofe.

In Hoofdstuk 6 generaliseerden we de CDM enigszins om Lorentz-atomen toe te laten die niet noodzakelijkerwijs atomaire afmetingen hebben. Vervolgens bestudeerden we de andere deeltjesinteractie die uitgerekend kan worden met de CDM: de geïnduceerde dipoolinteractie tussen deeltjes in een extern elektrisch veld. We leverden een formule voor de interactie-energie tussen twee induceerbare puntdipolen in een extern elektrisch veld, waarbij we rekening hielden met de invloed die het ene dipool uitoefent op het dipoolmoment van het andere. We vergeleken deze uitdrukking met zijn eerste-orde Taylorbenadering, welke het resultaat bleek te zijn dat men verkrijgt door de geïnduceerde dipolen te behandelen alsof ze permanente dipolen zijn. Vervolgens berekenden we de interactie-energie van clusterparen van verscheidene vormen in een extern elektrisch veld, namelijk bollen, kubussen en staven, en vergeleken de resultaten gegeven door de CDM

met resultaten uit allerlei andere rekenmethoden, om uiteindelijk te komen tot een aantal aanbevelingen, welke methode te gebruiken in welke situatie.

Hoofdstuk 7 bevat drie afzonderlijke onderzoeken. In het eerste onderzochten we de toestandsdichtheid van een ketting van Lorentz-atomen door het aantal normale trillingsmodes in elk frequentie-interval te plotten. We vonden dat het bereik van de frequenties beperkt is tot een interval tussen ongeveer 0.6 en 1.2 keer de karakteristieke frequentie van de Lorentz-atomen, en dat bepaalde frequenties de voorkeur hadden boven andere. Daarna onderzochten we hoe deze distributie verandert als we een tweede ketting van atomen laten interageren met de eerste, om uit te vinden of bepaalde frequentie-intervallen meer bijdragen aan VdW-interactie dan andere. Helaas waren we niet in staat een patroon te vinden dat voorspelt welke frequenties veranderen en welke niet. In plaats daarvan berekenden we vervolgens theoretisch de toestandsdichtheid van een oneindige ketting van Lorentz-atomen, waarvan het resultaat goed overeen komt met de numerieke resultaten voor eindige kettingen.

In het tweede onderzoek van Hoofdstuk 7 bestudeerden we de vibratieamplitude van individuele modes op interagerende vierkanten van Lorentz-atomen, en brachten we de evolutie van deze modes in beeld als functie van de afstand tussen de vierkanten. Zoals al werd vermoed bleken vooral modes die geconcentreerd waren nabij de tegenoverliggende randen van de vierkanten bij te dragen aan de interactie. We ontdekten echter ook dat als functie van de afstand een mode kan transformeren van een gewone mode tot zo'n randmode en vice versa. Als gevonden wordt dat een mode een randmode (dus een interactiemode) is bij een bepaalde afstand, kunnen we dientengevolge dus niet garanderen dat de mode ook een randmode is bij een andere afstand, zodat het alweer niet mogelijk was om voorspellingen te doen welke modes het meest aan VdW-interactie zullen bijdragen.

In het laatste onderzoek van Hoofdstuk 7 richtten we ons op geïnduceerde dipolen in de nabijheid van een geleidende plaat. We pasten de CDM een weinig aan om 'beelddipolen' (in analogie met beeldladingen) te omvatten en rekenden de interactie uit tussen een enkele induceerbare dipool alsook een ketting (staaf) van deze dipolen en de geleidende plaat. Voor het enkele dipool leidden we een analytische uitdrukking af voor de interactie-energie, terwijl we voor de staaf met numerieke berekeningen ontdekten dat bij kleine afstanden van de plaat de staaf zich in een lokaal minimum bevindt als hij plat op de plaat ligt; het globale minimum doet zich echter wel nog steeds voor als de staaf gericht is naar het elektrisch veld. Dit wijst erop dat als in een systeem van staven met een willekeurige oriëntatie en een geleidende plaat een elektrisch veld aan wordt gezet loodrecht op de plaat, en dit veld sterk genoeg is, een bepaald percentage van de staven dichtbij de plaat gevangen zal worden in dit lokale minimum en dus plat op de plaat zal liggen, terwijl de rest zich zal richten naar het elektrisch veld.

Acknowledgments

Well, here I am, writing the last few paragraphs of my PhD thesis. After four years of research in the SCM group (and ten at Utrecht University), my days here are drawing to an end. A good opportunity, therefore, to thank a number of people who have helped me along the way, and without some of whom this thesis would never have been written in the first place.

First on the list of people to thank, naturally, come my supervisors, René van Roij and Marjolein Dijkstra. René I encountered first, him being the lecturer for the Thermal Physics course I followed in my second year as a Bachelor student. I met him again at the Soft Condensed Matter Theory Masters course, but he only met me when I asked him to be my supervisor for my Masters research. He did not disappoint as a supervisor and so, when he offered me a PhD position, I quickly accepted. One sometimes hears that people can be very different as lecturers and as supervisors, but for René this is not the case. The inspiring enthusiasm and vitality he displays when he lectures are there just as much when he supervises, making him a very motivating person to be around; add a pinch of grand (sometimes unattainable) vision, and you have “idea machine” René.

Marjolein taught a part of my third-year Thermal Physics course, but I only really met her when I started my PhD research. In some ways, her supervisory style is complementary to René’s: with her practical, down-to-earth approach she helps projects move along; moreover she is more of a listener than a talker: in our joint meetings, René and I would usually do most of the talking while she would be listening and regularly interjecting remarks both smart and knowledgeable to move our discussion along or to correct mistakes we were making. She has an extensive knowledge of the scientific literature and is very skilled at connecting different studies. She was the supervisor nearest to my office and hence the person I would go to with various small questions that popped up and, if she did not happen to be in some other meeting, she literally always made time for me, which I very much appreciate.

I would furthermore like to thank Alfons van Blaaderen, Arnout Imhof, and Laura Filion for the various useful discussions, Judith Wijnhoven for putting up with my chemical garden in the Lab, Peter Helfferich for technical support, Marijn van Huis for getting me to present at the nanoseminar, and all the staff in general for making the SCM group the productive scientific group that it is.

Of the (former) (PhD or postdoc) students in the group, I would like to thank a lot of people. Joost de Graaf for steering me in the direction of soft condensed matter in the first place, for the excellent dinners I have enjoyed at his place at various times, for all the wine brought to my place every time he came over, for his help here and there during my PhD, and just for being my friend. Matthieu Marechal for his help in the first few months of my PhD. Teun Vissers for the legendary road trip to Granada, for which I also would like to thank the other participants Laura (again) and Niels Boon; and for the various times we played squash and subsequently had beer at Olympos, for the climbing frenzy that ensued after that, for the various beers we had with no sport preceding it, and for the humor we shared; thank you, also in name of the wife of Aariel Vrets. Kristina

Milinković, for the good times at the pub or over dinner, and for introducing me to your various friends, one in particular. Anjan Gantapara, Thijs Besseling, and Simone Dussi for occasionally dragging me out of my office to lunch. Henriëtte Bakker, Anjan (again), and John Edison for the fun times at the frisbee competition.

A special thanks goes out to my office mates Peter van Oostrum, Bo Peng, Linh Tran, Matthew Dennison, Henriëtte Bakker, and Rik Koster for making my office such a pleasant place to work in. Sorry for my messy desk, I will clean it up soon. Bo I would additionally like to thank for sharing his experience with the ins and outs of the promotion trajectory, for being my office mate for such a very long time, for our joint (sadly, failed) chemical garden project, and for the various interesting conversations we had about Chinese and Dutch culture. Matthew also gets an extra thanks for the spent pub time and for completing the “bridge club” of him, Kristina, Marina, and me, even though little bridge was played.

All of the above, as well as Johan, Marlous, Bart, Frank, Michiel, Anke, Marjolein van der Linden, Wessel, Nina, Simone Belli, Jissy, Nick, Wiebke, Arjen, Ahmet, Rao, Ran, Carlos, Ernest, Guido, and Thomas are thanked for the coffee breaks, lunches, and/or pub times we shared.

I would also like to thank all of my friends in (or from) Utrecht, Leiden, and abroad for the good times. My family, and especially my dad, mother, and brother are thanked for the help and support they could offer. My mom I would like to thank again for editing the Dutch summary of this thesis. And last, but most certainly not least, I would like to thank Marina Peneva, for editing the entirety of this thesis: there is not an English sentence in it that is not edited by her. But most of all I thank her for her love, support, understanding, patience, and generally for being so bubbly.

About the Author

Bas Kwaadgras was born in Dordrecht on August 2, 1985. He attended primary school De Driehoek there, until moving to Voorschoten at age 7, where he finished his primary education at Nutsbasisschool Voorschoten. After graduating from Stedelijk Gymnasium Leiden in 2003, he enrolled in the Physics & Astronomy Bachelor's program at Utrecht University, which he finished (cum laude) in 2006. At the same university, he went on to follow the Master's program Theoretical Physics, where he obtained his degree in 2009. His Master's research project on the subject of charge-patterned surfaces in a dielectric solvent was supervised by Prof. Dr. R. van Roij at the Institute for Theoretical Physics. Following this, in September 2009, he started his PhD research under the supervision of Prof. Dr. Ir. M. Dijkstra and Prof. Dr. R. van Roij at the Soft Condensed Matter Group of the Debye Institute for Nanomaterials Science. The result of this research is this thesis. At the time of writing, Bas has published three papers on the subject matter of this thesis in a peer-reviewed scientific journal, while more are in preparation. During his time as a PhD student, Bas has given oral and poster presentations at national and international conferences. He has also served as a teaching assistant for an undergraduate Statistical Physics course.